Optical and Electronic Properties of Atomically Thin Transition-Metal Dichalcogenides

Daniel Erben
University of Bremen

Optical and Electronic Properties of Atomically Thin Transition-Metal Dichalcogenides

dem Fachbereich Physik/Elektrotechnik
der Universität Bremen

zur Erlangung des akademischen Grades
Doktor der Naturwissenschaften (Dr. rer. nat)
genehmigte Dissertation

vorgelegt von
M. Sc. Daniel Erben
aus Bremen

1. Gutachter:	Prof. Dr. Frank Jahnke, Universität Bremen
2. Gutachter:	Prof. Dr. Caterina Cocchi, Universität Oldenburg

Eingereicht am:	21.02.2020
Tag des Promotionskolloquiums:	22.05.2020

Bremen, den 21.02.2020

Abstract

Two-dimensional semiconducting monolayers of transition metal dichalcogenides (TMDs) are of pivotal interest due to their fascinating optical and electronic properties. High optical yield, the direct band gap, sensitivity to the surrounding material or strain, and the ability to stack various heterostructures by exfoliation techniques opens up new possibilities for device concepts. The promising properties originate from the exceptionally strong Coulomb interaction between charge carriers due to the two-dimensional geometry and weak dielectric screening. It is necessary to analyse the interplay of many-body Coulomb interaction effects in order to provide a microscopic understanding of the underlying physics.

High densities of excited charge carriers populating the band structure valleys cause strong renormalizations that are investigated in this thesis for the typical monolayer TMDs MoS_2, $MoSe_2$, WS_2 and WSe_2. The semiconductor Bloch equations are evaluated, including many-body Coulomb interaction. Excitation-induced band structure renormalizations cause a transition from direct to indirect band gaps, which drains carriers from the bright optical transition to dark states. Thus the advantageous properties of a direct gap semiconductor vanish with increasing carrier density, which has strong implications for optical applications such as TMD nanolasers.

Monolayer TMDs are often studied in experiments that involve photoexcitation of charge carriers, which requires the knowledge of the charge carrier density in order to interpret the results. Estimating the density from the linear absorption coefficient is a common yet misleading concept that does not reflect optical non-linearities emerging at elevated pump power. Here, the evaluation of the population dynamics for a non-equilibrium state provides insight into the fluence dependence of the photoexcited density, which originates from the balance between Pauli-blocking and band structure renormalizations as well as scattering processes that dominate in a different regime.

The stacking of TMD layers to build van der Waals heterostructures has opened a growing field of research. TMD heterobilayers of type-II band-alignment exhibit interlayer excitons (ILX) that are characterized by spatial separation of electron and hole and long lifetimes. The twist angle between the two layers provides further possibilities to tailor the bilayer properties. The dependence of the ILX lifetime on the twist angle and the temperature is analysed in detail, revealing the physics behind indirect Moiré excitons.

Contents

1. Introduction

Semiconductor nanostructures are the core element of modern electronic devices. The urge for miniaturization in order to build smaller and faster devices such as microchips is a driving force in scientific research. Lowering the dimensionality from two-dimensional quantum-wells to zero-dimensional quantum dots and employing techniques to build nanostructures of different band alignments provide possible ways to tailor the electronic confinement for many applications. Layered materials have proven to be a promising new material class for a manifold of different applications in the two-dimensional limit. They challenge common semiconductors by offering simple functionalization possibilities, e.g. building heterostructures, in combination with high optical yield.

Since the first success in exfoliating and analyzing an atomically thin layer of graphene [1] in 2004, the class of two dimensional materials has been vastly expanded and investigated [2]. In 2010, the Nobel Prize in physics was awarded to Geim and Novoselov for their exfoliation technique and investigation on graphene [1, 3]. This material is the sp^2 hybridized form of a carbon crystal. Mechanically stability is given due to the covalent intralayer bond of the carbon atoms. Graphene forms a honeycomb lattice [4], which is a typical lattice form for 2d materials. It exhibits a linear dispersion relation near the edges of its hexagonal Brillouin zone, where two so-called Dirac-cones meet at the $\mathbf{K}$-point, causing a quasi-metallic behaviour (no band gap). The bulk crystal of graphene is called graphite, which is a prominent example for the layered nature of 2d materials. In graphite, the single layers of graphene are weakly bound by van der Waals-forces. Thus, exfoliation techniques provide a fairly easy method to prepare samples [1]. Graphene has also been cast into different forms other than a plain monolayer, e.g. also carbon nanotubes formed by rolled up graphene sheets have gained interest, as their electronic properties can be varied from metallic to semiconducting. Being a semi-metallic two-dimensional material, the conductance of graphene is very high. Thus it is often used to contact semiconductor devices. For electronic applications of graphene, progress has come to devices including quickly chargable batteries [5] and functional beyond-silicon microchips [6] using carbon nanotube field effect transistors (CNFETs).

The search for other 2d materials with different electronic properties has revealed a variety of isolating, (semi)metallic and semiconducting 2d materials [2]. This work focusses on semiconducting 2d materials, which can be produced by combining distinct transition metals such as molybdenum or tungsten with chalcogen atoms such as sulfur, selen or tellur, giving rise to the name transition metal dichalcogenides (TMDs). Among the most prominent representants of TMDs are MoS_2, $MoSe_2$, WS_2 and WSe_2. Though they have been of interest for years, this interest was limited merely to dry lubricants [7]. Thinned down to a monolayer, these TMDs show promising optical and electronic properties. The strong optical yield of these layers was first investigated by Mak et al. [8]. In contrast to their bulk crystal, TMDs exhibit a direct band gap [9] as monolayer. Due to the presence of other band structure valleys that are energetically close to the $\mathbf{K}$-valley, it is still debated whether these materials really have a direct gap [10, 11].

Other 2d materials of interest are hexagonal boron nitride (hBN), which is insulating and thus an ideal buffer material to encapsulate TMD samples [12]. $NbSe_2$ [13, 14] or $ReSe_2$ [15, 16] are examples for metallic TMDs that show interesting physics in terms of charge density waves and superconductivity. Also monolayers of non-layered III-IV semiconductors such as InSe have been synthesized [17]. The layered structure of van der Waals-bound materials can be utilized to tailor the material properties [2]. By stacking different monolayers on top of each other, so-called van der Waals heterostructures are built. These heterostructures are of recent interest as phenonema such as superconductivity [18] and long-lived delocalized electron-hole pairs [19] have been observed.

The direct band gap in the visible spectrum and the high optical yield render TMD monolayers as suitable candidates for optoelectronic device application [20, 21]. Due to their two-dimensional geometry Coulomb interaction within TMD monolayers is weakly screened. Thus, TMD monolayers are very susceptible to electric fields and environmental screening and show prominent features of strongly bound many-particle complexes such as bright and dark excitons, trions and biexcitons even at room temperature. Many experiments using TMDs as active material of a device have been performed. Among these devices are light-emitting diodes (LEDs) [22–25], solar cells [22, 23] or TMD lasers [26–30]. Flexible electronics have been a field of further experimental interest [31]. Such typical experiments aim for controlling the properties of the electrons in terms of confinement and carrier separation. In addition to this, the properties of the TMD monolayers are also shaped by the presence of photoexcited carriers due to quasi-particle renormalization effects, dephasing, and the interplay of excitons and unbound carriers [32–36]. Further mechanisms that affect the electronic and optical properties are dielectric screening from the substrate [37, 38] and strain [39–41] that can lead to a transition from a direct to an indirect band gap. Spin–orbit coupling also plays a crucial role, as for example with tungsten-based TMD monolayers the

lowest transition is spin-forbidden and therefore dark [42, 43]. On the other hand, the lack of inversion symmetry within the crystal, gives rise to a new degree of freedom in terms of spin-valley locking of charge carriers, which opens up the field of valleytronics [44–46].
Considering the magnitude of the Coulomb interaction that is characteristic for TMD monolayers, many-particle effects from excited carriers are strong in these materials. The question remains, how renormalization effects due to the presence of excited charge carriers influence the electronic properties. Existing preliminary work [47] will therefore be expanded in this thesis in order to shed light on the expected loss of the direct transition under device conditions.
The various Coulomb bound many-particle complexes exhibit distinct shifts in the presence of excited charge carriers. In order to gain understanding of the underlying physics, techniques of optical spectroscopy are used [48, 49]. Such techniques involve the photoexcitation of charge carriers, that end up filling the band structure valleys. The density of excited charge carriers is therefore a decisive parameter for describing many-body effects. As the interpretation of experiments usually requires comparison with microscopic theories, the knowledge of the density is essential. The accumulation of density for exciting lasers pulses of different power is therefore explored in this work.
The stacking of TMD monolayers with different band gaps has recently gained interest in experimental and theoretical studies [19, 50, 51]. Long-lived interlayer excitons emerge from heterobilayers with type-II band-alignment, where the band edges are located in different layers. A rotation between both layers produces a periodic variation of the band gap that provides an electronic superlattice. This directly influences the properties of interlayer excitons and provides a design parameter unique to van der Waals heterostructures. Further investigation on the angle-dependence of the lifetime is thus of high interest and will be subject to this work.

Outline of this Thesis

The overarching goal of this thesis is to shed light on the many-body interactions between excited charge carriers and the optical response of TMD monolayers upon photoexcitation. Due to the enhanced Coulomb interaction that prevails in TMD monolayers, the interacting particles are expected to cause significant changes of the optical and electronic properties of TMDs.
In Chap. (2) the real- and reciprocal-space properties of TMD crystal will be briefly described together with the optical properties. Leaving this introductory chapter, the single-

particle properties of TMD monolayers are subject to Chap. (3). The theory for obtaining the ground state properties - the band structure - is derived using two approaches of different nature: the tight-binding approximation and the DFT+GW method. Proceeding from the single-particle properties, the many-particle interactions of excited charge carriers are subject of Chap. (4). Using the formalism of non-equilibrium Green's functions, the semiconductor Bloch equations are derived. The many-body Coulomb interaction is described by the screened exchange Coulomb hole-approximation. Consecutive sections are devoted to screening, carrier scattering and light-matter interaction. In combination these sections describe the foundation of the theory used throughout this work. Using band structures obtained from DFT+GW calculations, the optical response of TMD monolayers to either pump or probe lasers is described by the semiconductor Bloch equations. The results obtained from this theory are presented in the remaining chapters of this work. In Chap. (5) basic properties of the exciton eigenvalue problem with and without magnetic fields are discussed. In the sense of pump and probe experiments, Chap. (6) describes the density-dependent optical response of monolayer TMDs by probing absorption spectra using a weak ultrashort laser pulse together with a detailed analysis of the band structure renormalizations. Subsequently, the power-dependence of the charge carrier density induced by a pump laser is subject to Chap. (7). Finally, Chap. (8) is dedicated to the description of TMD bilayer systems. These host long-lived interlayer excitons whose properties are shaped by the Moiré periodicity of the twisted layers. The influence of the Moiré superlattice on the ground state properties is analyzed. Successively a description of angle- and temperature-dependent lifetime of interlayer excitons is derived and discussed in detail. This thesis is concluded in Chap. (9), which also provides future perspectives and possible expansions of the theory presented.

2. Basic Properties of Transition Metal Dichalcogenides

TMDs are part of the class of layered 2d materials. Within the atomically thin layers transition metal atoms and chalcogen atoms are covalently bound, giving rise to a high mechanical stability. The different layers are weakly bound by van der Waals-forces, thus the bulk crystal is comparable to graphite. Due to the weak van der Waals-bond the neighbouring layers can be easily removed by using tape or polymer stamps [52]. This has been demonstrated first for graphene [53]. Though this is a fairly simple method it does not provide reproducability of the obtained samples in terms of their dimensions. The stacking of different 2d materials is key to the design of new semiconductor devices, forming so-called van der Waals heterostructures [2]. For bilayers system, that are of recent interest in research [18, 19], the exfoliation technique provides control over the twist angle [54]. Chemical vapor deposition (CVD) [55] or molecular beam epitaxy (MBE) [9] are also commonly used growth techniques in the synthesis of TMD monolayers.

After preparation of a sample the number of layers deposited has to be determined. This is often done by Raman spectroscopy, which is sensitive to the eigenmodes of the crystal lattice vibrations [56]. These eigenmodes provide charateristic patterns and shifts for changing the layer number. TMD monolayers provide interesting optical properties such as an increased photoluminescence [8] and strongly bound many-particle complexes [57]. The strong optical yield of a monolayer originates from the direct band gap, which becomes indirect when increasing the number of layers [9, 58]. Due to the small height of a monolayer, the screening of the Coulomb interaction is weak, which gives rise to strongly bound excitons. This chapter shall give a short overview on the crystal structure and optical properties of TMD monolayers.

2.1. Crystal and Reciprocal Space Properties of TMDs

As already shortly explained above TMDs consist of transition metals and chalcogen atoms. These atoms form a quasi 2d lattice with a layer of transition metal atoms in the middle, which is sandwiched between two layers of chalcogen atoms. Thus the general formula is MX_2, with M = Mo, W, ... and X = S, Se, Te and so on. From the top view a honeycomb lattice is formed, because the chalgocen atoms align in z-direction (compare Fig. (2.1a)). This is called the 2H phase of the crystal. Also another stable crystal is the 1T phase, where the chalcogen atoms do not align, which causes a change in the electronic properties from being a semiconductor to metallic behaviour [59].

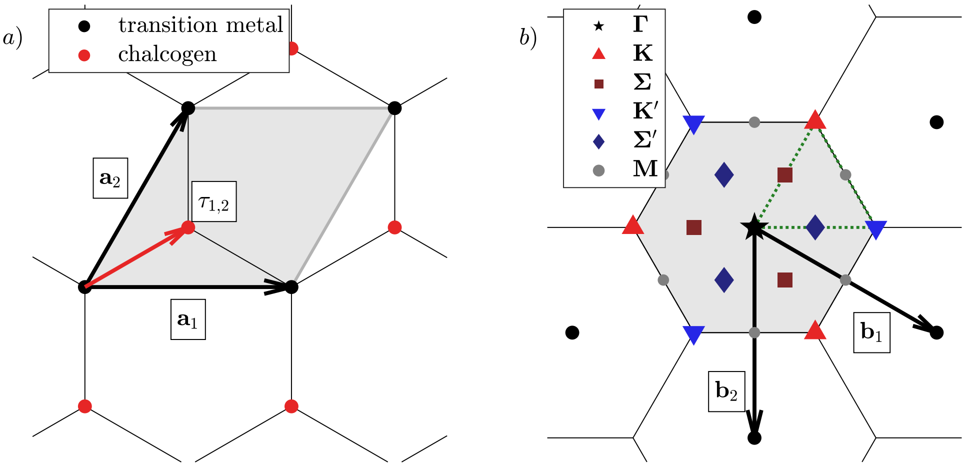

Figure 2.1.: **a)**: Top view of the real space lattice of TMDs forming a honeycomb structure as described in the main text. The chalcogen atoms extend from the shown xy-plane in z-direction. The basis vectors $\mathbf{a}_1$ and $\mathbf{a}_2$ define a possible choice of the unit cell (grey shaded). The position vectors of the chalcogen atoms are labeled by $\tau_{1,2}$. **b)**: The reciprocal lattice is describe by the basis vectors $\mathbf{b}_1$ and $\mathbf{b}_2$. The first Brillouin zone (BZ) has a hexagonal shape. Additionally the points of high symmetry are marked within the first BZ. Symmetries allow for using a sixth of the full BZ (dotted green line).

Crystal lattices are describe as Bravais lattices, which means that the full crystal is formed by periodically repeating one unit cell. Each point of a two-dimensional Bravais lattice $\mathbf{R}$ can be reached by a linear combination of the basis vectors $\mathbf{R}_{uv} = u\mathbf{a}_1 + v\mathbf{a}_2$. In TMDs these vectors are defined as

$$\mathbf{a}_1 = a \begin{pmatrix} 1 \\ 0 \\ 0 \end{pmatrix} \qquad \mathbf{a}_2 = \frac{a}{2} \begin{pmatrix} 1 \\ \sqrt{3} \\ 0 \end{pmatrix} . \tag{2.1}$$

The unit cell is thereby defined with a lattice constant of $a \sim 0.3\text{nm}$ (see Tab. (C.3)). Inside a unit cell one transition metal (M) and two chalcogen atoms (X) are placed at the positions

$$\tau_{\text{M}} = \begin{pmatrix} 0 \\ 0 \\ 0 \end{pmatrix} \qquad \tau_{1,2} = \frac{\mathbf{a}_1 + \mathbf{a}_2}{3} \pm \begin{pmatrix} 0 \\ 0 \\ c \end{pmatrix}, \tag{2.2}$$

where $c \sim a/2$ [60].

For a two-dimensional periodic lattice the reciprocal lattice is defined by the basis vectors $\mathbf{b}_1$ and $\mathbf{b}_2$. These can be obtained as

$$\mathbf{b}_1 = 2\pi \frac{\mathbf{a}_2 \times \mathbf{e}_z}{(\mathbf{a}_1 \times \mathbf{a}_2) \cdot \mathbf{e}_z} \qquad \mathbf{b}_2 = 2\pi \frac{\mathbf{a}_1 \times \mathbf{e}_z}{(\mathbf{a}_1 \times \mathbf{a}_2) \cdot \mathbf{e}_z}. \tag{2.3}$$

In analogy to the real space lattice all lattice points $\mathbf{G}$ of the reciprocal lattice can be reached by $\mathbf{G}_{hk} = h\mathbf{b}_1 + k\mathbf{b}_2$. The unit cell in reciprocal space contains all necessary $\mathbf{k}$ points to fully describe the solid state properties of the crystal. This unit cell is called Brillouin zone (BZ). Chosing the Wigner-Seitz cell, which contains all points closest to the central reciprocal lattice point, the BZ takes a hexagonal shape (see Fig. (2.1)). The symmetry of TMDs defines special BZ points that are marked in Fig. (2.1b). The $\mathbf{K}$-points are the edges of the hexagonal BZ. Due to the lack of inversion symmetry in the crystal structure of TMDS, the $\mathbf{K}$-points can be distinguished in $\mathbf{K}$ and $\mathbf{K}'$. The $\mathbf{M}$-point is at half of a reciprocal basis vector. These points are defined as

$$\mathbf{K} = \frac{\mathbf{b}_1 + \mathbf{b}_2}{3}, \qquad \mathbf{M} = \frac{\mathbf{b}_1}{2}. \tag{2.4}$$

Halfway from $\mathbf{\Gamma}$ to $\mathbf{K}$ the $\mathbf{\Sigma}$-point is found. Though it is not a point of high symmetry an additional valley in the band structure appears (see Sec. 3.4), defining the position of $\mathbf{\Sigma}$. The primed points $\mathbf{K}'$, $\mathbf{\Sigma}'$ can be obtained from the non-primed points via rotation by $60\,°$. These points will later on define the position of the unique band structure valleys that have been found in TMDs (see Chap. (3)).

2.2. Optical Properties of TMDs

Commonly used experimental techniques to optically charaterize TMD monolayers are photoluminescence and pump-probe spectroscopy [39, 48, 49, 61–63]. In photoluminescence the sample is excited with a high energy laser pulse in order to pump charge carriers to the

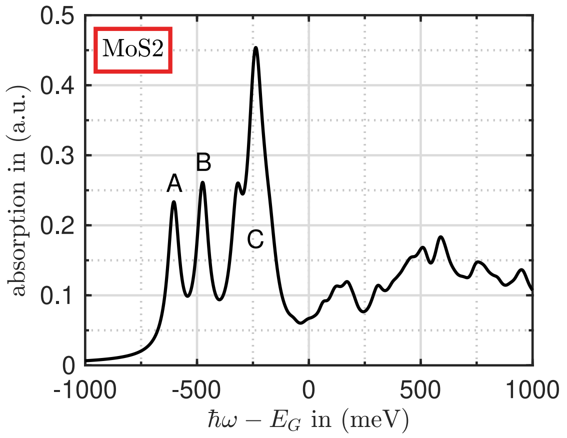

Figure 2.2.: Absorption spectrum of a freestanding MoS_2 monolayer. The three peaks A, B and C dominate the spectrum beneath the quasiparticle band gap. The spectrum has been obtained from the theory presented later on in this thesis.

conduction band. After these carriers have relaxed they recombine with holes in the valence band and emit photons that are spectrally analysed. Photoluminescence is thus sensitive to occupied optical transitions. Pump-probe experiments provide insight on the carrier dynamics. Here a pump laser excites charge carriers to the conduction band that will again scatter to lower-lying states. A second ultrashort and weak laser pulse, that is delayed to the pump pulse, is used as a broadband probe to obtain spectral data such as reflectivity, transmittivity or absorption. The dynamics of the optical response can be measured by varying the delay τ between the two laser pulses.

The absorption spectra of TMD monolayers provide a rich peak structure, which originate from the Coulomb bound many-particle complexes [57]. Bright and dark excitons as well as trions and biexcitons have been observed and identified. A collection of references concerning these many-particle complexes is given here [47, 57, 64–80]. The two most promiment peaks, labeled A and B exciton, originate from the direct transitions at the $\mathbf{K}$- and $\mathbf{K}'$-valley of the band structure. At the $\mathbf{K}$- and $\mathbf{K}'$-valley efficient light-matter coupling occurs for TMDs. The spin-up (down) $\mathbf{K}$- and $\mathbf{K}'$-valleys are energetically separated due to the spin-orbit interaction that causes a splitting of the valence-band states [81]. This makes the $\mathbf{K}$- and $\mathbf{K}'$-valley selectively addressable [35, 46] by choosing the respective polarization of the incident light. Due to the strong Coulomb interaction the binding energies of excitons in TMDs are on the order of 0.5 eV [47, 57, 64, 73]. The A and B exciton wave function are localized in the $\mathbf{K}/\mathbf{K}'$-valleys. Besides the A and B peaks a third peak is present, the so-called C-exciton [82]. The C-exciton is higher in energy but comparably strong bound as A and B. The ring-shaped wave function centered around the $\mathbf{\Gamma}$-point has its maximum between $\mathbf{\Gamma}$

and M.

The strong Coulomb interaction enables the tuning of the band gap due to the dielectric environment [37, 83] or strain [41, 84]. An often overlooked fact is that the interaction of excited charge carriers cause comparably strong shifts within the band structure [33, 85, 86]. Not only the band structure is subject to renormalizations, also the excitons shift and bleach [32, 34].

In order to gain detailed insight in the many-body effects that occur due to the interaction of excited charge carriers, this work starts by analysing the single-particle energies of the TMD monolayer in the ground state. Different methods to obtain the band structure as well as a general description of the band structure itself are part of the following chapter.

3. Band Structures of TMD Monolayers

In order to calculate many-particle effects of excited carriers it is necessary to know the ground state properties of the investigated system. These are the band structure of the crystal as well as the corresponding crystal wave functions. For an *ab-initio* band structure calculation, the state-of-the-art theory to use is the density functional theory (DFT+GW). The DFT makes use of the Hohenberg Kohn theorems, which state that the electronic ground state is a unique functional of the electron density. While this approach is numerically feasible for systems of some tens to hundreds of atoms, it becomes (numerically) very demanding to extend this method to large nanostructures. There are faster approaches available which are able to describe large structures. In contrast to DFT, these methods need more approximations which in turn have to be justified for the application on nanostructures.
The first method to be described in this chapter is the *tight-binding approximation* (TB) that makes use of the strong localization of the electrons to their host atoms in the crystal. This method relies on a set of assumptions and approximations that will be explained in the first part of this chapter. The TB-method can also be utilized for large nanostructures. The second method described here uses a DFT calculation as input for a *Wannier interpolation*. This method is comparably fast and mathematically similar to the TB-method. Therefore it can be seen as TB-ansatz with incorporated DFT wave functions which provides an advantageous starting point for many-body calculations of excited carriers.

3.1. Tight-Binding Description of TMD Band Structures

The TB-approximation [87, 88] is a method to describe the band structure of bulk crystals or nanostructures. The single-particle energies that form the band structure can be calculated for huge lattices of atoms in periodic supercells. Starting points are isolated atoms with strongly localized wave functions (that do not have to be known explicitly). These states are modified by the potential of the atoms on the periodic crystal grid, thereby inducing an interaction between adjacent sites that decreases with increasing distance. This corresponds to assuming tightly bound electrons and is the origin of the name of the method. The fundamental idea is to solve a single-particle Schrödinger equation where an electron is cast into the potential landscape of the crystal structure. Hence, Bloch's theorem is utilized, stating that wave functions on a periodic lattice of atoms can be written as as the product of a lattice-site-dependent phase factor and a periodic function $u_{\mathbf{k}}(\mathbf{r})$:

$$\begin{aligned} \Psi_{\mathbf{k}}(\mathbf{r}) &= e^{i\mathbf{k}\mathbf{r}} \cdot u_{\mathbf{k}}(\mathbf{r}), \\ u_{\mathbf{k}}(\mathbf{r}+\mathbf{R}) &= u_{\mathbf{k}}(\mathbf{r}) \end{aligned} \tag{3.1}$$

This can be illustrated by the fact that on a periodic lattice the eigenstates and eigenvalues on different atomic sites must not change, demanding equal probabilities $|\Psi_{\mathbf{k}}(\mathbf{r})|^2 = |\Psi_{\mathbf{k}}(\mathbf{r}+\mathbf{R})|^2$. Wave functions may therefore only differ by a phase factor.
To obtain the ground state band structure, the single-particle Schrödinger equation for the entire crystal has to be solved. The Hamiltonian of this equation contains the atomic eigenvalue problem and the total potential of all other atoms in the crystal lattice. The TB-wave function that has to fulfill the Bloch theorem. It is constructed as a Bloch sum of localized wave functions $\big|\mathbf{R}, \alpha\big\rangle$ e.g. atomic orbitals, Wannier functions or other basis states:

$$\big|\mathbf{k}, \nu\big\rangle = \frac{1}{\sqrt{N}} \sum_{\mathbf{R}} e^{i\mathbf{k}\mathbf{R}} \big|\mathbf{R}, \nu\big\rangle \qquad \text{with} \tag{3.2}$$

$$\sum_{\mathbf{k},\nu} \big|\mathbf{k}, \nu\big\rangle\big\langle\mathbf{k}, \nu\big| = \mathbb{1} \tag{3.3}$$

Here ν is a combined index, that refers to the atom type, band index, spin, orbital and to a sublattice site. It is common to use only a subset of orbitals, defined by the electron configuration of the material around the Fermi level. The Schrödinger equation for each band states:

$$H\big|\mathbf{k}, \lambda\big\rangle = \varepsilon_{\mathbf{k}}^{\lambda}\big|\mathbf{k}, \lambda\big\rangle\,, \tag{3.4}$$

where the Hamiltonian can be written as the Hamiltonian of an isolated atom plus the potential of all other atoms in the crystal

$$H(\mathbf{r}) = \left(-\frac{\hbar^2}{2m}\nabla^2 + V(\mathbf{r}-\mathbf{R})\right) + \sum_{\mathbf{R}'\neq\mathbf{R}} V(\mathbf{r}-\mathbf{R}')\,. \tag{3.5}$$

The wave function $\big|\mathbf{k}, \lambda\big\rangle$ can be represented by the TB-wave functions defined in Eq. (3.2) which results in $\big|\mathbf{k}, \lambda\big\rangle = \sum_{\mathbf{k},\nu} \big|\mathbf{k}, \nu\big\rangle\big\langle\mathbf{k}, \nu\big|\mathbf{k}, \lambda\big\rangle$, where the TB-coefficients are defined by $\big\langle\mathbf{k}, \nu\big|\mathbf{k}, \lambda\big\rangle = c_{\nu}^{\lambda}(\mathbf{k})$.
Due to the fact that the crystal bonding originates from the overlap of the wave functions

the Bloch sums defined in Eq. (3.2) do not necessarily have to be orthogonal on different lattice sites. There are different ways to overcome this problem, the first is to simply ignore the non-orthogonality by setting the overlap-matrix

$$\mathbf{S}_{\nu\mu} = \big\langle \mathbf{k}, \nu \big| \mathbf{k}, \mu \big\rangle = \frac{1}{N} \sum_{\mathbf{R},\mathbf{R}'} e^{i\mathbf{k}(\mathbf{R}-\mathbf{R}')} \big\langle \mathbf{R}, \nu \big| \mathbf{R}', \mu \big\rangle = \delta_{\nu\mu} + \sum_{\mathbf{R}\neq 0} e^{i\mathbf{k}\mathbf{R}} \big\langle \mathbf{R}, \nu \big| 0, \mu \big\rangle \tag{3.6}$$

to identity or either by performing a so called Löwdin transformation [89]. Here a unitary transformation matrix is defined in a way that the generalized eigenvalue problem originating from the non-orthogonal basis is transformed into a standard eigenvalue problem. Explicitly written the new basis is:

$$\big|\mathbf{k}, \nu\big\rangle = \mathbf{S}_{\nu\mu}^{-\frac{1}{2}} \big|\mathbf{k}, \mu\big\rangle \,. \tag{3.7}$$

The TB-problem can now be solved by diagonalizing the TB-matrix. In order to do so it is essential to calculate the matrix elements of $\mathcal{H}$:

$$\big\langle \mathbf{k}, \nu \big| H \big| \mathbf{k}, \mu \big\rangle = E^{\nu} \big\langle \mathbf{k}, \nu \big| \mathbf{k}, \nu \big\rangle + \frac{1}{N} \sum_{\mathbf{R},\mathbf{R}'} e^{i\mathbf{k}(\mathbf{R}-\mathbf{R}')} \sum_{\mathbf{R}''\neq\mathbf{R}} \big\langle \mathbf{R}, \nu \big| V(\mathbf{R}'') \big| \mathbf{R}', \mu \big\rangle \tag{3.8}$$

where E^{ν} are the energies of the state defined by index ν at place $\mathbf{R}$. Exploiting the constructed orthonormality the equation is transformed into

$$H_{\mathbf{R}\mathbf{R}'}^{\nu\mu} = E^{\nu} + \frac{1}{N} \sum_{\mathbf{R},\mathbf{R}'} e^{i\mathbf{k}(\mathbf{R}-\mathbf{R}')} \sum_{\mathbf{R}''\neq\mathbf{R}} \big\langle \mathbf{R}, \nu \big| V(\mathbf{R}'') \big| \mathbf{R}', \mu \big\rangle \tag{3.9}$$

While solving the integral $\big\langle \mathbf{R}, \nu \big| V(\mathbf{R}'') \big| \mathbf{R}', \mu \big\rangle$, two approximations are common:

i) the two-center-approximation [87] (leading to so called Slater-Koster type TB-models) and

ii) the truncation of neighbouring atoms at a certain distance,

originating from the initial assumption of a rapid decrease of the interaction with increasing distance to the lattice site $\mathbf{R}$. Both approximations take advantage of the fact that the wave functions of the tightly bound electrons approach zero as fast as the potential itself. Thus the two-center-approximation takes only integrals into account where one wave function and the potential are evaluated at the same $\mathbf{R}$ so that e.g. $\mathbf{R} = \mathbf{R}'' \neq \mathbf{R}'$. Integrals with $\mathbf{R} \neq \mathbf{R}' \neq \mathbf{R}'' \neq \mathbf{R}$ are completely neglected and integrals with $\mathbf{R} = \mathbf{R}' \neq \mathbf{R}''$ contribute only a constant value being equivalent to the expectation value of the total potential of all atoms and are successively set to zero. Applying these approximations one is left with

$$H^{\nu\mu}_{\mathbf{R}\mathbf{R}'} = E^{\nu} + \sum_{\langle \mathbf{R}\neq 0\rangle} e^{-i\mathbf{k}\mathbf{R}} \big\langle \mathbf{R}, \nu \big| V(\mathbf{R}) \big| \mathbf{0}, \mu \big\rangle \,. \tag{3.10}$$

Here $\langle \mathbf{R} \neq 0\rangle$ denotes that the sum is only to be taken to a specific order of neighbouring atoms. The remaining task is to calculate the integral term in Eq. (3.10). The integral describes the bonding between neighbouring atoms although the overlap of the basis functions has been eliminated. Thus, the potential mediates the bonding of the crystal or in other word the possibility of an electron to move (or 'hop') to another lattice site. Therefore, these are often called hopping parameters or in the sense of the two-center approximation also Slater-Koster parameters. It should be mentioned that these parameters obey symmetries of either the crystal or the orbitals. For example s-type orbitals are isotropic, while p-type orbitals are anti-symmetric $f(-x) = -f(x)$. This leads to the conclusion that the hopping probability between two neighbouring s-orbitals independent of the direction whereas p-to-s-hopping changes its sign depending on the orientation of the p-orbital. The Slater-Koster type models have the advantage that they can be obtained from straightforwardly calculating the sum over the chosen order of nearest neighbours of the Bloch factors $\sum_{\mathbf{R}} e^{i\mathbf{k}(\mathbf{R}_0-\mathbf{R})}$, cf. Eq. (3.10). Therefore it is easy to describe nanostructures or defects with this type of model. Nevertheless, one is left with an increasing number of parameters when taking more orders of neighbouring atoms and orbitals into account.

While it is in general a demanding task to calculate these hopping parameters, one wants to utilize the numerical advantages of the TB-method at the same time. In a *(semi-)empirical* approach, the hopping parameters $t = \big\langle \mathbf{R}, \nu \big| V(\mathbf{R}) \big| \mathbf{0}, \mu \big\rangle$ can be obtained from *ab-initio*-calculations by a fitting procedure and saved in e.g. a look-up-table. This way, the TB-method can be a good starting point for further many-particle calculations.

In summary, one is left with a representation of the Schrödinger equation of a single electron in the presence of a lattice-periodic potential. As has been shown, the TB-matrix can be written as an on-site part containing all orbital energies, or eigenenergies of the basis, and an off-site part that contains hopping matrix elements, thereby mediating the bonding between adjacent atomic sites. Generalizing the approach above, each basis function is given indices for the atom type i, the lattice site $\mathbf{R}$ and the orbital type α (and spin σ). In real space representation the basis reads $\big|\mathbf{R}, i, \alpha(,\sigma)\big\rangle$ and the full TB-matrix becomes:

$$\big\langle \mathbf{k}, i, \alpha \big| H \big| \mathbf{k}, i', \alpha' \big\rangle \;=\; E^{i,\alpha}\delta_{i,i'}\delta_{\alpha,\alpha'} + \sum_{\langle \mathbf{R}\neq 0\rangle} e^{-i\mathbf{k}\mathbf{R}} \big\langle \mathbf{R}, i, \alpha \big| V(\mathbf{R}) \big| \mathbf{0}, i', \alpha' \big\rangle \,. \tag{3.11}$$

Thus in combination with the representation of state $\big|\mathbf{k},\lambda\big\rangle$ the main task is solving the TB-matrix, obtaining the eigenenergies and the TB-coefficients:

$$\sum_{i',\alpha'}\left[E^{i,\alpha}\delta_{i,i'}\delta_{\alpha,\alpha'}+\sum_{\langle\mathbf{R}\neq 0\rangle}e^{-i\mathbf{k}\mathbf{R}}\big\langle\mathbf{R},i,\alpha\big|V(\mathbf{R})\big|\mathbf{0},i',\alpha'\big\rangle\right]c_{\mathbf{k}}^{\lambda,i',\alpha'} \quad = \quad \varepsilon_{\mathbf{k}}^{0,\lambda}c_{\mathbf{k}}^{\lambda,i,\alpha} \tag{3.12}$$

Generally in k-space the TB-Hamiltonian is represented by a $N_{orb.}\times N_{orb.}$-matrix for each k-point. In real-space the size depends on the size of the chosen supercell, thus it would be a $N_{site}\cdot N_{orb.}\times N_{site}\cdot N_{orb.}$-matrix. The real-space TB-matrix can be represented by projection operators pointing to the lattice sites:

$$H_{\mathbf{R},\mathbf{R}'}^{i\alpha,i'\alpha'} \quad = \quad \sum_{\mathbf{R}}E_{\mathbf{R}}^{i,\alpha}\big|\mathbf{R},i,\alpha\big\rangle\big\langle\mathbf{R},i,\alpha\big|+\sum_{\big\langle\mathbf{R},\mathbf{R}'\big\rangle}t_{\mathbf{R},\mathbf{R}'}^{i\alpha,i'\alpha'}\big|\mathbf{R},i,\alpha\big\rangle\big\langle\mathbf{R}',i',\alpha'\big| \tag{3.13}$$

For a periodic crystal the eigenenergies depending on $\mathbf{k}$ will form the band structure of the material. Though confinement of electrons due to a potential leads to discrete states, the band structure is assumed to be continuous for a large crystal. In semiconducting materials, which are investigated throughout this thesis, energetic regions without states form, leaving a band gap. The states up to that one highest in energy beneath the band gap are filled in the ground state, thereby defining the Fermi level. For TMDs the band gap is about $2-3$ eV in value. Thus electrons can still be excited into states above the gap, if enough energy is provided for example by a pump laser pulse. Electrons in a periodic crystal potential form so-called quasi-particles, the Bloch-electrons with crystal momentum $\mathbf{k}$. Their eigenenergies are represented by the band structure $\varepsilon_{\mathbf{k}}^{0,\lambda}$. The states $\big|\mathbf{k},\lambda\big\rangle$ are called Bloch states and represent the eigenbasis of the ground state. These will be used frequently throughout this work for the expansion of the many-body terms into the ground state basis. In order to gain more insight an example for a simple TB model of a 2d material, the band structure of graphene, will be discussed briefly. A TB-model for graphene has been proposed by [4]. Graphene is the 2d hybridized form of carbon, forming a honeycomb lattice due to the sp^2-hybrid orbitals. The remaining and empty p_z orbitals give rise to the important bands around the Fermi level. Owing to the shape of the honeycomb lattice, two sublattices A, B have to be defined, thereby providing two different sets of neighbouring atoms. The TB-wave function can thus be defined as $\big|\mathbf{k},\lambda\big\rangle = c_A\big|\mathbf{k},2p_z^A\big\rangle+c_B\big|\mathbf{k},2p_z^B\big\rangle$. This definition of two sublattices gives rise to the 2×2 TB-matrix for each $\mathbf{k}$ point. The on-site energies are constant and equal for both sublattices and thus set to zero. The off-diagonal part takes the simple form of $\gamma(\mathbf{k}) = e^{ik_x\frac{a}{\sqrt{3}}}+e^{ik_x\frac{a}{2\sqrt{3}}}\left(e^{-ik_y\frac{a}{2}}+e^{ik_y\frac{a}{2}}\right)$ from summing over the nearest neighbours in the exponential functions. The hopping matrix elements $t = 3\,\mathrm{eV}$ are fitted in the sense of the afore-mentioned empirical TB-model. The total matrix to diagonalize is:

$$\langle \mathbf{k}, \alpha, \nu | H | \mathbf{k}, \alpha', \nu' \rangle = \begin{pmatrix} 0 & -t \cdot \gamma(\mathbf{k}) \\ -t \cdot (\gamma(\mathbf{k}))^{*} & 0 \end{pmatrix} \tag{3.14}$$

The band structure plotted on a convenient path throughout the BZ, for example along $\mathbf{\Gamma} \to \mathbf{M} \to \mathbf{K} \to \mathbf{\Gamma}$, shows the most remarkable features at the $\mathbf{K}$ points of the hexagonal BZ. The so called 'Dirac-cones' form which exhibit a linear dispersion relation for the electrons. Graphene therefore provides good conductivity and transport properties.

3.1.1. Empirical Tight Binding Models for TMDs

There is a number of publications [26, 60, 90–95] that describe TB-models of TMD monolayers. Here two examples for each empirical TB-model shall be shortly discussed. Both use different approaches for describing the electronic structure of a TMD layer.

The first paper to discuss from Liu et al. [90] aims for a minimal symmetry-based model, which includes the three bands that are most relevant for optics and - speaking of orbital character - also mostly disentangled from all other bands. These three bands (one valence band and two conduction bands) have mainly the character of the transition metal $\mathrm{d}_{\mathrm{z}^2}$, d_{xy} and $\mathrm{d}_{\mathrm{x}^2-\mathrm{y}^2}$ orbitals. Only in the vicinity of the $\mathbf{\Gamma}$-point in the conduction bands and around the $\mathbf{M}$-point for the valence band appreciable admixtures of the p-orbitals, stemming from the chalcogen atoms, are found.

This model also aims for symmetry-based description of the wave functions, thereby performing in the end second best to the DFT-based Wannier interpolation, that will be favored in this thesis. In order to avoid a costly Wannier construction, this model seems to be the best alternative in terms of band structure and wave function reproduction with respect to the number of hopping parameters and TB-matrix size, which is only 3×3 for each $\mathbf{k}$-point. The determination of the hopping parameters is done by making use of the symmetry operations, that are inherent for the crystal symmetry of semiconducting TMDs. The unit cell of TMDs have a trigonal prismatic structure with the transition metal in the center and two chalcogenides in the corners of the prism. The associated symmetry group is therefore D_{3h}. The symmetry operations contained in D_{3h} separates the orbital subset $\mathrm{d}_{\mathrm{z}^2}$, d_{xy} and $\mathrm{d}_{\mathrm{x}^2-\mathrm{y}^2}$ from the remaining orbital basis. The symmetry operations $\{\hat{E}, 2\hat{C}3, 3\hat{\sigma}_v\}$ therefore dominated the electronic properties of TMDs. Those symmetry operations are the identity $\hat{E}$, two rotations $\hat{C}_3$ by $2\pi n/3$ and $2\pi n/3 + \pi/6$ respectively as well as three mirror planes $\hat{\sigma}_v$ perpendicular to the x, y-plane and along two opposed nearest neighbour vectors (e.g. $\mathbf{R}_1, \mathbf{R}_6$, c.f. Fig.(x)). Thus all $H^{\alpha,\beta}(\mathbf{R})$ have to be invariant to the named symmetry operations, which enables the calculation of the matrix elements by applying the matrix representations of the irreducible representations $D(g_n)$ of the symmetry operations as $H^{\alpha,\beta}(g_n\mathbf{R}) = D(g_n)H^{\alpha,\beta}(\mathbf{R})D^{\dagger}(g_n)$, where $g_n \in \{E, 2C_3, 3\sigma_v\}$. The calculation results in

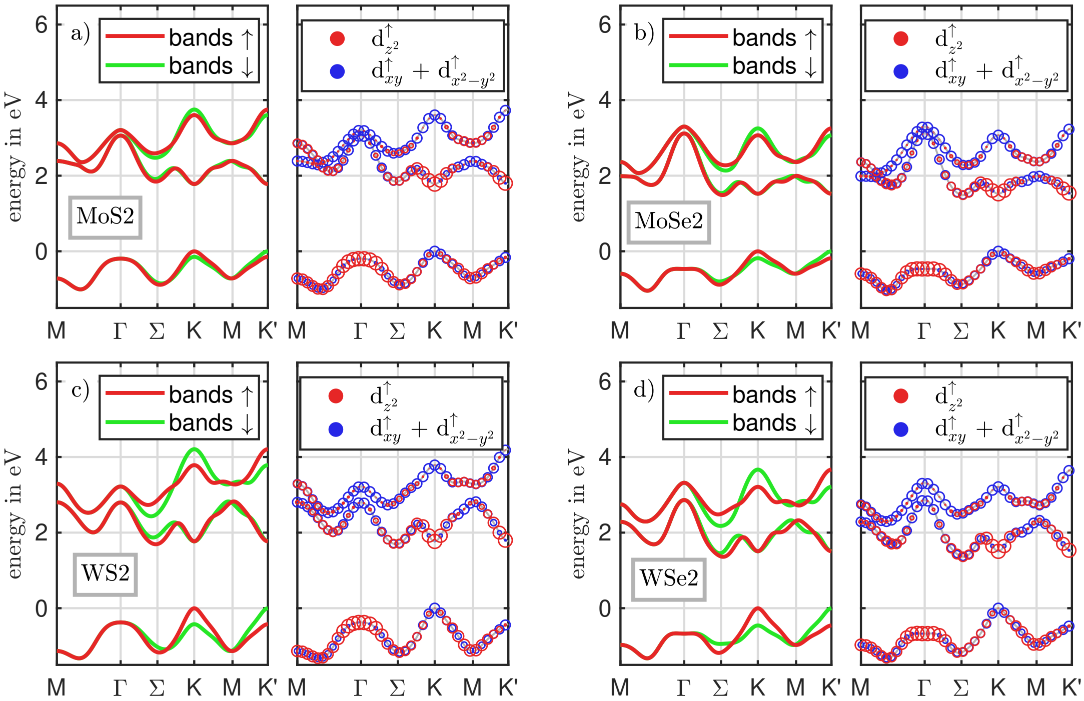

Figure 3.1.: Groundstate band structures of MoS_2, $MoSe_2$, WS_2, and WSe_2 are shown in (a) - (d) calculated from the model presented in Ref. [90]. The absolute value of the squared coefficients corresponding to the partition of the orbitals is plotted on the same path on the right to each band structure.

a 3×3 Hamiltonian in k-space either for nearest or up to third nearest neighbours, whose explicit form can be found in Ref. [90]. This model reproduces DFT band structure calculations of MoS_2, $MoSe_2$, $MoTe_2$, WS_2, WSe_2 and WTe_2 by fitting the hopping parameters $H^{\alpha,\beta}(\mathbf{R})$ to the *ab-initio*-calculations in GGA and LDA approximation (see the following section on DFT). The nearest neighbour model is able to reproduce low energy properties (effective mass) at both $\mathbf{K}$-valleys, while the model using third nearest neighbours describes the band structure very well except for $\mathbf{k}$-regions where the chalcogen p-orbitals have small admixtures. The orbital character of each band is well approximated (see Fig.(3.1)). An expansion of this model can be found in Ref. [26], where the remaining two orbitals $\mathrm{d_{xz}}$ and $\mathrm{d_{yz}}$ have been added using the same symmetry-based approach.

The advantage of this model is the high reproducibility of the underlying DFT calculations. In order to describe the bands well for all **k**-points, hoppings up to third nearest neighbours are be taken into account, which results overall in 19 parameters, that are fixed by fitting to DFT values. Hoppings between the transition metals atoms up to third nearest neighbours play an important role in reproducing the band structure [91]. On the other hand it is difficult to describe chalcogen defects or nanostructures with this type of model, as the real space interaction between different orbitals and atoms is incorporated in the parameters obtained from symmetry-based methods.

The second approach to a TB-description of TMD monolayers has been developed by Dias et al. in Ref. [91]. Most TB-models up to date are listed and compared. An advanced TB-model of Slater-Koster type is proposed. In their model all six p-orbitals of the top and bottom chalcogen atoms and the five d-orbitals of the transition metal are used as basis set. The top p-orbitals and the bottom p-orbitals are cast into symmteric and antisymmetric linear combinations $p_i^{A,S} = (p_i^t \pm p_i^b)/\sqrt{2}$ with respect to the x, y-mirror plane of TMDs in order to get the Hamiltonian into a block matrix form. The new basis allows for separating the orbitals with even and odd parity. Nevertheless using a unitary transformation $U^\dagger H U$ the final matrix could be transformed back to the pure p-orbital basis.

Using the straight-forward Slater-Koster method, the proposed model contains second nearest neighbour hopping between transition metal atoms (M-M) and chalcogen atoms (X-X) as well as hopping between the two species (M-X). It is stated, that in order to obtain a good precision for more than two bands (VB, CB) in the electronic band structure within the Slater-Koster approach, at least the second nearest neighbours of in-plane hopping M-M and X-X have to be taken into account. The M-X term decays fast with the distance. This is also most criticized in the models of Slater-Koster type that are discussed in [91].

3.1.2. Application of the TB-Approach to TMD-Nanobubbles

The TB-method provides a good approach to describe nanostructures. Though these do not exhibit a band structure, the TB treatment of these nanostructures is most suitable in this chapter of the thesis. The nanostructure to be modelled are nanobubbles made of $\mathrm{MoS_2}$ monolayers, that emerge when placing an exfoliated TMD layer on top of a substrate. These bubbles originate from either intercalating molecules or from reducing surface stress. These bubbles range from nm to μm scale in diameter while having a nearly constant height to radius ratio of $h/r = 0.175$ [96, 97].

It has been shown that these bubbles emit single photons [98] when illuminated. Single photon sources are one core element for quantum communication applications and therefore a field of high interest in research. These emitters have to generate single photons on-demand with high repetition rate and high indistinguishability of the photons, while the fabrication should be scalable but also deterministic, when placing them on a substrate. Beside different approaches [99] for these sources nanostructures formed of TMD monolayers can also provide single photon emission. Attempts using prestructured substrates in order to induce a strain potential to the monolayer have been reported [100–103]. Another interesting yet simple method has been realized by placing a TMD monolayer on a polymer film and subsequently pressing an atomic force microscope (AFM) tip into the material to produce a strain potential [104].

The microscopic origin of this single photon emission lies in the strong localization of electron and hole states. The goal of this part is to gain further understanding on the formation of these localized states. The model of such nanobubbles has to reproduce the main effects occurring in the bubble the first to be strain and the second one a change in the layer coupling and dielectric environment. Strain will induce renormalizations in the band structure in the order of 100 meV per percent strain, that lowers the conduction band $\mathbf{K}$-valley while rising the $\mathbf{\Gamma}$-point [47] for tensile strain. The second important effect originating from the bubble geometry is the change of the band gap due to the change in the dieletric environment and the interlayer coupling from a bulk-like type at the edges of the bubble to a monolayer-type environment in the center. This implies an indirect band gap in the bulk case, whereas a direct band gap can be found in the central region of the bubble [105].

In order to do so a real-space TB model is used that shall be modified locally by bond bending and stretching between the monolayer atoms and the dielectric environment. Strain therefore induces a local potential changing the single-particle properties. The potential induced by the change in the dielectric environment and the layer coupled varies on a larger scale. Combining both potentials an effective potential with strong local variations is present. A symmetry-based model with a minimal orbital basis in which the hopping parameters can be changed directly, is therefore employed. The bubble geometry itself is described by using experimental data to generate an initial geometry that is successively relaxed by valence force field methods with an appropriate potential [96]. The geometry consists of two layers of TMDs, one containing the bubble and one as fixed substrate layer. In order to describe these experimentally accessible bubble geometries, the real-space TB-matrix contains as many rows and columns as atoms are used for the geometry.

In the early stages of the work leading to the publication [96] different TB-models have been investigated by the author of this thesis before being implemented into a supercell calculation by Christian Carmesin. The model of choice is published in [96] and the employed TB-model will be shortly presented in the remaining part of this section.

The TB model uses a minimal basis set of three Mo-orbitals (d_{z^2},$d_{x^2-y^2}\pm id_{xy}$) labeled as (d_0,$d_{\pm 2}$) and next-nearest neighbour Mo-hoppings. The idea behind the transformed basis set is that the spherical harmonics, which describe the basis states, are invariant under rotation around the z-axis and only change their phase. This phase factor is written as $f_m(\varphi) = e^{im\varphi}$, where m is the magnetic quantum number and can be separated from the remaining hopping integral. The hopping matrix elements are be written using the spherical harmonics as ansatz:

$$\langle \alpha, 0 | H | \beta, \mathbf{R} \rangle = t_{\alpha\beta}(R) \cdot e^{-i\alpha\varphi + i\beta(\varphi+\pi)}, \tag{3.15}$$

where the total Hamiltonian is

$$H^{\alpha\beta} = \sum_{\mathbf{R}} e^{i\mathbf{kR}} \langle \alpha, 0 | H | \beta, \mathbf{R} \rangle . \tag{3.16}$$

Here the fact has been exploited, that the phase factor can be separated from the remaining overlap integral, which in turn is used as a fit parameter. The indices α and β are the magnetic quantum numbers of the orbitals of atoms at position $\mathbf{0}$ and $\mathbf{R}$, respectively. In order to regain the full symmetry of the TMDs, the phase factor is adjusted for the nearest and next-nearest neighbouring S-atoms. In the end one is left with

$$f_{\alpha\beta}(\varphi) = \begin{cases} e^{-i\alpha(\varphi-\pi/6)+i\beta(\varphi+\pi+\pi/6)}, & \text{if } \varphi = 0, 2\pi/3, 4\pi/3 \\ e^{-i\alpha(\varphi+\pi/6)+i\beta(\varphi+\pi-\pi/6)}, & \text{if } \varphi = \pi/3, \pi, 5\pi/3 \end{cases} \tag{3.17}$$

if $\mathbf{R}$ is a nearest neighbour M-atom and

$$f_{\alpha\beta}(\varphi) = \begin{cases} e^{-i\alpha\varphi+i\beta(\varphi+\pi)}, & \text{if } \varphi = \pi/6, 3\pi/2, 5\pi/5 \\ e^{-i\alpha(\varphi+\pi)+i\beta\varphi}, & \text{if } \varphi = \pi/2, 7\pi/6, 11\pi/6 \end{cases} \tag{3.18}$$

if $\mathbf{R}$ is a next-nearest neighbour Mo-atom. The obtained hopping matrix elements from fitting to a DFT + GW calculation as described in [96] and can be taken from Tab. (C.5).

To account for strain the TB matrix in $\mathbf{k}$-space representation is evaluated at points of high symmetry, namely $\mathbf{K}$ and $\mathbf{\Gamma}$. The hopping element responsible for the relative shift between these valleys ($E^c_K - E^v_\Gamma = -9t_0$) can be identified. This parameter is modified according to the Harrison rule [106] and thus rescaled by the relative interatomic distance $s = (r-a)/a$

yielding $t_0(r) = t_0/(1-s)^\eta$. Here $\eta = 11$ has been chosen to reproduce experimental band gaps of Ref. [40]. To account for the band gap shrinkage from changing dielectric environment (on MoS_2-substrate at the edges, nearls freestanding in the center) this shrinkage is modelled as a height dependent function that has been fitted to DFT data, see supplement of [96] for further details.

This model enables microscopic understanding of the formation of localized wave functions, that are responsible for single photon emission. The confinement potential originating from the change in the dielectric environment and the interlayer coupling induces a repulsive potential, that pushes the wave functions to the periphery of the bubble. For nanobubbles with a commonly measured aspect ratio of $h/r = 0.175$ or larger, the rigidity of the TMD layer causes wrinkles in order to maintain mostly flat surfaces. At the points, where these wrinkles meet (again at the periphery of the bubble), locally large strain potentials form and enforce strongly localized wave functions of the electrons and holes. The main experimental indicator for this localizations mechanism is a redshift of the sharp emission lines and a broadening of the PL spectra of such bubbles, together with an increase of the PL emission strength. Therefore these localization centers are experimentally accessible by spatially resolved PL.

3.2. Density Functional Theory

When it comes to calculations of the electronic ground state the state-of-the-art theory mostly used is the Density Functional Theory (DFT). It aims for calculating the ground state energy of the Hamiltonian

$$H = \sum_{i=1}^{N} \left(-\frac{\hbar^2 \nabla_i^2}{2m} \right) + \sum_{i=1}^{N} V(\mathbf{r}_i) + \sum_{i<j} \frac{e^2}{4\pi\varepsilon_0 |\mathbf{r}_i - \mathbf{r}_j|}. \tag{3.19}$$

This Hamiltonian describes an interacting many-body system (N particles) and obtaining the eigenspectrum and the ground state wave functions requires the solution of the full Schrödinger equation. The main idea of the DFT method is instead of calculating complex wave functions all terms in Eq. (3.19) can be expressed as functional of the ground state electron density $n_0(\mathbf{r}) = \langle \Psi_0 \big| \sum_{i=1}^{N} \delta(\mathbf{r} - \mathbf{r}_i) \big| \Psi_0 \rangle$. This fact is the main statement of the Hohenberg-Kohn theorem [107]: The energy in the ground state is a unique functional of the electron density $E_0 = E[n_0(\mathbf{r})]$. The density also determines the potential $V(\mathbf{r})$. Using the Ritz variational principle, it follows:

$$E[n_0(\mathbf{r})] \leq \langle\Psi|H|\Psi\rangle, \tag{3.20}$$

where the energy density functional $E[n(\mathbf{r})] = \langle\Psi|H|\Psi\rangle$ is minimized $\delta E[n(\mathbf{r})] = 0$ under the condition that the total number of particles is preserved. Therefore the method of Lagrangian multipliers can be used. Although the exact form of the density functional of the total energy is not known, it can be separated into the following terms [108]:

$$\begin{aligned}
E[n(\mathbf{r})] &= T[n(\mathbf{r})] + V[n(\mathbf{r})] + U[n(\mathbf{r})]\,, \text{with} && (3.21)\\
T[n(\mathbf{r})] &= \langle\Psi|\sum_{i=1}^{N}\frac{\mathbf{p}_i^2}{2m}|\Psi\rangle && (3.22)\\
U[n(\mathbf{r})] &= \frac{e^2}{8\pi\varepsilon_0}\langle\Psi|\sum_{i\neq j}\frac{1}{|\mathbf{r}_i-\mathbf{r}_j|}|\Psi\rangle && (3.23)\\
V[n(\mathbf{r})] &= \langle\Psi|\sum_{i=1}^{N}V(\mathbf{r}_i)|\Psi\rangle, && (3.24)
\end{aligned}$$

where T is the density functional of the kinetic energy, V is the density functional of the external potential (e.g. crystal potential) and U the density functional of the interaction. U can be separated further into a Hartree term (classical Coulomb interaction) and the exchange-correlation functional (terms arising from quantum mechanics):

$$U[n(\mathbf{r})] = \frac{e^2}{8\pi\varepsilon_0}\int \mathrm{d}^3\mathbf{r}\int \mathrm{d}^3\mathbf{r}'\frac{n(\mathbf{r})n(\mathbf{r}')}{|\mathbf{r}-\mathbf{r}'|} + V^{xc}[n(\mathbf{r})]. \tag{3.25}$$

DFT would be an exact theory solving the many-body problem, given the exact form of the exchange-correlation functional is known. In order to determine the total energy Kohn and Sham proposed the use of a non-interacting auxiliary system [108], which is exactly solvable, in order to aid the calculations. While the electron density uniquely defines an external potential, different single-particle wave functions can belong to the same density. Therefore a non-interacting system with the same electron density as the interacting one is defined. The wave function for this non-interacting many-body problem can be set as a Slater determinant, which on the other hand reduces the N-particle problem to N effective single-particle problems. The density is defined as:

$$n(\mathbf{r}) = \sum_{i=1}^{N}|\Psi_i(\mathbf{r})|^2, \tag{3.26}$$

which changes the boundary condition from the preservation of the particle number to the normalization of the wave function:

$$\frac{\delta}{\delta\Psi_i(\mathbf{r})}\left\{E[n(\mathbf{r})]-\sum_{j=1}^{N}\varepsilon_j\left(\int \mathrm{d}^3\mathbf{r}|\Psi_i(\mathbf{r})|^2-1\right)\right\} \quad = \quad 0 \tag{3.27}$$

Using the above relations for the density functional the functional derivative can be performed. This gives rise to the following expression:

$$\left\{-\frac{\hbar^2\nabla_i^2}{2m}+V(\mathbf{r})+\int \mathrm{d}^3\mathbf{r}'\frac{e^2}{|\mathbf{r}-\mathbf{r}'|}n(\mathbf{r}')+\frac{\delta V_{xc}[n(\mathbf{r})]}{\delta n(\mathbf{r})}\right\}\Psi_i(\mathbf{r}) \quad = \quad \varepsilon_i\Psi_i(\mathbf{r})\,. \tag{3.28}$$

These are the Kohn-Sham equations [109, 110], where the N-particle system has been cast into N single-particle problems, which are coupled by the exchange-correlation potential. It is advantageous, that approximations have to be made to the exchange-correlation potential instead of the kinetic energy term as before. In order to solve the Kohn-Sham equations a self-consistency cycle is used. The initial density is chosen to suit the given problem. Subsequently the effective single-particle potential is calculated to evaluate the Kohn-Sham equations. Given the solutions $\varepsilon_i^{\mathrm{KS}}$ and $\Psi_i^{\mathrm{KS}}(\mathbf{r})$ a new particle density can be calculated and is used in the following step as the initial density if the deviation from the old particle density is above a chosen threshold. This cycle is iterated until self-consistency is reached.
Until now only the knowledge of specific form of the exchange-correlation potential hinders the evaluation of the Kohn-Sham equations. Therefore, the most common approximation will be explained shortly. The local density approximation (LDA) assumes the exchange-correlation potential to be of the form of a homogeneous electron gas, where the exact form is analytically known.

$$E_x[n(\mathbf{r})] \quad = \quad -\frac{3e^2}{4}\left(\frac{3}{\pi}\right)^{1/3}\int \mathrm{d}^3\mathbf{r}\,n(\mathbf{r})^{4/3} \tag{3.29}$$

Thus the exchange correlation potential depends only on the density at $\mathbf{r}$, giving rise to the name LDA. In general this approximation can be extended as $E_x[n(\mathbf{r})]=\int \mathrm{d}^3\mathbf{r}\,\beta(n(\mathbf{r}))n(\mathbf{r})$ including a function β giving a certain dependence on the density that can be modified to produce better results, while it still has to reproduce the homogeneous electron gas. A common generalization is the local spin density approximation (LSDA), where both spins are considered by $\beta = \beta(n_\uparrow(\mathbf{r}), n_\downarrow(\mathbf{r}))$. An extension is the generalized gradient approximation (GGA), where $\beta = \beta(n(\mathbf{r}), \nabla n(\mathbf{r}))$ additionally depends on the gradient of the density [111]. Hybridized functionals, such as PBE [112] or HSE [113], are most exact and therefore popular, however computationally more demanding.

3.2.1. GW-Corrections

Though DFT is the state-of-the-art method for electronic structure calculations it suffers from the so called ”band gap problem” [114, 115]. Pure DFT (not using hybrid functionals) tends to underestimate the band gap of an insulator or a semiconductor. Therefore corrections are necessary in order to obtain reliable band gaps. In order to improve general understanding a small fraction of theory will already be introduced at this point. The method of Green’s functions, especially the GW-approximation, provides a well-established description of the carrier interaction [114, 116]. This method and the GW-approximation will be explained in detail in Chap.(4). The GW self-energy Σ^{GW} (see Sec. (4.3.3) is evaluated in the Kohn-Sham basis using the quasi-particle approximation with quasi-particle energies taken from the Kohn-Sham solutions $\omega_i^{\mathrm{KS}} = \varepsilon_i^{\mathrm{KS}}/\hbar$. The correction to the Kohn-Sham eigenenergies is then performed by a perturbation series of the GW-corrected exchange-correlation potential. The frequency-dependent GW self-energy in real-space reads

$$\Sigma^{\mathrm{GW}}(\mathbf{r},\mathbf{r}',\omega) \;=\; \frac{i\hbar}{2\pi}\int\limits_{-\infty}^{\infty} \mathrm{d}\omega' G_0(\mathbf{r},\mathbf{r}',\omega+\omega')W(\mathbf{r},\mathbf{r}',\omega')e^{i\omega'\eta}\,, \tag{3.30}$$

where G_0 is the non-interacting Green’s function (see Sec. 4.2.1) and W represents the screened Coulomb interaction The screening is mediated by the inverse dielectric function $\varepsilon(\mathbf{r},\mathbf{r}',\omega)$ that is mainly determined by the polarization function $P(\mathbf{r},\mathbf{r}',\omega)$. The polarization is evaluated in the RPA approximation (see Sec. 4.4).

To evaluate single-particle energies the quasi-particle equation is solved. Governing equation is the equation of motion for a stationary system

$$[\hbar\omega - H_0(\mathbf{r})]G(\mathbf{r},\mathbf{r}',\omega) - \int \mathrm{d}^3\mathbf{r}''\Sigma(\mathbf{r},\mathbf{r}'',\omega)G(\mathbf{r}'',\mathbf{r}',\omega) \;=\; \delta(\mathbf{r}-\mathbf{r}')\,, \tag{3.31}$$

where G_0 is again the Green’s function of the non-interacting system which is defined by the equation $H_0\phi_i^0(\mathbf{r}) = \varepsilon_i^0\phi_i^0(\mathbf{r})$. The full Green’s function G can be expressed in the Lehmann representation

$$G(\mathbf{r},\mathbf{r}',\omega) \;=\; \sum_i \frac{\psi_i^{N+1}(\mathbf{r})\psi_i^{N+1*}(\mathbf{r}')}{\hbar\omega - \varepsilon_i^{N+1} + i\gamma} + \sum_i \frac{\psi_i^{N-1}(\mathbf{r})\psi_i^{N+1*}(\mathbf{r}')}{\hbar\omega - \varepsilon_i^{N-1} - i\gamma}\,. \tag{3.32}$$

The $\psi_i^{N+1}(\mathbf{r})$ are the amplitudes of the Schrödinger field operators $\psi(\mathbf{r})$ from the projection onto on the eigenfunction $\left|\psi_i^{N+1}(\mathbf{r})\right\rangle$ of the interacting $(N \pm 1)$ particle system, that can be understood as the quasi-particle wave functions above and below the chemical potential. Thus the energies $\varepsilon_i^{N\pm1}$ are necessary to add or remove a particle. Inserting the representation (3.32) into the stationary Dyson equation (3.31) one obtains (for the sake of shortness the $(N \pm 1)$ has been neglected):

$$\sum_i \frac{\psi_i^*(\mathbf{r}')}{\hbar\omega - \varepsilon_i \mp i\gamma} \left\{ [\hbar\omega - H_0(\mathbf{r})]\psi_i(\mathbf{r}) - \int \mathrm{d}^3\mathbf{r}''\Sigma(\mathbf{r},\mathbf{r}'',\omega)\psi_i(\mathbf{r}'') \right\} = \delta(\mathbf{r}-\mathbf{r}') \tag{3.33}$$

Applying the quasi-particle approximation by multiplying with $(\hbar\omega - \varepsilon_i)$ and taking the limit $\lim \omega \rightarrow \varepsilon_j/\hbar$ leads for the left-hand side to

$$\psi_j^*(\mathbf{r}') \left\{ [\varepsilon_j - H_0(\mathbf{r})]\psi_j(\mathbf{r}) - \int \mathrm{d}^3\mathbf{r}''\Sigma(\mathbf{r},\mathbf{r}'',\varepsilon_j/\hbar)\psi_j(\mathbf{r}'') \right\} , \tag{3.34}$$

whereas the right-hand side vanishes to zero. The condition is fulfilled, if the part in the curly brackets vanishes and the $\psi_j^*(\mathbf{r}')$ are not zero for all $\mathbf{r}'$. Therefore, one obtains the quasi-particle equation

$$[\varepsilon_j - H_0(\mathbf{r})]\psi_j(\mathbf{r}) - \int \mathrm{d}^3\mathbf{r}''\Sigma(\mathbf{r},\mathbf{r}'',\varepsilon_j/\hbar)\psi_j(\mathbf{r}'') = \varepsilon_j\psi_j(\mathbf{r}) \, . \tag{3.35}$$

The quasi-particle equation is formally similar to the Kohn-Sham equations (3.28), which can be seen by interchanging the integral expression of the self-energy with the exchange-correlation potential and the eigenenergies and wave functions by the Kohn-Sham results $\varepsilon_i^{\mathrm{KS}}$, ϕ^{KS}. Often the ϕ^{KS} are a good approximation to the quasi-particle wave function [117], therefore assuming $\psi_i(\mathbf{r}) \approx \phi^{\mathrm{KS}}$ leads directly to the fact that the self-energy corrections are small. Thereby first order perturbation theory is justified, resulting in

$$\varepsilon_i^{\mathrm{KS+GW}} \approx \varepsilon_i^{\mathrm{KS}} + \left\langle \phi_i^{\mathrm{KS}} \middle| \Sigma^{GW}(\omega_i^{\mathrm{KS}}) - V_{xc} \middle| \phi_i^{\mathrm{KS}} \right\rangle \tag{3.36}$$

This energy correction is calculated self-consistently. Starting by evaluating the Kohn-Sham eigenfunctions and -energies, the polarization P and the inverse dielectric function ε^{-1} have to be calculated successively. This provides all input necessary for the evaluation of W. For the correction due to the GW self-energy the term Σ^{GW} is expanded into Kohn-Sham Green's functions G_0^{KS}, that replace the G_0. Thus all ingredients for Eq. (3.36) are available and the corrections of the eigenenergies can be calculated.

The GW-corrected DFT provides band structure with corrected band gaps and quasi-particle wave functions of the interacting many-particle system in the ground-state and are thus ideal for evaluation of the excited system. It is time consuming to perform a DFT+GW calculation each time the equations of the excited system are evaluated. This bottleneck can be overcome by the so-called Wannier interpolation that is described in the next section.

3.2.2. Wannier Interpolation

The Wannier interpolation scheme introduced within the *wannier90* framework [118, 119] uses the freedom of choice for the basis vectors of any matrix diagonalization to obtain maximally localized Wannier functions (MLWF) from an *ab-initio*-calculation. The numerically demanding many-body calculations are cast in a form, that is mathematically similar to a TB-calculation. Therefore, a numerical advantage is gained when utilizing ground state *ab-initio*-calculations for the many-body theory of excited system, as it is done in this work. At the same time and even more important is the fact, that the ground state properties are reproduced with the precision of the *ab-initio*-methods, which provide material-realistic band structures and wave functions that are desirable for the matrix elements of the many-body calculation.

Wannier functions are connected to the Bloch functions by

$$\big|\mathbf{R},\lambda\big\rangle \;=\; \frac{V}{(2\pi)^3}\int\limits_{BZ} \mathrm{d}^3\mathbf{k}\,e^{i\mathbf{k}\mathbf{R}}\big|\mathbf{k},\lambda\big\rangle\,. \tag{3.37}$$

The basis of *ab-initio* calculation is usually large in the sense that many bands λ are included. For calculations in the spectral region of the optically active bands, such a large basis is not necessary. For extracting a subset of bands the freedom of choice in the phase factor of $\big|\mathbf{k},\lambda\big\rangle$ can be exploited. Thus $\big|\mathbf{k},\lambda\big\rangle$ can be replaced by $\sum_\lambda' \mathbf{U}_\mathbf{k}^{\lambda\lambda'}\big|\mathbf{k},\lambda\big\rangle$ resulting in different Wannier functions with different spatial extend, that nonetheless describe the same manifold. In the published wannier90 scheme, this unitary transformation $\mathbf{U}_\mathbf{k}^{\lambda\lambda'}$ is chosen in order to minimize the spatial spread of the Wannier functions, resulting in the mentioned MLWF. However, this is not an ideal choice for many-body calculations. For spin-orbit interaction, which is important in TMDs it is necessary to identify the orbitals, that are involved in the respective bands. Note, that the choice of a subset of bands is not arbitrary. It has to be made sure that the $\big|\mathbf{k},\lambda\big\rangle$ are mostly decoupled from the rest of the bands, to obtain a complete subset.

To achieve the goals stated above, an initial guess for the matrix $\mathbf{U}_\mathbf{k}^{\lambda\lambda'}$ has to be made. The optically active bands in TMDs are those, which are formed by the three d-orbital $\mathrm{d}_{\mathrm{z}^2}$, d_{xy}, and $\mathrm{d}_{\mathrm{x}^2-\mathrm{y}^2}$ [90]. The number of chosen bands has to be $N_\lambda \leq N_{tot}$. In order to obtain nearly

pure orbitals, only one step of the minimization process for the MLWF is performed. Thus the new orbitals will not be pure d-states, but will also have small admixtures, especially from the p-orbitals from the chalcogen atoms.
The ansatz for the unitary transformation is thus chosen to be the projection on the three mentioned d-orbitals.

$$\begin{aligned} \mathbf{P}_{\mathbf{k}}^{\lambda\lambda'} &= \left\langle \mathbf{k}, \lambda | g^{\lambda'} \right\rangle && (3.38) \\ \left|\mathbf{k}, \lambda'\right\rangle &= \sum_{\lambda=1}^{N_\lambda} \mathbf{P}_{\mathbf{k}}^{\lambda\lambda'} \left|\mathbf{k}, \lambda\right\rangle && (3.39) \end{aligned}$$

The Löwdin transformation (3.7) is used to orthonormalize the new orbitals, where again the overlap matrix $\mathbf{S}_{\mathbf{k}}^{\lambda\lambda'} = \left\langle \mathbf{k}, \lambda | \mathbf{k}, \lambda' \right\rangle$ is calculated. the full transformation defines the matrix $\mathbf{U}$, that has been introduced in the text above.

$$\mathbf{U}_{\mathbf{k}}^{\lambda\lambda'} = \tilde{\mathbf{P}}_{\mathbf{k}}^{\lambda\lambda'} (\mathbf{S}_{\mathbf{k}}^{\lambda\lambda'})^{-\frac{1}{2}} \qquad (3.40)$$

This allows for the transformation of the Hamiltonian:

$$H_{\mathbf{k}}^{\mathrm{W}} = \mathbf{U}_{\mathbf{k}}^{\lambda\lambda',\dagger} H_{\mathbf{k}} \mathbf{U}_{\mathbf{k}}^{\lambda\lambda'} . \qquad (3.41)$$

Transforming to a real-space grid one obtains the coefficients of the Wannier interpolation. This appears to be mathematically similar to a TB-model, though the hopping matrix elements are obtained from the Wannier construction described above. The advantage is, that this Hamiltonian can be calculated for arbitrary $\tilde{\mathbf{k}}$, resulting in single-particle energies and wave functions of the ground state, which have the same precision as the underlying *ab-initio* calculation.

$$H_{\tilde{\mathbf{k}}}^{\lambda\lambda'} = \sum_{\mathbf{R}} e^{i\tilde{\mathbf{k}}\mathbf{R}} H_{\mathbf{R}}^{\lambda\lambda'} \qquad (3.42)$$

This way all ground state properties can be calculated on a much finder $\mathbf{k}$-mesh, which is necessary for convergence in the many-body calculations.
The band structure of the for investigated TMDs extracted by Matle Rösner using a Wannier construction and successively plotted using the Wannier interpolation method can be found in Fig. (3.2).

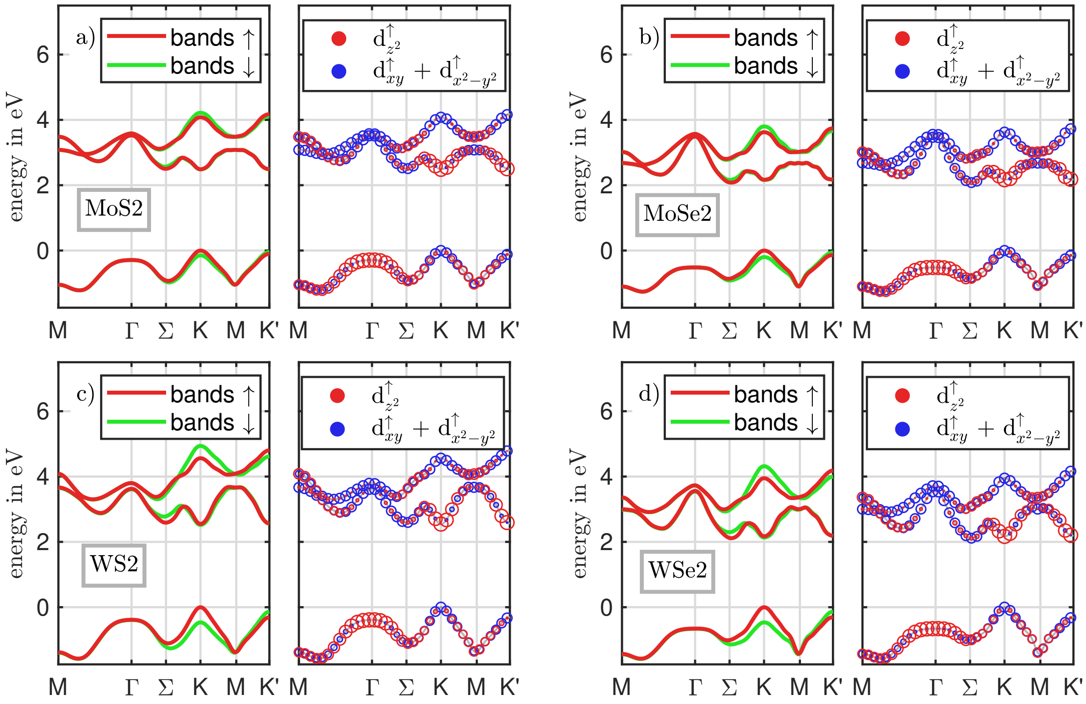

Figure 3.2.: Groundstate spin up (red) and spin down (green) band structures of MoS_2, $MoSe_2$, WS_2, and WSe_2 are shown in (a) - (d) calculated using the Wannier interpolation scheme. The absolute value of the squared coefficients corresponding to the partition of the orbitals within the spin up bands is plotted on the same path on the right to each band structure.

3.3. Spin-Orbit Coupling in TMDs

The spin-orbit coupling (SOC) describes the interaction between the magnetic moments of the electron spin and the orbit momentum of the shell-electrons of the atoms. The degeneracy of the SOC-states is lifted due to the lack of inversion symmetry in TMDs [47, 90, 120, 121]. The strength of the SOC is on the order of up several hundred meV. For TMDs the SOC can be expressed by the Hamiltonian [47, 90]

$$H_{SOC} = \lambda(\mathbf{k})\mathbf{LS}\,, \tag{3.43}$$

which can be cast into the form

$$H_{SOC} = \frac{\lambda(\mathbf{k})}{2}\begin{pmatrix} L_z & 0 \\ 0 & L_z \end{pmatrix}. \tag{3.44}$$

Here, $\lambda(\mathbf{k})$ is the SOC-constants that is $\mathbf{k}$-dependent in order to reproduce the p-orbital admixture throughout the BZ. It is inherently assumed, that a three-band model as presented in Sec. (3.1.1) or (3.2.2) is used. Due to the orthonormality relations of the d-orbitals being involved the matrix representation of L_z reads

$$L_z = \begin{pmatrix} 0 & 0 & 0 \\ 0 & 0 & 2i \\ 0 & -2i & 0 \end{pmatrix} \tag{3.45}$$

The full Hamiltonian describing the ground state band structure including SOC is given by

$$H = H_{\text{GS}} \otimes H_{SOC} \,, \tag{3.46}$$

where the dimension has doubled. The equations above indicate, that different spins states are not coupled by the SOC. Only the degeneracy of the band structure is lifted. The SOC lifts the degeneracy mostly for the valence band $\mathbf{K}/\mathbf{K}'$-points which is modeled by chosing a $\mathbf{k}$-dependent $\lambda(\mathbf{k})$. This splitting is the main cause of the two exciton peaks A and B [122] as it acts on $\mathbf{K}$ and $\mathbf{K}'$ inversely by lifting $\mathbf{K}_\uparrow/\mathbf{K}'_\downarrow$ while lowering $\mathbf{K}_\downarrow/\mathbf{K}'_\uparrow$ in the valence band. For the conduction band the situation is more complex as the molybdenum-based TMDs exhibit the lowest transition to be spin-allowed ($\varepsilon^{h,\uparrow}_{\mathbf{K}}$ to $\varepsilon^{e,\uparrow}_{\mathbf{K}}$) whereas for the tungsten-based TMDs this transition is spin-forbidden ($\varepsilon^{h,\uparrow}_{\mathbf{K}}$ to $\varepsilon^{e,\downarrow}_{\mathbf{K}}$) [90]. As the $\mathbf{K}/\mathbf{K}'$ valleys are primarily build of the orbitals $1/\sqrt{2}(\,|\mathrm{d}_{\mathrm{x}^2-\mathrm{y}^2}\rangle \pm i\,|\mathrm{d}_{\mathrm{xy}}\rangle)$ character they couple to light of different polarizations. Due to the lifting of the degeneracy these valleys are selectively addressable by choosing the respective linear polarization (horizontal or vertical) giving rise to a valley degree of freedom [46, 123].

The explicit form of $\lambda(\mathbf{k})$ is chosen to be [90]

$$\lambda(\mathbf{k}) = \lambda_0 e \left(1 - \frac{|\mathbf{k}|}{|\mathbf{K}|}\right)^2 e^{-\left(1-\frac{|\mathbf{k}|}{|\mathbf{K}|}\right)^2} . \tag{3.47}$$

Thus the SOC is dampened with increasing distance to the $\mathbf{K}$-points. The parameter λ_0 defines the energetic distance between the A and B peak in the spectra. Values can be found in [90]. For all figures showing the band structure the spin-up bands are plotted in red and the spin-down bands in green (see e.g. Fig. (3.2)).

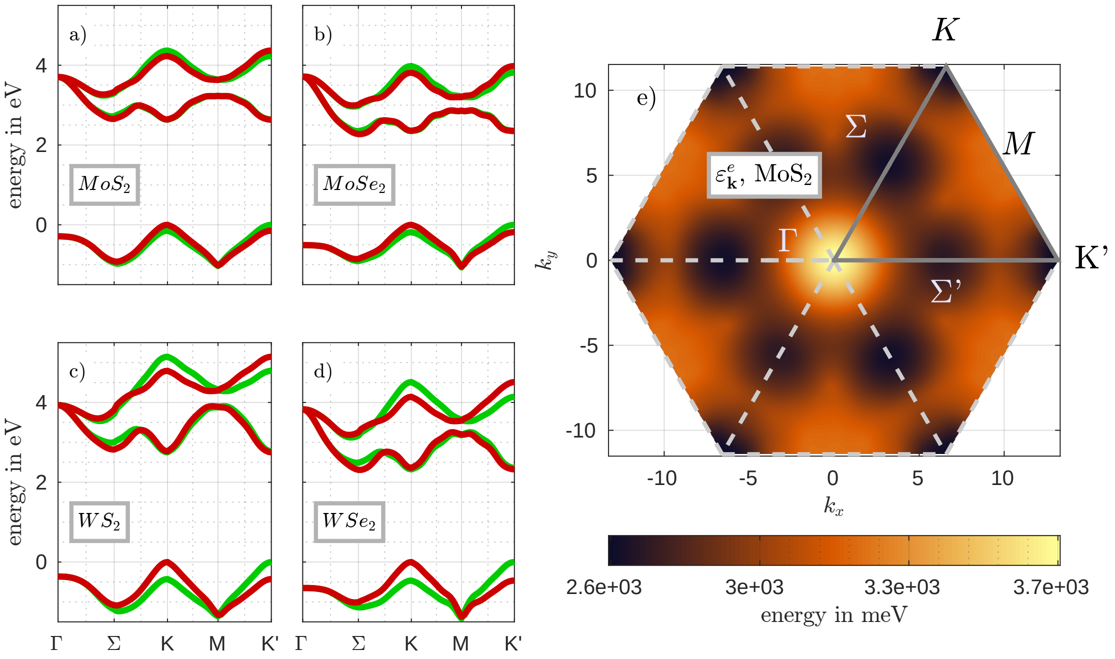

Figure 3.3.: Ground state band structures of MoS$_2$, MoSe$_2$, WS$_2$, and WSe$_2$ are presented in (a) - (d). The difference in the spin-orbit coupling at $\mathbf{K}/\mathbf{K}'$ between molybdenum and tungsten compounds as well as the sulfide/selenide compounds can be seen. Figure (e) contains the colormap of the lowest conduction band for MoS$_2$ with all important BZ points marked.

3.4. General Properties of TMD Band Structures

In contrast to their bulk counterparts [124] monolayers of TMDs show a direct band gap [9, 63] together with a complex valley structure in reciprocal space [125, 126]. In Fig. (3.3) both the highest valence an the lowest conduction band in the ground state for MoS$_2$, MoSe$_2$, WS$_2$, and WSe$_2$ on the path $\mathbf{\Gamma}$-$\mathbf{\Sigma}$-$\mathbf{K}$-$\mathbf{M}$-$\mathbf{K}'$ in the hexagonal BZ as well as a colormap of the lowest conduction band of MoS$_2$ are plotted. The valence bands of all four investigated materials show three maxima at $\mathbf{\Gamma}$, at $\mathbf{K}$ and at $\mathbf{K}'$. There is no minimum in the conduction band at $\mathbf{\Gamma}$, but four minima at $\mathbf{\Sigma}/\mathbf{\Sigma}'$ and $\mathbf{K}/\mathbf{K}'$, respectively, see Fig. (3.3). In the monolayer case the DFT+GW calculation predict within its accuracy a direct band gap at $\mathbf{K}$ and $\mathbf{K}'$ so that $E_G = \varepsilon^e_{\mathbf{K}} - \varepsilon^h_{\mathbf{K}}$ for the sulfides, whereas the selenides appear to be indirect $E_G = \varepsilon^e_{\mathbf{\Sigma}} - \varepsilon^h_{\mathbf{K}}$ [10, 11]. This intrinsic indirectness is nevertheless on the order of only tens of meV. The different band gaps of the four materials from *ab-initio*-calculations are compared to experimental values in Tab. (3.1).

Valence and conduction bands are splitted due to the spin-orbit coupling, explained in Sec. (3.3). The spin-orbit splitting is larger for the TMDs containing tungsten which originates from the higher mass of tungsten in comparison with molybdenum. In the conduction band at the $\mathbf{K}$-point the spin-orbit splitting changes the order of bands for the tungsten compounds which means that in comparison to MoX_2 the lowest possible transition in WX_2 is spin-forbidden and therefore dark [42, 43].

(eV)	E^A_{opt}	E^G_{exp}	E^G_{DFT+GW}
MoS_2	1.89 [56]	2.46 [127]	2.638
	1.87 [128]		
$MoSe_2$	1.63 [56]	2.18 [35]	2.355
	1.59 [128]	2.10 [126]	
WS_2	1.90 [49]	2.15 [49]	2.775
WSe_2	1.60 [48]	2.02 [48]	2.360

Table 3.1.: Optical band gaps (A-Exciton) compared to the experimental band gaps and the band gaps from the DFT+GW-calculations of all four investigated TMD monolayers.

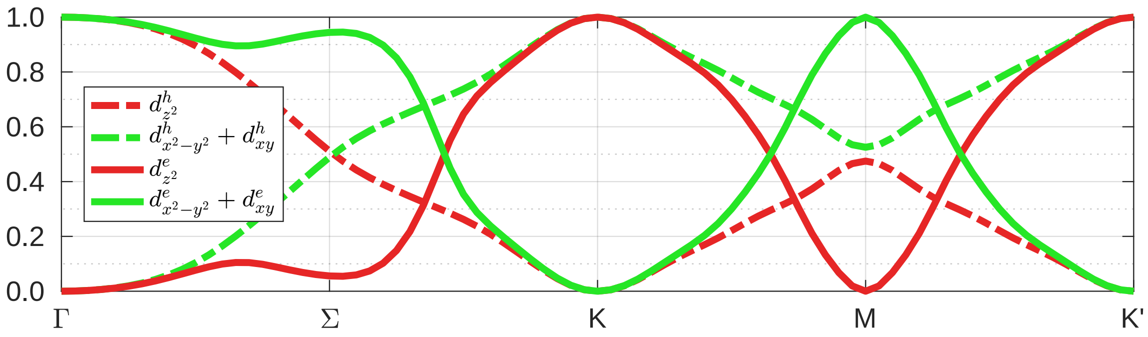

Figure 3.4.: Orbital character ($|c_\nu|^2$) of the highest valence band (h, dash-dotted line) and the lowest conduction band (e, solid line) of monolayer MoS_2. The $\mathbf{K}/\mathbf{K}'$-point consist of the d_{z^2} in the conduction band whereas $\mathbf{\Gamma}$ has a main d_{xy} and $d_{x^2-y^2}$ character and viceversa for the valence band. For the $\mathbf{\Sigma}$-point in the conduction band the orbital character consists of the in-plane orbitals d_{xy} and $d_{x^2-y^2}$ whereas for the valence band it consists in equal parts of in- an out-of-plane (d_{z^2}) orbitals.

The band structures in Fig. (3.3) are obtained from a Wannier interpolation (cf. Sec. (3.2.2)), where originally a DFT calculation on a $12 \times 12 \times 1$ Monkhorst-Pack grid [47] has been used to create the Wannier construction of the Hamiltonian.

Due to the nature of the Wannier construction, the subspace of the three exctracted bands contains the d_{z^2}, d_{xy}, and $d_{x^2-y^2}$ orbitals of the transition metal, whereas small admixtures of the p-orbitals are nevertheless included. The orbital character of the different bands and valleys is shown in Fig. (3.4). It can clearly be seen, that the in-plane (d_{xy}, $\mathrm{d}_{\mathrm{x}^2-\mathrm{y}^2}$) and out-of-plane ($\mathrm{d}_{\mathrm{z}^2}$) orbitals are counterparts of each other. They change place when comparing the valence band to the conduction band allowing for an optically bright transition at $\mathbf{K}$.

4. Many-Body Theory for TMD Monolayers

As this work aims for analyzing the optical properties of monolayer TMDs under the influence of excited carriers, it is necessary to discuss the implications of an interacting many-particle system. Coulomb effects are dominant in monolayer TMDs as they are weakly screened by the environment. Quasi-particles such as excitons (bound electron-hole pairs) are therefore strongly bound. The absorption of TMDs is dominated by characteristic peaks that can be associated with those same exciton states. The absorption spectra are determined by the polarization dynamics of the layer that can be revealed upon probing with a laser pulse. The polarization can be expressed via the dipole density:

$$\mathbf{P}(t) \;=\; \frac{1}{\mathcal{A}} \sum_{\mathbf{k},\lambda,\lambda'} \mathbf{d}_{\mathbf{k}}^{\lambda'\lambda} \big\langle a_{\mathbf{k}}^{\dagger,\lambda}(t) a_{\mathbf{k}}^{\lambda'}(t) \big\rangle \,. \tag{4.1}$$

Upon knowledge of this macroscopic polarization it is possible to calculate the optical susceptibility χ, whose imaginary part corresponds to the absorption. Exciting charge carriers from the valence to the conduction band using a pump laser leads to a carrier distribution that, considering a thermalized situation, will occupy states according to a Fermi-Dirac function of a given density and temperature. The Coulomb interaction between these charge carriers provides many-body effects such as renormalizations of the single-particle energies and shifts of the exciton states that will cause drastical change to the optical properties. In order to evaluate the many-body effects in dependence of the density, a careful treatment of the Coulomb interaction is necessary.

Moreover the evaluation of the power-dependent total charge carrier density is needed in order to be able to compare theory and experiment, which requires the knowledge of the carrier density. Investigating carrier pump processes upon excitation of varying intensity is of interest as well as the density directly determines the performance of a device. The carrier density is given by

$$n \;=\; \frac{1}{\mathcal{A}} \sum_{\mathbf{k},\lambda} \big\langle a_{\mathbf{k}}^{\dagger,\lambda}(t) a_{\mathbf{k}}^{\lambda}(t) \big\rangle \,. \tag{4.2}$$

In the beginning a look on the general crystal Hamiltonian will be given in order to evaluate two decisive quantities, the macroscopic polarization and the carrier density. This followed by the time evolution of the single particle density matrix elements. In order to properly describe interaction effects, the overarching goal of this chapter is to derive the semiconductor Bloch equations (SBE) together with an appropriate description of the many-body Coulomb interaction. The formalism of Green's functions will be applied, where the Coulomb interaction will be included in terms of the self-energy. The derivation of the theory presented in this chapter follows Refs. [108, 129–138] and others, whom will be cited accordingly.
Furthermore the effects of dielectric screening on the single-particle properties will be investigated using the GdW-method. For the treatment of the absorption spectra the Maxwell equations will provide the description of the optical environment. Other important effects mentioned will be the spin-orbit coupling in TMD monolayer and also basic insight into superconductivity will be given.
To summarize, a model for the optical response of a TMD monolayer embedded in a layered dielectric material will be presented in this section. Different quantities such as the renormalized band structure or the carrier density can be extracted during the calculations.

4.1. General Solid State Hamiltonian

The full Hamiltonian of an interacting many body system contains in principle all kinds of interaction between all involved charged particles. Interactions between electrons in the crystal or between electrons and phonons (quantized lattice vibrations) create new quasi-particles such as polarons. The full Hamiltonian can be expressed as the sum of all contributing Hamiltonians. Starting from the crystal ground-state, carrier-carrier or carrier-phonon interaction can be included systematically:

$$H = H_0 + H_{el.-el.} + H_{el.-phon.} + H_{LM} + \dots \tag{4.3}$$

In this work the single-particle energies of the crystal ground-state H_0 (band structure), the electron-electron and electron-hole interaction $H_{el.-el.}$ respectively as well as the light-matter (dipole) interaction H_{LM} between the crystal electrons and an incident electric field (e.g. an exciting laser pulse) are included in H in order to investigate on the optical properties of TMD monolayers. The electron-phonon interaction will not be included on a microscopic level. It will contribute only as a constant intrinsic dephasing and scattering processes will be modeled as a relaxation into thermalized carrier distributions.

In terms of the Schrödinger field operators $\hat{\psi}$ the Hamiltonian is given by:

$$\begin{aligned}
H &= H_0 + H_{LM} + H_{Coul} \\
&= \sum_s \int \mathbf{d r} \hat{\psi}_s^\dagger(\mathbf{r}, t) h_0(\mathbf{r}) \hat{\psi}_s(\mathbf{r}) \\
&\quad + \sum_s \int \mathbf{d r} \hat{\psi}_s^\dagger(\mathbf{r}, t) \mathbf{d E}(\mathbf{r}, t) \hat{\psi}_s(\mathbf{r}, t) \\
&\quad + \frac{1}{2} \sum_{s,s'} \int \mathbf{d r} \int \mathbf{d r}' \hat{\psi}_s^\dagger(\mathbf{r}, t) \hat{\psi}_{s'}^\dagger(\mathbf{r}', t) V(\mathbf{r} - \mathbf{r}') \hat{\psi}_{s'}(\mathbf{r}', t) \hat{\psi}_s(\mathbf{r}, t) \,. \qquad (4.4)
\end{aligned}$$

The Schrödinger field operators $\hat{\psi}_s^\dagger(\mathbf{r}, t)$ ($\hat{\psi}_s(\mathbf{r}, t)$) create (annihilate) a particle in the state characterized by $\{\mathbf{r}, t, s\}$. They obey the fermionic anticommutation relation $\{A, B\} = AB + BA$:

$$\begin{aligned}
\left\{ \hat{\psi}_s(\mathbf{r}, t_1), \hat{\psi}_{s'}^\dagger(\mathbf{r}', t_2) \right\}_{t_1 = t_2} &= \delta(\mathbf{r} - \mathbf{r}') \delta_{ss'} \\
\left\{ \hat{\psi}_s^\dagger(\mathbf{r}, t_1), \hat{\psi}_{s'}^\dagger(\mathbf{r}', t_2) \right\}_{t_1 = t_2} &= \left\{ \hat{\psi}_s(\mathbf{r}, t_1), \hat{\psi}_{s'}(\mathbf{r}', t_2) \right\}_{t_1 = t_2} = 0 \qquad (4.5)
\end{aligned}$$

As marked by the subscripts at the commutator this relation holds only for the equal time limit. The single-particle Hamiltonian $h_0(\mathbf{r})$ contains the ground-state kinetic energy eigenvalues of electrons within the periodic crystal potential. This is described in terms of the band structure (see Chap. (3)) including energy shifts due to the interaction with the dielectric environment. It obeys the eigenvalue equation

$$h_0 \phi_\nu(\mathbf{r}) = \varepsilon_\nu \phi_\nu(\mathbf{r}) \,. \qquad (4.6)$$

For future problems it is useful to expand the field operators into the eigenbasis $\phi_\nu(\mathbf{r})$ of the single-particle problem.

$$\hat{\psi}(\mathbf{r}, t) = \sum_\nu \hat{a}_\nu(t) \phi_\nu(\mathbf{r}) \qquad (4.7)$$

The $\phi_\nu(\mathbf{r})$ have to fulfill the properties of a complete orthonormal basis set, namely they have to be orthogonal and provide a resolution of unity, or in other words be complete:

$$\int \mathbf{d r} \phi_\nu^*(\mathbf{r}) \phi_{\nu'}(\mathbf{r}) = \delta_{\nu\nu'} \qquad \sum_\nu \phi_\nu(\mathbf{r}) \phi_\nu^*(\mathbf{r}) = \mathbf{1} \,. \qquad (4.8)$$

The creation and annihilation operators $\hat{a}_\nu^{(\dagger)}$ inherit the fermionic commutation relation (4.5) of the field operators. The crystal electrons occupy the Bloch states $|\phi_\nu\rangle$ in the periodic crystal potential. For the derivations necessary in this work it is most convenient to divide the index ν of the used Bloch state introduced in Chap. (3) into quasi-momentum index $\mathbf{k}$ of the crystal electrons and a band index λ resulting in $\nu = \{\mathbf{k}, \lambda, s\}$, while the time dependence will be written explicitly. Thus $\phi_\nu(t) = \phi_{\mathbf{k}}^\lambda(t)$ and the spin index s will be dropped from now on as all interactions considered here are spin-diagonal, exceptions will be labeled. The Hamiltonian in the eigenbasis expansion (see Eq. (4.7)) is given by:

$$\begin{aligned} H &= \sum_{\mathbf{k}} \varepsilon_{\mathbf{k}}^\lambda \hat{a}_{\mathbf{k}}^{\dagger,\lambda}(t)\hat{a}_{\mathbf{k}}(t) \\ &+ \sum_{\mathbf{k}} \hat{a}_{\mathbf{k}}^{\dagger,\lambda}(t)\hat{a}_{\mathbf{k}}^{\lambda'}(t)[\mathbf{dE}(\mathbf{r},t)]_{\mathbf{k}}^{\lambda,\lambda'} \\ &+ \frac{1}{2} \sum_{\mathbf{k}_1\ldots\mathbf{k}_4,\lambda_1\ldots\lambda_4} \hat{a}_{\mathbf{k}_1}^{\dagger,\lambda_1}(t)\hat{a}_{\mathbf{k}_2}^{\dagger,\lambda_2}(t)\hat{a}_{\mathbf{k}_3}^{\lambda_3}(t)\hat{a}_{\mathbf{k}_4}^{\lambda_4}(t)V_{\mathbf{k}_1\mathbf{k}_2\mathbf{k}_3\mathbf{k}_4}^{\lambda_1\lambda_2\lambda_3\lambda_4} \end{aligned} \tag{4.9}$$

More insight into the derivation of the Coulomb and dipole matrix elements will be given later.

4.1.1. Statistical Operator and Time-Evolution

In order to gain more information on the full many-body system the density matrix formalism is a commonly used theory. The statistical operator $\hat{\varrho}$ allows for the calculation of any observable by tracing it out after multiplication with the statistical operator [nolting]:

$$\langle \hat{O} \rangle = \mathrm{tr}\left\{\hat{\varrho}\hat{O}\right\}. \tag{4.10}$$

While it is not feasible to calculate the full statistical operator, the single-particle density matrix (spdm) is obtained by trancing out all other degrees of freedom. The definition of the spdm is given by

$$\hat{\varrho}(t) = \sum_i p_i |\phi_i(t)\rangle\langle\phi_i(t)|. \tag{4.11}$$

All single-particle information on the system are contained, the states $|\phi_i(t)\rangle$ are mixed with probabilities p_i, $\sum_i p_i = 1$.

Using the eigenbasis expansion especially the state-diagonal ($\mathbf{k} = \mathbf{k}'$) matrix elements of the spdm contain all information on coherences ψ (or microscopic polarizations) and occupation probabilities f of the system:

$$\psi_{\mathbf{k}}^{\lambda\lambda'}(t) = \langle a_{\mathbf{k}}^{\dagger,\lambda}(t) a_{\mathbf{k}}^{\lambda'}(t) \rangle \tag{4.12}$$

$$f_{\mathbf{k}}^{\lambda}(t) = \langle a_{\mathbf{k}}^{\dagger,\lambda}(t) a_{\mathbf{k}}^{\lambda}(t) \rangle , \tag{4.13}$$

where the first one is needed to calculate the polarization

$$\mathbf{P}(t) = \sum_{\mathbf{k},\lambda\lambda'} \left(\mathbf{d}_{\mathbf{k}}^{\lambda\lambda'}\right)^* \langle a_{\mathbf{k}}^{\dagger,\lambda}(t) a_{\mathbf{k}}^{\lambda'}(t) \rangle = \sum_{\mathbf{k},\lambda\lambda'} \left(\mathbf{d}_{\mathbf{k}}^{\lambda\lambda'}\right)^* \psi_{\mathbf{k}}^{\lambda\lambda'}(t) \tag{4.14}$$

and the latter one can be extended to the charge carrier density n^λ of the respective band by summing over all **k**, or the total density by additionally summing over all λ:

$$n = \frac{1}{\mathcal{A}} \sum_{\mathbf{k},\lambda} f_{\mathbf{k}}^{\lambda} = \frac{1}{\mathcal{A}} \sum_{\mathbf{k},\lambda} \langle a_{\mathbf{k}}^{\dagger,\lambda}(t) a_{\mathbf{k}}^{\lambda}(t) \rangle . \tag{4.15}$$

In general time-evolution of the statistical operator can be expressed using the time evolution operator $U(t_1, t_2)$. While in the Schrödinger representation the full time dependence is cast into the wave functions and the operators are time independent, the Dirac or interaction representation states the opposite: the wave functions are time independent and the operators carry the full time dependence. In the interaction representation the time dependence of the wave functions is determined by the interaction Hamiltonian while the operators obey the trivial time dependence of the single-particle Hamiltonian. For the operator it reads:

$$\hat{O}^D(t) = U_0^\dagger(t, t_0) \hat{O}^S U_0(t, t_0) , \tag{4.16}$$

with U_0 being the trivial time-evolution operator of the non-interacting part of the Hamiltonian H_0.

$$U_0(t_1, t_2) = e^{-\frac{i}{\hbar} H_0 (t_1 - t_2)} \tag{4.17}$$

For the states one finds

$$\left|\psi^D(t)\right\rangle = S(t, t_0) \left|\psi(t_0)\right\rangle , \tag{4.18}$$

which directly leads to the Dirac representation of the density matrix

$$\varrho^D(t) \;=\; S(t_0,t)\varrho^S S(t,t_0) \tag{4.19}$$

with the S-operator being defined by the Hamiltonian containing all interactions $H_{\text{Int.}}$:

$$S(t_1,t_2) \;=\; \hat{T}e^{-\frac{i}{\hbar}\int\limits_{t_1}^{t_2} \mathrm{d}t' H_{\text{Int.}}(t')} \,. \tag{4.20}$$

To assure the correct ordering of all time arguments the time ordering operator has been introduced. The operator sorts all expressions afterwards starting with later times to the left side and proceeding to t_0 on the right side ('late goes left'). Exponential functions of operators are defined as usual by their series expansion.
Using the S-operators to reformulate the expectation value Eq. (4.10) into operator expressions in the interaction representation one obtains

$$\left\langle \hat{O}(t)\right\rangle \;=\; \text{tr}\left\{\varrho^D S(t_0,\infty)\hat{T}[S(\infty,t_0)\hat{O}^D(t)]\right\}\,, \tag{4.21}$$

where it has been used that a product of time evolution operators always develops from the first time of the left-most operator to the last time of the right-most operator. Regardless how many infinitely small timesteps are taken, any S-operator can be expressed as multiplication of two operators according to (semi-group property):

$$S(t_2,t_1) \;=\; S(t_2,t_3)S(t_3,t_1)\,. \tag{4.22}$$

The time evolution operator formalism as obtained above is useful for obtaining the time dependence of the system observables for $T = 0$ K in an equilibrium state. Further effort has to be made to describe non-equilibrium states in order to obtain the time evolution or equations of motion of the density matrix elements. Therefore a short presentation of the so-called cluster expansion approach will be given in the next section.

4.1.2. Equation of Motion and Cluster Expansion

The dynamics of the matrix elements of $\hat{\varrho}$ can be obtained by deriving their Heisenberg equation of motion:

$$i\hbar\frac{\partial}{\partial t}\hat{O}(t) \;=\; [H,\hat{O}(t)]\,, \tag{4.23}$$

where the brackets denote the commutator $[H, \hat{O}(t)] = H\hat{O}(t) - \hat{O}(t)H$ of the respective operators. For electron annihilation operators one obtains by using the Hamiltonian in Eq. (4.9):

$$\begin{aligned} i\hbar\frac{\mathrm{d}}{\mathrm{d}t}\hat{a}^{\lambda}_{\mathbf{k}}(t) &= \varepsilon^{\lambda}_{\mathbf{k}}\hat{a}^{\lambda}_{\mathbf{k}}(t) + [\mathbf{dE}(\mathbf{r},t)]^{\lambda,\lambda'}_{\mathbf{k}}\hat{a}^{\lambda}_{\mathbf{k}}(t) \\ &+\frac{1}{2}\sum_{\mathbf{k}_1\ldots\mathbf{k}_4,\lambda_1\ldots\lambda_4} V^{\lambda_1\lambda_2\lambda_3\lambda_4}_{\mathbf{k}_1\mathbf{k}_2\mathbf{k}_3\mathbf{k}_4}\Big[\ \hat{a}^{\dagger,\lambda_2}_{\mathbf{k}_2}(t)\hat{a}^{\lambda_3}_{\mathbf{k}_3}(t)\hat{a}^{\lambda_4}_{\mathbf{k}_4}(t)\delta_{\mathbf{k}_1,\mathbf{k}} \\ &\qquad -\hat{a}^{\dagger,\lambda_1}_{\mathbf{k}_2}(t)\hat{a}^{\lambda_3}_{\mathbf{k}_3}(t)\hat{a}^{\lambda_4}_{\mathbf{k}_4}(t)\delta_{\mathbf{k}_2,\mathbf{k}}\ \Big] \end{aligned} \tag{4.24}$$

Exploiting the equation derived above together with

$$\frac{\mathrm{d}}{\mathrm{d}t}\big\langle\hat{a}^{\dagger,\lambda}_{\mathbf{k}}(t)\hat{a}^{\lambda'}_{\mathbf{k}}(t)\big\rangle = \big\langle\frac{\mathrm{d}}{\mathrm{d}t}\hat{a}^{\dagger,\lambda}_{\mathbf{k}}(t)\hat{a}^{\lambda'}_{\mathbf{k}}(t)\big\rangle + \big\langle\hat{a}^{\dagger,\lambda}_{\mathbf{k}}(t)\frac{\mathrm{d}}{\mathrm{d}t}\hat{a}^{\lambda'}_{\mathbf{k}}(t)\big\rangle \tag{4.25}$$

is one way to derive the SBE. The interpretation and derivation of the SBE using the technique of Green's functions is part of the next chapters. Obviously for the Coulomb interaction a two particle expectation value occurs. These two-particle expectation values obey an equation of motion that contains three-particle expectation values and so on. Therefore one has to deal with a hierarchy problem. An appropriate truncation in order to obtain a closed set of equations can be obtained e.g. from the Hartree-Fock factorization scheme [108], where

$$\begin{aligned} \big\langle\hat{a}^{\dagger,\lambda_1}_{\mathbf{k}_1}\hat{a}^{\dagger,\lambda_2}_{\mathbf{k}_2}\hat{a}^{\lambda_3}_{\mathbf{k}_3}\hat{a}^{\lambda_4}_{\mathbf{k}_4}\big\rangle &= \big\langle\hat{a}^{\dagger,\lambda_1}_{\mathbf{k}_1}\hat{a}^{\lambda_3}_{\mathbf{k}_3}\big\rangle\big\langle\hat{a}^{\dagger,\lambda_2}_{\mathbf{k}_2}\hat{a}^{\lambda_4}_{\mathbf{k}_4}\big\rangle\delta_{\mathbf{k}_1,\mathbf{k}_3}\delta_{\mathbf{k}_2,\mathbf{k}_4} \\ &-\big\langle\hat{a}^{\dagger,\lambda_1}_{\mathbf{k}_1}\hat{a}^{\lambda_4}_{\mathbf{k}_4}\big\rangle\big\langle\hat{a}^{\dagger,\lambda_2}_{\mathbf{k}_2}\hat{a}^{\lambda_3}_{\mathbf{k}_3}\big\rangle\delta_{\mathbf{k}_1,\mathbf{k}_4}\delta_{\mathbf{k}_2,\mathbf{k}_3}\,. \end{aligned} \tag{4.26}$$

Another possibility is the so called cluster expansion scheme. Here the remaining correlation functions from the factorization are determined. Thus N-particle expectation values are factorized into their singlet, doublet, ... contribution according to the number of particles they involve. Thus the factorization contains all operator averages up to $N-1$-particle expectation values and all possible combinations of N-particle factorizations. The cluster expansion is schematically given by [139]

$$\begin{aligned}
\langle 1 \rangle &= \delta\langle 1 \rangle && (4.27)\\
\langle 2 \rangle &= \langle 1 \rangle\langle 1 \rangle + \delta\langle 2 \rangle && (4.28)\\
\langle 3 \rangle &= \langle 1 \rangle\langle 1 \rangle\langle 1 \rangle + \langle 1 \rangle\delta\langle 2 \rangle + \delta\langle 3 \rangle && (4.29)\\
\langle 4 \rangle &= \langle 1 \rangle\langle 1 \rangle\langle 1 \rangle\langle 1 \rangle + \langle 1 \rangle\langle 1 \rangle\delta\langle 2 \rangle + \langle 1 \rangle\delta\langle 3 \rangle + \delta\langle 2 \rangle\delta\langle 2 \rangle + \delta\langle 4 \rangle && (4.30)\\
&\vdots
\end{aligned}$$

Here $\langle N \rangle$ is the N-particle expectation value containing $2N$ operators. The correlation functions that are defined by the difference of the full N-particle average and the factorization are labeled as $\delta\langle N \rangle$.

4.2. Non-Equilibrium Green's Functions

The method of choice for this work is the method of non-equilibrium Green's functions using the Schwinger-Keldysh formalism [135]. In order to do so the general properties of Green's functions will be introduced first. The so called Keldysh contour, which has been explicitly developed for evaluating non-equilibrium situations, is presented afterwards. The method of Green's functions is a well-established method to describe excitations of an interacting many-particle system.

4.2.1. Properties of Green's Functions

If one generalizes the expectation values within the spdm to different times one obtains the so-called greater and lesser Green's functions $G^{\gtrless}$. These contain the information on the probability whether to find a particle (or not) at $\mathbf{r}_2$ and time t_2 with spin s_2 if beforehand a particle at $\mathbf{r}_1$ and time t_1 with spin s_1 has been added (removed). Therefore these functions are also called electron and hole propagator. They are defined as:

$$\begin{aligned}
-i\hbar G^{<}_{s_1,s_2}(\mathbf{r}_1, t_1; \mathbf{r}_2, t_2) &= \left\langle \psi^{\dagger}_{s_2}(\mathbf{r}_2, t_2)\psi_{s_1}(\mathbf{r}_1, t_1) \right\rangle && (4.31)\\
-i\hbar G^{>}_{s_1,s_2}(\mathbf{r}_1, t_1; \mathbf{r}_2, t_2) &= \left\langle \psi_{s_1}(\mathbf{r}_1, t_1)\psi^{\dagger}_{s_2}(\mathbf{r}_2, t_2) \right\rangle . && (4.32)
\end{aligned}$$

If $t_1 > t_2$ then one deals with the electron propagator $G^{>}$ as first the creation operator is applied. For $t_2 > t_1$ one obtains $G^{<}$, which is also called hole propagator as a particle is removed first. For further calculations the abbreviation $1 = \{r_1, t_1, s_1\}$ for the indices will be used. Especially for the equal time limit these functions reproduce the normal ordered expectation values of the density matrix, meaning that always:

$$G^{\gtrless}(t,t) \quad = \quad \lim_{\epsilon\to 0} G^{\gtrless}(t,t+\epsilon) \tag{4.33}$$

and also for both propagators the normal order of the operators is restored. Often this is also written as $G^{\gtrless}(t,t^{+})$. For equal time and $\mathbf{k}$ arguments the propagators resemble the single-particle expectation values known from the density matrix (cf. Eq. (4.13)):

$$-i\hbar G^{\gtrless,\lambda\lambda'}_{\mathbf{k}}(t,t^{+}) \quad = \quad \psi^{\lambda\lambda'}_{\mathbf{k}}(t) \tag{4.34}$$

$$-i\hbar G^{\gtrless,\lambda}_{\mathbf{k}}(t,t^{+}) \quad = \quad f^{\lambda}_{\mathbf{k}}(t) \tag{4.35}$$

The time-ordered Green's function is defined as:

$$-i\hbar G(1,2) \quad = \quad \left\langle \hat{T}[\psi(1)\psi^{\dagger}(2)] \right\rangle \tag{4.36}$$

Here the time ordering operator $\hat{T}$ has been used again to always ensure the correct time ordering ('late goes left') by rearranging the respective expressions of the operators leading to:

$$\hat{T}[\psi(1)\psi^{\dagger}(2)] \quad = \quad \begin{cases} \psi(1)\psi^{\dagger}(2), & \text{if} \quad t_1 > t_2 \\ -\psi^{\dagger}(2)\psi(1), & \text{if} \quad t_2 > t_1 \end{cases} \tag{4.37}$$

$G(1,2)$ contains for example arbitrary single-particle expectation values as well as the expectation value of the total energy [140].

By linearly combining the propagators, the retarded and advanced Green's functions $G^{\mathrm{R/A}}$ are built. They describe the causal (the response of the system follows the excitation) and the anti-causal (system response before the excitation) response of the system.

$$G^{\mathrm{R/A}}(1,2) \quad = \quad \pm\theta\left(\pm(t_1-t_2)\right)\left[G^{>}(1,2)-G^{<}(1,2)\right] \tag{4.38}$$

Furthermore the so called spectral function, which contains information on the excitation spectrum, is defined as:

$$\hat{A}(1,2) \quad = \quad G^{>}(1,2)-G^{<}(1,2) = G^{\mathrm{R}}(1,2)-G^{\mathrm{A}}(1,2) \tag{4.39}$$

$$G^{\mathrm{R/A}}(1,2) \quad = \quad \pm\theta\left(\pm(t_1-t_2)\right)\hat{A}(1,2)\,. \tag{4.40}$$

In the simplified picture of quasi-particles each elementary excitation of the system is described as a particle. The spectral function has peaks at every quasi-particle eigenenergy. Each peak is broadened by the lifetime of the respective quasi-particle as will be shown later on in this work. In the quasi-particle approximation, that assumes a weak interaction, the energies will be shifted by the real part of the chosen self-energy while the imaginary part contributes the broadening.

As conclusion of the first section the eigenbasis expansion of the Green's functions shall be mentioned here:

$$G(1,2) = G(\mathbf{r}_1, t_1; \mathbf{r}_2, t_2) = \sum_{\nu_1,\nu_2} \phi_{\nu_1}(\mathbf{r}_1) G_{\nu_1\nu_2}(t_1,t_2) \phi^*_{\nu_2}(\mathbf{r}_2) \tag{4.41}$$

$$G^{>,\lambda_1\lambda_2}_{\mathbf{k}}(t_1,t_2) = -\frac{i}{\hbar}\big\langle a^{\lambda_1}_{\mathbf{k}}(t_1) a^{\lambda_2,\dagger}_{\mathbf{k}}(t_2)\big\rangle \tag{4.42}$$

$$G^{<,\lambda_1\lambda_2}_{\mathbf{k}}(t_1,t_2) = \frac{i}{\hbar}\big\langle a^{\lambda_1,\dagger}_{\mathbf{k}}(t_1) a^{\lambda_2}_{\mathbf{k}}(t_2)\big\rangle \,. \tag{4.43}$$

When obtaining the time evolution of the Green's functions mentioned here, special care has to be taken for the time ordering. The next section will provide a derivation of the dynamics for the two-time quantities.

4.2.2. Keldysh Contour and Hedin's Equations

For the ground state at $T = 0$ K it is possible to extract the anti-time ordered part $S(t_0, \infty)$ of Eq. (4.21) as a phase factor by using the theorem of Gell-Mann and Low [141]. This cannot be done for the non-equilibrium case until a new time-ordering is introduced, the so-called Keldysh contour. This will be part of the following section.

An external perturbation $H_{\text{ext}}(t)$, for example controllable charges or fields, shall bring the system out of equilibrium. They either act as real perturbation (e.g. exciting charges) or as a probe for testing the system response.

$$H_{\text{full}} = H_0 + H_{\text{Int.}} + H_{\text{ext}}(t) \tag{4.44}$$

In order to evaluate expectation values with the system being perturbed, it is convenient to change into the interaction or Dirac picture again. In this case the time dependence of the wave functions $U(t_1, t_2)$ is obtained from $H_0 + H_{\text{Int.}}$, while the S-operators contain the external perturbation. The S-operators take the form

$$\begin{aligned} S_{\mathcal{C}} &= \hat{T}_{\mathcal{C}} e^{-\frac{i}{\hbar}\int_{\mathcal{C}} \mathrm{d}\underline{\tau} H_{\text{ext}}(\underline{\tau})} \\ \text{with} \quad \int_{\mathcal{C}} \mathrm{d}\underline{\tau} &= \int\limits_{-\infty}^{+\infty} \mathrm{d}\tau_{+} - \int\limits_{-\infty}^{+\infty} \mathrm{d}\tau_{-}\,, \end{aligned} \tag{4.45}$$

where all quantities have been defined on the hereby introduced Keldysh contour $\mathcal{C}$ [142, 143]. On this contour the time is split into two branches, the upper and the lower branch, ranging from $\mp\infty$ to $\pm\infty$ respectively. On the lower branch it is the other way round. This new time $\underline{t}$ carries an additional contour index $\eta = \pm 1$, where $+1$ is for times on the upper branch and -1 on the lower branch. Any $\underline{t}$ on the upper branch is always before times on the lower branch even if the physical times are not. After each calculation the so-called 'physical limit' $H_{\text{ext}}(t_{+}) = H_{\text{ext}}(t_{-})$ has to be performed in order to return to physical times. The time-ordering operator $\hat{T}_{\mathcal{C}}$ acts as $\hat{T}$ for times on the upper branch and as $\tilde{\hat{T}}$ for times on the lower branch. The advantage gained is the possibility to treat the further calculations formally equivalent to the equilibrium case at $T = 0$ K, while describing the non-equilibrium system, because the time-ordering is given on $\mathcal{C}$. The expectation value of an operator becomes

$$\left\langle \hat{O}(\underline{t}) \right\rangle_{\mathcal{C}} = \frac{\langle T_{\mathcal{C}} \left[S_{\mathcal{C}} \hat{O}^{D}(\underline{t}) \right] \rangle}{\left\langle S_{\mathcal{C}} \right\rangle}\,, \tag{4.46}$$

and a phase factor can be separated in analogy to the Gell-Mann and Low theorem [141]. The Keldysh Green's function is defined similarly to Sec. (4.2.1)

$$G(\underline{1}, \underline{2}) = -\frac{i}{\hbar} \langle \hat{\psi}(\underline{1}) \hat{\psi}^{\dagger}(\underline{2}) \rangle_{\mathcal{C}}\,, \tag{4.47}$$

which represents a matrix according to the Keldysh index. In the physical limit one obtains for the different Keldysh index combinations of Eq. (4.47):

$$\begin{aligned} G(1_{+}, 2_{+}) &= G(1, 2) \\ G(1_{-}, 2_{-}) &= \tilde{G}(1, 2) \\ G(1_{+}, 2_{-}) &= G^{<}(1, 2) \\ G(1_{-}, 2_{+}) &= G^{>}(1, 2)\,. \end{aligned} \tag{4.48}$$

Further treatment of the Keldysh Green's functions lead to the fundamental set of equation [132, 144].

$$\begin{aligned}
G(\underline{1},\underline{2}) &= G_0(\underline{1},\underline{2}) + \int \mathrm{d}\underline{3} \int \mathrm{d}\underline{4}\, G_0(\underline{1},\underline{3})\Sigma(\underline{3},\underline{4})G(\underline{3},\underline{2}) &(4.49)\\
W(\underline{1},\underline{2}) &= V(\underline{1},\underline{2}) + \int \mathrm{d}\underline{3} \int \mathrm{d}\underline{4}\, V(\underline{1},\underline{3})P(\underline{3},\underline{4})W(\underline{4},\underline{2}) &(4.50)\\
\Sigma(\underline{1},\underline{2}) &= \int \mathrm{d}\underline{3} \int \mathrm{d}\underline{4}\, G(\underline{1},\underline{3})W(\underline{1},\underline{4})\Gamma(\underline{3},\underline{4},\underline{2}) &(4.51)\\
P(\underline{1},\underline{2}) &= \int \mathrm{d}\underline{3} \int \mathrm{d}\underline{4}\, G(\underline{1},\underline{3})\Gamma(\underline{3},\underline{2},\underline{4})G(\underline{4},\underline{1}) &(4.52)\\
\Gamma(\underline{1},\underline{2},\underline{3}) &= -i\hbar\delta(\underline{1},\underline{2})\delta(\underline{1},\underline{3}) \\
&\quad + i\hbar \int \mathrm{d}\underline{4} \int \mathrm{d}\underline{5} \int \mathrm{d}\underline{6} \int \mathrm{d}\underline{7} \frac{\delta\Sigma(\underline{1},\underline{2})}{\delta G(\underline{4},\underline{5})} G(\underline{4},\underline{6})G(\underline{7},\underline{5})\Gamma(\underline{6},\underline{7},\underline{3}) &(4.53)
\end{aligned}$$

This closed set of equations yields the (single-particle) Keldysh Green's function G, the plasmon Green's function W, the self-energy Σ, the polarization P and the vertex-function Γ. The most common approximation is the so-called random phase approximation, where $\frac{\delta\Sigma(\underline{1},\underline{2})}{\delta G(\underline{4},\underline{5})} = 0$ is chosen. This leads to $P = GG$ and $\Sigma = GW$ and is also often called GW-approximation. Note that the choice of approximation has to be consistent for Σ and P [145, 146]. These approximations will be explained more detailed in later sections of this chapter.

In order to regain Green's functions with real time arguments the Langreth Wilkens theorems [129] are used. For integral expression of the type $C(\underline{1},\underline{2}) = \int \mathrm{d}\underline{3} A(\underline{1},\underline{3})B(\underline{3},\underline{2})$ that occur frequently in Eq. (4.49) to (4.53) they state:

$$\begin{aligned}
C^{\gtrless}(1,2) &= \int \mathrm{d}3\, \left[A^{\mathrm{R}}(1,3)B^{\gtrless}(3,2) + A^{\gtrless}(1,3)B^{\mathrm{A}}(3,2)\right] &(4.54)\\
C^{\mathrm{R/A}}(1,2) &= \int \mathrm{d}3\, A^{\mathrm{R/A}}(1,3)B^{\mathrm{R/A}}(3,2) &(4.55)
\end{aligned}$$

To obtain equations of motion for the propagators $G^{\gtrless}$ and the retarded (advanced) Green's functions $G^{\mathrm{R/A}}$ the Langreth Wilkens theorems are applied to Eq. (4.49) in its differential form

$$\int \mathrm{d}\underline{3} \left[G_0^{-1}(\underline{1},\underline{3}) - \Sigma(\underline{1},\underline{3})\right] G(\underline{3},\underline{2}) = \delta(\underline{1},\underline{2})\,. \qquad (4.56)$$

The inverse free Green's function $G_0^{-1}(\underline{1},\underline{2})$ acts as a differential operator. Explicitely written it states

$$G_0^{-1}(\underline{1},\underline{2}) \quad = \quad \left[i\hbar\frac{\partial}{\partial \underline{t}_1} - H_0(\underline{1})\right]\delta(\underline{1},\underline{2}) \tag{4.57}$$

Using the eigenfunction expansion and all single-particle terms of the full Hamiltonian it becomes

$$G^{-1}_{0,\nu_1\nu_2}(t_1,t_2) \quad = \quad \left[\frac{\partial}{\partial t_1} - \varepsilon_{\nu_1}\right]\delta_{\nu_1,\nu_2}\delta(t_1-t_2) + \left[\mathbf{dE}(t_1)\right]_{\nu_1\nu_2}\delta(t_1-t_2)\,. \tag{4.58}$$

Choosing the different possible combinations of Keldysh indices together with the Langreth Wilkens theorems Eq. (4.56) a set of coupled integro-differential equations is obtained. These are the so-called Kadanoff Baym Equations (KBE) [137].

$$\int \mathrm{d}3\left[G_0^{-1}(1,3) - \Sigma^{\mathrm{R}}(1,3)\right]G^{\mathrm{R}}(3,2) \quad = \quad \delta(1,2) \tag{4.59}$$

$$\int \mathrm{d}3 G^{\mathrm{R}}(1,3)\left[G_0^{-1}(3,2) - \Sigma^{\mathrm{R}}(3,2)\right] \quad = \quad \delta(1,2) \tag{4.60}$$

$$\int \mathrm{d}3\left\{\left[G_0^{-1}(1,3) - \Sigma^{\mathrm{R}}(1,3)\right]G^{<}(3,2) - \Sigma^{<}(1,3)G^{\mathrm{A}}(3,2)\right\} \quad = \quad 0 \tag{4.61}$$

$$\int \mathrm{d}3\left\{G^{<}(1,3)\left[G_0^{-1}(3,2) - \Sigma^{\mathrm{R}}(3,2)\right] - G^{\mathrm{R}}(1,3)\Sigma^{<}(3,2)\right\} \quad = \quad 0 \tag{4.62}$$

These equations mark the starting point for the derivation of the semiconductor Bloch equations, which will be shown in the following section.

4.2.3. Semiconductor Bloch Equations

The semiconductor Bloch equations can be derived directly from the KBE [147–149]. They are the equation of motion for the lesser Green's function [150], which, if assumed to be diagonal in the state when expanded with eigenfunctions, corresponds to the occupation probabilities and the microscopic polarizations as already written in Eqs. (4.35) and (4.34). Taking the sum and the difference of both KBE for the lesser and the retarded Green's function one is left with two equations, first for the sum

$$\begin{aligned} i\hbar\left[\frac{\partial}{\partial t_1}+\frac{\partial}{\partial t_2}\right]G^{<}(1,2) &= (H_0(1)-H_0(2))G^{<}(1,2) \\ &\quad+\int \mathrm{d}3\,\left\{\Sigma^{\mathrm{R}}(1,3)G^{<}(3,2)+\Sigma^{<}(1,3)G^{\mathrm{A}}(3,2)\right. \\ &\quad\left.-G^{<}(1,2)\Sigma^{\mathrm{A}}(3,2)-G^{\mathrm{R}}(1,3)\Sigma^{<}(3,2)\right\} \end{aligned} \tag{4.63}$$

and secondly for the difference one obtains

$$\begin{aligned} i\hbar\left[\frac{\partial}{\partial t_1}-\frac{\partial}{\partial t_2}\right]G^{\mathrm{R}}(1,2) &= 2\delta(t_1-t_2)+2H_0(1)G^{\mathrm{R}}(1,2) \\ &\quad+\int \mathrm{d}3\,\left\{\Sigma^{\mathrm{R}}(1,3)G^{\mathrm{R}}(3,2)+G^{\mathrm{R}}(1,3)\Sigma^{\mathrm{R}}(3,2)\right\}\,. \end{aligned} \tag{4.64}$$

The single-particle Hamiltonian $H_0(1)$ contains the single-particle kinetic energy term as well as the dipole interaction according to Eq. (4.58).

To be more specific: the SBE are equations of motion for state and time-diagonal lesser Green's functions. After applying the eigenbasis expansion only Green's functions diagonal in $\mathbf{k}$ and in t are kept. As mentioned before, this will lead to the requested physical quantities $\psi_{\mathbf{k}}^{\lambda\lambda'}(t)$ and $f_{\mathbf{k}}^{\lambda}(t)$. The dipole interaction will be explained later on, for now it is only important to note that the incident angle of the electric field $\mathbf{E}(t)$ is assumed to be perpendicular to the monolayer plane. Due to the small thickness of the monolayer it is assumed that dipoles $\mathbf{d}_{\mathbf{k}}^{\lambda\lambda'}$ can only arise within the plane. The electric field that will represent the envelope function of the laser pulse will not carry any band λ or momentum index $\mathbf{k}$. The specific form of the electronic self-energy will be chosen in the next section. The self-energy contributions $\Sigma^{\gtrless}$ are therefore left variable. Using the eigenfunction expansion one obtains

$$\begin{aligned} i\hbar\frac{\partial}{\partial t}G_{\mathbf{k}}^{<,\lambda\lambda'}(t) &= (\varepsilon_{\mathbf{k}}^{\lambda}-\varepsilon_{\mathbf{k}}^{\lambda'})G_{\mathbf{k}}^{<,\lambda\lambda'}(t) \\ &\quad+\sum_{\lambda''}\left(\mathbf{d}_{\mathbf{k}}^{\lambda\lambda''}G_{\mathbf{k}}^{<,\lambda''\lambda'}(t)-G_{\mathbf{k}}^{<,\lambda\lambda''}(t)\mathbf{d}_{\mathbf{k}}^{\lambda''\lambda'}\right)\mathbf{E}(t) \\ &\quad+\sum_{\lambda''}\int_{-\infty}^{\infty}\mathrm{d}t'\,\left\{\Sigma_{\mathbf{k}}^{\mathrm{R},\lambda\lambda''}(t,t')G_{\mathbf{k}}^{<,\lambda''\lambda'}(t',t)+\Sigma_{\mathbf{k}}^{<,\lambda\lambda''}(t,t')G_{\mathbf{k}}^{\mathrm{A},\lambda''\lambda'}(t',t)\right. \\ &\quad\left.-G_{\mathbf{k}}^{<,\lambda\lambda''}(t,t')\Sigma_{\mathbf{k}}^{\mathrm{A},\lambda''\lambda'}(t',t)-G_{\mathbf{k}}^{\mathrm{R},\lambda\lambda''}(t,t')\Sigma_{\mathbf{k}}^{<,\lambda''\lambda'}(t',t)\right\} \end{aligned} \tag{4.65}$$

for the equation of motion for $G^{<,\lambda\lambda'}_{\mathbf{k}}(t)$. Here, as explained before in Eq. (4.9), the $\varepsilon^{\lambda}_{\mathbf{k}}$ are the single-particle eigenenergies of $H_0(1)$, $\mathbf{E}(t)$ is the electric field and $\mathbf{d}^{\lambda''\lambda'}_{\mathbf{k}}$ are the dipole matrix elements.

Each retarded or advanced Green's function can be separated into greater and lesser Green's functions according to the definition in Eq. (4.38). For the self-energy this is also done. Additionally a singular part $\Sigma^{\delta}(1,2)$ arises, due to the instantaneous nature of the Coulomb interaction. This term contains the Hartree-Fock interaction (as will be shown later) and is written as $\Sigma^{\delta}(1,2) = \Sigma^{\mathrm{HF}}(1,2)\delta(t_1 - t_2)$. This is expressed as [147]

$$\begin{aligned}
\Sigma^{\mathrm{R/A}}(1,2) &= \Sigma^{\mathrm{HF}}(1,2)\delta(t_1 - t_2) \pm \theta(t_1 - t_2)\left[\Sigma^{>}(1,2) - \Sigma^{<}(1,2)\right] , && (4.66)\\
G^{\mathrm{R/A}}(1,2) &= \pm\theta\left(\pm(t_1 - t_2)\right)\left[G^{>}(1,2) - G^{<}(1,2)\right] . && (4.67)
\end{aligned}$$

Further discussions concerning $\Sigma^{\mathrm{HF}}(1,2)$ are part of the next section. If these definitions are inserted in Eq. (4.65) one obtains:

$$\begin{aligned}
i\hbar\frac{\partial}{\partial t}G^{<,\lambda\lambda'}_{\mathbf{k}}(t) =& (\varepsilon^{\lambda}_{\mathbf{k}} - \varepsilon^{\lambda'}_{\mathbf{k}})G^{<,\lambda\lambda'}_{\mathbf{k}}(t)\\
&+\sum_{\lambda''}\left(\mathbf{d}^{\lambda\lambda''}_{\mathbf{k}}G^{<,\lambda''\lambda'}_{\mathbf{k}}(t) - G^{<,\lambda\lambda''}_{\mathbf{k}}(t)\mathbf{d}^{\lambda''\lambda'}_{\mathbf{k}}\right)\mathbf{E}(t)\\
&+\sum_{\lambda''}\int_{-\infty}^{\infty}\mathrm{d}t'\ \Big\{\left[\Sigma^{\mathrm{HF}}\delta(t,t') + \Theta(t-t')\left(\Sigma^{>} - \Sigma^{<}\right)\right]^{\lambda\lambda''}_{\mathbf{k}}(t,t')G^{<,\lambda''\lambda'}_{\mathbf{k}}(t',t)\\
&- G^{<,\lambda\lambda''}_{\mathbf{k}}(t,t')\left[\Sigma^{\mathrm{HF}}\delta(t',t) + \Theta(t-t')\left(\Sigma^{<} - \Sigma^{>}\right)\right]^{\lambda''\lambda'}_{\mathbf{k}}(t',t)\\
&+ \Sigma^{<,\lambda\lambda''}_{\mathbf{k}}(t,t')\left[\Theta(t-t')\left(G^{>} - G^{<}\right)\right]^{\lambda''\lambda'}_{\mathbf{k}}(t',t)\\
&- \left[\Theta(t-t')\left(G^{<} - G^{>}\right)\right]^{\lambda\lambda''}_{\mathbf{k}}(t,t')\Sigma^{<,\lambda''\lambda'}_{\mathbf{k}}(t',t)\Big\} , \qquad (4.68)
\end{aligned}$$

where $[\ldots]^{\lambda''\lambda'}_{\mathbf{k}}(t',t)$ shall denote that all functions inside of the brackets carry the same indices. One can reformulate and summarize further using the new quantities [148]:

$$\begin{aligned}
\tilde{\varepsilon}^{\mathrm{HF},\lambda}_{\mathbf{k}}(t) &= \varepsilon^{\lambda,0}_{\mathbf{k}} + \Sigma^{\mathrm{HF},\lambda\lambda}_{\mathbf{k}}(t)\\
\Omega^{\lambda\lambda'}_{\mathbf{k}}(t) &= \mathbf{d}^{\lambda\lambda'}_{\mathbf{k}}\mathbf{E}(t) + \Sigma^{\mathrm{HF},\lambda\lambda'}_{\mathbf{k}}(t)
\end{aligned}$$

Here $\Omega^{\lambda\lambda'}_{\mathbf{k}}(t)$ is the Rabi energy. It causes an oscillation of the occupancies $f^{\lambda}_{\mathbf{k}}$ and $f^{\lambda'}_{\mathbf{k}}$ and the polarization of the transition from band λ to λ', which originates from the light-matter interaction. Both expressions above already indicate the implications of an excitation to the system. The Rabi energy $\mathbf{dE}(t)$ as well as the single-particle energies $\varepsilon_{\mathbf{k}}^{\lambda,0}$ are renormalized due to the many-body interactions of the involved excited particles. These abbreviations are used to finally obtain the most general form of the SBE:

$$\begin{aligned}\left[i\hbar\frac{\partial}{\partial t} - \tilde{\varepsilon}_{\mathbf{k}}^{\mathrm{HF},\lambda}(t) - \tilde{\varepsilon}_{\mathbf{k}}^{\mathrm{HF},\lambda'}(t)\right] G_{\mathbf{k}}^{<,\lambda\lambda'}(t) - \left(G_{\mathbf{k}}^{<,\lambda\lambda}(t) - G_{\mathbf{k}}^{<,\lambda'\lambda'}(t)\right)\Omega_{\mathbf{k}}^{\lambda\lambda'}(t)& \\ + \sum_{\lambda''\neq\lambda,\lambda'} \left\{G_{\mathbf{k}}^{<,\lambda\lambda''}(t)\Omega_{\mathbf{k}}^{\lambda''\lambda'}(t) - \Omega_{\mathbf{k}}^{\lambda\lambda''}(t)G_{\mathbf{k}}^{<,\lambda''\lambda'}(t)\right\}& \\ = \sum_{\lambda''}\int_{-\infty}^{t} \mathrm{d}t' \left\{\Sigma_{\mathbf{k}}^{>,\lambda\lambda''}(t,t')G_{\mathbf{k}}^{<,\lambda''\lambda'}(t',t) - \Sigma_{\mathbf{k}}^{<,\lambda\lambda''}(t,t')G_{\mathbf{k}}^{>,\lambda''\lambda'}(t',t)\right.& \\ \left. + G_{\mathbf{k}}^{<,\lambda\lambda''}(t,t')\Sigma_{\mathbf{k}}^{>,\lambda''\lambda'}(t',t) - G_{\mathbf{k}}^{>,\lambda\lambda''}(t,t')\Sigma_{\mathbf{k}}^{<,\lambda''\lambda'}(t',t)\right\}&\,. \end{aligned} \tag{4.69}$$

Here, further scattering, dephasing and renormalization contributions can be summarized into the scattering or collision integral $S_{\mathbf{k}}^{\lambda\lambda'}(t,t')$ being defined as

$$\begin{aligned} S_{\mathbf{k}}^{\lambda\lambda'}(t,t') = \sum_{\lambda''}\int_{-\infty}^{t} \mathrm{d}t' &\left\{\Sigma_{\mathbf{k}}^{>,\lambda\lambda''}(t,t')G_{\mathbf{k}}^{<,\lambda''\lambda'}(t',t) - \Sigma_{\mathbf{k}}^{<,\lambda\lambda''}(t,t')G_{\mathbf{k}}^{>,\lambda''\lambda'}(t',t)\right. \\ &\left. + G_{\mathbf{k}}^{<,\lambda\lambda''}(t,t')\Sigma_{\mathbf{k}}^{>,\lambda''\lambda'}(t',t) - G_{\mathbf{k}}^{>,\lambda\lambda''}(t,t')\Sigma_{\mathbf{k}}^{<,\lambda''\lambda'}(t',t)\right\}\,. \end{aligned} \tag{4.70}$$

Choosing an appropriate form of the self-energy beyond Hartree-Fock and further evaluating Eq. (4.70) will be part of the next chapter.

In the ground state all charge carriers populate the valence band, while the conduction band is empty due to the band gap of $2 - 3$ eV in TMDs. Illuminating a monolayer with a laser pulse will excite carriers from the valence band states to conduction band states. Thus it is convenient to analyze the propagators for an excitation from band v to c, in other words to calculate the dynamics of $G_{\mathbf{k}}^{\gtrless,cv}$. Though this cv-picture seems intuitive, the electron-hole picture is more convenient for describing pairs of excited carriers or electron-hole plasmas and will be introduced here.

In a first step explicit band indices indicating conduction (c) and valence (v) bands are introduced. Transforming into the eh-picture the occupation of the valence band $f_{\mathbf{k}}^{h}$, just as the occupation of the conduction band $f_{\mathbf{k}}^{e}$, equals zero. As long as no electrons have been excited, no holes will be present. In total one obtains the following relations for a transformation into the electron-hole picture:

$$
\begin{aligned}
\varepsilon_{\mathbf{k}}^{c} &= \varepsilon_{\mathbf{k}}^{e} && (4.71)\\
\varepsilon_{\mathbf{k}}^{v} &= -\varepsilon_{\mathbf{k}}^{h} && (4.72)\\
G_{\mathbf{k}}^{<,cv}(t) &= G_{\mathbf{k}}^{<,eh}(t) && (4.73)\\
G_{\mathbf{k}}^{<,cc}(t) &= G_{\mathbf{k}}^{<,ee}(t) && (4.74)\\
G_{\mathbf{k}}^{<,vv}(t) &= 1 - G_{\mathbf{k}}^{<,hh}(t)\,, && (4.75)
\end{aligned}
$$

where the band gap energy E_G of the semiconducting system is contained in the conduction band values. Only the single-time propagators can be identified by their density matrix element counterparts, reducing the complexity of the notation. It is:

$$
\begin{aligned}
-i\hbar G_{\mathbf{k}}^{\gtrless,eh}(t) &= \psi_{\mathbf{k}}^{he}(t) && (4.76)\\
-i\hbar G_{\mathbf{k}}^{\gtrless,\lambda\lambda}(t) &= f_{\mathbf{k}}^{\lambda}(t)\,. && (4.77)
\end{aligned}
$$

Therefore it is appropriate to separate Eq. (4.70) into two equations for each $\psi_{\mathbf{k}}^{he}(t)$ and $f_{\mathbf{k}}^{\lambda}(t)$. Considering this and using the relations (4.71) to (4.75), the SBE for the microscopic polarizations $\psi_{\mathbf{k}}^{he}(t)$ is cast into the form

$$
\begin{aligned}
&\left[i\hbar\frac{\partial}{\partial t} - \tilde{\varepsilon}_{\mathbf{k}}^{\mathrm{HF},e}(t) - \tilde{\varepsilon}_{\mathbf{k}}^{\mathrm{HF},h}(t) - E_G\right]\psi_{\mathbf{k}}^{he}(t) - \big(1 - f_{\mathbf{k}}^{e}(t) - f_{\mathbf{k}}^{h}(t)\big)\,\Omega_{\mathbf{k}}^{eh}(t)\\
&= \sum_{\lambda}\int_{-\infty}^{t}\mathrm{d}t'\,\Big[\;\Sigma_{\mathbf{k}}^{>,e\lambda}(t,t')G_{\mathbf{k}}^{<,\lambda h}(t',t) - \Sigma_{\mathbf{k}}^{<,e\lambda}(t,t')G_{\mathbf{k}}^{>\lambda'' h}(t',t)\\
&\qquad + G_{\mathbf{k}}^{<,e\lambda}(t,t')\Sigma_{\mathbf{k}}^{>,\lambda h}(t',t) - G_{\mathbf{k}}^{>,e\lambda}(t,t')\Sigma_{\mathbf{k}}^{<,\lambda h}(t',t)\;\Big]\,, \qquad (4.78)
\end{aligned}
$$

where all inter-subband polarizations, for example $\psi_{\mathbf{k}}^{ee'}$, have been neglected. This is due to the fact that the main focus of this work is on excitons and band-toband transitions, which are spectrally located around the band gap. Nevertheless, inter-subband transitions exist but will most likely have a small dipole moment and the transition energies are not in the spectral region of interest.

Using the same assumptions as above, one obtains as equation of motion of the occupation probability $f_{\mathbf{k}}^{\lambda}(t)$:

$$\begin{aligned}
&i\hbar\frac{\partial}{\partial t}f_{\mathbf{k}}^{\lambda}(t) - 2i\sum_{\lambda'\neq\lambda}\mathrm{Im}\left(\psi_{\mathbf{k}}^{\lambda'\lambda}(t)\Omega_{\mathbf{k}}^{\lambda'\lambda}(t)\right) \\
&= i\hbar\sum_{\lambda'}\int\limits_{-\infty}^{t}\mathrm{d}t'\,\Big[\;\Sigma_{\mathbf{k}}^{<,\lambda\lambda'}(t,t')G_{\mathbf{k}}^{>,\lambda'\lambda}(t',t) - \Sigma_{\mathbf{k}}^{>,\lambda\lambda'}(t,t')G_{\mathbf{k}}^{<,\lambda'\lambda}(t',t) \\
&\qquad + G_{\mathbf{k}}^{>,\lambda\lambda'}(t,t')\Sigma_{\mathbf{k}}^{<,\lambda'\lambda}(t',t) - G_{\mathbf{k}}^{<,\lambda\lambda'}(t,t')\Sigma_{\mathbf{k}}^{>,\lambda'\lambda}(t',t)\;\Big]\,.
\end{aligned}\tag{4.79}$$

Both equations (4.78) and (4.79) form a coupled set of equations and provide a microscopic description of excited semiconductors (in general) [129, 131, 147, 151, 152]. Special features of TMD monolayers will be implemented into these equations throughout the remaining chapter.

When aiming for optical properties, one is interested in the frequency dependent absorption that results from the polarization $P(\omega) = \chi(\omega)E(\omega)$, as will be shown later in this thesis. The SBE provide the polarization not only in linear ($P^{(1)}(\omega)$), but also in higher order due to the intrinsic dependencies of ψ and f.

Concluding this section it shall be mentioned that it is numerically disadvantageous to evolve a differential equation with large frequencies, which necessitates a high temporal resolution. To overcome this, high frequencies ω_0 can be cancelled by applying the rotating frame picture. Therefore $\psi(t) = \tilde{\psi}(t)e^{i\omega_0 t}$ is inserted in Eq. (4.78). Carrying out the time derivative, the SBE reproduce for $\tilde{\psi}(t)$ but the transition energies $\varepsilon_{\mathbf{k}}^{0,h} + \varepsilon_{\mathbf{k}}^{0,e} - \hbar\omega_0$ are now shifted by $\hbar\omega_0$. This is used to compensate for the band gap energy.

To move on a straight-forward idea would be to directly calculate the two time functions that are still appearing. This is in general numerically not feasible [146]. To solve this challenge the quasi-equilibrium assumption will be applied in the next sections. Having in mind pump-probe experiments, a strong laser pulse excites carriers that successively relax via carrier-carrier and carrier-phonon interaction. The probe laser is weak and short in time in order to provide a broadband probe. Due to the weakness of the probe beam the $f_{\mathbf{k}}^{\lambda}$ do not change, $\frac{\mathrm{d}}{\mathrm{d}t}f_{\mathbf{k}}^{\lambda}(t) = 0$. This is a valid assumption for a population that is thermalized, for example after a strong excitation (pump) and before recombination of electrons and holes set in. The occupation takes the form of a (quasi) Fermi distribution of a finite charge carrier density:

$$F_{\mathbf{k}}^{\lambda} = \frac{1}{e^{\frac{1}{k_B T}(\varepsilon_{\mathbf{k}}^{\lambda}-\mu)} + 1}\,. \tag{4.80}$$

The distribution depends on the single-particle energies $\varepsilon^{\lambda}_{\mathbf{k}}$, the chemical potential μ^{λ} and on the temperature T, while k_B is the Boltzmann constant.
In a quasi-equilibrium regime the two-time Green's functions only depend on the relative time $\tau = t - t'$ and therefore a Fourier transformation is performed. The SBE are written directly in frequency space. All remaining Green's functions in the scattering terms can be expressed as

$$G^{\gtrless,\lambda\lambda'}_{\mathbf{k}}(t-t') = \int\limits_{-\infty}^{+\infty} \frac{\mathrm{d}\omega}{2\pi} G^{\gtrless,\lambda\lambda'}_{\mathbf{k}}(\omega) e^{-i\omega(t-t')} \tag{4.81}$$

The next section will discuss the choice of the self-energy. In order to gain insight in different mechanisms of the renormalizations present, the self-energy of choice will be the static limit of the GW self-energy, which will result in the so-called screened exchange Coulomb hole (SXCH) approximation.

4.3. Self-Energy Contributions

The explicit form of the self-energy, especially $\Sigma^{\lessgtr}$, will be given in this section. In order to treat correlation effects such as screening, the choice will be the GW approximation, which extends beyond the instantaneous Hartree-Fock approximation. This approximation contains the polarization function in RPA approximation and vertex corrections are neglected as $\frac{\delta\Sigma(\underline{1},\underline{2})}{\delta G(\underline{4},\underline{5})} = 0$ is assumed. For the self-energy the term $\Sigma = GW$ remains from Eq. (4.49) to (4.53), giving rise to the name: GW-approximation. The resulting terms will be further approximated using the properties of a quasi equilibrium state and the static limit of the involved frequency dependence. Finally the result will be the screened exchange Coulomb hole approximation (SXCH).
The Coulomb interaction in general will be treated briefly in the beginning of this chapter, followed by the detailed description of the instantaneous Hartree-Fock part of the self-energy. The different mechanisms renormalizing the single-particle energies will be discussed afterwards.

4.3.1. Coulomb Interaction

The bare Coulomb interaction between two charged particles at $\mathbf{r}$ and $\mathbf{r}'$ is given by

$$V(\mathbf{r}-\mathbf{r}') = \frac{q_1 q_2}{2\varepsilon_0} \frac{1}{|\mathbf{r}-\mathbf{r}'|} \, . \tag{4.82}$$

It is dependent on the inverse distance between the two charges. In momentum space the Coulomb interaction depends on the transferred momentum of the two charges. In two dimensions the bare Coulomb potential is given by

$$U^{2d}_{\mathbf{q}} = \frac{q_1 q_2}{2\varepsilon_0}\frac{1}{|\mathbf{q}|}\,. \tag{4.83}$$

Due to the instantaneous nature of the Coulomb interaction, all terms including $V(1,2)$ are defined as $V(1,2) = V(1,2)\delta(t_1 - t_2)$. The Hamiltonian of the two particle Coulomb interaction can be written in second quantization as:

$$H_{el.-el.} = \frac{1}{2}\sum_{\lambda_1\ldots\lambda_4,\mathbf{k},\mathbf{k}',\mathbf{q}} V^{\lambda_1,\lambda_2,\lambda_3,\lambda_4}_{\mathbf{k},\mathbf{k}'-\mathbf{q},\mathbf{k}',\mathbf{k}-\mathbf{q}} a^{\dagger,\lambda_1}_{\mathbf{k}} a^{\dagger,\lambda_2}_{\mathbf{k}'-\mathbf{q}} a^{\lambda_3}_{\mathbf{k}'} a^{\lambda_4}_{\mathbf{k}-\mathbf{q}}\,. \tag{4.84}$$

It has been directly employed that for a Coulomb scattering process between two states $|\mathbf{k}\rangle$ and $|\mathbf{k}'\rangle$ a finite momentum $\mathbf{q} = \mathbf{k} - \mathbf{k}'$ has to be transferred. The momentum conservation is more generally expressed by $\delta_{\mathbf{k}_1-\mathbf{k}_4,\mathbf{k}_3-\mathbf{k}_2}$.
The matrix elements are obtained in the respective eigenbasis of the ground state description of the TMD monolayer. Hence, the matrix element is

$$\begin{aligned} V^{\lambda_1,\lambda_2,\lambda_3,\lambda_4}_{\mathbf{k},\mathbf{k}'-\mathbf{q},\mathbf{k}',\mathbf{k}-\mathbf{q}} &= \int \mathrm{d}^3\mathbf{r} \int \mathrm{d}^3\mathbf{r}' \psi^{\dagger,\lambda_1}_{\mathbf{k},\sigma}(\mathbf{r}) \psi^{\dagger,\lambda_2}_{\mathbf{k}'-\mathbf{q},\sigma'}(\mathbf{r}') V(\mathbf{r}-\mathbf{r}') \psi^{\lambda_3}_{\mathbf{k}',\sigma'}(\mathbf{r}') \psi^{\lambda_4}_{\mathbf{k}-\mathbf{q},\sigma}(\mathbf{r}) \\ &= \sum_{\alpha,\beta} \left(c^{\lambda_1}_{\alpha,\mathbf{k}}\right)^* \left(c^{\lambda_2}_{\beta,\mathbf{k}'-\mathbf{q}}\right)^* c^{\lambda_3}_{\beta,\mathbf{k}'} c^{\lambda_4}_{\alpha,\mathbf{k}-\mathbf{q}} V^{\alpha\beta\beta\alpha}_{\mathbf{q}} \end{aligned} \tag{4.85}$$

The possible forms of $V^{\alpha\beta\beta\alpha}_{\mathbf{q}}$ depend on the applied level of approximation as well as on the ground state screening of a monolayer within a dielectric environment. This will be presented in sections (4.4.2) to (4.4.4).
The Coulomb interaction does not couple electrons of different spins, therefore the spin index is omitted unless stated otherwise. Assuming large samples the physical limit is applied to all sums over carrier momenta $\mathbf{k}$. Assuming a huge crystal implies that the states are dense in $\mathbf{k}$ so $\mathcal{A}^{-1}\sum_{\mathbf{k}}$ becomes $(2\pi)^{-2}\int \mathrm{d}^2\mathbf{k}$, which is successively discretized for numerical evaluation.

4.3.2. Instantaneous Self-Energy

The instantaneous interaction of excited charge carriers is described by the Hartree-Fock terms. These provide the classical (Hartree) interaction between charges and the exchange interaction that both renormalize the single-particle energies. As these interactions occur instantaneously in time, effects such as screening, dephasing or scattering are not captured by the Hartree-Fock approximation. Starting point for the derivation of the Hartree-Fock terms is the retarded (advanced) self-energy

$$\Sigma^{\mathrm{R/A}}(1,2) \quad = \quad \Sigma^{\delta}(1,2) \pm \theta(t_1-t_2)\left[\Sigma^{>}(1,2)-\Sigma^{<}(1,2)\right] , \tag{4.86}$$

where a singular part $\Sigma^{\delta}(1,2)$ occurs that is instantaneous in time. Writing this expression in terms of Green's functions one obtains in first order perturbation series of the time-evolution operators S [145]:

$$\begin{aligned} \Sigma^{\delta}(1,2) &= \Sigma^{\mathrm{HF}}(1)\delta(t_1-t_2) \\ &= -i\hbar\int \mathrm{d}3\, G(3,3_+)V(1,3) + i\hbar G(1,1)V(1,1) , \end{aligned} \tag{4.87}$$

which corresponds to the Hartree and the Fock (exchange) Coulomb interaction. The eigenfunction expansion of all involved Green's functions is applied. These propagators are requested to be diagonal in their state index $\mathbf{k}=\mathbf{k}'$, while the band indices λ and $\bar\lambda$ shall still originate from electron and hole bands. The choice of the remaining band indices is restrained. Only index combinations where $\lambda\lambda'\lambda''\lambda'''$, $\lambda\bar\lambda\bar\lambda'\lambda'$ or $\lambda\bar\lambda\lambda'\bar\lambda'$ holds are taken into account as all other matrix elements are small. The $\bar\lambda$ indicates indices from the opposite band type as λ, for example $\lambda=h \Rightarrow \bar\lambda=e$. This allows for the separation of Hartree-Fock terms that contribute to either band structure renormalizations or to renormalizations of the Rabi energy.

Considering the band structure renormalizations there are only state-diagonal self-energy matrix elements taken into account, where the band indices are either both electron band or both hole band indices ($\Sigma^{\mathrm{HF},\lambda\lambda'}$).

$$\Sigma^{\mathrm{HF},\lambda\lambda'}_{\mathbf{k}}(t_1,t_2) \quad = \quad -i\hbar\delta(t_1-t_2)\frac{1}{\mathcal{A}}\sum_{\mathbf{k}',\bar\lambda''}\left[G^{<,\bar\lambda''}_{\mathbf{k}'}(t_1)V^{\lambda\bar\lambda''\bar\lambda''\lambda'}_{\mathbf{kk'k'k}} - G^{<,\lambda''}_{\mathbf{k}'}(t_1)V^{\lambda\bar\lambda''\lambda'\bar\lambda''}_{\mathbf{kk'kk'}}\right] \tag{4.88}$$

A Fourier transformation with respect to the relative time $\tau=t_1-t_2$ is performed. Writing the Fourier integral, one obtains

$$\begin{aligned} \Sigma^{\mathrm{HF},\lambda\lambda'}_{\mathbf{k}}(\omega) \quad = \quad -i\hbar\frac{1}{\mathcal{A}}\sum_{\bar\lambda'',\mathbf{k}'}\Bigg[& \int\limits_{-\infty}^{\infty} \mathrm{d}\tau e^{i\omega\tau}\delta(\tau)G^{<,\bar\lambda''}_{\mathbf{k}'}(\tau)V^{\lambda\bar\lambda''\lambda'\bar\lambda''}_{\mathbf{kk'k'k}} \\ & \int\limits_{-\infty}^{\infty} \mathrm{d}\tau e^{i\omega\tau}\delta(\tau)G^{<,\bar\lambda''}_{\mathbf{k}'}(\tau)V^{\lambda\bar\lambda''\bar\lambda''\lambda'}_{\mathbf{kk'kk'}} \Bigg] . \end{aligned} \tag{4.89}$$

Considering the delta-function that demands $\tau = 0$, the evaluation of the integral yields $G^{<,\bar{\lambda}''}_{\mathbf{k}'}(\tau = 0)$, which successively is replaced by its Fourier representation $G^{<,\bar{\lambda}''}_{\mathbf{k}'}(\tau = 0) = \int_{-\infty}^{+\infty} \frac{\mathrm{d}\omega}{2\pi} G^{<,\bar{\lambda}''}_{\mathbf{k}'}(\omega)$. As a quasi-equilibrium situation is assumed, the Kubo-Martin-Schwinger [153] relations (KMS) are applied. They directly connect the Green's functions with the Fermi function $F^{\bar{\lambda}''}(\omega)$ and the spectral function $\hat{A}^{\bar{\lambda}''}_{\mathbf{k}'}(\omega)$.

$$G^{<,e/h}_{\mathbf{k}'}(\omega) = -\,F^{e/h}(\omega)\ \hat{A}^{e/h}_{\mathbf{k}'}(\omega) \tag{4.90}$$

$$G^{>,e/h}_{\mathbf{k}'}(\omega) = (1 - F^{e/h}(\omega))\hat{A}^{e/h}_{\mathbf{k}'}(\omega) \tag{4.91}$$

Evaluating the remaining frequency integral, the KMS occupation functions $f^{\mathrm{KMS},\lambda}_{\mathbf{k}}$ arise and the Hartree-Fock term becomes independent of the frequency. As the electron-hole picture has been used, it has to be taken care that the electrons in the valence band must not be counted twice in the calculation of the Hartree-Fock terms. The interactions and resulting renormalizations of these electrons, already present in the ground state, are accounted for in the band structure calculation. Therefore, the hole population will appear as 'f^{h}' and not '$1 - f^{h}$' in order to assure vanishing renormalizations from excited carriers in the zero density limit.

$$\Sigma^{\mathrm{HF},\lambda\lambda'}_{\mathbf{k}} = -\frac{1}{\mathcal{A}} \sum_{\bar{\lambda}'',\mathbf{k}'} \left[V^{\lambda\bar{\lambda}''\bar{\lambda}''\lambda'}_{\mathbf{k}\mathbf{k}'\mathbf{k}'\mathbf{k}} - V^{\lambda\bar{\lambda}''\lambda'\bar{\lambda}''}_{\mathbf{k}\mathbf{k}'\mathbf{k}\mathbf{k}'} \right] f^{\mathrm{KMS},\bar{\lambda}''}_{\mathbf{k}'} \,. \tag{4.92}$$

Writing the band indices explicitly (omitting the KMS superscript, while the occupations are still to be understood in quasi-equilibrium) one obtains:

$$\begin{aligned} \Sigma^{\mathrm{HF},hh'}_{\mathbf{k}} &= -\frac{1}{\mathcal{A}} \sum_{e',\mathbf{k}'} \left[V^{he'e'h'}_{\mathbf{k}\mathbf{k}'\mathbf{k}'\mathbf{k}} - V^{he'h'e'}_{\mathbf{k}\mathbf{k}'\mathbf{k}\mathbf{k}'} \right] F^{e'}_{\mathbf{k}'} \\ &\quad +\frac{1}{\mathcal{A}} \sum_{h'',\mathbf{k}'} \left[V^{hh''h''h'}_{\mathbf{k}\mathbf{k}'\mathbf{k}'\mathbf{k}} - V^{hh''h'h''}_{\mathbf{k}\mathbf{k}'\mathbf{k}\mathbf{k}'} \right] F^{h''}_{\mathbf{k}'} \end{aligned} \tag{4.93}$$

and

$$\begin{aligned} \Sigma^{\mathrm{HF},ee'}_{\mathbf{k}} &= +\frac{1}{\mathcal{A}} \sum_{e'',\mathbf{k}'} \left[V^{ee''e''e'}_{\mathbf{k}\mathbf{k}'\mathbf{k}'\mathbf{k}} - V^{ee''e'e''}_{\mathbf{k}\mathbf{k}'\mathbf{k}\mathbf{k}'} \right] F^{e''}_{\mathbf{k}'} \\ &\quad -\frac{1}{\mathcal{A}} \sum_{h',\mathbf{k}'} \left[V^{eh'h'e'}_{\mathbf{k}\mathbf{k}'\mathbf{k}'\mathbf{k}} - V^{eh'e'h'}_{\mathbf{k}\mathbf{k}'\mathbf{k}\mathbf{k}'} \right] F^{h'}_{\mathbf{k}'} \,, \end{aligned} \tag{4.94}$$

where it has to be considered that the sign of the expression is depending on the signs of the associated charge carriers. As it is obtained here, for this work there will be only Coulomb matrix elements taken into account, that conserve the number of involved particles, according to the choice of band index combinations made above. It has to be noted, that the exchange terms above do not couple different spins. They have to be read as $V^{\mathrm{F}}\delta_{\sigma,\sigma'}$. This does not hold for the Hartree-type Coulomb matrix elements.

For the interband polarizations the renormalizations of the Rabi energy can be derived in the same way presented above. Considering the restrictions for the band indices one obtains

$$\Sigma^{\mathrm{HF},he}_{\mathbf{k}} = -\frac{1}{\mathcal{A}} \sum_{\mathbf{k}',h',e'} V^{eh'he'}_{\mathbf{k}\mathbf{k}'\mathbf{k}\mathbf{k}'} \psi^{h'e'}_{\mathbf{k}'}(t)\,. \tag{4.95}$$

In contrast to the terms concerning band structure renormalizations an exchange interaction between two states corresponding to transitions he and $h'e'$ occurs. This gives rise to the formation of excitons and is often referred to as 'binding term'. At the same time band-to-band transitions contribute to the Coulomb enhancement of the continuum states.

The Hartree-Fock approximation or the instantaneous part of the retarded self-energy is the best effective single-particle approximation [108]. On the other hand correlations between two particles are completely neglected (only single-particle Green's functions occur within the Hartree-Fock approximation). It follows directly that no collision, scattering or dephasing terms can arise from Hartree-Fock.

For the numerical evaluation the band structure renormalization terms given above are calculated using a self-consistency loop as has been introduced in Sec. (3.2.1). The initial band structure defines an initial carrier distribution. This renormalizes the band structure thereby again changing the distribution. This scheme is repeated until a condition e.g. $N_{\mathbf{k}}^{-1}\sum_{\mathbf{k}}|\varepsilon^{\lambda,i-1}_{\mathbf{k}} - \varepsilon^{\lambda,i}_{\mathbf{k}}| \leq \epsilon$ for a defined tolerance ϵ is reached.

4.3.3. Static GW-Approximation

The GW self-energy [114, 116, 145] accounts for many-particle correlations beyond the Hartree-Fock approximation. It contains the Hartree-Fock terms and is the simplest term from the first order perturbation series of the screened Coulomb interaction W. Dephasing, scattering and screening are described on the level of the *random phase approximation* (RPA), which will be discussed later. The GW scheme is used to evaluate the correlation part Eq. (4.70). In the end, the static limit of the interaction will be applied in order to simplify the GW approximation to the *screened exchange Coulomb hole* approximation (SXCH). In this limit specific properties of semiconducting TMDs arise, that will be revealed in the following section.

Starting point for the derivation of the SXCH approximation, or the static limit of GW, is the GW self-energy

$$\Sigma^{\mathrm{GW}}(\underline{1},\underline{2}) \;=\; i\hbar G(\underline{1},\underline{2})W(\underline{1},\underline{2})\,. \tag{4.96}$$

Using the Langreth Wilkens theorems as mentioned in Sec. (4.2.2) and the eigenbasis expansion, one obtains for the greater and lesser self-energies that enter the correlation terms in Eq. (4.70)

$$\Sigma_{\mathbf{k}}^{\mathrm{GW},\gtrless,\lambda_1\lambda_2}(t,t') \;=\; i\hbar\sum_{\mathbf{k}',\lambda_3,\lambda_4} G_{\mathbf{k}}^{\gtrless,\lambda_3\lambda_4}(t,t')W_{\mathbf{kk'kk'}}^{\lessgtr,\lambda_1\lambda_4\lambda_2\lambda_3}(t',t)$$

Single-time propagators are needed to evaluated the SBE. Using the *generalized Kadanoff-Baym ansatz* (GKBA) the two-time propagators can be approximately cast into a single-time form. For non-interacting systems, the GKBA is exact. It corresponds to the assumption of a weak interaction, for which the dominant contributions of the propagators originate from their time diagonal elements. The maximally retarded form of the GKBA is given by

$$G_{\mathbf{k}}^{\gtrless,\lambda\lambda'}(t,t') \;=\; i\hbar\left(G_{\mathbf{k}}^{\mathrm{R},\lambda\lambda}(t,t')G_{\mathbf{k}}^{\gtrless,\lambda\lambda'}(t') - G_{\mathbf{k}}^{\gtrless,\lambda\lambda'}(t)G_{\mathbf{k}}^{\mathrm{A},\lambda'\lambda'}(t',t)\right)\,. \tag{4.97}$$

These terms occur only within the collision integrals. Therefore the constraint $t \geq t'$ holds, meaning that the time t' will always be earlier than the time t. This originates from the Heaviside function $\theta(t-t')$ that limits the integral boundaries. The GKBA simplifies to

$$\begin{aligned}
G_{\mathbf{k}}^{\gtrless,\lambda\lambda'}(t,t') &= i\hbar G_{\mathbf{k}}^{\mathrm{R},\lambda\lambda}(t,t')G_{\mathbf{k}}^{\gtrless,\lambda\lambda'}(t') \\
G_{\mathbf{k}}^{\gtrless,\lambda\lambda'}(t',t) &= -i\hbar G_{\mathbf{k}}^{\gtrless,\lambda\lambda'}(t')G_{\mathbf{k}}^{\mathrm{A},\lambda'\lambda'}(t',t)\,.
\end{aligned} \tag{4.98}$$

Using the contraint $t \geq t'$ in the collision integral, either G^{R} or G^{A} can be written as their corresponding spectral functions, cf. Eq. (4.40). After using the GKBA, the GW self-energy becomes

$$\begin{aligned}
\Sigma_{\mathbf{k}}^{\mathrm{GW},\gtrless,\lambda_1\lambda_2}(t,t') &= -\hbar^2\sum_{\mathbf{k}',\lambda_3,\lambda_4} G_{\mathbf{k}'}^{\mathrm{R},\lambda_3}(t,t')G_{\mathbf{k}'}^{\gtrless,\lambda_3\lambda_4}(t')W_{\mathbf{kk'kk'}}^{\gtrless,\lambda_1\lambda_4\lambda_2\lambda_3}(t',t) \\
\Sigma_{\mathbf{k}}^{\mathrm{GW},\gtrless,\lambda_1\lambda_2}(t',t) &= +\hbar^2\sum_{\mathbf{k}',\lambda_3,\lambda_4} G_{\mathbf{k}'}^{\gtrless,\lambda_3\lambda_4}(t')G_{\mathbf{k}'}^{\mathrm{A},\lambda_4}(t',t)W_{\mathbf{kk'kk'}}^{\gtrless,\lambda_1\lambda_4\lambda_2\lambda_3}(t,t')\,.
\end{aligned} \tag{4.99}$$

Moreover the GKBA is applied to the two-time propagators that appear within the collision integral. More single-time propagators and retarded/advanced Green's functions therefore arise. Sorting them according to their time argument, the collision integral becomes

$$\begin{aligned}(-i\hbar)^3\frac{1}{\mathcal{A}}\sum_{\lambda,\mathbf{k}',\lambda_3,\lambda_4}\int\limits_{-\infty}^{t}\mathrm{d}t'\Big[\;& G_{\mathbf{k}'}^{>,\lambda_3\lambda_4}(t')G_{\mathbf{k}}^{<,\lambda h}(t')W_{\mathbf{k}\mathbf{k}'\mathbf{k}\mathbf{k}'}^{<,e\lambda_4\lambda\lambda_3}(t',t)G_{\mathbf{k}'}^{\mathrm{R},\lambda_3}(t,t')G_{\mathbf{k}}^{\mathrm{A},h}(t',t)\\ &-G_{\mathbf{k}'}^{<,\lambda_3\lambda_4}(t')G_{\mathbf{k}}^{>,\lambda h}(t')W_{\mathbf{k}\mathbf{k}'\mathbf{k}\mathbf{k}'}^{>,e\lambda_4\lambda\lambda_3}(t',t)G_{\mathbf{k}'}^{\mathrm{R},\lambda_3}(t,t')G_{\mathbf{k}}^{\mathrm{A},h}(t',t)\\ &+G_{\mathbf{k}}^{<,e\lambda}(t')G_{\mathbf{k}'}^{>,\lambda_3\lambda_4}(t')W_{\mathbf{k}\mathbf{k}'\mathbf{k}\mathbf{k}'}^{<,\lambda\lambda_4h\lambda_3}(t,t')G_{\mathbf{k}}^{\mathrm{R},e}(t,t')G_{\mathbf{k}'}^{\mathrm{A},\lambda_4}(t',t)\\ &-G_{\mathbf{k}}^{>,e\lambda}(t')G_{\mathbf{k}'}^{<,\lambda_3\lambda_4}(t')W_{\mathbf{k}\mathbf{k}'\mathbf{k}\mathbf{k}'}^{>,\lambda\lambda_4h\lambda_3}(t,t')G_{\mathbf{k}}^{\mathrm{R},e}(t,t')G_{\mathbf{k}'}^{\mathrm{A},\lambda_4}(t',t)\;\Big]\,.\end{aligned} \tag{4.100}$$

Appendix (B) provides a detailed description of the steps necessary to derive Eq. (4.103) below. Applying the quasi-equilibrium state, all remaining two-time quantities depend on $\tau = t - t'$. It has to be considered that in this limit the occupations f will be static in time and correspond to (quasi) Fermi distributions F. A Fourier transformation is performed. Afterwards the quasi-particle approximation is used, which states that the retarded Green's function is expressed via the retarded self-energy

$$G_{\mathbf{k}}^{\mathrm{R},\lambda}(\omega) \;=\; \frac{1}{\hbar\omega - \varepsilon_{\mathbf{k}}^{0,\lambda} - \Sigma_{\mathbf{k}}^{\mathrm{R},\lambda}}\,. \tag{4.101}$$

Due to the limits of the time integral the retarded Green's functions can be expressed as spectral functions

$$\hat{A}_{\mathbf{k}}^{\lambda}(\omega) \;=\; \frac{\mathrm{Im}\Sigma_{\mathbf{k}}^{\mathrm{R},\lambda}}{\left(\hbar\omega - \varepsilon_{\mathbf{k}}^{0,\lambda} - \mathrm{Re}\Sigma_{\mathbf{k}}^{\mathrm{R},\lambda}\right)^2 - \left(\mathrm{Im}\Sigma_{\mathbf{k}}^{\mathrm{R},\lambda}\right)^2}\,. \tag{4.102}$$

In the quasi-particle approximation the real part of the retarded self-energy renormalizes the single-particle energies, while the imaginary part provides dephasing. This dephasing is chosen to be a phenomenological constant $\mathrm{Im}\Sigma_{\mathbf{k}}^{\mathrm{R},\lambda} = \gamma$ to account for carrier-phonon and carrier-carrier interaction.

The band indices $\lambda, \lambda_3, \lambda_4$ will be put into the same form as performed for the Hartree-Fock matrix elements in Sec. (4.3.2). Only Coulomb matrix elements with the index combination $\lambda\lambda'\lambda''\lambda'''$, $\lambda\bar{\lambda}\bar{\lambda}'\lambda'$ or $\lambda\bar{\lambda}\lambda'\bar{\lambda}'$ will be considered. Furthermore the KMS relations for the plasmon propagator W (see (B.4) - (B.7)) are exploited. In the end the correlation contributions can be summarized as effective energy renormalization $\Delta^{\lambda}_{\mathbf{k}}(\omega)$ and as an effective Coulomb interaction $V^{\mathrm{eff},\lambda\lambda'}_{\mathbf{kk'}}(\omega)$. Therefore the full frequency-dependent correlation integral in quasi-particle approximation for a quasi-equilibrium state becomes

$$S^{he}_{\mathbf{k}}(\omega) \;=\; \sum_{e'} \Delta^{e'}_{\mathbf{k}}(\omega)\psi^{he'}_{\mathbf{k}}(\omega) + \sum_{h'} \Delta^{h'}_{\mathbf{k}}(\omega)\psi^{h'e}_{\mathbf{k}}(\omega) + \sum_{h',e',\mathbf{k}'} V^{\mathrm{eff},eh'he'}_{\mathbf{kk'kk'}}(\omega)\psi^{h'e'}_{\mathbf{k}'}(\omega)\,. \tag{4.103}$$

Here, one identifies

$$\begin{aligned}
\Delta^{e'}_{\mathbf{k}}(\omega) \;=\;& i\hbar\frac{1}{\mathcal{A}}\sum_{e'',\mathbf{k}'}\int_{-\infty}^{+\infty}\frac{\mathrm{d}\omega'}{2\pi}\frac{(1-F^{e''}_{\mathbf{k}'}+n_B(\omega'))V^{e'e''ee''}_{\mathbf{kk'kk'}}2i\mathrm{Im}\varepsilon^{\mathrm{R},-1}_{\mathbf{k}-\mathbf{k}'}(\omega')}{\hbar\omega-\hbar\omega'-\varepsilon^{e'}_{\mathbf{k}'}-\varepsilon^{h}_{\mathbf{k}}+2i\gamma} \\
&-i\hbar\frac{1}{\mathcal{A}}\sum_{h',\mathbf{k}'}\int_{-\infty}^{+\infty}\frac{\mathrm{d}\omega'}{2\pi}\frac{(1-F^{h'}_{\mathbf{k}'}+n_B(\omega'))V^{eh'e'h'}_{\mathbf{kk'kk'}}2i\mathrm{Im}\varepsilon^{\mathrm{R},-1}_{\mathbf{k}-\mathbf{k}'}(\omega')}{\hbar\omega-\hbar\omega'-\varepsilon^{h'}_{\mathbf{k}'}-\varepsilon^{h}_{\mathbf{k}}+2i\gamma}\,,
\end{aligned} \tag{4.104}$$

$$\begin{aligned}
\Delta^{h'}_{\mathbf{k}}(\omega) \;=\;& i\hbar\frac{1}{\mathcal{A}}\sum_{h'',\mathbf{k}'}\int_{-\infty}^{+\infty}\frac{\mathrm{d}\omega'}{2\pi}\frac{(1-F^{h''}_{\mathbf{k}'}+n_B(\omega'))V^{h'h''hh''}_{\mathbf{kk'kk'}}2i\mathrm{Im}\varepsilon^{\mathrm{R},-1}_{\mathbf{k}-\mathbf{k}'}(\omega')}{\hbar\omega-\hbar\omega'-\varepsilon^{e}_{\mathbf{k}}-\varepsilon^{h'}_{\mathbf{k}'}+2i\gamma} \\
&-i\hbar\frac{1}{\mathcal{A}}\sum_{e',\mathbf{k}'}\int_{-\infty}^{+\infty}\frac{\mathrm{d}\omega'}{2\pi}\frac{(1-F^{e'}_{\mathbf{k}'}+n_B(\omega'))V^{h'e'he'}_{\mathbf{kk'kk'}}2i\mathrm{Im}\varepsilon^{\mathrm{R},-1}_{\mathbf{k}-\mathbf{k}'}(\omega')}{\hbar\omega-\hbar\omega'-\varepsilon^{e'}_{\mathbf{k}'}-\varepsilon^{e}_{\mathbf{k}}+2i\gamma}
\end{aligned} \tag{4.105}$$

and

$$\begin{aligned}
V^{\mathrm{eff},eh'he'}_{\mathbf{kk'kk'}}(\omega) \;=\;& i\hbar\int_{-\infty}^{+\infty}\frac{\mathrm{d}\omega'}{2\pi}\frac{(1-F^{e}_{\mathbf{k}}+n_B(\omega'))V^{eh'he'}_{\mathbf{kk'kk'}}2i\mathrm{Im}\varepsilon^{\mathrm{R},-1}_{\mathbf{k}-\mathbf{k}'}(\omega')}{\hbar\omega-\hbar\omega'-\varepsilon^{e}_{\mathbf{k}}-\varepsilon^{h'}_{\mathbf{k}'}+2i\gamma} \\
&+i\hbar\int_{-\infty}^{+\infty}\frac{\mathrm{d}\omega'}{2\pi}\frac{(1-F^{h}_{\mathbf{k}}+n_B(\omega'))V^{eh'he'}_{\mathbf{kk'kk'}}2i\mathrm{Im}\varepsilon^{\mathrm{R},-1}_{\mathbf{k}-\mathbf{k}'}(\omega')}{\hbar\omega-\hbar\omega'-\varepsilon^{e'}_{\mathbf{k}'}-\varepsilon^{h}_{\mathbf{k}}+2i\gamma}\,.
\end{aligned} \tag{4.106}$$

$V^{\text{eff},eh'he'}_{\mathbf{kk'kk'}}(\omega)$ acts as an effective Coulomb interaction that directly influences the binding term of the SBE. The SBE in the approximations presented above are given by

$$\begin{aligned} &\Big(\hbar\omega - \varepsilon^{\text{HF},h}_{\mathbf{k}} - \varepsilon^{\text{HF},e}_{\mathbf{k}} - \Delta^{e}_{\mathbf{k}}(\omega) - \Delta^{h}_{\mathbf{k}}(\omega) + i\gamma\Big)\,\psi^{he}_{\mathbf{k}}(\omega) \\ &\qquad - \sum_{e'\neq e} \Delta^{e'}_{\mathbf{k}}(\omega)\psi^{he'}_{\mathbf{k}}(\omega) - \sum_{h'\neq h} \Delta^{h'}_{\mathbf{k}}(\omega)\psi^{h'e}_{\mathbf{k}}(\omega) \\ &+ \left(1 - F^{e}_{\mathbf{k}} - F^{h}_{\mathbf{k}}\right)\left(\mathbf{d}^{eh}_{\mathbf{k}}\cdot\mathbf{E}(\omega) + \frac{1}{\mathcal{A}}\sum_{h',e',\mathbf{k}'} V^{eh'he'}_{\mathbf{kk'kk'}}\psi^{h'e'}_{\mathbf{k}'}(\omega)\right) \\ &\qquad - \sum_{h',e',\mathbf{k}'} V^{\text{eff},eh'he'}_{\mathbf{kk'kk'}}(\omega)\psi^{h'e'}_{\mathbf{k}'}(\omega) \;=\; 0\,. \end{aligned} \tag{4.107}$$

Calculating the SBE with the full frequency dependence is computationally very demanding as the integrals presented above have to be solved for each ω [154]. Additionally a static approximation is performed. The validity of the static approximation will be confirmed when comparing both theories in Chap. (6).

The basic assumption of the static approximation is that any excitation energy involving pairs of free quasi-particles, $\hbar\omega - \varepsilon^{\lambda}_{\mathbf{k}} - \varepsilon^{\lambda'}_{\mathbf{k}'}$, is small compared to characteristic energies $\hbar\omega'$ occurring in the dielectric function [137, 155]. Each denominator within the correlation integrals reduces to $\hbar\omega'$ and only the $\omega = 0$ contribution of the screened Coulomb interaction remains.

The Kramers-Kronig relations are exploited in order to further evaluate the remaining integrals stating that:

$$\mathcal{P}\int_{-\infty}^{\infty} \frac{d\omega'}{2\pi i}\frac{\text{Im}\,\varepsilon^{-1}_{\mathbf{q}}(\omega')}{\omega'-\omega} = \text{Re}\,\varepsilon^{-1}_{\mathbf{q}}(\omega) - 1\,. \tag{4.108}$$

Moreover it is

$$\int_{-\infty}^{\infty} \frac{d\omega'}{2\pi}\frac{\text{Im}\,\varepsilon^{-1}_{\mathbf{q}}(\omega')(n_{\text{B}}(\omega')+\frac{1}{2})}{\hbar\omega'} = 0\,, \tag{4.109}$$

which stems from the bosonic occupation $n_B(\omega)+\frac{1}{2}$ as well as $\text{Im}\,\varepsilon^{-1}_{\mathbf{q}}(\omega)$ being an odd functions in ω. Using both relations (4.108) and (4.109) together, one is left with the following expressions:

$$\begin{aligned}\Delta^{\lambda'}_{\mathbf{k}} &= \frac{1}{\mathcal{A}}\sum_{\lambda'',\mathbf{k}'}\left(\frac{1}{2}-F^{\lambda''}_{\mathbf{k}'}\right)\left[W^{\lambda'\lambda''\lambda\lambda''}_{\mathbf{kk'kk'}}(\omega=0)-V^{\lambda'\lambda''\lambda\lambda''}_{\mathbf{kk'kk'}}\right]\\ &\quad -\frac{1}{\mathcal{A}}\sum_{\bar{\lambda}',\mathbf{k}'}\left(\frac{1}{2}-F^{\bar{\lambda}'}_{\mathbf{k}'}\right)\left[W^{\lambda\bar{\lambda}'\lambda'\bar{\lambda}'}_{\mathbf{kk'kk'}}(\omega=0)-V^{\lambda\bar{\lambda}'\lambda'\bar{\lambda}'}_{\mathbf{kk'kk'}}\right]\end{aligned} \tag{4.110}$$

and

$$V^{\text{eff},eh'he'}_{\mathbf{kk'kk'}} = \left(1-F^e_{\mathbf{k}}-F^h_{\mathbf{k}}\right)\left[W^{eh'he'}_{\mathbf{kk'kk'}}(\omega=0)-V^{eh'he'}_{\mathbf{kk'kk'}}\right]. \tag{4.111}$$

Again $\bar{\lambda}$ denotes the opposite band type of λ. The screened Coulomb interaction is defined as $W^{\lambda\lambda\lambda\lambda}_{\mathbf{kk'kk'}}(\omega=0)=V^{\lambda\lambda\lambda\lambda}_{\mathbf{kk'kk'}}\varepsilon^{-1}_{\text{exc},\mathbf{k}-\mathbf{k}'}(\omega=0)$. If no carriers are present, it follows from $\varepsilon^{-1}_{\text{exc},\mathbf{k}-\mathbf{k}'}=1$ (see Sec. (4.4.1) that the renormalizations vanish to zero. Both terms Δ and V^{eff} have become frequency-independent and real. Due to their present form containing the difference of screened and unscreened Coulomb interaction multiplied by $(1/2-F)$ and the binding term replaced by a screened interaction these expressions are referred to as *screened exchange Coulomb hole* (SXCH) terms. The terms are iterated self-consistently until convergence is reached.

4.3.4. Characteristics of SXCH in TMDs

When exploring optical spectra of TMD monolayer characteristic properties of the SXCH approximation can be exploited in order to obtain additional analytical insight. This derivation is part of the thesis and has been published in Ref. [156]. Two facts support further recast of the expressions (4.110) and (4.111). The energy $\hbar\omega$ occurring in the integral denominators of (4.105) and (4.106) will be on the order of the band gap energy, which is about $2-3$ eV for TMDs, for the evaluation of optical spectra. Thus it will be approximately $\hbar\omega\sim\varepsilon^e+\varepsilon^h$. The characteristics of the band structure presented throughout Chap. (3) providse unique carrier distributions in addition to the valley structure of the bands. Both arguments will select a distinctive form of the Coulomb interaction depending on the band index combination given.

The evaluation of the Δ-terms at frequencies $\hbar\omega\sim\varepsilon^e+\varepsilon^h$ will cause the denominator of inter-band terms to be for example

$$\varepsilon^e_{\mathbf{k}}+\varepsilon^h_{\mathbf{k}}-\hbar\omega'-\varepsilon^{e'}_{\mathbf{k}'}-\varepsilon^e_{\mathbf{k}}-2i\gamma\Rightarrow\hbar\omega'\sim\varepsilon^h_{\mathbf{k}}-\varepsilon^{e'}_{\mathbf{k}'}-2i\gamma \tag{4.112}$$

Thus the integral contributes only for large energies. The imaginary part of the inverse dielectric function goes to zero for large $\hbar\omega$ while the real part approaches one for excited carriers. This leads finally to vanishing correlation contributions for the inter-band $(\lambda\bar{\lambda})$ and intra-subband $(\lambda \neq \lambda' \dots)$ terms. The only exception are the intra-band terms, where $\lambda = \lambda' = \lambda'' = \lambda'''$ holds. Here the dielectric function will have non-vanishing contributions. This leads to the conclusion that for the band structure renormalization the SXCH approximation will only affect band index-diagonal terms.

Characteristic features of TMD band structures affect the remaining exchange terms $\Sigma^{\mathrm{F}}_{\mathbf{k}}$. While all self-energy terms diagonal in λ are replaced by the SXCH-expression as written above, the off-diagonal parts split into two groups: the inter-band exchange $\Sigma^{\mathrm{U},\lambda\bar{\lambda}}_{\mathbf{k}}$ and the intra-subband exchange $\Sigma^{\mathrm{V},\lambda\lambda'}_{\mathbf{k}}$. The intra-subband terms remain as presented in the paragraph above. The Coulomb matrix elements V, which contain only dielectric screening, determine these renormalizations.

The inter-band exchange is affected differently. In order to gain understanding of this fact the total inter-band term is split into a bare exchange term U and a correlation term. The correlation term is chosen to contain screening from background contributions and from excited carriers [116] in contrast to the part before, where only the screening from excited carriers was included in W. This results in an expression similar to Eq. (4.105)

$$\tilde{\Sigma}^{\mathrm{U},\lambda\bar{\lambda}}_{\mathbf{k}}(\omega) = \frac{1}{\mathcal{A}} \sum_{\mathbf{k}'} F^{\bar{\lambda}}_{\mathbf{k}'} \left[U^{\lambda\bar{\lambda}\lambda\bar{\lambda}}_{\mathbf{k}\mathbf{k}'\mathbf{k}\mathbf{k}'} + i\hbar \int_{-\infty}^{\infty} \frac{\mathrm{d}\omega'}{2\pi} \frac{2i\,\mathrm{Im}\, W^{\lambda\bar{\lambda}\lambda\bar{\lambda}}_{\mathbf{k}\mathbf{k}'\mathbf{k}\mathbf{k}'}(\omega')}{\hbar\omega - \hbar\omega' + \varepsilon^{\bar{\lambda}}_{\mathbf{k}} + \varepsilon^{\bar{\lambda}}_{\mathbf{k}'} + 2i\gamma} \right] . \tag{4.113}$$

In this case the correlation term is sensitive to the screened Coulomb matrix element at energies larger than the band gap, which prohibits the application of the static limit. While it is the task of this section to provide a complete theory for interacting charge carriers in optically excited TMD monolayers, it is imperative to quantify the strength of the inter-band correlations.

The denominator in expression (4.113) provides energies at which the inverse dielectric function of excited carriers will cause the integral to vanish (cf. the beginning of this section). Only background screening will contribute to W. Using the background dielectric matrix in the RPA approximation (see Sec. (4.4.4)) and band structures from Sec. (3.2.2) together with a phenomenological quasi-particle broadening of 10 meV provides the requested input to calculate Eq. (4.113). The resulting renormalization with and without correlations is shown in Fig. (4.1). The calculation containing frequency-dependent background screening has been performed by Alexander Steinhoff while the bare renormalizations have been calculated by the author of this thesis.

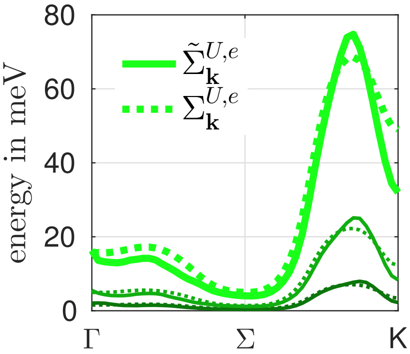

Figure 4.1.: Single-particle energy shifts of the conduction band due to the hole population for freestanding $\mathrm{MoS_2}$ along the $\mathbf{\Gamma}$-$\mathbf{K}$ direction at $T = 300$ K with (solid lines) and without (dashed lines) correlation contributions according to Eq. (4.113). The results are shown for increasing charge carrier densites $(3 \times 10^{12}, 1 \times 10^{13}, 3 \times 10^{13}\ \mathrm{cm}^{-2})$.

While at the $\mathbf{K}$ point the correlations yield a correction of about 30% the overall behaviour of the inter-band renormalizations is already described well by the bare electron-hole exchange term. Thereby it is validated that the inter-band renormalizations can be approximated well by the bare exchange for TMDs:

$$\Sigma^{\mathrm{U},\lambda\bar{\lambda}}_{\mathbf{k}} = \frac{1}{\mathcal{A}} \sum_{\mathbf{k}'} U^{\lambda\bar{\lambda}\lambda\bar{\lambda}}_{\mathbf{k}\mathbf{k}'\mathbf{k}\mathbf{k}'} F^{\bar{\lambda}}_{\mathbf{k}'} \tag{4.114}$$

Besides the inter-band exchange also the justification for the static limit of the binding term has to be provided. The static limit is not valid if the condition $\hbar\omega - \varepsilon^{\lambda}_{\mathbf{k}} - \varepsilon^{\lambda'}_{\mathbf{k}'} \ll \hbar\omega'$ is not true. This is relevant for matrix elements that couple different transitions such as $W^{e_1h_1e_2h_1}_{\mathbf{k}\mathbf{k}'\mathbf{k}\mathbf{k}'}$. This is important for the chosen three-band model from DFT+GW calculations as presented in Sec.(3.2.2) when taking into account the higher conduction band. The named Coulomb matrix elements enhance the C exciton which originates from states between $\mathbf{\Gamma}$ and $\mathbf{M}$ (see Chap. (3)). In this area of the BZ the two lowest conduction bands mostly run parallel without band extrema wherefore no carriers will occupy these states. Both bands are close enough in energy to justify the static approximation.

In the vicinity of the $\mathbf{K}$ point it is possible for carriers to occupy states in the lowest conduction band, but the energy difference to the second conduction band is large, which thereby diminishes the correlation term. Populating the upper conduction band is not probable by typical excitation energies and relaxation times. In conclusion, applying the static limit to the binding term is valid for any band index combination, because either no population is present that will cause energy shifts or the energy difference prohibits contributions from the correlation term.

Summarizing all the above, the full SBE in SXCH approximation are given in the frequency domain by

$$\begin{aligned} &\left(\hbar\omega - \tilde{\varepsilon}^h_{\mathbf{k}} - \tilde{\varepsilon}^e_{\mathbf{k}} + i\gamma\right)\psi^{he}_{\mathbf{k}}(\omega) \\ + \left(1 - F^e_{\mathbf{k}} - F^h_{\mathbf{k}}\right) &\left(\mathbf{d}^{eh}_{\mathbf{k}} \cdot \mathbf{E}(\omega) + \frac{1}{\mathcal{A}} \sum_{h',e',\mathbf{k}'} W^{eh'he'}_{\mathbf{kk}'\mathbf{kk}'} \psi^{h'e'}_{\mathbf{k}'}(\omega)\right) \;=\; 0\,. \end{aligned} \tag{4.115}$$

The effective Coulomb potential arising in the static limit replaces the binding term by a screened binding term, representing the weaker binding of electrons and holes due to the screening from excited charge carriers. The renormalized single-particle energies are summarized in $\tilde{\varepsilon}^\lambda_{\mathbf{k}}$. They are given by

$$\begin{aligned} \tilde{\varepsilon}^\lambda_{\mathbf{k}} &= \varepsilon^{0,\lambda}_{\mathbf{k}} + \Sigma^{\mathrm{H},\lambda}_{\mathbf{k}} + \Sigma^{\mathrm{U},\lambda}_{\mathbf{k}} + \Sigma^{\mathrm{V},\lambda}_{\mathbf{k}} + \Sigma^{\mathrm{SX},\lambda}_{\mathbf{k}} + \Sigma^{\mathrm{CH},\lambda}_{\mathbf{k}} \\ &= \varepsilon^{0,\lambda}_{\mathbf{k}} + \Sigma^{\mathrm{H},\lambda}_{\mathbf{k}} + \underbrace{\frac{1}{\mathcal{A}} \sum_{\mathbf{k}',\bar{\lambda}} U^{\lambda\bar{\lambda}\lambda\bar{\lambda}}_{\mathbf{kk}'\mathbf{kk}'} F^{\bar{\lambda}}_{\mathbf{k}'}}_{\text{inter-band X}} + \underbrace{\frac{1}{\mathcal{A}} \sum_{\mathbf{k}',\lambda'\neq\lambda} V^{\lambda\lambda'\lambda\lambda'}_{\mathbf{kk}'\mathbf{kk}'} F^{\lambda'}_{\mathbf{k}'}}_{\text{intra-subband X}} \\ &\quad \underbrace{-\frac{1}{\mathcal{A}} \sum_{\mathbf{k}'} W^{\lambda\lambda\lambda\lambda}_{\mathbf{kk}'\mathbf{kk}'} F^{\lambda}_{\mathbf{k}'}}_{\text{SX}} + \underbrace{\frac{1}{2\mathcal{A}} \sum_{\mathbf{k}'} \left[W^{\lambda\lambda\lambda\lambda}_{\mathbf{kk}'\mathbf{kk}'} - V^{\lambda\lambda\lambda\lambda}_{\mathbf{kk}'\mathbf{kk}'}\right]}_{\text{CH}}\,. \end{aligned} \tag{4.116}$$

The energies contain the screened-exchange interaction (SX) term and the Coulomb-hole term (CH). The SX term represents the exchange interaction that is screened due to the presence of excited carriers, while the CH term is the difference of the screened and unscreened Coulomb potential. The CH term describes the reduction of the single-particle energies due to the fact that the electrons avoid each other because of their mutual Coulomb repulsion. The remaining part of the exchange interaction splits into the bare inter-band exchange and the intra-subband exchange, which experiences screening from the environment.

The term $\left(1 - F^e_{\mathbf{k}}(t) - F^h_{\mathbf{k}}(t)\right)$ provides the implications of the phase space filling due to the Pauli exclusion principle and is therefore called Pauli blocking factor. It efficiently reduces the binding term and shifts the optical transition according to the presence of electrons and holes. Thus the oscillator strength of optical transitions is reduced with increasing carrier density (bleaching). Optical gain may occur, if the Pauli blocking factor changes it's sign causing the absorption to be negative as well.

4.4. Screening

Applying the RPA [157] on the vertex equation (4.53), the term reduces to the δ-functions and all vertex corrections are neglected.

$$\Gamma^{\mathrm{RPA}}(\underline{1},\underline{2},\underline{3}) \quad = \quad -i\hbar\delta(\underline{1},\underline{2})\delta(\underline{1},\underline{3}) \tag{4.117}$$

Hence, for the polarization equation (4.52) in RPA remains:

$$P^{\mathrm{RPA}}(\underline{1},\underline{2}) \quad = \quad i\hbar G(\underline{1},\underline{2})G(\underline{2},\underline{1})\,. \tag{4.118}$$

As before standard methods of Green's function calculus are applied to obtain the retarded polarization function. The polarization function enters the Dyson equation of the screened Coulomb interaction (4.50), acting as a self-energy for the screened Coulomb potential. In the quasi-particle picture the GW-polarization can be understood as a polarization cloud. Due to the repulsive nature of the Coulomb potential, carriers of the same charge are repelled, giving rise to the formation of a polarization cloud, that has effectively the opposite charge. The presence of an electron-hole plasma therefore screens the bare Coulomb interaction. The screened interaction is considerably weaker than the bare Coulomb interaction. For excited semiconductors two contributions to the screening arise that are described separately. The dielectric background and the excited carriers contribute as $P = P_{\mathrm{b}} + P_{\mathrm{exc}}$. The first term contains all polarizations present in the unexcited semiconductor, while the second term arises from optically excited electrons and holes or from doping charge carriers into the system. The screening is described by two longitudinal dielectric functions ε_{b} and $\varepsilon_{\mathrm{exc}}$, respectively. By iterating Eq. (4.50), the bare Coulomb interaction is turned into a screened interaction. The Coulomb matrix elements $\tilde{V}^{\alpha\beta\beta\alpha}$ are expressed in the localized Wannier function eigenbasis $|\alpha\rangle$ as obtained from the Wannier construction (3.2.2). Thus the transition metal d-orbital character is dominant.

$$\tilde{V}^{\lambda_1\lambda_2\lambda_3\lambda_4}_{\mathbf{k}_1\mathbf{k}_2\mathbf{k}_3\mathbf{k}_4} = \sum_{\alpha,\beta} \left(c^{\lambda_1}_{\alpha,\mathbf{k}_1}\right)^* \left(c^{\lambda_2}_{\beta,\mathbf{k}_2}\right)^* c^{\lambda_3}_{\beta,\mathbf{k}_3} c^{\lambda_4}_{\alpha,\mathbf{k}_4} \tilde{V}^{\alpha\beta\beta\alpha}_{|\mathbf{k}_1-\mathbf{k}_4|}\,, \tag{4.119}$$

Here, the element $\tilde{V}$ takes the role of a dummy interaction, being either U or V for the bare or background screened Coulomb interaction. In general the term $\tilde{V}^{\alpha\beta}_{\mathbf{q}} = \tilde{V}^{\alpha\beta\beta\alpha}_{\mathbf{q}}$ carries a dependence on the orbitals of the chosen basis. From the Dyson equation of the screened Coulomb interaction a matrix equation arises [157, 158] for this Coulomb matrix element within the eigenbasis.

$$\begin{aligned}\tilde{V}_{\mathbf{q}}^{\alpha\beta}(\omega) &= \left(\tilde{U}_{\mathbf{q}}^{-1} - P_{\mathbf{q}}^{\mathrm{R}}(\omega)\right)^{-1,\alpha\beta} \\ &= \sum_{\gamma} \left(\mathbf{1} - \tilde{U}_{\mathbf{q}} P_{\mathbf{q}}^{\mathrm{R}}(\omega)\right)^{-1,\alpha\gamma} \tilde{U}_{\mathbf{q}}^{\gamma\beta} \\ &= \sum_{\gamma} \varepsilon_{\mathbf{q}}^{\mathrm{R},-1,\alpha\gamma} \tilde{U}_{\mathbf{q}}^{\gamma\beta}(\omega) \qquad (4.120)\end{aligned}$$

4.4.1. Plasma Screening

The first subsection is subjected to the plasma screening originating from excited carriers, which stems from the polarization $P^{\mathrm{R}}_{\mathrm{exc},\mathbf{q}}(\omega)$. The equation for the plasma screened Coulomb interaction reads:

$$W_{\mathbf{q}}^{\alpha\beta}(\omega) = \sum_{\gamma} \varepsilon_{\mathrm{exc},\mathbf{q}}^{\mathrm{R},-1,\alpha\gamma} V_{\mathbf{q}}^{\gamma\beta}(\omega) \qquad (4.121)$$

Here the matrix elements of the Coulomb interaction screened by the dielectric background enter the equations. From Eq. (4.121) one can directly identify the definition of the retarded longitudinal dielectric function:

$$\varepsilon_{\mathrm{exc},\mathbf{q}}^{\mathrm{R},\alpha\beta}(\omega) = \delta_{\alpha\beta} - \sum_{\gamma} V_{\mathbf{q}}^{\alpha\gamma}(\omega) P_{\mathrm{exc},\mathbf{q}}^{\mathrm{R},\gamma\beta}(\omega) \,. \qquad (4.122)$$

In order to simplify numerical calculations, the goal of this derivation is a macroscopic dielectric function $\varepsilon_{\mathbf{q}}^{\mathrm{R},-1}(\omega)$. Therefore a static ($\omega = 0$) Coulomb potential $\tilde{V}_{\mathbf{q}}$ is chosen and the dependence on α, β is averaged over all elements. Thereby local-field effects in the dielectric function are neglected, which is justified for a plasma of excited electrons and holes that behave like quasi-free carriers [159]. For the retarded polarization function the Lindhard formula is obtained:

$$P_{\mathbf{q}}^{\mathrm{R},\alpha\beta}(\omega) = \frac{1}{\mathcal{A}} \sum_{\lambda,\lambda',\mathbf{k}} \left(c_{\alpha,\mathbf{k}}^{\lambda}\right)^{*} \left(c_{\beta,\mathbf{k}-\mathbf{q}}^{\lambda'}\right)^{*} c_{\beta,\mathbf{k}}^{\lambda} c_{\alpha,\mathbf{k}-\mathbf{q}}^{\lambda'} \frac{f_{\mathbf{k}-\mathbf{q}}^{\lambda'} - f_{\mathbf{k}}^{\lambda}}{\varepsilon_{\mathbf{k}-\mathbf{q}}^{\lambda'} - \varepsilon_{\mathbf{k}}^{\lambda} + \hbar\omega + i\gamma} \qquad (4.123)$$

The energies $\varepsilon_{\mathbf{k}}^{\lambda}$ and occupancies $f_{\mathbf{k}}^{\lambda}$ are chosen as $\varepsilon_{\mathbf{k}}^{0,\lambda}$ and the corresponding electron and hole occupancies $F_{\mathbf{k}}^{\lambda}$. These Fermi functions are determined by the temperature as well as electron and hole chemical potentials in the quasi-equilibrium state. In consistency with the splitting of the polarization in a background and an excitation part, a splitting of the self-energy $\Sigma = \Sigma_{\mathrm{b}} + \Sigma_{\mathrm{exc}}$ is performed. Σ_{b} contains only renormalization effects due to carriers in the ground state that are obtained as will be presented in Sec. (4.4.4). For the polarization due to excited carriers, interband processes in Eq. (4.123) are neglected. The dielectric response induced by excited carriers is dominated by intraband processes. The dielectric function therefore becomes

$$\varepsilon_{\mathrm{exc},\mathbf{q}}(\omega) \quad = \quad 1 - V_{\mathbf{q}} \frac{1}{\mathcal{A}} \sum_{\lambda,\mathbf{k}} \frac{F^{\lambda}_{\mathbf{k}-\mathbf{q}} - F^{\lambda}_{\mathbf{k}}}{\varepsilon^{0,\lambda}_{\mathbf{k}-\mathbf{q}} - \varepsilon^{0,\lambda}_{\mathbf{k}} + \hbar\omega + i\gamma} \,. \tag{4.124}$$

The static limit is obtained by setting $\omega \to 0$. The Debye approximation is applied, which follows directly from the long-wavelength limit $\mathbf{q} \to 0$. Thereby the dielectric function takes the form:

$$\varepsilon^{\mathrm{ret}}_{\mathbf{q}\to 0} = 1 + V_{\mathbf{q}} \sum_{\lambda} \sum_{\boldsymbol{\nu}} \frac{m^{\lambda}_{\boldsymbol{\nu}} F^{\lambda}_{\boldsymbol{\nu}}}{2\pi\hbar^2} \tag{4.125}$$

with effective masses $m^{\lambda}_{\boldsymbol{\nu}}$ within the valley $\boldsymbol{\nu}$, being $\mathbf{K}, \mathbf{K}', \boldsymbol{\Sigma}, \boldsymbol{\Sigma}'$ and $\boldsymbol{\Gamma}$. Material-realistic static background dielectric functions for TMD monolayers are obtained as will be shown in the next section.

4.4.2. Wannier Function Continuum Electrostatics

It is important for describing a TMD monolayer in a structured dielectric environment to take the macroscopic screening into account. Atomically thin material sheets, especially the 2d materials, consist only of material surface. Thus they are very susceptible to the dielectric environment. The approach used to model the non-local influence of dielectric screening on the Coulomb interaction in this work is the *Wannier function continuum electrostatics* (WFCE) approach, that has been developed by Malte Rösner and Tim Wehling [158]. It is used to describe the screening induced by the dielectric environment of the monolayer in the ground state, while the screening of the excited carriers has been described in the section before. Therefore, this section focusses on $P_b(\mathbf{q}, \omega)$. An introduction to the WFCE scheme will be given in the following.

When building a many-body theory upon *ab-initio*-derived quantities the dielectric environment has to be applied after the *ab-initio*-calculation has been performed. Therefore Rösner et al. derived a model, that combines the Wannier function representation of the Coulomb interaction with continuum medium electrostatic. Dielectric environments such as layered heterostructures are easily accessible by the WFCE scheme as the model keeps the most important properties from non-local (macroscopic) screening.

Recalling the RPA-terms from the introduction of Sec. (4.4) one obtains for the screened Coulomb potential in frequency space:

$$\bar{V}(\mathbf{q},\omega) \;=\; \frac{\bar{U}_{\mathbf{q}}}{1-\bar{U}_{\mathbf{q}}P_R(\mathbf{q},\omega)} = \varepsilon_R^{-1}(\mathbf{q},\omega)\bar{U}_{\mathbf{q}} \tag{4.126}$$

with the polarization function $P_R(\mathbf{q},\omega)$. Within the WFCE scheme the polarization is split into two contributions as has been performed above as well. The first term contains screening from charge fluctuations between a subspace of bands in the energetic region of interest and the second term P_R contains screening from all other transitions. This effectively lowers the bare Coulomb interaction $\bar{U}_{\mathbf{q}}$ inside the monolayer giving rise to the screened interaction $\bar{V}_{\mathbf{q}}$. In the following the continuum formulation of dielectric screening will be combined with the Wannier representation of the Coulomb interaction. The continuum medium description starts from Poisson's equation in the presence of a dielectric medium:

$$\begin{aligned}\frac{1}{\varepsilon_0}\rho_{ext}(\mathbf{r}) \;&=\; \nabla\mathbf{D}(\mathbf{r})\\ &=\; \nabla\int \mathrm{d}^3\mathbf{r}'\left[\delta(\mathbf{r}-\mathbf{r}')+\chi(\mathbf{r}-\mathbf{r}')\right]\mathbf{E}(\mathbf{r}')\,,\end{aligned} \tag{4.127}$$

where the external charge density $\rho_{ext}(\mathbf{r})$ induces a dielectric displacement field $\mathbf{D}(\mathbf{r})$ due to the emerging polarization $\mathbf{P}(\mathbf{r}) = \int \mathrm{d}^3\mathbf{r}'\chi(\mathbf{r}-\mathbf{r}')\mathbf{E}(\mathbf{r}')$. The susceptibility $\chi(\mathbf{r}-\mathbf{r}')$ describes the response of a (homogeneous) material to an external perturbation.

The electric field is defined by the electrostatic potential $\mathbf{E}(\mathbf{r}') = -\nabla\Phi(\mathbf{r}')$. Separating $\mathbf{r}$ in Eq. (4.127) into components $\mathbf{r}_{||}, z$ and performing a Fourier transformation gives rise to the Poisson equation in q-space, where $\mathbf{q} = \mathbf{q}_{||}$ will be used. As solution the dielectric function is obtained

$$\varepsilon(\mathbf{q},q_z) = \frac{\Phi_{ext}(\mathbf{q},q_z)}{\Phi(\mathbf{q},q_z)}\,, \tag{4.128}$$

where the electrostatic potential of the external charge can be linked to the bare Coulomb potential $\bar{U}^{3d}(\mathbf{q},q_z) \;=\; -e\Phi_{ext}(\mathbf{q},q_z)$ and $\bar{V}^{3d}(\mathbf{q},q_z) \;=\; -e\Phi(\mathbf{q},q_z)$ corresponds to the screened interaction. The superscript '$3d$' shall denote, that the Coulomb interaction still depends on q_x, q_y, q_z.

The dielectric function can also be obtained from *ab-initio*-calculations. In order to connect the microscopic dielectric function with the dielectric environment, non-localities in z-direction are neglected by averaging over an effective monolayer thickness. Thus $\varepsilon(\mathbf{q},q_z)$ is compressed to $\varepsilon(\mathbf{q})$ still being of microscopic nature in the x,y-plane. To account for macroscopic screening the method of mirror charges is used. An oscillating charge density located in the central layer, this experiences a mirror charge density at equal distance on the other side of the interface. The mirrored charge density has a reduced magnitude of

$$\tilde{\varepsilon}_i \;=\; \frac{\varepsilon_{i+1} - \varepsilon_i}{\varepsilon_{i+1} + \varepsilon_i}\,, \tag{4.129}$$

where i labels the specific dielectric slab of the surrounding material. The main idea of the WFCE method is to perform an eigenvalue decomposition of the *ab-initio* calculated Coulomb interaction matrix $V^{3d}(\mathbf{q}, z = 0)$ (for example in the Wannier basis). The leading eigenvalue, that corresponds to long-wavelength charge density modulations, is corrected by the modified dielectric function of the continuum model that describes the macroscopic screening. The long-wavelength part of $\varepsilon(\mathbf{q})$ is thus modified according to the dielectric screening.

The obtained and modified dielectric function takes the form:

$$\varepsilon^{2d}(\mathbf{q}) \;=\; \varepsilon^{2d}_{\text{eff}}(\mathbf{q}, z = 0)\big|v_1\big\rangle\big\langle v_1\big| + \varepsilon^{2d}_{rest}(\mathbf{q}) \tag{4.130}$$

Here, $\varepsilon^{2d}_{\text{eff}}(\mathbf{q}, z = 0) = \varepsilon_1(\mathbf{q})$ is the modified leading eigenvalue of the decomposition of the microscopic 3d dielectric matrix, that is evaluated as

$$\varepsilon_1(\mathbf{q}) \;=\; \frac{h_{\text{eff}}}{2\pi} \int\limits_{\pi/h_{\text{eff}}}^{\pi/h_{\text{eff}}} \mathrm{d}q_z \varepsilon(\mathbf{q}, q_z)\,. \tag{4.131}$$

The vectors $\big|v_1\big\rangle$ are the eigenvectors of the first (leading) eigenvalue. While the leading eigenvalue itself is modified, the rest of the dielectric matrix $\varepsilon^{2d}_{rest}(\mathbf{q})$ is kept as is. Thus the 2d Coulomb matrix V depicted the chosen macroscopic screening can be calculated from $\varepsilon^{2d}(\mathbf{q})$ by

$$V(\mathbf{q}) \;=\; \sum_i \big|v_i\big\rangle\big\langle v_i\big|\varepsilon_i^{2d,-1}(\mathbf{q})\bar{U}_i(\mathbf{q})\,. \tag{4.132}$$

The WFCE scheme provides a versatile tool in order to model macroscopic screening in *ab-initio*-obtained Coulomb matrix elements without having to perform a numerically demanding DFT+GW calculation for each new sample structure. This method will be used throughout this thesis.

4.4.3. Intrinsic Screening

The WFCE scheme is applied to gain the material-realistic intrinsic ('bare') Coulomb interaction and the screening within the layer. The necessary quantities $\bar{U}_i$ and ε_i are obtained by fitting the DFT+GW calculation presented in Sec. (3.2.2). For this three-band model one is left with two diagonal 3×3 matrices $\bar{\mathbf{U}}(q)$ and $\varepsilon(q)$ representing the solved eigenvalue problem [36, 160].

$$\bar{\mathbf{U}}(q) = \begin{pmatrix} \bar{U}_1(q) & 0 & 0 \\ 0 & \bar{U}_2 & 0 \\ 0 & 0 & \bar{U}_3 \end{pmatrix} \qquad \varepsilon(q) = \begin{pmatrix} \varepsilon_1(q) & 0 & 0 \\ 0 & \varepsilon_2 & 0 \\ 0 & 0 & \varepsilon_3 \end{pmatrix} \tag{4.133}$$

The leading eigenvalue $\bar{U}_1(q)$ has the specific form [36]

$$\bar{U}_1(q) = \frac{3e^2}{2\varepsilon_0 A} \frac{1}{q(1+\gamma q+\delta q^2)} . \tag{4.134}$$

The function $\varepsilon_1(q)$ contains information on the dielectric structure of the sample. Thereby the intrinsic dielectric screening $\varepsilon_{\mathrm{TMD}}(q)$ is always contained. This dielectric function describes the microscopic screening of the layer itself and is also obtained by fitting the *ab-initio*-data. It may additionally be modified to depict layered substrates as will be presented in Sec. (4.4.4). The fitted microscopic screening function is given by [36]

$$\varepsilon_{\mathrm{TMD}}(\mathbf{q}) = \frac{a+q^2}{\frac{a\sin(qc)}{bqc}+q^2} + e . \tag{4.135}$$

The fit parameters of both functions are given in Tab. (C.1) and (C.2) in the appendix. Using the eigenvectors

$$\mathbf{v}_1 = \frac{1}{\sqrt{3}} \begin{pmatrix} 1 \\ 1 \\ 1 \end{pmatrix}, \qquad \mathbf{v}_2 = \frac{1}{\sqrt{6}} \begin{pmatrix} +2 \\ -1 \\ -1 \end{pmatrix}, \qquad \mathbf{v}_3 = \frac{1}{\sqrt{2}} \begin{pmatrix} 0 \\ +1 \\ -1 \end{pmatrix} \tag{4.136}$$

the Coulomb matrix modified by the dielectric function can be transformed back into the Wannier basis α, β with $\alpha, \beta \in \{\mathrm{d_{z^2}},\mathrm{d_{xy}},\mathrm{d_{x^2-y^2}}\}$. Applying $V_i(q) = U_i(q)/\varepsilon_i(q)$ one obtains

$$\mathbf{V}_{\mathbf{q}}^{\alpha\beta} = \mathbf{v}\bar{V}(q)\mathbf{v}^{\dagger} \tag{4.137}$$

$$\mathbf{U}_{\mathbf{q}}^{\alpha\beta} = \mathbf{v}\bar{U}(q)\mathbf{v}^{\dagger} \tag{4.138}$$

The matrix v contains the eigenvectors as columns. The resulting Coulomb interaction $\mathbf{V}_{\mathbf{q}}^{\alpha\beta}$ is in the following identified as the material-realistic ground state Coulomb interaction including screening from the dielectric environment while $\mathbf{U}_{\mathbf{q}}^{\alpha\beta}$ is the bare intrinsic interaction. This model scheme can be expanded considering more complex layered dielectric environments that are present in van der Waals heterostructures or substrate structures of the sample [161] yielding different $\mathbf{V}_{\mathbf{q}}^{\alpha\beta}$. This will be shown in the next section, together with the simple approach of taking $h_{\text{eff}} \to 0$ and taking a bare 2d Coulomb matrix element for $\bar{U}_1(q)$, that will result in the so called Keldysh potential [162, 163]. These different approaches to be shown next will yield a specific form of $\varepsilon_1(q)$ that can be inserted above.

4.4.4. Dielectric Screening

Samples made of TMD monolayers mostly come in layered substrate structures, e.g. being encapsulated in hBN or contacted by graphene. This chapter will give an overview on the methods used to derive a specific form of the macroscopic screening. Starting point will be a 2d layer embedded in a 3d environment. While the WFCE scheme embeds the chosen macroscopic dielectric function in $V_{\mathbf{q}}^{\alpha\beta}$, the following parts focus on obtaining the dielectric functions that describes the leading eigenvalue. Complex dielectric environments also provide renormalizations of the ground state band structure that have to be post processed on the *ab-initio*-results. They are described in the so called GdW-approach that will be shown here.

Screening of a 2d Layer: Keldysh-Potential

The most significant geometric property of TMD monolayers is their thickness, which is ~ 0.6 nm. The Coulomb interaction in such a layer is better described by assuming a 2d polarizable sheet in a 3d environment than by a pure 2d Coulomb interaction [162]. Thus in the following the macroscopic screening of an infinitly thin sheet will be discussed. Starting point for the electro dynamical description is again Poisson's equation:

$$\nabla^2\Phi(\mathbf{r}) \quad = \quad -\frac{\rho(\mathbf{r})}{\varepsilon_r} \tag{4.139}$$

Here the charge densitiy ρ can be written as the sum of an external point source and the induced charge density within the 2d layer:

$$\rho(\mathbf{r}) \quad = \quad e\delta(\mathbf{r}) + \delta(z)\rho_{2d}(\mathbf{r}) \,. \tag{4.140}$$

The local electric field will induce dipole momenta within the 2d layer, that in turn will polarize the layer. The polarization of the layer can thus be expressed as:

$$\begin{aligned}\mathbf{P}_{2d} &= \mathbf{d}_{ind} && (4.141)\\ &= \quad \alpha_{2d}\mathbf{E}_{local} && (4.142)\\ &= -\alpha_{2d}\nabla_{\mathbf{r}}\phi(\mathbf{r}_{\|}, z=0)\,, && (4.143)\end{aligned}$$

with α_{2d} being the polarizability of the 2d layer. The spatial variation of the polarization is equal to the carge density

$$\nabla_{\mathbf{r}}\mathbf{P}_{2d} \;=\; -\rho_{2d}(\mathbf{r})\,, \tag{4.144}$$

which leads to the following expression for the induced charge density:

$$\rho_{ind}(\mathbf{r}) \;=\; \alpha_{2d}\delta(z)\nabla^2_{\mathbf{r}}\Phi(\mathbf{r}_{\|}, z=0) \tag{4.145}$$

After inserting this expression into the Poisson equation and performing a spatial Fourier transformation one is left with:

$$\begin{aligned}\mathcal{F}(\nabla^2\Phi(\mathbf{r}))(\mathbf{k}) &= k^2\Phi(\mathbf{k}) && (4.146)\\ e\mathcal{F}(\delta(\mathbf{r}))(\mathbf{k}) &= e && (4.147)\\ \alpha_{2d}\mathcal{F}(\delta(z)\nabla^2_{\mathbf{r}}\Phi(\mathbf{r}_{\|}, z=0)) &= \alpha_{2d}k^2\Phi_{2d}(\mathbf{k}_{\|})\,, && (4.148)\end{aligned}$$

with $\mathbf{k}_{\|}$ being the momentum in the x, y-plane, which for convenience will be renamed to $\mathbf{q}$. Here $\Phi_{2d}(\mathbf{q})$ can be written as:

$$\Phi_{2d}(\mathbf{q}) \;=\; \int \frac{\mathrm{d}k_z}{2\pi}\Phi(\mathbf{q}, k_z)e^{ik_z 0}\,. \tag{4.149}$$

The total expression for the Fourier transformed Poisson equation is thus:

$$k^2\Phi(\mathbf{k}) \;=\; -\frac{1}{\varepsilon}\left(e + \alpha_{2d}q^2\Phi_{2d}(\mathbf{q})\right) \tag{4.150}$$

The expression for the 2d charge density can now be obtained by calculating the integral expression for $\Phi_{2d}(q)$ as written above:

$$\Phi_{2d}(q) = \int \frac{\mathrm{d}k_z}{2\pi}\Phi(\mathbf{q},k_z) \tag{4.151}$$

$$= -\frac{1}{\varepsilon}\int \frac{\mathrm{d}k_z}{2\pi}\frac{1}{k^2}\left(e+\alpha_{2d}q^2\Phi_{2d}(q)\right) \tag{4.152}$$

Solving this integral results in:

$$\Phi_{2d}(\mathbf{q}) = -\frac{e}{2\varepsilon q\left(1+\frac{\alpha_{2d}}{2\varepsilon}q\right)} \tag{4.153}$$

In general the two-dimensionality of the layer causes a momentum-dependency of the dielectric function:

$$\Phi_{2d}(\mathbf{q}) = -\frac{e}{2\varepsilon_0 q}\frac{1}{\varepsilon(q)} \tag{4.154}$$

$$\varepsilon(q) = \varepsilon_r + \frac{\alpha_{2d}}{2\varepsilon_0}q \tag{4.155}$$

The 2d Coulomb potential takes the form:

$$V_{\mathbf{q}}^{\mathrm{K}} = \frac{e^2}{2\varepsilon_0}\frac{1}{aq+bq^2} \tag{4.156}$$

$$= \frac{e^2}{2a\varepsilon_0}\left(\frac{1}{q}-\frac{1}{q+\frac{a}{b}}\right) \tag{4.157}$$

This is often called 'Keldysh potential', which describes macroscopically screened Coulomb interaction within a 2d layer. Here a can be written as the mean value of the dielectric screening of the upper and lower halfplane dielectric $a = (\varepsilon_1+\varepsilon_2)/2$, while $b = 2\pi\alpha_{2d}$ is the polarizability of the material. For the TMDs investigated in this work, values of α_{2d} can be found in Ref. [164]. The values are for MoS_2 $\alpha_{2d} = 0.66$ Å, for $MoSe_2$ $\alpha_{2d} = 0.823$ Å, for WS_2 $\alpha_{2d} = 0.603$ Å and finally for WSe_2 it is $\alpha_{2d} = 0.718$ Å.

The q-dependence of the dielectric function is a direct result of embedding a polarizable 2d material sheet within a 3d environment. The next step would be to assume a finite thickness of the monolayer. This seems not to be necessary though as there are methods for obtaining a material-realistic description of the Coulomb interaction. Nevertheless, the Keldysh potential is a useful approximation that depicts the real screening situation of a monolayer better than a bare 2d Coulomb potential (4.83) as will be shown in Chap. (5).

Substrate Screening

It has been experimentally shown that stacked monolayers do not lie directly on top of each other [161, 165]. Van der Waals-forces provide a small air or vacuum gap. In exfoliated samples also small particles, air or other impurities can be trapped between two layers. Annealing cleanses the samples and causes the interlayer gap to shrink to an equilibrium value. Thereby the dielectric screening changes. Such a gap reduces the screening due to surrounding material and enlarges the binding energies of Coulomb bound many-particle complexes (excitons, trions, ...). A model for this macroscopic dielectric screening in the sense of continuum electrostatics has been developed by Matthias Florian in Ref. [161]. As this extends the number of possible scenarios of the dielectric screening, this model has been implemented and will be explained in this section. The obtained dielectric functions are applied to the Coulomb interaction using the WFCE scheme presented in Sec (4.4.2). This has been used in order to model freestanding monolayers, monolayers on top of SiO_2 and monolayers encapsulated in hBN as shown in Fig. (4.2). For all calculations presented throughout this thesis a gap thickness of 0.3 nm has been used.

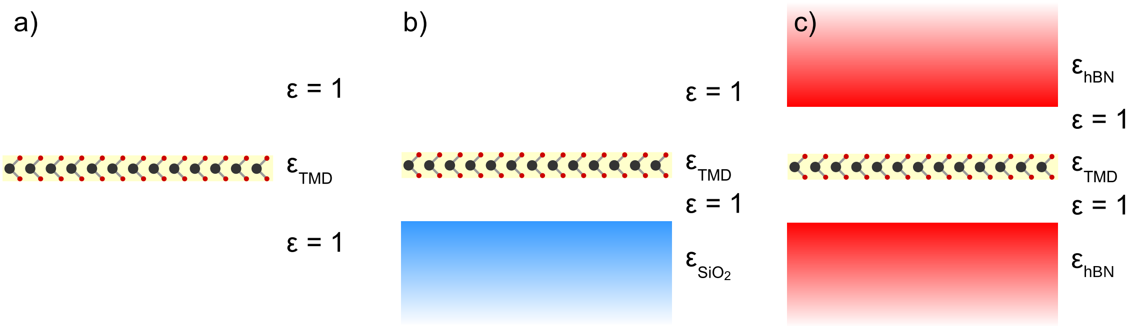

Figure 4.2.: Macroscopic screening situation for **a)** a freestanding monolayer, **b)** a monolayer on top of SiO_2 substrate including a small vacuum gap, and **c)** a monolayer encapsulated in multiple layers of hBN again leaving a small gap.

Using the findings of Sec. (4.4.2) Poisson's equation (4.127) can be adapted as

$$\nabla_{\mathbf{r}} \int d^3\mathbf{r}\varepsilon(\mathbf{r},\mathbf{r}')\nabla_{\mathbf{r}'}\Phi(\mathbf{r}') \quad = \quad -\frac{\rho(\mathbf{r})}{\varepsilon_0}\,. \tag{4.158}$$

The dielectric function $\varepsilon(\mathbf{r},\mathbf{r}')$ provides non-local screening effects for the charge density $\rho(\mathbf{r})$ resulting in the electric potential $\Phi(\mathbf{r})$. Again the z-dependence of the dielectric function is neglected and the charge density is located at the center of the TMD layer. Therefore the Fourier transformation of Eq. (4.158) reads

$$(\partial_z^2 - \mathbf{q}^2)\Phi(\mathbf{q}, z) \;=\; -\frac{\rho(\mathbf{q})\delta(z)}{\varepsilon_0 \varepsilon_r(\mathbf{q})}\,. \tag{4.159}$$

The ansatz for the electric potential has to fulfill the continuity conditions for the interfaces. Additionally the field has to vanish for $x, y \to \infty$. The ansatz is

$$\Phi(\mathbf{q}, z) \;=\; \frac{\rho(\mathbf{q})}{2\varepsilon_0 \varepsilon_{\mathrm{TMD}}(\mathbf{q}) q} e^{-q|z|} + \sum_{j=1}^{N-1} B_j e^{-q|z-z_j|}\,. \tag{4.160}$$

The first term on the right hand side accounts for the inhomogeneity due to the charge density within the TMD layer, while the second term represents the homogeneous solutions of the Poisson equation in each layer. Index j labels the interfaces of the N layers. Thus the ansatz describes the potential of a 2d charge density that is superimposed with potentials arising at the interfaces of the different dielectric layers. The continuity condition in z-direction states that the potential has to be continuous but may have a kink. Therefore the derivative is allowed to have a sudden jump of the function value. This exploited to fix the magnitude of the interface charges according to Eq. (4.129).

$$\varepsilon_j(\mathbf{q})\partial_z \Phi(\mathbf{q}, z_j - 0) \;=\; \varepsilon_{j+1}(\mathbf{q})\partial_z \Phi(\mathbf{q}, z_j + 0) \tag{4.161}$$

This gives rise to a matrix equation that determines the B_j and thereby the macroscopic 2d dielectric function. It describes the screening within the TMD layer ($z = 0$) of the layered structure and is used as modification of the leading eigenvalue in Eq. (3.33):

$$\varepsilon_1(\mathbf{q}) \;=\; \frac{\phi_0(\mathbf{q}, z=0)}{\phi(\mathbf{q}, z=0)} = \varepsilon_{\mathrm{TMD}}(\mathbf{q}) \left(1 - \sum_{ij} M_{ji}^{-1} x_i e^{-q|z_j|}\right)^{-1} \tag{4.162}$$

The matrix $\mathbf{M}$ and the vector $\mathbf{x}$ contain $\tilde{\varepsilon}_i$ and $e^{-q|z_i - z_j|}$ according to Eq. (4.161). The solution of Eq. (4.162) provides background screening for any vertically stacked layered sub- and superstrate structure. In this work three different setups are investigated: a freestanding monolayer, a TMD monolayer on SiO_2 substrate and a TMD monolayer encapsulated by hBN. Eq. (4.162) also allows to include the small air gaps, that have been mentioned in the beginning of the section.

Ground State Renormalizations from Dielectric Environment

By virtue of the changed dielectric situation when applying one of the scenarios explained beforehand (expect of course for the freestanding monolayer), the ground state single-particle energies will be renormalized. As explained in Refs. [161, 166, 167] these renormalizations can be expressed in the GdW-formalism. The main idea is to calculate the renormalizations effects only for the the difference between the unscreened (freestanding) and the screened (due to the dielectric environment) Coulomb interaction:

$$\Delta V = V^{HS} - V^{free} . \tag{4.163}$$

The renormalizations are calculated in SXCH-approximation (see Sec. (4.3.3)). Considering the ground state the occupations for electrons and holes are $f^h_{\mathbf{k}} = 1$, $f^e_{\mathbf{k}} = 0$, which directly leads to renormalizations of the type

$$\begin{aligned} \Sigma^{\mathrm{GdW},\lambda}_{\mathbf{k}} &= \frac{1}{\mathcal{A}} \sum_{\mathbf{k}'} \Delta V^{\lambda\lambda\lambda\lambda}_{\mathbf{k}\mathbf{k}'\mathbf{k}\mathbf{k}'} \left(\frac{1}{2} - f^{\lambda}_{\mathbf{k}'} \right) \\ &= \frac{1}{2\mathcal{A}} \sum_{\mathbf{k}'} \Delta V^{\lambda\lambda\lambda\lambda}_{\mathbf{k}\mathbf{k}'\mathbf{k}\mathbf{k}'} \end{aligned} \tag{4.164}$$

These renormalizations provide a shift, which is nearly constant in $\mathbf{k}$, thereby changing the band gap as presented in Tab. (4.1). This in turn has implications on the dipole matrix elements (see Sec. (4.6.1)) as well as on the exciton binding energies that will be obtained later on.

(meV)	$E_K^{G,\mathrm{DFT+GW}}$	$\Delta E_K^{G,GdW}$	
		SiO_2	enc. hBN
MoS_2	2638	-262	-357
$MoSe_2$	2355	-239	-318
WS_2	2775	-280	-390
WSe_2	2359	-255	-350

Table 4.1.: Band gaps of monolayer MoS_2,$MoSe_2$, WS_2 and WSe_2 obtained from the Wannier interpolation together with GdW shifts induced by the macroscopic screening of different substrate geometries.

4.5. Charge Carrier Scattering

The dynamics of excited carriers induced by pulsed optical excitation in Eq. (4.79) are determined by scattering processes. These scattering processes are described by a collision integral. Due to carrier-carrier or carrier-phonon scattering processes the excited carriers experience a change of momentum. Thereby arbitrary initial distributions are able to relax into a thermodynamic equilibrium state. Commonly the description of the scattering can be split into two scattering rates [137]:

$$\left.\frac{\mathrm{d}}{\mathrm{d}t} f_{\mathbf{k}}^{\lambda}(t)\right|_{scatt.} = \left(1 - f_{\mathbf{k}}^{\lambda}(t)\right) S_{\mathbf{k}}^{\lambda,in} - f_{\mathbf{k}}^{\lambda}(t) S_{\mathbf{k}}^{\lambda,out} \,. \tag{4.165}$$

A collision between e.g. two carriers in states $\left|\mathbf{k},\lambda\right\rangle$ and $\left|\mathbf{k}',\lambda'\right\rangle$ will change their momenta and thus the occupation number $f_{\mathbf{k}}^{\lambda}(t)$. This occurs in two possible ways. Either a carrier is scattered out of state $\left|\mathbf{k},\lambda\right\rangle$ with probability $S_{\mathbf{k}}^{\lambda,out}$ and occupation $f_{\mathbf{k}}^{\lambda}(t)$ thereby effectively reducing the occupation or a carrier will be scattered into state $\left|\mathbf{k},\lambda\right\rangle$ with probability $S_{\mathbf{k}}^{\lambda,in}$ and occupation $1 - f_{\mathbf{k}}^{\lambda}(t)$ and effectively increase the occupation. For fermions it has to be considered that already occupied states cannot be filled more than once due to the Pauli blocking.

Population dynamics in monolayer TMDs have been shown for example in Ref. [127]. For Chap. (7) it is important that scattering or relaxation can occur in order to describe the optical excitation of charge carriers and the behaviour of the total charge carrier density with the exciting pulse strength properly. Nevertheless, the focus of that chapter is on the steady-state value of the equation system, where $\frac{\mathrm{d}}{\mathrm{d}t} f_{\mathbf{k}}^{\lambda}(t) = \frac{\mathrm{d}}{\mathrm{d}t}\psi_{\mathbf{k}}^{\lambda}(t) = 0$ has been reached. Therefore a microscopic model of scattering processes is not necessary. As consequence the relaxation time approximation has been used, which will be described in the following.

4.5.1. Relaxation Time Approximation

In the quasi equilibrium state it can be assumed, that the change of the occupation is not large in between two discretized time steps. The carrier population will finally relax into a Fermi distribution. Assuming the carrier population to be close to the final Fermi distribution it can be set:

$$f_{\mathbf{k}}^{\lambda}(t) = F_{\mathbf{k}}^{\lambda} + \delta f_{\mathbf{k}}^{\lambda}(t) \,. \tag{4.166}$$

It shall be noted that the Fermi function $F_{\mathbf{k}}^{\lambda}$ depends on the current status of the full system. The single-particle energies will be renormalized according to the actual presence of charge carrier within the band structure valleys. The chemical potential of electrons and holes will change as well, due to the accumulation of carriers. Inserting the ansatz (4.166) into Eq. (4.165) one obtains:

$$\left.\frac{\mathrm{d}}{\mathrm{d}t} f_{\mathbf{k}}^{\lambda}(t)\right|_{scatt.} = \left(1 - F_{\mathbf{k}}^{\lambda} - \delta f_{\mathbf{k}}^{\lambda}(t)\right) S_{\mathbf{k}}^{\lambda,in} - \left(F_{\mathbf{k}}^{\lambda} + \delta f_{\mathbf{k}}^{\lambda}(t)\right) S_{\mathbf{k}}^{\lambda,out} \tag{4.167}$$

If the difference between the actual occupation and the Fermi distribution $\delta f_{\mathbf{k}}^{\lambda}(t)$ is small, it is valid to assume equal in and out scattering rates. This allows for writing

$$\left.\frac{\mathrm{d}}{\mathrm{d}t} f_{\mathbf{k}}^{\lambda}(t)\right|_{scatt.} = -\delta f_{\mathbf{k}}^{\lambda}(t) \left(S_{\mathbf{k}}^{\lambda,in} + S_{\mathbf{k}}^{\lambda,out}\right) . \tag{4.168}$$

Identifying $\left(S_{\mathbf{k}}^{\lambda,in} + S_{\mathbf{k}}^{\lambda,out}\right)$ as an inverse time τ_R^{-1} that is in average needed for a scattering event between two particles, one is left with the final form of the scattering term in the relaxation time approximation:

$$\left.\frac{\mathrm{d}}{\mathrm{d}t} f_{\mathbf{k}}^{\lambda}(t)\right|_{scatt.} = -\frac{f_{\mathbf{k}}^{\lambda}(t) - F_{\mathbf{k}}^{\lambda}}{\tau_R} . \tag{4.169}$$

Typical relaxation times for TMDs are in the order of 100 fs [127], which has been used throughout this work for all material constellations.

4.6. Light-Matter Interaction

Optical experiments, for example measuring the absorption, reflectivity or transmittivity, are performed in the presence of polarizable media, as it is the case for van der Waals heterostructures or encapsulated TMDs. Light that propagates through this layered samples interacts differently with each dielectric slab. Electromagnetic waves propagating through such a dielectric structure are described by the macroscopic version of Maxwell's equations:

$$\nabla \cdot \mathbf{D} = \rho_{free} , \tag{4.170}$$

$$\nabla \cdot \mathbf{B} = 0 , \tag{4.171}$$

$$\nabla \times \mathbf{E} = -\frac{\partial \mathbf{B}}{\partial t} , \tag{4.172}$$

$$\nabla \times \mathbf{H} = \mathbf{j}_{free} + \frac{\partial \mathbf{D}}{\partial t} , \tag{4.173}$$

where $\mathbf{D} = \varepsilon_0 \mathbf{E} + \mathbf{P}$ is the displacement field with $\mathbf{E}$ being the electric field and $\mathbf{P}$ the polarization, while $\mathbf{H} = \mu_0^{-1}\mathbf{B} - \mathbf{M}$ is the magnetic field in the presence of a magnetization $\mathbf{M}$ with the external magnetic field $\mathbf{B}$. Both $\mathbf{P}$ and $\mathbf{M}$ describe, how a material reacts on an incident electric (magnetic) field. This work is focussed on optical properties, thus $\mathbf{P}$ is most important. Here it describes the field, that is induced when dipoles in the system respond to external electric fields or are created by them. Thus it is described by the density of dipole moments. The polarization can be written as $\mathbf{P} = \varepsilon_0 \chi_e \mathbf{E}$, where χ_e is the susceptibility that describes the response by excited charge carriers. Background contributions are neglected.

The first part of this section will discuss the dipoles, that are induced by exciting carriers due to a laser pulse. The second part will describe how to calculate the optical absorption, reflection or transmission in the presence of surrounding dielectric matter, such as an encapsulation of the monolayer in hBN, which is often done in experiments.

4.6.1. Semi-classical Dipole Interaction

The interaction between photons and electrons in matter can be described in the sense of minimal coupling. Here the momentum $\mathbf{p}$ is replaced by momentum $\mathbf{p} + e\mathbf{A}(\mathbf{r}, t)$, where $\mathbf{A}(\mathbf{r}, t)$ is the vector potential of the magnetic field $\mathbf{B}(\mathbf{r}, t) = \nabla \times \mathbf{A}(\mathbf{r}, t)$. The Hamiltonian of the light-matter interaction H_{LM} becomes

$$H_{\text{LM}} = \frac{(\mathbf{p} - q\mathbf{A}(\mathbf{r}, t))^2}{2m} + q\Phi(\mathbf{r}, t) + V(\mathbf{r}) \,, \tag{4.174}$$

with $\Phi(\mathbf{r}, t)$ being the electric potential. In Chap. 5 this Hamiltonian will be expanded in order to study the effects of magnetic fields interacting with excitons. Further evaluating the expression above using the Coulomb gauge ($\nabla \mathbf{A} = 0, \Phi = 0$) only linear coupling of $\mathbf{p}$ to $\mathbf{A}$ remains, giving rise to the light-matter interaction Hamiltonian (cf. Eq. (4.9)):

$$H_{LM} = -\frac{q}{m}\mathbf{p}\mathbf{A}(\mathbf{r}, t) \tag{4.175}$$

The interaction with the light field will cause an oscillating behaviour of the bound charges around their ions [130]. Due to this fact it is possible to approximate the light matter interaction as an oscillating dipole. Assuming that $\mathbf{A}$ is almost constant among the unit cell of the crystal this oscillation will cause a time-dependent and finite change of the position operator $\langle \mathbf{r} \rangle$ of the charge density. The time-dependence of this charge displacement is determined by the electric field describing the light pulse, thus the Hamiltonian H_{LM} can be expressed by the scalar potential [131]

$$H_{LM} \quad = \quad e\mathbf{r}\mathbf{E}(t)\,. \tag{4.176}$$

The oscillation will induce a finite momentum $\langle\mathbf{p}\rangle$. From the commutation relation $-i\hbar/m_e\mathbf{p} = [H_0, \mathbf{r}]$ it is evident that the expectation value of the momentum can be expressed by the expectation value of the position operator. Using the Bloch states $|\mathbf{k}, \lambda\rangle$ for calculating the expectation value the microscopic transition dipole matrix elements $\mathbf{d}$ are introduced

$$\mathbf{d}^{he}_{\mathbf{k}} \quad = \quad e\langle\mathbf{k}, e|\mathbf{r}|\mathbf{k}, h\rangle\,. \tag{4.177}$$

The eigenenergies of H_0 can be used to further evaluate the expression above, leading to

$$\mathbf{d}^{he}_{\mathbf{k}} \quad = \quad \frac{e\hbar}{im_e}\frac{\langle\mathbf{k}, e|\mathbf{p}|\mathbf{k}, h\rangle}{\varepsilon^e_{\mathbf{k}} + \varepsilon^h_{\mathbf{k}} + E_G}\,, \tag{4.178}$$

with E_G being the band gap. Due to the similarity of the momentum and the current operator $\mathbf{j} = e/m_e\mathbf{p}$ [131] the dipole matrix elements can be expressed using the matrix elements $\mathbf{j}^{\alpha\beta}_{\mathbf{k}}$. These are proportional to the gradient of the ground state Hamiltonian H_0 containing the band structure as derived in Sec. (3.2.2). The final form of the transition dipole matrix elements is

$$\mathbf{d}^{he}_{\mathbf{k}} \quad = \quad \frac{e}{i}\frac{1}{\varepsilon^h_{\mathbf{k}} + \varepsilon^e_{\mathbf{k}} + E_G}\sum_{\alpha,\beta}\left(c^{h,\alpha}_{\mathbf{k}}\right)^* c^{e,\beta}_{\mathbf{k}}\;\nabla_{\mathbf{k}}H^{\alpha\beta}_{\mathbf{k}}\,. \tag{4.179}$$

Here the expansion of the current operator matrix elements into the Bloch states has been used additionally. As a concluding remark: the gradient of the Hamiltonians $H_{\mathbf{k}}$ can be derived analytically if the explicit form of the Hamiltonian is known (which is the case for the Hamiltonians used here). When discretizing the Hamiltonian numerically, especially for the Monkhorst-Pack grid [168], which is used throughout this thesis, a finite difference approximation can be derived for smooth functions in $\mathbf{k}$ [119].

The dipole determines the strength of an optical transition. Transition are allowed or forbidden depending on the symmetries of the involved Bloch states. Furthermore the dipole is sensitive to the polarization of the electric field. In this thesis the electric field carries a circular polarization, as circular polarized light couples to the valleys $\mathbf{K}, \mathbf{K}'$ in the hexagonal BZ differently. The envelope function of the laser pulse is describe as a Gaussian function, as any main frequency of the light has been transformed out using the rotating frame picture. Thus the pulse is described as

$$\mathbf{E}(t) = \mathbf{e}_\sigma E_0 e^{\left(\frac{t-t_0}{\tau}\right)^2 4\ln(2)}, \tag{4.180}$$

$$\text{with} \quad \mathbf{e}_\sigma = \frac{1}{\sqrt{2}} \begin{pmatrix} 1 \\ \sigma i \end{pmatrix}, \quad \sigma = \pm 1 . \tag{4.181}$$

Here, E_0 is the field strength, τ is the full width at half maximum (FWHM) of the Gaussian (pulse duration) and e_σ is the vector of left or right circular polarized light. The strength of the electric field E_0 is not accessible in experiments. A more useful quantity is the pump fluence, that gives insight on the amount of energy that is pumped into the system by the laser pulse. The fluence can be obtained by utilizing the Poynting vector $\mathbf{S} = \mathbf{E} \times \mathbf{H}$. It is defined as the energy per pulse area and duration applied to the monolayer, being proportional to the squared absolute value of the electric field:

$$S = \varepsilon_0 c_0 \int \mathrm{d}t \, |\mathbf{E}(t)|^2 \tag{4.182}$$

The evaluation of this integral yields the relation between field strength E_0 and fluence S that will be useful later on in this thesis:

$$S = \sqrt{\frac{\pi}{32\ln(2)}} \cdot c_0 \cdot \varepsilon_0 \cdot \tau \cdot E_0^2 \tag{4.183}$$

The evaluation of the equation above gives the fluence in meV nm^{-2}. The fluence is a function of the pulse duration $S = S(\tau)$. To cast the fluence in common experimental units of μJ cm^{-2}, the conversion factor is $1 \times 10^{17} e$, with e being the elementary charge in SI units. Using μJ cm^{-2} will be useful for comparison with experiments where the pump laser defines the density of excited charge carriers. By inverting relation (4.183) the field strength E_0 can be obtained from the fluence S.

4.6.2. Optical Absorption

As it is part of this work to investigate TMD monolayer in layered dielectric environments, the propagation of the light through this dielectric structure has to be considered. From Maxwell's equations one obtains the wave equation for the electric field $\mathbf{E}(t)$ in the presence of matter. The goal is to obtain an expression for the frequency-dependent absorption of TMD monolayers. The laser illuminates the TMD monolayer perpendicular to the monolayer plane. All vector products can thus be expressed by their absolute values. The polarization can only extend in lateral direction (cf. Sec. (4.4.4)). The wave equation is given by

$$\left[\Delta - \frac{1}{c^2}\frac{\partial^2}{\partial t^2}\right]\mathbf{E}(z,t) \quad = \quad -\mu_0\frac{\partial^2}{\partial t^2}\mathbf{P}(z,t)\,. \tag{4.184}$$

The monolayer thickness in z-direction can be expressed as $\delta(z-z_0)$ as it is small compared to the wavelength. Inserting $\mathbf{P} = \varepsilon_0\chi_e\mathbf{E}$ and performing a Fourier transformation one finds $P(\omega) = \chi_e(\omega)E(\omega)$. The electric field is effectively reduced by the assumption of infinitely small expansion in z-direction.

$$\left[\frac{\partial^2}{\partial z^2} - \frac{\omega^2 n^2}{c_0^2}\right]E(z,\omega) \quad = \quad -\mu_0\omega^2\delta(z-z_0)\tilde{E}(z_0,\omega) \tag{4.185}$$

To solve this equation an ansatz for the electric field and its derivative has to be made. This ansatz provides the correct continuity condition to connect wave functions and their derivative at layer interfaces. For each layer the ansatz therefore consists in general of two waves, one propagating to the top and one to the bottom.

$$E_j(z) \quad = \quad A_j e^{ik_j(z-z_j)} + B_j e^{-ik_j(z-z_j)} \tag{4.186}$$

The monolayer (and additional air gaps, that are described later on) contribute to the susceptibility $\chi(\omega)$. The susceptibility describes the optical response of a material to an external electric field:

$$P(t) \quad = \quad \int\limits_{-\infty}^{+\infty} \mathrm{d}t'\chi(t,t')E(t')\,. \tag{4.187}$$

For the system being in a stationary, or quasi-equilibrium state, the susceptibility reduces to

$$P(t) \quad = \quad \int\limits_{-\infty}^{t} \mathrm{d}t'\chi(t-t')E(t')\,, \tag{4.188}$$

where the convolution theorem is exploited in order to obtain:

$$P(\omega) = \chi(\omega)E(\omega) \qquad \Rightarrow \qquad \chi(\omega) = \frac{P(\omega)}{E(\omega)}\,. \tag{4.189}$$

The susceptibility contributes absorptive phenomena by its imaginary part, which reduces the strength of a propagating wave. Due to the small thickness of a monolayer it is assumed that it does not provide modulations of the propagating wave other than absorption. The optically active layered substrate on the other hand will modify the wave, because interference effects of the propagating waves between the layer interfaces occur. This interference effects becomes strong, if the length of the layer and the wavelength are of comparable order of magnitude. The modulation of the wave caused by layered structure is described by the transfer matrix formalism [130]. Each interface or free propagation path provides a matrix-multiplication-type equation for the change in transmitted, absorbed and reflected amplitudes of the respective propagating wave in a way that:

$$\begin{pmatrix} A_{j+1} \\ B_{j+1} \end{pmatrix} = \mathbf{M}_{j+1} \begin{pmatrix} A_j \\ B_j \end{pmatrix} \tag{4.190}$$

Here, the propagating wave is always perpendicular to the layer structure. For the free propagation of a wave in a material layer of length L_j with an index of refraction of n_j on obtains:

$$\mathbf{M}_{\mathrm{F},j} = \begin{pmatrix} e^{i\phi_j} & 0 \\ 0 & e^{-i\phi_j} \end{pmatrix}, \tag{4.191}$$

with $\phi_j = n_j k L_j$ and $k = \omega/c_j$ being the 1d wave vector of the propagating wave. At a dielectric interface, where the index of refraction changes from n_j to n_{j+1} the matrix takes the form:

$$\mathbf{M}_j = \frac{1}{2} \begin{pmatrix} 1 + \frac{n_{j-1}}{n_j} & 1 - \frac{n_{j-1}}{n_j} \\ 1 - \frac{n_{j-1}}{n_j} & 1 + \frac{n_{j-1}}{n_j} \end{pmatrix}. \tag{4.192}$$

The propagation of the wave changes due to the different indices of refraction, therefore at each interface k is changed. After dielectric step the wave propagates through the remaining layer until the next interface is reached, therefore each layer j is in total described as $\mathbf{M}_{\mathrm{F},j}\mathbf{M}_j$. The monolayer itself contributes the complex $\chi(\omega)$ that has been described above as well as a dielectric interface between the substrates to the top and to the bottom. Its matrix representation is:

$$\mathbf{M}_{\mathrm{ML}} = \frac{1}{2} \begin{pmatrix} 1 + \frac{n_{j-1}}{n_j} + \frac{2iY(\omega)}{n_j} & 1 - \frac{n_{j-1}}{n_j} + \frac{2iY(\omega)}{n_j} \\ 1 - \frac{n_{j-1}}{n_j} - \frac{2iY(\omega)}{n_j} & 1 + \frac{n_{j-1}}{n_j} - \frac{2iY(\omega)}{n_j} \end{pmatrix}. \tag{4.193}$$

Here, it is defined, that $Y(\omega) = \frac{\omega}{2c_0\varepsilon_0 n_j}\chi(\omega)$. The total optical structure is therefore described as a set of matrix multiplications:

$$\mathbf{M}_{\text{total}} = \mathbf{M}_N \mathbf{M}_{\text{F},N-1} \dots \mathbf{M}_{\text{F},N-j_{\text{ML}+1}} \mathbf{M}_{\text{ML}} \mathbf{M}_{\text{F},N-j_{\text{ML}-1}} \dots \mathbf{M}_{\text{F},1} \mathbf{M}_1 \tag{4.194}$$

In the end, the absorption is obtained from:

$$\alpha(\omega) = 1 - |r|^2 - \frac{n_B}{n_T}|t|^2 \tag{4.195}$$

$$r = -\frac{M_{21}}{M_{22}} \tag{4.196}$$

$$t = M_{11} + M_{12} \cdot r\,, \tag{4.197}$$

where the matrix elements of $\mathbf{M}_{\text{total}}$ are used. In this thesis two halfplanes of dielectric media to the top and to the bottom of the monolayer are investigated. This enables the description of a freestanding, an encapsulated monolayer and a monolayer lying on a substrate. The expression for the absorption $\alpha(\omega)$ Eq. (4.195) can be specified to:

$$r = -\frac{1 - \sqrt{\varepsilon_T/\varepsilon_B} - 2Y(\omega)}{1 + \sqrt{\varepsilon_T/\varepsilon_B} - 2Y(\omega)} \tag{4.198}$$

$$t = 1 + \frac{\sqrt{\varepsilon_T/\varepsilon_B}}{2} + Y(\omega) + \left(1 - \frac{\sqrt{\varepsilon_T/\varepsilon_B}}{2} + Y(\omega)\right) r\,, \tag{4.199}$$

where $n \approx \sqrt{\varepsilon}$ has been used. Using this formalism the absorption spectrum $\alpha(\omega)$ is calculated for typical experimental scenarios. The results are presented in Chap. (6) and (7).

4.7. Summary of the Theory

Closing the theory chapter of this thesis, a short overview of the derived equations will be given in this section. In summary a theory for calculating the optical properties of photoexcited TMD monolayers in a layered dielectric environment has been presented in the sections before.

Starting point of each calculation is the generation of the $\mathbf{k}$ grid, where the Monkhorst-Pack [168] routine has been used in order to reduce numerical efforts and for better convergence.

The next step is to calculate the ground state properties of the unexcited TMD monolayer. Therefore it is necessary to obtain Coulomb matrix elements $U_{\mathbf{q}}$, $V_{\mathbf{q}}$ and the band structure $\varepsilon^{0,\lambda}_{\mathbf{k}} + \Sigma^{\text{GdW},\lambda}_{\mathbf{k}}$. This necessitates the knowledge of the dielectric environment $\varepsilon_b(\mathbf{q})$ in order to calculate $\Sigma^{\mathrm{GdW},\lambda}_{\mathbf{k}}$. The ground state Hamiltonian H_0 with eigenvalues $\varepsilon^{0,\lambda}_{\mathbf{k}}$ can in general be expressed by three commonly used approximations or methods in order to tackle problems of different complexity or required accuracy:

i) effective mass approximation

ii) Tight-Binding parametrizations (see 3.1.1)

iii) interpolation of *ab-initio* calculated band structures (see 3.2.1 and 3.2.2)

When it is important to regain certain symmetries of the system, here for example the $\hat{C}_{3v}$ of the TMD crystal structure, the band structure has to be post processed enforcing the named symmetries to avoid numerical inaccuracies. Time reversal symmetry affects the eigenvectors as $c(-\mathbf{k}) = -c^*(\mathbf{k})$.
Given the band structure the Coulomb matrix elements have to be calculated expanded with the same basis set (Bloch states). Thereby the expansion coefficients $c^{\alpha}_{\mathbf{k}}$ are introducing. Intrinsic screening of the layer itself, fitted to *ab-initio*-results, as well as dielectric environment have to be accounted for (see Sec. (4.4). Different choices can be made:

i) bare 2d Coulomb matrix elements: $U^{2d}_{\mathbf{q}}$ (see 4.3.1)

ii) Keldysh potential: $V^{\mathrm{K}}_{\mathbf{q}}$ (see 4.4.4)

iii) material-realistic Coulomb matrix elements from *ab-initio* methods: $U^{\alpha\beta}_{\mathbf{q}}/V^{\alpha\beta}_{\mathbf{q}}$ (see 4.4.2)

Using the *WFCE* scheme and its extensions the dielectric environment can be cast onto all possible choices of Coulomb potentials. Thereby V emerges from the bare interaction U. The dielectric environment also induces renormalizations of the ground state band structure, which are calculated from the GdW-scheme, resulting in

$$\varepsilon^{\lambda}_{\mathbf{k}} = \varepsilon^{0,\lambda}_{\mathbf{k}} + \Sigma^{\mathrm{GdW},\lambda}_{\mathbf{k}} \tag{4.200}$$

$$\Sigma^{\mathrm{GdW},\lambda}_{\mathbf{k}} = \frac{1}{2\mathcal{A}} \sum_{\mathbf{k}'} \Delta V^{\lambda\lambda\lambda\lambda}_{\mathbf{k}\mathbf{k}'\mathbf{k}\mathbf{k}'} \,, \tag{4.201}$$

where ΔV is obtained from the difference of the Coulomb interaction of a freestanding layer and the Coulomb interaction screened by the surrounding structure.
The transition dipole matrix elements $\mathbf{d}^{he}_{\mathbf{k}}$ have to be calculated as well, which requires knowledge of the gradient of the ground state Hamiltonian (see Sec. (4.6.1)). It can be derived by applying standard calculus onto the given Hamiltonian, if the $\mathbf{k}$-dependence is

known. If the exact form of the Hamiltonian is unknown, the gradient $\nabla_{\mathbf{k}} H_{\mathbf{k}}$ has to be calculated numerically.
The SBE are used in different context throughout the remaining part of this thesis. In the first case a quasi equilibrium state is assumed. The density-dependent renormalized band structure can be calculated by self-consistently evaluating either the Hartree-Fock terms in Sec. (4.3.2) or the SXCH-approximation in Sec. (4.3.4). SXCH allows for including effects such as screening of the interacting charge carriers. For the quasi-equilibrium state the band structure renormalizations are evaluated using Fermi distributions $F^{\lambda}_{\mathbf{k}}$ of a given density, that are developed together with the band structure itself, until self-consistency is reached.

$$\varepsilon^{\mathrm{HF},\lambda}_{\mathbf{k}} = \varepsilon^{0,\lambda}_{\mathbf{k}} + \Sigma^{\mathrm{H},\lambda}_{\mathbf{k}} + \Sigma^{\mathrm{F},\lambda}_{\mathbf{k}} \left(+\Sigma^{\mathrm{GdW},\lambda}_{\mathbf{k}}\right) \tag{4.202}$$

$$\varepsilon^{\mathrm{SXCH},\lambda}_{\mathbf{k}} = \varepsilon^{0,\lambda}_{\mathbf{k}} + \Sigma^{\mathrm{H},\lambda}_{\mathbf{k}} + \Sigma^{\mathrm{U},\lambda}_{\mathbf{k}} + \Sigma^{\mathrm{V},\lambda}_{\mathbf{k}} + \Sigma^{\mathrm{SX},\lambda}_{\mathbf{k}} + \Sigma^{\mathrm{CH},\lambda}_{\mathbf{k}} \left(+\Sigma^{\mathrm{GdW},\lambda}_{\mathbf{k}}\right) \tag{4.203}$$

Together with the dipole and Coulomb matrix elements the renormalized band structure defines the input for the equation of motion of the microscopic polarizations $\psi^{he}_{\mathbf{k}}(t)$:

$$\frac{\mathrm{d}}{\mathrm{d}t}\psi^{he}_{\mathbf{k}}(t) = -\frac{i}{\hbar}\left(\tilde{\varepsilon}^{h}_{\mathbf{k}} + \tilde{\varepsilon}^{e}_{\mathbf{k}} - i\gamma\right)\psi^{he}_{\mathbf{k}}(t) + \frac{i}{\hbar}\Omega^{he}_{\mathbf{k}}(t)\left(1 - F^{e}_{\mathbf{k}} - F^{h}_{\mathbf{k}}\right) , \tag{4.204}$$

which can also be cast directly into Fourier space:

$$\left(\hbar\omega - \tilde{\varepsilon}^{h}_{\mathbf{k}} - \tilde{\varepsilon}^{e}_{\mathbf{k}} + i\gamma\right)\psi^{he}_{\mathbf{k}}(\omega) + \Omega^{he}_{\mathbf{k}}(\omega)\left(1 - F^{e}_{\mathbf{k}} - F^{h}_{\mathbf{k}}\right) = 0 . \tag{4.205}$$

Here the system is probed by a short and weak probe laser in order to obtain broadband absorption. The probe pulse is contained in the renormalized Rabi energy $\Omega^{he}_{\mathbf{k}}(t) = \mathbf{d}^{he}_{\mathbf{k}}\mathbf{E}(t) + \sum_{h',e',\mathbf{k}'} W^{eh'he'}_{\mathbf{k}\mathbf{k}'\mathbf{k}\mathbf{k}'}$. A constant phenomenological dephasing γ has been introduced to account for broadening due to carrier-carrier or carrier-phonon interaction.
In order to analyze the dynamics of the occupations using the SBE the equation of motion for the population function $f^{e/h}_{\mathbf{k}}(t)$ has to be calculated as well:

$$\frac{\mathrm{d}}{\mathrm{d}t} f^{e/h}_{\mathbf{k}}(t) = \frac{2}{\hbar}\mathrm{Im}\left(\Omega^{he*}_{\mathbf{k}}(t)\psi^{he}_{\mathbf{k}}(t)\right) - \frac{f^{e/h}_{\mathbf{k}}(t) - F^{e/h}_{\mathbf{k}}}{\tau_R} \tag{4.206}$$

$$\frac{\mathrm{d}}{\mathrm{d}t}\psi^{he}_{\mathbf{k}}(t) = -\frac{i}{\hbar}\left(\tilde{\varepsilon}^{h}_{\mathbf{k}} + \tilde{\varepsilon}^{e}_{\mathbf{k}} - i\gamma - \hbar\omega_{\text{det.}}\right)\psi^{he}_{\mathbf{k}}(t) + \frac{i}{\hbar}\Omega^{he}_{\mathbf{k}}\left(1 - f^{e}_{\mathbf{k}}(t) - f^{h}_{\mathbf{k}}(t)\right) \tag{4.207}$$

In this case $\mathbf{E}(t)$ takes the role of a pump laser rather than the role of a probe laser, thereby exciting charge carries from the valence band to the conduction band. The laser energy is detuned to the band gap by $\hbar\omega_{\text{det.}}$. The band structure renormalizations therefore have to be calculated for each time step, which renders a self-consistent evaluation numerically demanding. Thus a fine time grid has to be used to obtain converged renormalization. Instead of a constant dephasing, also a density dependent dephasing $\Gamma(n)$ can be introduced. For the population function a scattering process using the relaxation time approximation from Sec. (4.5) with $\tau_R = 100$ fs has been introduced.

After having calculated the time evolution of one of the cases presented beforehand the polarization of the active layer and the density of excited charge carriers have to be evaluated. These are given by

$$\begin{aligned} \mathbf{P}(\omega) &= \frac{1}{\mathcal{A}}\sum_{\mathbf{k}}(\mathbf{d}^{he}_{\mathbf{k}})^{*}\psi^{he}_{\mathbf{k}}(\omega) && (4.208)\\ n^{\lambda} &= \lim_{t\to\infty}\frac{1}{\mathcal{A}}\sum_{\mathbf{k}} f^{\lambda}_{\mathbf{k}}(t)\,. && (4.209) \end{aligned}$$

The binding energies of the excitons can be obtained by either analysing the evaluated absorption spectrum (cf. $\chi(\omega) = P(\omega)/E(\omega)$, $\alpha(\omega) \propto \text{Im}(\chi(\omega))$ in Sec. (4.6.2)) or evaluating the exciton eigenvalue problem. The exciton eigenvalue problem is contained in the SBE in form of the homogeneous Wannier equation

$$\left(\hbar\omega - \varepsilon^{h}_{\mathbf{k}} - \varepsilon^{e}_{\mathbf{k}} + i\gamma\right)\psi^{he}_{\mathbf{k}}(\omega) + \sum_{h',e',\mathbf{k}'} V^{eh'he'}_{\mathbf{k}\mathbf{k}'\mathbf{k}\mathbf{k}'}\psi^{h'e'}_{\mathbf{k}'}(\omega) = 0\,. \tag{4.210}$$

The Wannier equation can be solved by diagonalizing the matrix representation of Eq. (4.210)

$$\left(\varepsilon^{h}_{\mathbf{k}} + \varepsilon^{e}_{\mathbf{k}}\right)\delta_{\mathbf{k},\mathbf{k}'}\psi^{he}_{\mathbf{k}} + \sum_{h',e',\mathbf{k}'} V^{eh'he'}_{\mathbf{k}\mathbf{k}'\mathbf{k}\mathbf{k}'}\psi^{h'e'}_{\mathbf{k}'} = E^{n}_{\mathbf{k}}\psi^{he}_{\mathbf{k}}\,. \tag{4.211}$$

The eigenvalues of this diagonalization are defined as bound states (below the gap) or the continuum states (above the gap). The eigenvectors correspond to exciton wave functions for the bound states.

This chapter presents a consistent theory for calculating the optical properties of photoexcited TMD monolayers in differently layered dielectric environments. The static limit of the GW-approximation has been utilized to treat the many-body Coulomb interaction resulting in the well-established SXCH-approximation. In this context material-realistic Coulomb matrix elements originating from *ab-initio* calculations have been employed. The many-body effects included will provide a realistic prediction of the excitation process as well as the optical response. Different mechanisms that lead to band structure renormalizations have been identified and will be analyzed in the following sections as well as the pump-dependent accumulation of charge carriers. Basic properties of the ground state, excitons in TMD monolayers, and long-lived interlayer excitons that form in TMD bilayer systems will be investigated.

5. Excitons in TMD Monolayers

The two peaks from the spin-split $\mathbf{K}$- and $\mathbf{K}'$-valley transitions in the hexagonal Brillouin zone are the most prominent features in the TMD absorption spectrum. Thus the $\mathbf{K}$-valley excitons A (direct spin-up transition at $\mathbf{K}$) and B (direct spin-down transition at $\mathbf{K}'$) have been intensly investigated [46, 48, 57, 73, 169]. This chapter shall provide insight in basic features and descriptions of the absorption spectrum of TMDs comparing different approaches for the Coulomb interaction and the influence of a magnetic field. Basis of the calculations presented in the following sections is the exciton eigenproblem described by the Wannier equation (4.211), which is part of the SBE. The following two sections contain results that have been obtained jointly with Leon Hetzel and Laura Martens while the author of this thesis has co-supervised their Bachelor's thesis. In the first subchapter the comparison of the Keldysh-Coulomb-potential [162] derived in Chap. (4.4.4) to the bare 2d Coulomb potential from Sec. (4.3.1) can be found. The Keldysh potential provides a more realistic description of a polarizable 2d sheet of a material embedded in a 3d environment rather than the 2d Coulomb-potential, which in fact reduces the dimensionality. The second subsection summarizes the results on excitons in a magnetic field [170], which is for low magnetic fields often used to lift the degeneracy of the valley polarizations [171] but can also be used to determine the effective mass of the excitons [172].

5.1. Comparison of Keldysh and Coulomb Potential

The eigenvalue for bound electron-hole pairs in TMD monolayers is governed by the equation

$$\left(\varepsilon^h_{\mathbf{k}} + \varepsilon^e_{\mathbf{k}}\right)\psi^{he}_{\mathbf{k}} - \sum_{\mathbf{k}} V^{ehhe}_{\mathbf{k}\mathbf{k}'\mathbf{k}\mathbf{k}'}\psi^{he}_{\mathbf{k}'} \quad = \quad E^n_{\mathbf{k}}\psi^{he}_{\mathbf{k}}\,, \tag{5.1}$$

which contains the transition energies $\varepsilon^h_{\mathbf{k}} + \varepsilon^e_{\mathbf{k}}$ as well as the Coulomb interaction $V^{ehhe}_{\mathbf{k}\mathbf{k}'\mathbf{k}\mathbf{k}'}$ that provides energectially favorable states below the band gap. From Eq. (5.1) the eigenvalues $E^n_{\mathbf{k}}$ are obtained by diagonalizing the corresponding matrix representation. This homo-

geneous equation is called Wannier equation and can also be obtained by a Fourier transform of the real-space Schrödinger equation, that describes the relative motion between electron and hole. The whole equation thus describes a hydrogen-like problem, where the mass of the hole (positive charge) is comparable to the effective electron mass. One expects (and obtains) wave functions categorized by their principle (n) and magnetic $(m = -n \dots n)$ quantum numbers, for example the 2s-state corresponds to $n = 1$ and $m = 0$.
Applying an effective mass approximation to the band structure, the whole equation reduces to a spherical symmetric problem. Perfoming perturbation theory on the Hamiltonian at $\mathbf{k} = \mathbf{K}$ leads to $\varepsilon^{\lambda}_{\mathbf{k}} = \hbar^2 k^2/(2m^*_\lambda)$. The term m^*_λ is defined as the second derivative of the energy with respect to the wave number:

$$\left(\frac{1}{m^*_\lambda}\right)_{\alpha\beta} = \frac{1}{\hbar^2}\frac{\partial^2 \varepsilon^{\lambda}_{\mathbf{k}}}{\partial k_\alpha \partial k_\beta} . \tag{5.2}$$

As this is reminiscent of the energy of a free particle with mass m^*_λ it is called effective mass approximation. When using the effective mass approximation, all radial dependence of the band structure is neglected. Only s-shaped exciton wave functions appear, that are peaked at $\mathbf{k} = 0$. In order to keep radial dependence, a more elaborate band structure calculation is beneficial for understanding the underlying physics. Here, the three band model from Ref. [90] described in Chap. (3) is used.
In principle both A and B exciton, stemming from the different transitions at $\mathbf{K}$ and $\mathbf{K}'$ for spin up and down electrons, can be calculated using Eq. (5.1) with or without the effective mass approximation as they are 1s-excitons. No further information is gained when calculating the B-exciton (see Sec. (3.3)), whereas the numerical effort is doubled. Therefore it is omitted in the following.
The Coulomb matrix elements $V^{ehhe}_{\mathbf{k}\mathbf{k}'\mathbf{k}\mathbf{k}'}$ are obtained from the expansion of the Coulomb interaction into the Bloch states of the ground state model. In this first part the two different forms of the Coulomb potential V_q will be compared. As a short reminder of the specific form:

$$U^{2d}_{\mathbf{q}} = \frac{e^2}{2\varepsilon_0\varepsilon_r}\frac{1}{q} \qquad V^{\mathrm{Ky}}_{\mathbf{q}} = \frac{e^2}{2\varepsilon_0}\frac{1}{\varepsilon_r\, q + 2\pi\alpha_{2d} q^2} , \tag{5.3}$$

where $\varepsilon_r = (\varepsilon_1 + \varepsilon_2)/2$ is the average dielectric constant of the top and bottom material surrounding the TMD and α_{2d} is the 2d polarizability that can be obtained from experiment [164]. The bare 2d Coulomb potential yields the 2d Rydberg-series known from the hydrogen atom [129]

$$E^n = -\frac{E_B}{\left(n-\frac{1}{2}\right)^2}, \tag{5.4}$$

where the ground state is at -4 times the binding energy E_B of the 3d exciton. The binding energy of the lowest state (1s) obtained from the bare 2d Coulomb interaction is larger than the one obtained from the Keldysh potential. Considering the dielectric constant ε_r as fit parameter the binding energy may be corrected. Nevertheless this is physically not justified and misleading, as the dielectric environment is artificially changed in order to diminish the strong Coulomb interaction. The large binding energy obtained from using $U^{2d}_{\mathbf{q}}$ in Eq. (5.1) originates from the conservation of the spherical symmetry of the wave function in 2d. Confinement due to the reduced thickness is therefore accompanied by a decrease in the Bohr radius and an increase of the binding energy. Obviously the reduction of the dimensionality implied in $U^{2d}_{\mathbf{q}}$ does not reflect realistic physics. The real situation is described better, if a polarizable 2d material sheet embedded in a 3d environment is accounted for. The Keldysh-potential contains a dielectric function that itself has a linear dependence on $\mathbf{q}$ due to the Coulomb interaction, which is of long-range nature due to the weak dielectric screening. For short ranged interaction between charge carriers this model is limited due to the infinitesimally small thickness that has been assumed initially, see derivation of Eq. (4.157) in Sec. (4.4.4).

The linear dependence of the dielectric function $\varepsilon(q) = \varepsilon_r + 2\pi\alpha_{2d}q$ has a large influence on the energie tic order of the eigenstates as the s-state is always the energetically highest for every n, inverting the usual sequence. The q-dependence of the dielectric function causes a stronger screening at short range and weak screening at long range. As the exciton radius increases with n and $|m|$, this directly screens the states with higher m weaker than the corresponding s-state of the respective n-series. The screening thus behaves inversely with the exciton radius, leading to stronger binding of the respective states. This can be understood from analyzing the dielectric environment qualitatively. The electric field between electron and hole permeates both the monolayer as well as the surrounding material. Therefore large parts of the electric field are weakly screened by the dielectric. Increasing the spatial separation between the charges, more of the electric field is in a region where the screening is reduced [64, 173, 174].

The binding energy of the 2d exciton screened by a Keldysh potential can be derived by modifying the dielectric constant to be depending on the principle quantum number n [64, 174, 175] while the general $(n-1/2)^{-2}$ dependence remains. Thus one obtains:

$$E^n = -\frac{\mu e^4}{2\hbar^2 \varepsilon_r^{(n)}} \cdot \frac{1}{\left(n-\frac{1}{2}\right)^2} \tag{5.5}$$

$$\text{with} \quad \varepsilon_r^{(n)} = \frac{1}{2}\left[1+\sqrt{1+\frac{32\pi\alpha_{2D}\mu}{9n(n-1)+3}}\right] . \tag{5.6}$$

To this end the dielectric function occuring in the Keldysh potential (cf. Sec. (4.4.4)) that effectively screens the electron-hole interaction and reduces the binding energy is averaged up to a certain effective bohr radius a_{eff} to be only q-dependent. It can be shown that $a_{\text{eff}} = a_{\text{eff}}(n)$ [174], which leads to the relation shown in Eq. (5.6).

It is found, that the Keldysh potential is more capable of describing the screening situation in a material-realistic way [174]. The Keldysh potential also works well, when considering a complex layered substrate. It has been shown in [161] and Sec. (4.4.4) that a small vacuum gap in between neighbouring van der Waals-bound layers effectively reduces the dielectric screening. Thereby the binding energy of the excitons is increased compared to the case of two layers in direct contact. The dependence of the dielectric function on q therefore deviates from a linear one. Especially for small q the deviation depends strongly on the height of the vacuum gap. On the other hand the influence of substrate phonons of encapsulated monolayers counteracts this reduction of the screening by the vacuum gap [62]. These two effects, the reduction of screening due to an vacuum gap and the influence of substrate phonons, tend to compensate each other. Therefore the use of the Keldysh potential, e.g. for the case of encapsulated monolayers, is verified.

5.2. Excitons in a Magnetic Field

Applying magnetic fields to monolayers of TMDs [44, 170–172, 176, 177] lifts the valley degeneracy of $\sigma_\pm$ polarized light and shifts the spectral peak position. From the dependence of this energetical shift on the magnetic field strength excitonic properties can be extracted. The magnetic field will force the electrons within the TMD layer into Landau states. The Coulomb interaction will cause electrons and holes in these Landau states to form magneto-excitons. Thus this chapter is subjected to Landau diamagnetism and magneto-excitons in TMD monolayers.

In order to describe these magneto-excitons it is difficult to start with the full problem but rather to first evaluate the equations of the electrons and holes in the Landau basis which is successively used to obtain Coulomb matrix elements. Assuming a magnetic field being oriented in z-direction and neglecting further effects from spin-orbit interaction (that are already included in the ground state basis) and Coulomb interaction, the Hamiltonian in minimal coupling provides

$$H = \frac{\mathbf{p}^2}{2m} + \mu_B l_z B + \frac{e^2 B^2}{8m}\mathbf{r}^2 \,. \tag{5.7}$$

Introducing the magnetic length $l^2 = \hbar/Be$ with $\mathbf{r} = l\varrho$ will help to distinguish different coupling regimes later on. Formely introducing inter- ($a^\dagger/a$) and intra- ($b^\dagger/b$) Landau level creation and annihilation operators render the equations mathematically similar to the harmonic oscillator. One obtains for electrons and holes

$$H^e = \hbar\omega_c^e \left(a^\dagger a + \frac{1}{2}\right) \tag{5.8}$$

$$H^h = \hbar\omega_c^h \left(b^\dagger b + \frac{1}{2}\right) \,, \tag{5.9}$$

with $\omega_c^{e/h} = q_{e/h}B/m$ and $q_{e/h} = \mp e$ being the cyclotron frequency that defines the classical rotation of an electron (hole) moving perpendicular to a magnetic field. The eigenvalue equations of (5.8) and (5.9) provide the Landau levels and the eigenfunctions that will be used for deriving Coulomb matrix elements. In the second quantization defining the number operator as $\hat{n} = a^\dagger a$ and $\hat{n}' = b^\dagger b$ one obtains

$$\hbar\omega_c^e \left(\hat{n} + \frac{1}{2}\right) \Phi_n(\varrho_\mathbf{e}) = E_n^e \Phi_n(\varrho_\mathbf{e}) \quad \text{with} \quad E_n^e = \hbar\omega_c^e \left(n + \frac{1}{2}\right) \tag{5.10}$$

$$\hbar\omega_c^h \left(\hat{n}' + \frac{1}{2}\right) \Phi_{n'}(\varrho_\mathbf{h}) = E_{n'}^h \Phi_{n'}(\varrho_\mathbf{h}) \quad \text{with} \quad E_{n'}^h = \hbar\omega_c^h \left(n' + \frac{1}{2}\right) \tag{5.11}$$

Considering the orbital momentum in Eq. (5.7) the eigenfunctions of an electron will also depend on the intra-Landau operators

$$\Phi_{nn'} = \frac{(a^\dagger)^n (b^\dagger)^{n'}}{\sqrt{n! n'!}} \Phi_{00} \tag{5.12}$$

In order to describe magneto-excitons the Coulomb interaction $V(\mathbf{r})$ is added to Eq. (5.7). A unitary transformation is used to obtain an equation for the relative electron and hole coordinate $\mathbf{r} = \mathbf{r}_e - \mathbf{r}_h$

$$H_\mathbf{r}^{\mathrm{MX}} = H_\mathbf{r}^e + H_\mathbf{r}^h - V(\mathbf{r}) \quad \text{with} \quad H_\mathbf{r}^{e/h} = \frac{1}{2m_{e/h}} \left(\mathbf{p} \pm \frac{e}{2}\mathbf{B} \times \mathbf{r}\right)^2 \tag{5.13}$$

Using the eigenfunctions (5.12) as basis set for an expansion one obtains the eigenvalue equation for $H_{\mathbf{r}}^{\mathrm{MX}}$

$$H_{\mathbf{r}}^{\mathrm{MX}}\Phi_{\alpha}(\varrho) = E_{\alpha}\Phi_{\alpha}(\varrho) \tag{5.14}$$

$$\Phi_{\alpha}(\varrho) = \sum_{n} c_{\alpha n}\Phi_{nn}(\varrho)\,. \tag{5.15}$$

Therefore a Wannier equation for the magneto-exciton states E_{α} and the coefficients $c_{\alpha n}$ arises

$$\sum_{n}\left[\hbar\omega_{c}\left(n+\frac{1}{2}\right)\delta_{nn'} - \int \mathrm{d}^{2}\varrho\,\Phi^{*}_{n'n'}(\varrho)V(\mathbf{r})\Phi_{nn}(\varrho)\right]c_{\alpha n} \;=\; E_{\alpha}\sum_{n} c_{\alpha n}\delta_{nn'}\,. \tag{5.16}$$

For the Keldysh potential this equation can only be solved numerically. Due to the necessary evaluation of Laguerre-polynomials within the Coulomb matrix elements $V_{nn'} = \int \mathrm{d}^{2}\varrho\Phi^{*}_{n'n'}(\varrho)V(\mathbf{r})\Phi_{nn}(\varrho)$ this is only possible for a limited number of basis states $\Phi_{nn'}$.
Eq. (5.16) has strong implications on the absorption spectrum. The higher s-states are split according to the Landau levels contained in Eq. (5.16). For increasing magnetic field strength the higher states shift closer to the band gap due to their smaller binding energy.
The magneto-exciton states exhibit two different regimes of field dependence for increasing magnetic field strength. For low field strength the diamagnetic part dominates causing a quadratic shift behaviour of the exciton states

$$\Delta E_{\mathrm{dia}} \;=\; \frac{e^{2}}{8\mu}\left\langle \mathbf{r}^{2}\right\rangle_{nl}B^{2}\,. \tag{5.17}$$

The Wannier equation (5.16) has been solved in the effective mass approximation, thus the reduced mass μ occurs. From the induced shift with increasing field strength the radius $r_{nl} = \sqrt{\left\langle \mathbf{r}^{2}\right\rangle_{nl}}$ of the exciton state with quantum numbers nl can be found from the curvature. For large magnetic fields the exciton states shift linearly, which in turn allows for the extraction of the effective mass

$$\Delta E_{\mathrm{Landau}} \;=\; \frac{\hbar eB}{\mu}\left(n+\frac{1}{2}\right)\,. \tag{5.18}$$

The Bohr radii and the effective masses of WSe_2 for the 1s to 3s states have been compared to literature values [172] and are in good agreement. The Bohr radius of the 1s state of MoS_2 is in good agreement with theoretical values from Ref. [164]. The magnetic length in comparison to the exciton Bohr radius indicates, whether the excitons experience a weak ($l > r_{nl}$)

or a strong ($l < r_{nl}$) magnetic field. The large binding energy of excitons in TMDs causes weak coupling to magnetic fields for field strength of up to several tens of T. Thus it is experimentally very difficult to measure in the linear regime. For MoS_2 the 1s state shifts about 10 meV for $B = 250$ T. The higher lying states provide lower binding energies. Therefore a reduced magnetic field of 40 T causes a comparable shift of $\sim$ 10 meV for the 2s state.

5.3. Conclusion

Excitons in TMD monolayers have been described by solving the Wannier equation in effective mass approximation. Basic properties of these excitons have been investigated. The Keldysh potential provides a more realistic approach for the Coulomb interaction, as it describes a polarizable 2d sheet in a 3d environment rather than a reduction of the dimensionality. This implies a better description of the exciton states, especially reproducing the energetical order of the s and p states. Due to their different Bohr radii, higher p-states are energetically lower than the s-states of the same main quantum number n. Also a non-hydrogenic Rydberg series of the ns-states originates from the Keldysh description.
Applying magnetic fields to TMD layers does not affect the lowest states much, as they have a large binding energies. Strong magnetic fields of hundreds of T (for MoS_2) are necessary to cause a significant shift. Even stronger fields are necessary to change from the diamagnetic (quadratic shifting behaviour of the exciton state) regime to the linear one. Nevertheless the Keldysh potential provides a realistic description that enables the extraction of the 1s to 3s state Bohr radii and masses in WSe_2 which are in good agreement with literature values.

6. Excitation Induced Many-Particle Effects in TMDs

After discussing the ground state properties of TMDs and also models for excitons in TMDs (with and without a magnetic field) in Chap. (3) and (5), the many-body theory developed for TMD monolayers in Chap. (4) is applied to the cases of MoS_2, $MoSe_2$, WS_2 and WSe_2. This way access to the optical properties based on material-realistic band structures is granted and effects of excited charge carriers can thus be described. Moreover, the theory can be systematically enhanced by including processes such as scattering due to carrier-carrier Coulomb or carrier-phonon interaction. The focus of this section is on many-body effects that are induced due to the interaction of optically excited charge carriers with each other. A quasi-equilibrium is assumed, leaving the occupation probabilities to be quasi Fermi distributions $f_{\mathbf{k}}^{\lambda}(t) = F_{\mathbf{k}}^{\lambda}$, which are self-consistently calculated together with the single-particle renormalizations. Hence, dynamical processes for charge carrier populations are not discussed here and left for the following chapter. The optical absorption is obtained as linear response to an ultrashort and weak probe pulse. The results presented in this chapter have been published in cooperative work in Ref. [156]. Unless stated otherwise the author of this thesis performed the numerical calculations presented throughout this chapter. The figures from [156] have been reprinted with permission.

The presence of a direct band gap in monolayers of TMDs is advantageous for an application in optical and electronic devices. An indirect band gap therefore counteracts the promising electronic properties of TMD monolayers. In contrast to changing the properties of a monolayer by applying strain [47] or Coulomb engineering [37] due to the dielectric environment [105], a mostly overlooked fact is, that a transition to an indirect band gap can also occur when inducing charge carriers via optical excitation or doping into a monolayer TMD. Considering the strong Coulomb interaction that prevails in optically excited TMD monolayers, the band structure renormalizations are expected to be strong. Therefore it is necessary to investigate on the many-body renormalizations that describe the transition to an indirect band gap - the charge carrier distribution, band-structure renormalizations, and optical properties in response to a weak optical probe field.

6.1. Transition from Direct to Indirect Band Gaps

Many-body interactions of excited carriers are known to cause band gap renormalizations. Due to the strong Coulomb interaction in TMD monolayers the strength of the renormalizations is higher in comparison to conventional semiconductors. The d-orbital character of the bands contributing to the optical transitions additionally cause the momentum dependence of the renormalizations to gain significance. Thus the valleys $\mathbf{K}$ and $\mathbf{\Sigma}$ are shifted differently as will be pointed out later. Starting point for the investigation are the semiconductor Bloch equations for one electron and one hole band:

$$\frac{\mathrm{d}}{\mathrm{d}t}\psi^{he}_{\mathbf{k}}(t) \;=\; -\frac{i}{\hbar}\left(\tilde{\varepsilon}^{h}_{\mathbf{k}}+\tilde{\varepsilon}^{e}_{\mathbf{k}}-i\gamma\right)\psi^{he}_{\mathbf{k}}(t)+\frac{i}{\hbar}\Omega^{he}_{\mathbf{k}}\left(1-F^{e}_{\mathbf{k}}-F^{h}_{\mathbf{k}}\right) \tag{6.1}$$

where the $\psi^{he}_{\mathbf{k}}(t)$ is the single-particle expectation value of the transition amplitude of the corresponding electron and hole creation and annihilation operators. $\Omega^{he}_{\mathbf{k}} = \mathbf{d}^{eh}_{\mathbf{k}}\mathbf{E}(t) + \frac{1}{\mathcal{A}}\sum_{\mathbf{k}'} W^{ehhe}_{\mathbf{kk}'\mathbf{kk}'}\psi^{he}_{\mathbf{k}'}(t)$ is the generalized Rabi energy originating from the included light-matter coupling with the dipole matrix elements $\mathbf{d}^{eh}_{\mathbf{k}}$. $\mathbf{E}(t)$ is the envelope of the exciting laser pulse, which is here in right circular polarization to excite both $\mathbf{K}/\mathbf{K}'$-valleys. In the quasi equilibrium that is assumed throughout this chapter the laser pulse describes a weak probe pulse, which is resonant with the band gap energy. The screened Coulomb interaction matrix elements $W^{ehhe}_{\mathbf{kk}'\mathbf{kk}'} = \varepsilon^{-1}(|\mathbf{k}-\mathbf{k}'|)V^{ehhe}_{\mathbf{kk}'\mathbf{kk}'}$ provide bound states. The interaction is screened due to both excited carriers, where the plasma screening is treated in the static Debye approximation (see Eq. (4.125)), and also dielectric screening from the substrate, that is taken into account by using the WFCE approach described in Sec. (4.4.2) [36, 158]. The phase space filling term $\left(1-F^{e}_{\mathbf{k}}-F^{h}_{\mathbf{k}}\right)$ consists of the self-consistently calculated quasi Fermi distributions of the respective excited charge carriers. All calculations are performed at a temperature of $T = 300$ K. Dephasing processes of the polarization are implemented via a constant dephasing factor γ. This accounts for electron-phonon scattering and adds a finite lifetime for the quasi-particles.

In the sense of pump-probe experiments carriers have been optically excited and successively relaxed into the band structure valleys. Before recombination sets in, these carriers occupy states according to the Fermi distribution $F^{\lambda}_{\mathbf{k}}$ of a finite carrier density and are probed by a weak pulse $\mathbf{E}(t)$. The presence of these excited carriers renormalizes the band structure $\tilde{\varepsilon}^{\lambda}_{\mathbf{k}}$ according to the instantaneous parts of the chosen SXCH self-energy, see Sec. (4.3.4). The contributions of the renormalized single-particle energies are

$$\tilde{\varepsilon}^{\lambda}_{\mathbf{k}} = \varepsilon^{0,\lambda}_{\mathbf{k}} + \Sigma^{\mathrm{H},\lambda}_{\mathbf{k}} + \Sigma^{\mathrm{U},\lambda}_{\mathbf{k}} + \Sigma^{\mathrm{SX},\lambda}_{\mathbf{k}} + \Sigma^{\mathrm{CH},\lambda}_{\mathbf{k}}\,, \tag{6.2}$$

where no ground state renormalizations $\Sigma_{\mathbf{k}}^{\mathrm{GdW},\lambda}$ are present, as only a freestanding monolayer is investigated here. Intra-subband exchange renormalizations $\Sigma_{\mathbf{k}}^{\mathrm{V},\lambda}$ do not occur, as only one hole and one electron band are considered. The ground state band structure $\varepsilon_{\mathbf{k}}^{0,\lambda}$ is renormalized due to Hartree interactions $\Sigma_{\mathbf{k}}^{\mathrm{H},\lambda}$ as well as intraband *screened exchange* interaction $\Sigma_{\mathbf{k}}^{\mathrm{SX},\lambda}$, intraband *Coulomb hole* interaction, which is the difference between screenend and unscreened Coulomb interaction, and the unscreened interband exchange interaction $\Sigma_{\mathbf{k}}^{\mathrm{U},\lambda}$. In detail these terms are given by

$$\begin{aligned} \tilde{\varepsilon}_{\mathbf{k}}^{\lambda} &= \varepsilon_{\mathbf{k}}^{0,\lambda} + \Sigma_{\mathbf{k}}^{\mathrm{H},\lambda} + \frac{1}{\mathcal{A}} \sum_{\mathbf{k}'\lambda'\neq\lambda} U_{\mathbf{k}\mathbf{k}'\mathbf{k}\mathbf{k}'}^{\lambda\lambda'\lambda\lambda'} f_{\mathbf{k}'}^{\lambda'} \\ &\quad - \frac{1}{\mathcal{A}} \sum_{\mathbf{k}'} W_{\mathbf{k}\mathbf{k}'\mathbf{k}\mathbf{k}'}^{\lambda\lambda\lambda\lambda} f_{\mathbf{k}'}^{\lambda} + \frac{1}{2\mathcal{A}} \sum_{\mathbf{k}'} \left(W_{\mathbf{k}\mathbf{k}'\mathbf{k}\mathbf{k}'}^{\lambda\lambda\lambda\lambda} - V_{\mathbf{k}\mathbf{k}'\mathbf{k}\mathbf{k}'}^{\lambda\lambda\lambda\lambda} \right) . \end{aligned} \tag{6.3}$$

Equation (4.116) allows for distinguishing the mechanisms of the resulting band structure renormalizations. These renomalizations have been calculated in dependence of the excited charge carrier density and also for the case of either electron or hole doping. The effects of the renormalizations in the band structure are shown in Fig. (6.1) for a high density excited charge carriers of 3.2×10^{13} cm^{-2}. The quasi-thermal charge carrier distributions, which are equally important to the renormalizations as they are of the general form $V/W \cdot f$ (except for the Coulomb hole term) are also shown.

Comparing Fig. (6.1) with Eq. (6.3) is essential in understanding the underlying mechanisms of the renormalizations. The different self-energy terms lead to $\mathbf{k}$-dependent shifts in the band structure that in general lower the conduction bands and raise the valence bands. From the momentum dependence of these effects a relative shift between the $\mathbf{K}$- and the $\mathbf{\Sigma}$-valley results, leading finally to an indirect band gap. The shifts originating from the renormalizations can be seen in the band structures plotted in Fig. (6.1). For elevated densities shifts of about 500 meV are found.

Within the accuracy and known limitations, DFT+GW calculations predict an intrinsically indirect band gap at the $\mathbf{K}$-point for MoSe$_2$ and WSe$_2$ as can be seen from a closer look on Fig. (6.1b) and (6.1d). This initially drains charge carriers from $\mathbf{K}$ to $\mathbf{\Sigma}$. In comparison, MoS$_2$ and WS$_2$ show a direct band gap. The indirect band gap from $\mathbf{\Sigma}^e$ to $\mathbf{K}^h$ is energetically only slightly larger. This leads to almost equal populations in the conduction-band $\mathbf{K}$ and $\mathbf{\Sigma}$-valleys. On the other hand, both tungsten-based TMDs have a larger energy difference between $\mathbf{\Sigma}/\mathbf{\Sigma}'$ and $\mathbf{K}/\mathbf{K}'$, which leads to small occupancies of the $\mathbf{\Sigma}'$-valley.

As already mentioned, the different spin-orbit splitting has to be considered for MoS$_2$ and WS$_2$. This results in an intrinsic loss of electrons at $\mathbf{K}$ for bright transitions in tungsten-

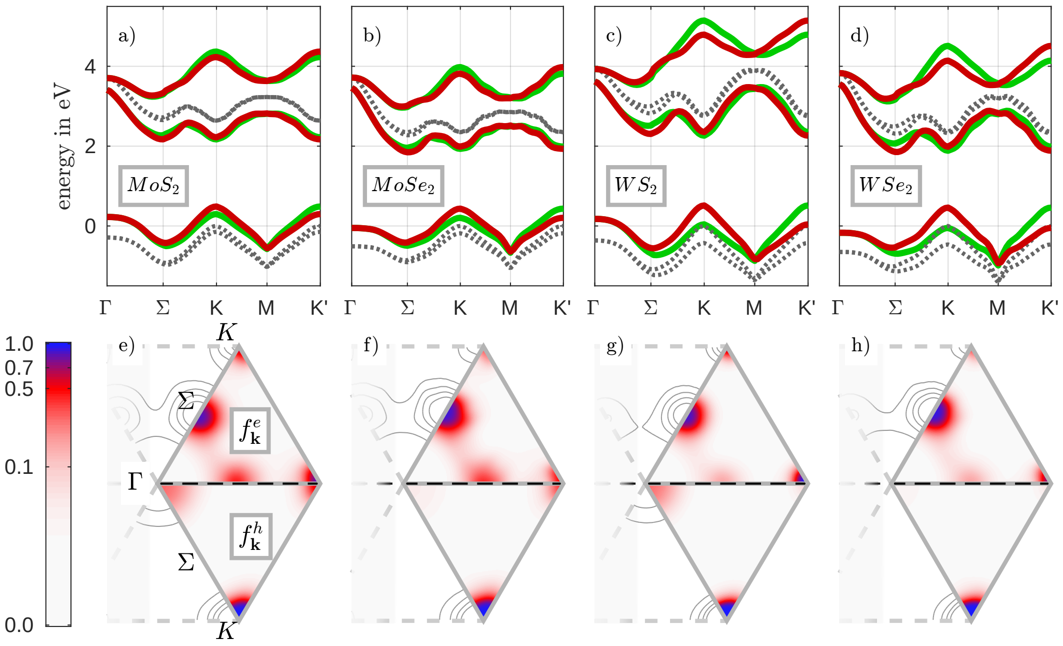

Figure 6.1.: The renormalized band structures of MoS_2, $MoSe_2$, WS_2, and WSe_2 are shown in (a) - (d). The zero-density band structure as guidance for the changes due to renormalizations is shown as grey dashed line. In the bottom row (e) - (h) the thermalized charge carrier population functions (Fermi distribution) in the lowest conduction and highest valence band are plotted for the respective materials at a density of 3.2×10^{13} cm^{-2}. The high occupations at both $\mathbf{K}$ and $\mathbf{\Sigma}$ are clearly visible as well as the differences in occupation of $\mathbf{K}/\mathbf{K}'$ and $\mathbf{\Sigma}/\mathbf{\Sigma}'$. The differences between molybdenum and tungsten compounds as well as between the sulfides/selenides can also be distinguished. Figure reprinted with permission from [156].

based compounds.

Comparing the differences in the band structure as explained in Chap. (3), no $\mathbf{\Sigma}$-valley exists in the valence band. This means, that the holes gather solely at $\mathbf{K}$ and $\mathbf{K}'$ with small hole occupancies in the $\mathbf{\Gamma}$-valleys for MoS_2 and WS_2. The $\mathbf{\Gamma}$-point is renormalized more strongly than the $\mathbf{K}$-point similar to the effects of tensile strain [39, 40], but as the energetical zero density separation between $\mathbf{K}$ and $\mathbf{\Gamma}$ is large compared to the distance between $\mathbf{K}$ and $\mathbf{\Sigma}$, this is not relevant for the $\mathbf{\Sigma}$-point renormalizations.

In experiments using angular-resolved photoemission spectroscopy (ARPES) [123, 178, 179] the high occupancies at $\mathbf{K}$ and $\mathbf{\Sigma}$ have been directly observed. Band gap and binding-energy shrinkage on the order of several 100 meV have also been reported in [33], where optical spectroscopy has been used.

To reveal this relative shift, the quantity $\Delta_{\mathbf{K}\mathbf{\Sigma}}(n) = \tilde{\varepsilon}^e_{\mathbf{K}}(n) - \tilde{\varepsilon}^e_{\mathbf{\Sigma}}(n)$ is used in the following, which is the density-dependent energetical difference between the $\mathbf{K}$-point and the

(meV)	$E_K^{G,\text{DFT+GW}}$	$\Delta^0_{K\Sigma}$		
		free	SiO_2	enc. hBN
MoS_2	2638	-14	-13	-13
$MoSe_2$	2355	82	83	84
WS_2	2775	-44	-43	-41
WSe_2	2359	49	50	51

Table 6.2.: Band gaps of freestanding MoS_2,$MoSe_2$, WS_2 and WSe_2 obtained from the Wannier interpolation together with the zero-density value of $\Delta_{\mathbf{K}\Sigma}$ on different substrates.

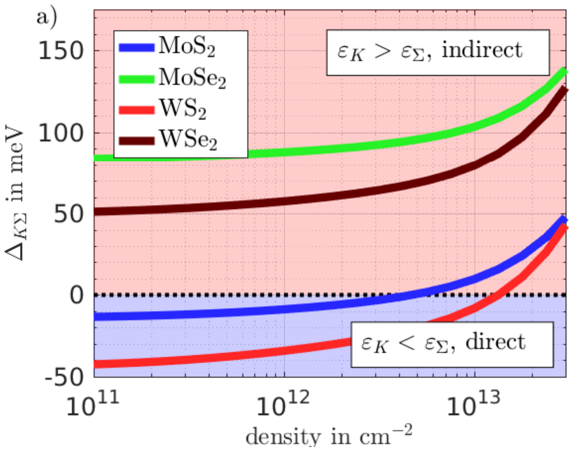

Figure 6.2.: Energy difference between the $\mathbf{K}$- and Σ-valley ($\Delta_{\mathbf{K}\Sigma}$) for photodoping with electrons and holes obtained in SXCH approximation plus electron-hole exchange. A clear trend of Σ shifting energetically below $\mathbf{K}$ (increasing $\Delta_{\mathbf{K}\Sigma}$) is visible for all four materials. Figure reprinted with permission from [156].

Σ-point both in the lowest conduction band. $\Delta_{\mathbf{K}\Sigma}(n)$ is plotted in Fig. (6.2) for a density ranging from 0cm^{-2} up to $3.2\times10^{13}\text{cm}^{-2}$. The zero-density value for $\Delta_{\mathbf{K}\Sigma}$ for different substrates can be found in Tab. (6.1). If the Σ-valley is energetically higher than the $\mathbf{K}$-valley, $\Delta_{\mathbf{K}\Sigma}$ is negative. This means, that the band gap is direct ($\mathbf{K}^e$-$\mathbf{K}^h$). While positive values of $\Delta_{\mathbf{K}\Sigma}$ represent an indirect band gap (Σ^e-$\mathbf{K}^h$), the tendency for all four investigated materials to become (more) indirect semiconductors is clearly visible. This will strongly influence optical properties as for example the photoluminescence yield or gain, which are both sensitive to the populations of electrons and holes at the direct band gap [39, 49]. The consequence is, that for high excitation scenarios, for example when dealing with strong laser pulses as used for photoluminescence or photoemission spectroscopy pumping resonantly with the band gap, the advantage of a semiconducting material vanishes as carriers are drawn to the lower lying Σ-valley, which is successively more renormalized as more carriers are present until the mechanisms saturate. In the next section the main terms in the

renormalizations, that lead to this transition will be analyzed in detail. First the choice of the Debye approximation for calculating the screening shall be validated.
To identify the influence of different approximations for the plasma screening $\varepsilon_{Pl}(|\mathbf{k}-\mathbf{k}'|)$, the Debye-approximation is compared to a more elaborate theory. First of all the Debye-approximation is the static limit of the RPA-screening. The full intraband Lindhard screening (RPA-screening) formula for excited carriers reads:

$$\varepsilon(\mathbf{q},\omega) = 1 - V_{\mathbf{q}}\frac{1}{\mathcal{A}}\sum_{\lambda,\mathbf{k}}\frac{f^{0,\lambda}_{\mathbf{k}-\mathbf{q}} - f^{0,\lambda}_{\mathbf{k}}}{\varepsilon^{0,\lambda}_{\mathbf{k}-\mathbf{q}} - \varepsilon^{0,\lambda}_{\mathbf{k}} + \hbar\omega + i\gamma}\,. \tag{6.4}$$

The Debye limit can be obtained by setting $\omega = 0$ and letting $\mathbf{q} \to 0$. In order to validate the SXCH approximation as derived for TMDs (4.3.4) a comparison to frequency-dependent GW-calculations performed by Alexander Steinhoff has been done. The GW-terms are calculated as presented in Sec. (4.3.3). It is numerically demanding to evaluate these energy shifts and therefore this calculation serves the purpose to validate the Debye-approximation in the chosen intervall of densities. In Fig. (6.3) the three different approximations are compared. One can clearly see, that the values of $\Delta(\mathbf{K\Sigma})$ do not differ much. Qualitatively the increase in magnitude is well aproximated, comparing Debye and Lindhard to the frequency-dependent GW. The zero-crossing marking the point at which the TMD has become indirect is at smaller densities for GW, while Lindhard and Debye screening show nearly the same value. Quantitatively all three curves are in good agreement. Hence, it has been shown, that the plasma screening calculated in Debye approximation is capable of depicting the correct behaviour of $\Delta(\mathbf{K\Sigma})$ both qualitatively and quantitatively.

6.2. Renormalization Mechanisms

Two mechanisms determine the renormalizations of the band structure. On the one hand the orbital character of the Coulomb matrix elements defines a $\mathbf{k}$-dependent strength of the shifts and on the other hand the different inter- and intraband contributions of the self-energy add different Coulomb interaction mechanisms, cf. Eq. (4.116).
Obtained from the Wannier interpolation (see Chap. (3.2.2) or Ref. [47, 90]) the Coulomb matrix elements obey the following formula:

$$V^{\lambda\lambda'\lambda\lambda'}_{\mathbf{k}_1\mathbf{k}_2\mathbf{k}_3\mathbf{k}_4} = \sum_{\alpha,\beta}\left(c^{\lambda}_{\alpha,\mathbf{k}_1}\right)^{*}\left(c^{\lambda'}_{\beta,\mathbf{k}_2}\right)^{*}c^{\lambda}_{\beta,\mathbf{k}_3}c^{\lambda'}_{\alpha,\mathbf{k}_4}V^{\alpha\beta\beta\alpha}_{|\mathbf{k}_1-\mathbf{k}_4|}\,. \tag{6.5}$$

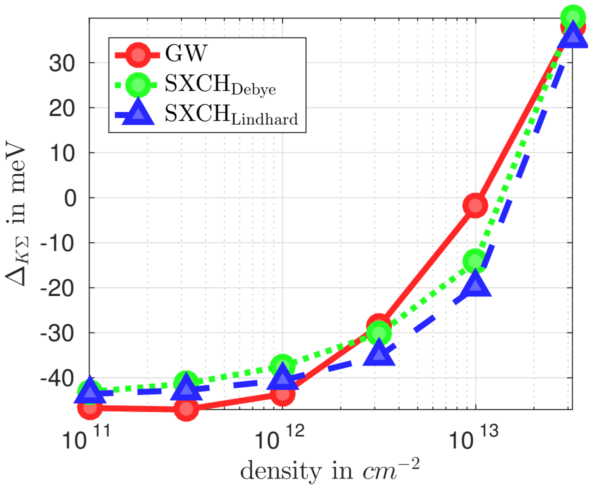

Figure 6.3.: $\Delta_{K\Sigma}$ in monolayer $\mathrm{WS_2}$ on $\mathrm{SiO_2}$ substrate on different levels of approximation for comparison. The plot shows GW-calculations (solid red line) including dynamical screening, static Debye-approximation (long-wavelength, dotted green line) and screening in Lindhard (RPA, dashed blue line). Figure reprintet with permission from [156].

The coefficients c_ν with $\nu = \{\mathbf{k}, \lambda, \alpha\}$ therefore represent the weighting of the Wannier functions identified with $\mathrm{d_{z^2}}$, $\mathrm{d_{xy}}$ and $\mathrm{d_{x^2-y^2}}$. Different orbital characters of the involved Bloch states $\left|\mathbf{k}, \nu\right\rangle$ in the $\mathbf{K}$- and $\mathbf{\Sigma}$-valleys as shown in Fig. (3.4) and (6.4) cause a valley sensitivity of the resulting energy renormalizations. In Fig. (6.4) the orbital 'fingerprint' of the interaction, defined by $C^{\lambda\lambda'\lambda\lambda'}_{\mathbf{k}_1\mathbf{k}'\mathbf{k}_1\mathbf{k}'} = \sum_{\alpha,\beta} \left(c^{\lambda}_{\alpha,\mathbf{k}_1}\right)^* \left(c^{\lambda'}_{\beta,\mathbf{k}'}\right)^* c^{\lambda}_{\beta,\mathbf{k}_1} c^{\lambda'}_{\alpha,\mathbf{k}'}$ for $\lambda, \lambda' = \{e, h\}$ is plotted. A bare Coulomb interaction $|\mathbf{k}_1 - \mathbf{k}'|^{-1}$ is plotted as guid to the eye for the point of interest $\mathbf{k}_1$. Analyzing Fig. (6.4) it can be seen, that for the intraband Coulomb interaction ($eeee$) the most weight of the renormalized Coulomb matrix elements in the conduction band originates directly from the vicinity of the respective $\mathbf{k}_1$-point. Hence, if $\mathbf{k}_1$ is close to the $\mathbf{\Sigma}$-valley the coefficients contributing most originate from the $\mathbf{\Sigma}$-valley. The same holds e.g. for $\mathbf{K}$. As there is the same orbital character present the product of the coefficients reaches its maximum value.

For the interband renormalizations ($eheh$) most contributions originate from regions rather far away from the point of interest ($\mathbf{k}_1$). This is a direct consequence of the orbital character in the valence and conduction band as can be seen from comparing Fig. (3.4) to Fig. (6.4). The coefficients at the same $\mathbf{k}_1$-point have opposite character for a transition from the conduction to the valence band, thereby reducing their product to vanishing values.

The second main mechanism to the renormalizations is the particular form of the self-energy terms in Eq. (4.116). First of all the Hartree terms are the $\mathbf{q} \to 0$ limit of the background screened Coulomb interaction V. For low densities these contributions are on the

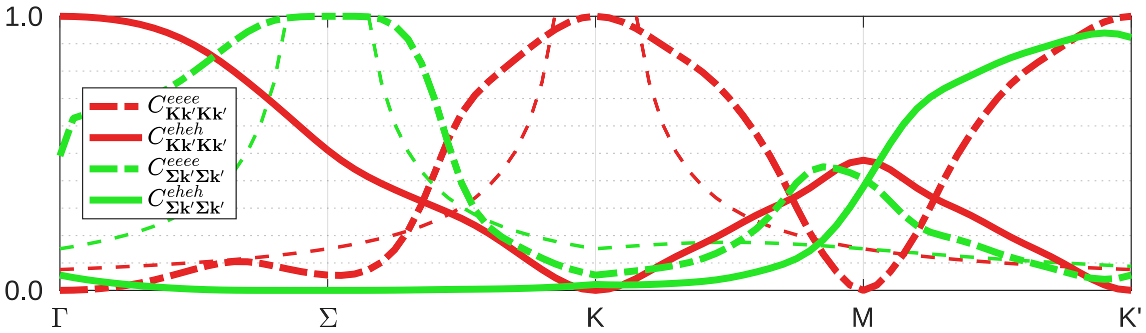

Figure 6.4.: Orbital 'fingerprint' $C^{\lambda\lambda'\lambda\lambda'}_{\mathbf{k}_1\mathbf{k}'\mathbf{k}_1\mathbf{k}'}$ of the Coulomb matrix elements for the K- and the Σ-point in the irreducible part of the BZ. Shown are intraband coefficients for the lowest conduction band ($eeee$) and interband coefficients ($eheh$). The colored dashed lines represent $|\mathrm{K}-\mathbf{k}'|^{-1}$ (red) and $|\mathbf{\Sigma}-\mathbf{k}'|^{-1}$ (green) respectively. The colors correspond to the respective $C^{\lambda\lambda'\lambda\lambda'}_{\mathbf{k}_1\mathbf{k}'\mathbf{k}_1\mathbf{k}'}$.

order of 1 meV and thus small. They rise about one order of magnitude per one order of magnitude increase in the density.

There are two possible ways to group the remaining terms $\Sigma^{\lambda,U}_{\mathbf{k}}$, $\Sigma^{\lambda,SX}_{\mathbf{k}}$ and $\Sigma^{\lambda,CH}_{\mathbf{k}}$. First they may be grouped by the involved band indices λ. Thereby the two categories *intraband* contributions (same λ for all four coefficients, for example $eeee$), which includes $\Sigma^{\lambda,SX}_{\mathbf{k}}$ and $\Sigma^{\lambda,CH}_{\mathbf{k}}$, and the *interband* contributions, consisting of $\Sigma^{\lambda,U}_{\mathbf{k}}$ (different λ, for example $eheh$) arise. The second way of grouping distinguishes between self-energy terms that contain an occupation function f or not. In this second case $\Sigma^{\lambda,U}_{\mathbf{k}}$ and $\Sigma^{\lambda,SX}_{\mathbf{k}}$ both contain $f^{\lambda}_{\mathbf{k}}$ forming a group, while the Coulomb hole shift $\Sigma^{\lambda,CH}_{\mathbf{k}}$ do not contain contributions from the carrier population. Either way of grouping is helpful in understanding the mechanisms behind the momentum-dependent shifts. Subsequently each term will be discussed seperately and put into context.

The SX- and CH-terms appear as intraband terms, where the electrons (holes) in the conduction band (valence band) induce plasma screening. Their exchange interaction nevertheless is of attractive nature and therefore the respective bands are lowered. Recalling the screened exchange term

$$\Sigma^{\lambda,\mathrm{SX}}_{\mathbf{k}} \;=\; -\frac{1}{\mathcal{A}}\sum_{\mathbf{k}'} W^{\lambda\lambda\lambda\lambda}_{\mathbf{kk}'\mathbf{kk}'} f^{\lambda}_{\mathbf{k}'} \,. \tag{6.6}$$

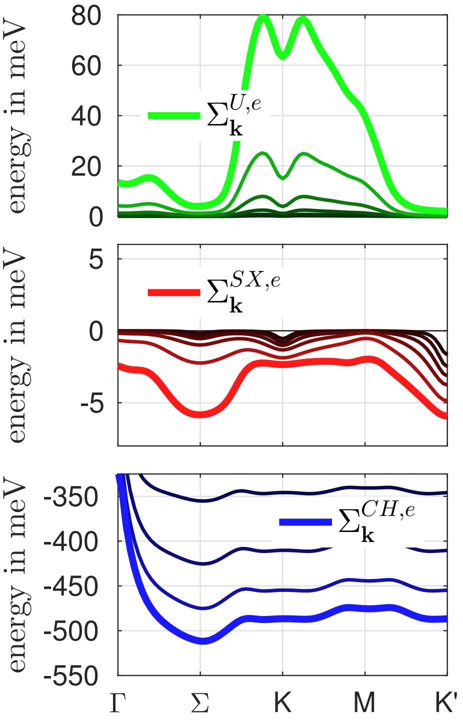

Figure 6.5: Renormalizations of the conduction band for WS$_2$ along the $\mathbf{\Gamma}$-$\mathbf{\Sigma}$-$\mathbf{K}$-$\mathbf{M}$-$\mathbf{K}'$ path. Bare electron-hole exchange, intraband screened exchange interaction and Coulomb-hole shifts are separately shown from top to bottom in dependence of the charge-carrier density. Shown are the densities $(1.0 \times 10^{11}, 3.2 \times 10^{11}, 1.0 \times 10^{12}, 3.2 \times 10^{12}, 1.0 \times 10^{13}, 3.2 \times 10^{13}$ cm$^{-2})$. $\Sigma_{\mathbf{k}}^{SX,e}$ shifts the $\mathbf{\Sigma}$-valley downwards more strongly than $\mathbf{K}$, while the unscreened electron-hole exchange $\Sigma_{\mathbf{k}}^{U,e}$ lifts $\mathbf{K}$ and its surroundings. Especially the $\Sigma_{\mathbf{k}}^{CH,e}$ term is large in numbers, note the different energy scales. Figure reprinted with permission from [156].

The calculation for increasing densities from 1.0 to 3.2×10^{13} cm^{-2} can be seen in the middle panel of Fig. (6.5). The strongest shifts occur in the vicinity of the Σ-point and the $\mathbf{K}'$-point. Although the overall shifts are small (~ -6 meV at the minimum), the relative shift between $\mathbf{K}$ and $\mathbf{\Sigma}$ is increased in favor of the $\mathbf{\Sigma}$-valley. When looking closely at Fig. (6.5) it can be seen, that this behaviour changes with increasing the density. For low densities up to 3.2×10^{12} cm^{-2} the $\mathbf{K}$-valley is shifted stronger than $\mathbf{\Sigma}$. This is due to the fact that for this range of densities the $\mathbf{K}$-valley is occupied more than $\mathbf{\Sigma}$, but for increasing densities the $\mathbf{\Sigma}$-valley drains more and more carriers (see next paragraph), thereby increasing the shift in the vicinity of $\mathbf{\Sigma}$. The Coulomb-hole self-energy is also an attractive intraband term and thus lowering the bands. This can be seen in Fig. (6.5) in the lowest panel. It contains the difference between the plasma screened (W)and the intrinsically screened (V) exchange interaction

$$\Sigma_{\mathbf{k}}^{\lambda,\mathrm{CH}} = +\frac{1}{2\mathcal{A}} \sum_{\mathbf{k}'} \left(W_{\mathbf{k}\mathbf{k}'\mathbf{k}\mathbf{k}'}^{\lambda\lambda\lambda\lambda} - V_{\mathbf{k}\mathbf{k}'\mathbf{k}\mathbf{k}'}^{\lambda\lambda\lambda\lambda} \right) . \tag{6.7}$$

The dependence on the density is only indirectly included in the plasma screening of the W-term. As this screening gets stronger with increasing density the difference to the unscreened exchange interaction becomes larger and thus the hole self-energy term. In fact, the $\mathbf{k}$-dependence stays constant throughout the increasing charge carrier densities. Even for small densities this term is much larger in numbers due to the fact that first no occupation function is multiplied with the Coulomb interactions and secondly the unscreened V is larger than W. Again the $\boldsymbol{\Sigma}$-valley is shifted more than the $\mathbf{K}$-valley. This holds for all densities and leads to the above mentioned increased drain of carriers with increasing charge carrier densities. This is the main source of the change of renormalization strength in the screened exchange term, giving rise to larger shifts at the $\boldsymbol{\Sigma}$-valley for elevated densities.

The third and remaining term to discuss is the unscreened interband exchange interaction $\Sigma_{\mathbf{k}}^{\lambda,U}$, which reads

$$\Sigma_{\mathbf{k}}^{\lambda,\mathrm{U}} = -\frac{1}{\mathcal{A}}\sum_{\mathbf{k}'} U_{\mathbf{k}\mathbf{k}'\mathbf{k}\mathbf{k}'}^{\lambda\lambda'\lambda\lambda'} f_{\mathbf{k}}^{\lambda'} \,. \tag{6.8}$$

This term represents the bare electron hole exchange interaction, it comes with the opposite sign compared with the renormalizations discussed before. Due to its repulsive nature, it rises the bands. This is shown in Fig. (6.5) in the top panel. As it is unscreened, it is an order of magnitude larger in numbers than the screened exchange interaction, but still an order of magnitude smaller than the Coulomb hole shifts. It is important to notice that the renormalization due to this term come with the occupation of the respective other charge carrier type. In the renormalization of the conduction band the hole population masks the Coulomb matrix elements. For the renormalization of the valence band the opposite is the case. This will be important when considering doping scenarios in the following sections. As can be concluded from Fig. (6.5), $\Sigma_{\mathbf{k}}^{\lambda,U}$ shifts the $\mathbf{K}$-valley upwards and also narrows the $\mathbf{K}$-valley due to the increased shifts near $\mathbf{K}$, thereby changing its effective mass. Not much shift is observed in the vicinity of the $\boldsymbol{\Sigma}$-valley, hence $\Sigma_{\mathbf{k}}^{\lambda,U}$ is the main source of the large relative shift between $\mathbf{K}$ and $\boldsymbol{\Sigma}$. To conclude this paragraph, all intra- (SX, CH) and interband (U) self-energy terms and their implications on the band structure are sketched in Fig.(6.6). In general $\Sigma_{\mathbf{k}}^{\mathrm{SX}}$ and $\Sigma_{\mathbf{k}}^{\mathrm{CH}}$ lower the bands, while $\Sigma_{\mathbf{k}}^{\mathrm{U}}$ rises them. The Coulomb hole term provides a nearly constant shift throughout the densities, that shifts $\boldsymbol{\Sigma}$ more than $\mathbf{K}$. The SX term - depending on the plasma screening and the carrier population - prefers $\mathbf{K}$ over $\boldsymbol{\Sigma}$ for low densities and the opposite for high densities. Though small compared to the CH shift, this term supports the relative shift between $\mathbf{K}$ and $\boldsymbol{\Sigma}$. The unscreened interband exchange mainly shifts $\mathbf{K}$ upwards, but does not contribute much in the vicinity of the $\boldsymbol{\Sigma}$-valley, thereby primarily enhancing the relative shift between $\mathbf{K}$ and $\boldsymbol{\Sigma}$. All these effects combined yield a rise in $\Delta_{\mathbf{K}\boldsymbol{\Sigma}}$ for the investigated TMD monolayers. The $\boldsymbol{\Sigma}$-valley is

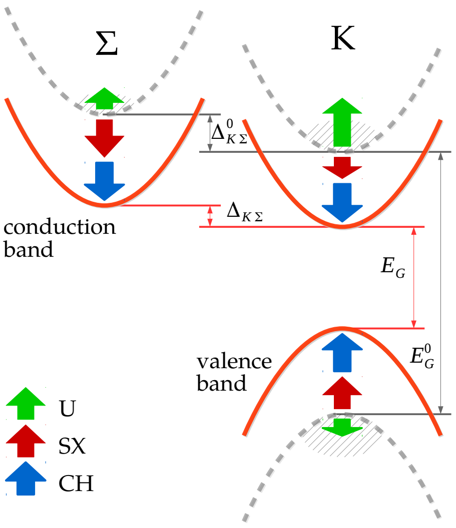

Figure 6.6: Schematic illustrating the renormalization mechanisms of excited carriers (shaded areas): Shown are the band-structure renormalization at $\mathbf{K}$ and Σ due to intraband screened exchange (SX, red), Coulomb hole (CH, blue) and interband electron-hole exchange (U, green) shifts, where the length of the arrows corresponds to the strength of the respective term at the chosen $\mathbf{k}$-point. Figure reprinted with permission from [156].

shifted more downwards than the $\mathbf{K}$-valley, which results in a transition from a direct to an indirect band gap for the intrinsic direct TMDs.

The total amount of the shift for renormalization terms containing an occupation function is lower due to the fact, that these occupation functions mask the Coulomb matrix elements. Therefore, it is important to mention the different number of the valleys in the band structure, cf. Chap.(3.4). In the conduction band there are two valleys $\mathbf{K}/\mathbf{K}'$ and Σ/Σ', while there is only one valley in the valence band at $\mathbf{K}/\mathbf{K}'$. Hence, only the values at occupied $\mathbf{k}$-states contribute to the shift.

Considering doped TMD monolayers, the aforementioned difference in the occupation is important, as either the electron or the hole population will directly affect the respective self-energy term by increasing or decreasing it. The renormalizations have also been calculated for the two cases where there are either only electrons or only holes in the system, in order to distinguish between the underlying effects. For the two different doping scenarions $\Delta_{\mathbf{K}\Sigma}(n_{e/h})$ has been calculated and plotted in Fig. (6.7). For the sake of clarity only the results of MoS_2 und WS_2 are shown. In Fig. (6.7) both species of charge carriers are present, which is shown for comparison. The curves originating from photodoping are the same as already shown in Fig. (6.2). It can be seen, that the strong shift of Σ compared to $\mathbf{K}$ still holds for both doping-scenarios, while the effect is more pronounced for hole-doping (p-doping). This is due to the fact, that the hole occupation enables the interband self-energy $\Sigma^{e,\mathrm{U}}_{\mathbf{k}}$ (cf. Eq. (4.116)) to shift $\mathbf{K}$ upwards, while the screened exchange interaction $\Sigma^{e,\mathrm{SX}}_{\mathbf{k}}$ is zero, as there are no electrons ($f^e_{\mathbf{k}} = 0$) in the system. This leads to a large positive shift at $\mathbf{K}$ in the conduction band due to the interband electron hole exchange. In electron-doped (n-doped) materials, the exchange interaction always shifts the band structure to lower en-

Figure 6.7: $\Delta_{\mathbf{K}\mathbf{\Sigma}}(n_{e/h})$ for the comparison of photodoping (solid lines) with hole doping (p-doping, dashed lines) and electron doping (n-doping, dotted lines). The main part of the renormalization for photodoped systems originates from the holes within the $\mathbf{K}^h$-valley, as the dashed curve indicates. Figure reprinted with permission from [156].

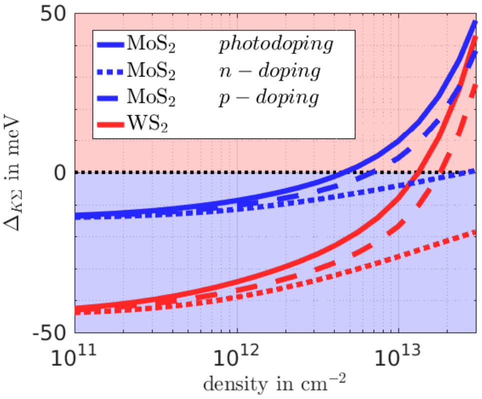

ergies as there is no additional positive shift at $\mathbf{K}$ due to the missing holes in the valence band, which disable the $\Sigma^{e,\mathrm{U}}_{\mathbf{k}}$ term. Therefore, the overall direct-to-indirect effect is weaker than in the photodoped materials.

The lowering of the $\mathbf{\Sigma}$-valley may also contribute to superconductivity in TMDs. Superconductivity is driven by phonons, which enable a quasi-particle of two electrons (Cooper-pair), that has bosonic character. This has so far been analyzed for TMDs by DFT calculations [160, 180], where in the sense of a Lifshitz transition superconductivity is enabled. A Lifshitz transition is described as the formation of a new 'pocket' in the Fermi surface of a material [160, 181]. As soon as both, the $\mathbf{K}$- and $\mathbf{\Sigma}$-valley, become populated with electrons [180], the $\mathbf{\Sigma}$-valley as well as the $\mathbf{K}$-valley cross the Fermi level forming such pockets. As this will occur at higher densities for $\mathbf{\Sigma}$, shorter momenta for the Cooper-pairs to form will be allowed at a certain density and hence the probability for superconductivity to set in is increased. The relative valley shift thereby determines the onset of superconductivity in electron-doped TMDs. A comparison of the results obtained in this work to DFT calculations in LDA and GGA done by Gunnar Schönhoff for the case of n-doped TMDs is shown in Fig. (6.8). It can be seen that the SXCH plus electron-hole exchange approximation predicts stronger relative valley shifts at low densities, while the DFT calculations predict stronger shifts at densities above 5×10^{13} cm^{-2}. The main reason for this is the screening due to excited carriers, which is treated differently in DFT. The main part of the shift in the calculations presented here originates from hole occupations as explained above. The results also suggest, that a Lifshitz transition in an initially n-doped TMD monolayer could be enforced by slightly photodoping the system, exploiting the advantages of the strong electron-hole exchange.

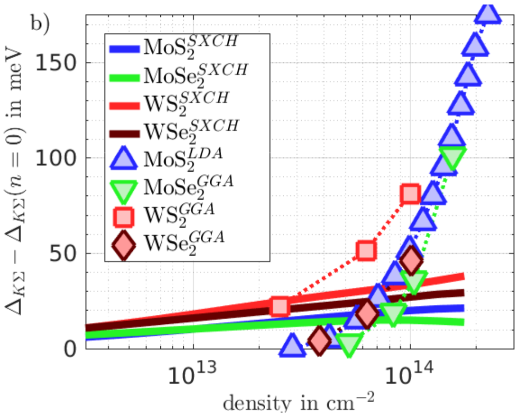

Figure 6.8: $\Delta_{\mathbf{K}\mathbf{\Sigma}}(n)$ relative to $\Delta_{\mathbf{K}\mathbf{\Sigma}}(0)$ for electron-doping in SXCH approximation (solid lines), compared to the results obtained from DFT calculations (dashed lines with symbols) using different approximations (LDA/GGA) for the exchange-correlation functionals. Figure reprinted with permission from [156].

6.3. Density-Dependent Absorption Spectra

Optical properties of atomically thin TMDs are of great interest especially for optical device application. The presented theory allows us to investigate the effects of many-particle renormalizations on the optical spectra. Not only the band structure is renormalized by many-body Coulomb effects in the formalism of the SBE, but also the light-matter interaction, as has been shown in Sec. (4.2.3). This is described in Eq. (6.1) via the coupling of the interband transition amplitudes $\psi_{\mathbf{k}}^{he}$ for different carrier momenta $\mathbf{k}$ mediated by the screened Coulomb interaction $W_{\mathbf{k}\mathbf{k}'\mathbf{k}\mathbf{k}'}^{ehhe}$ within the generalized Rabi energy $\Omega_{\mathbf{k}}^{he}$. This screened Coulomb interaction gives rise to excitonic resonances in the optical response and is directly influenced by excited carriers in the system. The optical response of the system is accessible via the macroscopic polarization. To obtain the linear optical susceptibility the polarization $P(t)$ and the weak optical probe field $E(t)$ are Fourier transformed, which results, as shown in Sec. (4.6.2), in:

$$\chi(\omega) = \frac{P(\omega)}{E(\omega)}. \tag{6.9}$$

From the imaginary part of Eq. (6.9) the absorption coefficient can be calculated subsequently. The four investigated materials show absorption spectra as shown in Fig. (6.9a) to (6.9d). The A- and B-exciton lines are the dominant low-energy peaks. They are separated by spin-orbit coupling constant as they stem from the direct optical transitions at $\mathbf{K}$ and $\mathbf{K}'$. In general the excitons show a redshift with increasing carrier density. This is the result of two competing effects: First the band structure is renormalized due to many-body renormalizations as derived in Sec. (4.3.4) and discussed in Sec. (6.2). This results in a shrinkage of the band gap (marked by vertical lines in the plots in Fig. (6.9)). On the other hand the exciton binding energy decreases due to plasma screening of the Coulomb inter-

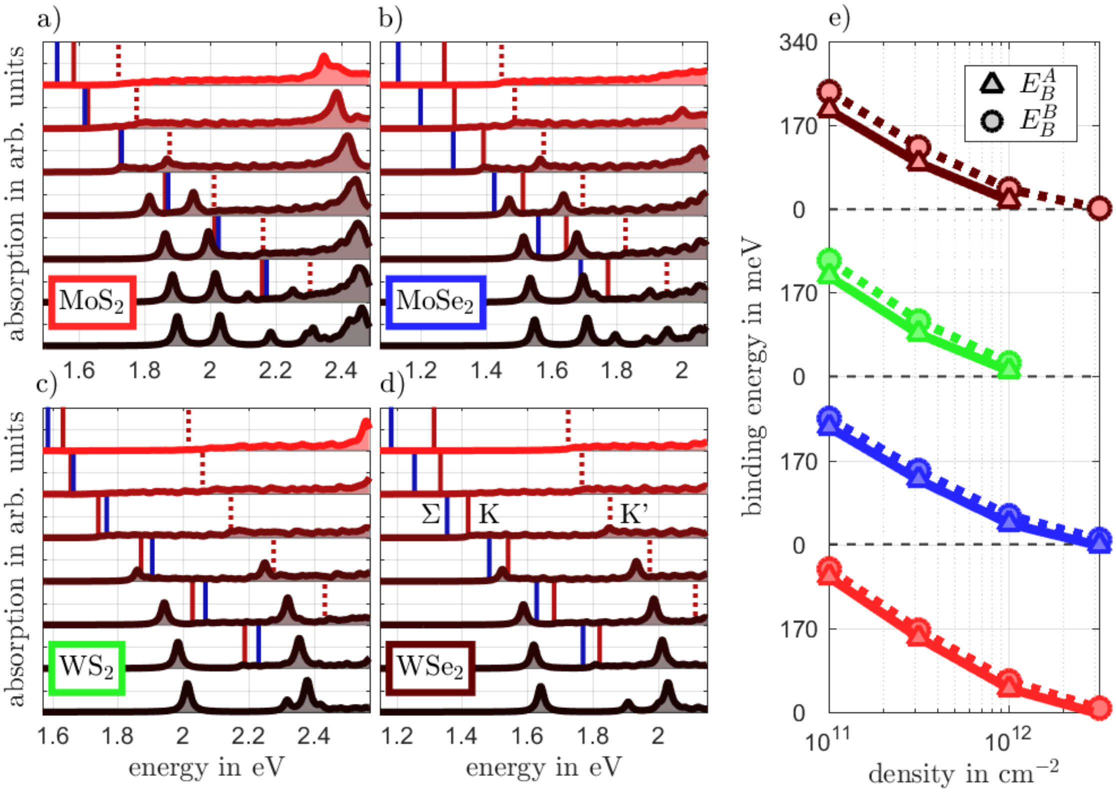

Figure 6.9.: a) - d): Absorption spectra for MoS$_2$, MoSe$_2$, WS$_2$ and WSe$_2$ versus increasing electron-hole density from bottom to top (ground state, $1.0 \times 10^{11}, 3.2 \times 10^{11}, 1.0 \times 10^{12}, 3.2 \times 10^{12}, 1.0 \times 10^{13}, 3.2 \times 10^{13}$ cm^{-2}). The spectra are shifted such that the exciton peak positions at zero density agree with experiment due to the fact that the band gap is over-estimated by G$_0$W$_0$. The vertical lines indicate the quasi-particle band gaps at ($\tilde{\varepsilon}^h_K \to \tilde{\varepsilon}^e_K$, direct gap, solid red), Σ ($\tilde{\varepsilon}^h_K \to \tilde{\varepsilon}^e_\Sigma$, indirect gap, solid blue) and K' ($\tilde{\varepsilon}^h_{K'} \to \tilde{\varepsilon}^e_{K'}$, direct gap, dashed red) taken from the renormalized band structures, see Fig. (6.1). For MoS$_2$ and WS$_2$ there is a transition to an indirect band gap visible. The binding energies of the A and B excitons are also dependending on the density are shown in panel e). The vanishing of excitons is marked by the zero-crossing of the binding energies ($E_B^X < 0$) indicating the excitonic Mott transition. Figure reprinted with permission from [156].

action (see Sec.4.4.1) and the Pauli blocking in the presence of excited carriers, cf. Eq.(6.1). This is shown in panel Fig. (6.9e). The binding energy can be obtained by substracting the optical band gap (exciton position in the spectrum) from the band gap of the material. The calculated binding energies are listed in Tab. (6.3). The exciton binding energies are in the range of 0.5 to 0.6 eV, which is in good agreement with literature [35, 47, 164, 182].

For experimental scenarios it is more realistic to investigate TMD monolayers on a substrate, that therefore induces dielectric screening. The many-body renormalizations follow

	MoS_2(/SiO_2)	$MoSe_2$(/SiO_2)	WS_2(/SiO_2)	WSe_2(/SiO_2)
E_B^A (meV)	588(301)	527(288)	557(268)	508(253)
E_B^B (meV)	601(312)	543(301)	593(295)	547(283)

Table 6.3.: Results for exicton binding energies of the 1s-state for all four investigated materials with and without SiO_2 substrate.

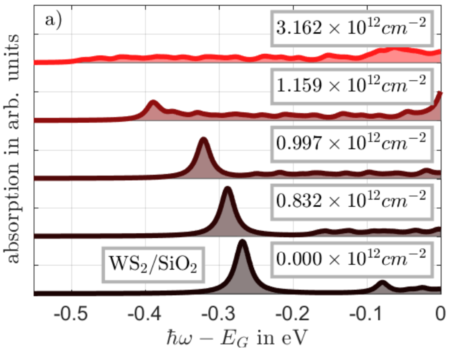

Figure 6.10: Absorption spectra of WS_2 on an SiO_2 substrate at $T = 300$ K. In principle the spectrum shows the same features as for the freestanding case explained in the text. The density labels mark the total density for bound excitons and unbound eletrons and holes. Figure reprinted with permission from [156].

the mechanisms as described in the section before and the excitonic behaviour in the presence of substrates do not differ much from the case of freestanding TMD monolayers. In contradiction to the freestanding case, on a substrate the influence of the Coulomb-hole term is weakened most, as it involves the Coulomb matrix elements V and W, that are both reduced by environmental screening, as described in Chap. (4.4.4). For example in WS_2 the band-gap shift is reduced to 570 meV compared to 940 meV for the freestanding case and highest calculated density. Nevertheless the difference in energy shift between $\mathbf{K}$ and Σ is almost not affected by environmental screening. This is due to the fact that most of this relative shift originates from $\Sigma_{\mathbf{k}}^{\mathrm{U},e}$, which is not screened by excited carriers and the environment. In conclusion, environmental screening slows down the direct-to-indirect transition process slightly due to the influence on the Coulomb hole term.

The effect of the binding-energy reduction due to environmental screening is summarized in Tab. (6.3). Again as an example for WS_2 a binding energy of 557 meV is obtained in the freestanding case while for WS_2 on SiO_2 a reduction to 268 meV is found. This is nearly 50% reduction occurs due to the additional screening of the Coulomb interaction $W_{\mathbf{k}\mathbf{k}'\mathbf{k}\mathbf{k}'}^{ehhe}$ by the substrate. This effect has been discussed in literature for TMD monolayers in their ground state [35, 105, 174, 183–185]. While there is a large binding energy for 2d excitons in the ground state the Coulomb interaction between both particles is weakened due to the plasma screening from additional excited carriers. This not only results in a decrease of the binding energy but also leads to the dissociation of the bound states for a specific density. This transition to only ionized states is called Mott transition, which happens at the Mott density. The Mott density can be determined from the zero-crossing of the exciton binding energy shown in Fig. (6.9e). The presented results yield Mott densities around 3×10^{12} cm^{-2} for MoX$_2$ and 1×10^{12} cm^{-2} for WX$_2$. In Ref. [36] a slightly lower Mott density has been found. Therefore it is concluded, that the band-gap shrinkage obtained from a static calculation should be seen as an upper bound in comparison with frequency-dependent screening calculations.

In general, excited carriers can be present in the form of an unbound (quasi-free) electron-hole plasma or the form of bound excitons [36, 186]. Above the Mott transition excitons have dissociated while below the Mott transition both forms can exist simultaneously. When excitons are present in principle renormalization effects due to their interaction should be included, but as the contribution of bound excitons to renormalizations and screening is typically much smaller than contributions from unbound electrons and holes these are neglected in the calculations. In this sense carrier densities are interpreted as ionized fraction of a total electron-hole pair density that includes both phases. According to the results present in Ref. [36] this effect is illustrated using the example of monolayer WS$_2$ on a SiO$_2$ substrate. The results considering the fraction of the density of free carriers to the total density of charge carriers from Ref. [36] have been fitted in order to rescale the densities of the excited carriers used for calculating the spectra in Fig. (6.10). The rescaled densities are shown in the labels of Fig. (6.10) and separately in Fig. (6.11).

The excitons shown in Fig. (6.10) exhibit only a weak line shift up to charge carrier densities of 1×10^{12} cm^{-2}, since most carriers are bound as excitons at intermediate densities. These bound carriers contribute negligible many-body renormalizations, thus over a large range of densities the exciton peak remains constant. Strong redshifts appear between 1×10^{12} cm^{-2} and 3×10^{12} cm^{-2} before excitons dissociate at the Mott density. This behavior is in good agreement with experiments [34], except for the regime of high excitation, where a blueshift of the exciton resonance due to exciton-exciton interaction is observed. Exciton-exciton interaction is neglected in the theory presented in this work. In principle these are accessible from two-particle Green's functions.

Fig. (6.11) provides the relative oscillator strength of the A-exciton peak plotted according to the fraction of excitons and ionized carriers. Rescaling the density to the total density including both excitons and quasi-free carriers, the red curve in Fig. (6.11) is in support of the conclusions from the paragraph before. For densities up to 1×10^{12} cm^{-2} the oscillator strength remains constant and drops significantly above the Mott density.

In order to extract the oscillator strength from the calculations, the peaks of the A exciton are compared to an oscillator model, where each transition contributes a Lorentzian-shaped peak to the absorption spectrum. The oscillator strength f_i of a specific peak is de-

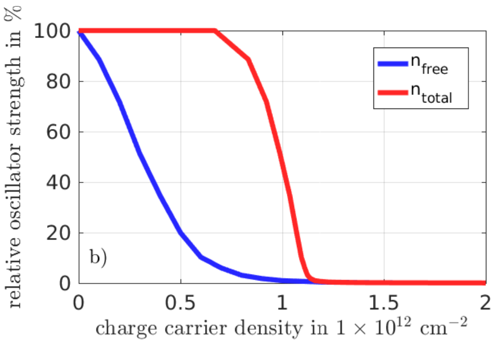

Figure 6.11: Relative oscillator strength for the A-exciton in WS_2 on SiO_2 as a function of the total density (red) and the free carrier density (blue). The total density includes both excitons and unbound carriers, while the blue curve neglects the exciton contribution to the density. Figure reprinted with permission from [156].

fined as the integral over the corresponding Lorentzian. Using the known broadening of $\gamma = 10$ meV in combination with the height of the peak I_0 obtained from the calculated absorption spectrum one finds

$$f_i = \int_{-\infty}^{+\infty} \mathrm{d}\omega \frac{\gamma^2 I_0}{(\hbar\omega - \varepsilon_i)^2 + \gamma^2} = \pi I_0 \,, \tag{6.10}$$

which reduces the comparison of the oscillator strength to the comparison of the peak heights, cf. Fig. (6.11).

6.4. Implications on TMD nanolasers

The implications of an indirect band gap, especially with excited carriers being involved, become clear when investigating TMDs as an active material of a laser device. Different types of TMD lasers have been presented in literature [26–29] so far. The question arises, whether TMDs proof to be efficient gain materials.

A laser emits coherent light from stimulated emission of photons, if the active material is excited so strongly, that optical gain is achieved. The main condition for optical gain is a population inversion [49] at the direct optical transition. The population inversion is described by $(1 - F^e_{\mathbf{k}} - F^h_{\mathbf{k}})$, which also corresponds to the Pauli blocking factor. Population inversion is indicated by negative values of $(1 - F^e_{\mathbf{k}} - F^h_{\mathbf{k}})$, which leads to negative absorption in the spectra. Considering the distribution of excited charge carriers in the conduction band of a TMD monolayer it is obvious that for elevated charge carrier densities the electrons fill both the $\mathbf{K}$- and the Σ-valley. Thus it becomes difficult to reach a population inversion when increasing the density. Due to the growing indirectness with increasing carrier density even more carriers of the $\mathbf{K}$-valley are drained to the Σ-valley. Thereby the direct optical transition at $\mathbf{K}$ loses more and more charge carriers and the inversion starts to decrease.

Therefore a charateristic roll-over behaviour of the peak gain is predicted for MoS_2, $MoSe_2$, WS_2, and WSe_2 [30]. This roll-over has been found in model studies done bei Frederik Lohof, that uses input generated from calculations the author of this thesis. These calculations also show a characteristic roll-over. For $MoTe_2$ gain calculations have been reported [187]. As presented in [30] this roll-over is also found in gain spectra calculations that additionally include the line broadening in consistency with the full-frequency dependent GW-self-energy.

The charateristic gain roll-over originates directly from the band structure renormalizations that cause a direct-to-indirect transition of the band gap. The excitation regime at which coherent emission is possible is thereby limited.

6.5. Conclusion

The SBE have been used to analyze single- and two-particle properties of MoS_2, $MoSe_2$, WS_2 and WSe_2 upon optical excitation of charge carriers as well as under doping of either carrier species. The optical response has been probed by a weak and short laser pulse, assuming an excitation of carriers beforehand, that have relaxed into a Fermi distribution. The interplay of many-particle renormalizations in the presence of excited carriers has been analyzed in detail. The renormalizations of the band gap and the plasma screening induced reduction of the exciton binding energy leads to a redshift of the exciton resonances on the order of 100 meV. Bleaching is observed due to phase space filling. In the presence of substrates and environmental screening effects, that have been employed using the WFCE scheme, these effects remain strong.

The magnitude of the density-dependent many-body band structure renormalizations originated from the orbital character of the involved Bloch states from the DFT+GW ground state calculation and the electron and hole populations in the different band-structure valleys. A tendency for a transition from a direct to an indirect band gap of all considered monolayer TMDs has been found. The bare electron-hole exchange interaction causes a relative shift between the neighbouring $\mathbf{K}$- and Σ-valley. This relative shift implies a loss of charge carriers from the bK- to the Σ-valley, which is more pronounced for the molybdenum-based compounds, where the energetically lowest interband transition at $\mathbf{K}$ is optically bright due to the spin-orbit interaction. The advantage of a two-dimensional direct gap semiconductor thus slowly disappears for elevated densities. It is important to take the Σ-

valley into account explicitly when describing the influence of excited carriers. The loss of carrier from the $\mathbf{K}$- to the $\mathbf{\Sigma}$-valley is expected to cause a quenching of the PL intensity for high excitations [39] and to hamper population inversion at the $\mathbf{K}$ point, which is crucial for TMD laser applications [30].

Due to the dependence of the renormalization on the carrier population, electron- or hole-doping affects the renormalizations of the valence and conduction bands differently. For hole-doping (p) the direct-to-indirect transition is strong as holes gather only in the valence band $\mathbf{K}$-valley. Thus they enforce a blueshift of the conduction band states at $\mathbf{K}$ via the bare electron-hole exchange. Only the conduction band $\mathbf{K}$-valley is renormalized, as there is no Σ-valley for holes enabling corresponding redshifts. Hole-doping also causes an enhancement of the vspin-orbit splitting at the valence band $\mathbf{K}$-point by tens of meV, which stems from different renormalizations of the upper and lower valence band. The relative valley shift between $\mathbf{K}$ and Σ is weak in the electron-doping regime due to the lack of a hole population. These conduction band renormalization strongly affect the carrier densities, at which a Lifshitz transition, that would enable phonon-driven superconductivity, is expected. A comparison of DFT calculations to the resulting shifts obtained here revealed that the relative valley shifts in DFT are overestimated at high densities for electron-doping. The opposite holds at low densities. Thus, to be able to predict critical charge carrier densities for phonon-driven superconductivity within TMD monolayers, the electron-hole exchange and plasma screening of electron-electron exchange have to be taken into account explicitly. These results suggest that in electron-doped monolayers a photodoping could induce a Lifshitz transition via electron-hole exchange. This might provide a possibility to induce superconductivity in two-dimensional materials.

7. Pump-Induced Charge Carrier Densities

After adressing the optical response and the renormalization of single-particle properties in detail in Chap. (3), (5), and (6) respectively, the following chapter is devoted to the dynamical accumulation of population during optical excitation. Upon optical excitation the charge carriers occupy the complex valley structure in TMD monolayers forming a variety of Coulomb-bound many-particle complexes. To obtain a fundamental understanding of the underlying physics and to explore the prospects of TMD monolayers being used in future optoelectronic devices, experimental techniques such as photoluminescence are used. [39, 48, 49, 61, 62] These experiments involve the photoexcitation of electron-hole pairs with energies equal to or larger than the quasi-particle band gap and the subsequent measurement of e.g. reflectivity. For the interpretation of such experiments comparison with microscopic theories is required, which in turn necessitate the knowledge of the current density. This quantity is not directly accessible in experiment. The simplest approach to access the density is an estimation from the absorption coefficent [34, 64, 188, 189] which yields a reasonable yet linear approximation for low pump intensities. However, the many-body effects explained in the chapters before are expected to change the absorption coefficient in a nonlinear way. The question on the microscopical mechanisms shaping the power-dependence of the density remains to be answered in this chapter.

The SBE are used for a numerical analysis of the total density of photoexcited charge carriers in dependence of the pump fluence. Hence, the changes of the carrier population $f_{\mathbf{k}}^{e/h}(t)$ have to be calculated, while these have been given in the previous chapter. In contrast to the calcuations of absorption spectra the electric field $\mathbf{E}(t)$ takes the role of a pump laser, whose intensity is linearly increased. Different spectral positions of the pump laser are expected to yield different behaviour of the density considering the complex peak structure of the absorption spectra in Chap. (6). When pumping at the band gap, instant Pauli blocking due to excited electrons and holes should be a limiting factor for accumulating carriers. For a pump above the gap Pauli blocking is expected to be insignificant compared to the clearing of the states by scattering processes. The spectral detuning of the laser to the band gap can be found in Tab. (7).

Many-body effects originating from the interaction of excited carriers as well as from envi-

$\hbar\omega_{det}$ in (meV)	hBN enc.	405nm	533nm
MoS_2	-389	423	-312
$MoSe_2$	-351	706	- 29
WS_2	-418	285	-449
WSe_2	-379	702	- 34

Table 7.2.: Detuning used to pump at the band edge for encapsulated monolayers and with a laser wavelength of 405nm and 533nm, respectively.

ronmental influences due to dielectric screening are included the same way as described in Chap. (4) and (6). The carrier density is calculated in detail for fluences of up to 100μJ cm^{-2}, as these are typical experimental values. Larger fluences provide insight in the saturating behaviour. The results of this chapter are in preparation for publication. All numerical calculations have been performed by the author of this thesis while the results have been interpreted in close collaboration with Alexander Steinhoff, Michael Lorke, and Frank Jahnke. To start with the chapter the microscopical picture of an excitation of charge carriers will be presented first.

7.1. Microscopical Picture of Charge Carrier Excitation in TMD Monolayers

In the following a situation is considered, in which a TMD monolayer is successively illuminated by two laser pulses, a pump pulse and a probe pulse. The pump pulse excites charge carriers from the valence band to the conduction band which subsequently equilibrate and occupy the valleys of the band structure. [12, 127, 179, 190]. Optical properties are probed by a second weak and short laser pulse. By variation of the intensity of the pump laser a series of power-dependent spectra is measured. To be able to interpret these spectra a direct comparison to theoretical models of the respective experiment is desired. This requires the knowledge of the total density of excited charge carriers.

For a constant absorbance, the fluence, the pulse duration and the laser repetition rate determine the number of absorbed photons which hereby cause a defined number of electron-hole pairs. Considering this simple approach the only mechanism limiting the achievable carrier density is the recombination of electron-hole pairs. In order to exclude recombination from the analysis, the pulse duration is chosen to be 150 fs. This value corresponds to typical experimental setups, but is short compared to the time scale of recombination reported for example in [191, 192]. The assumption of all photoexcited electrons and holes

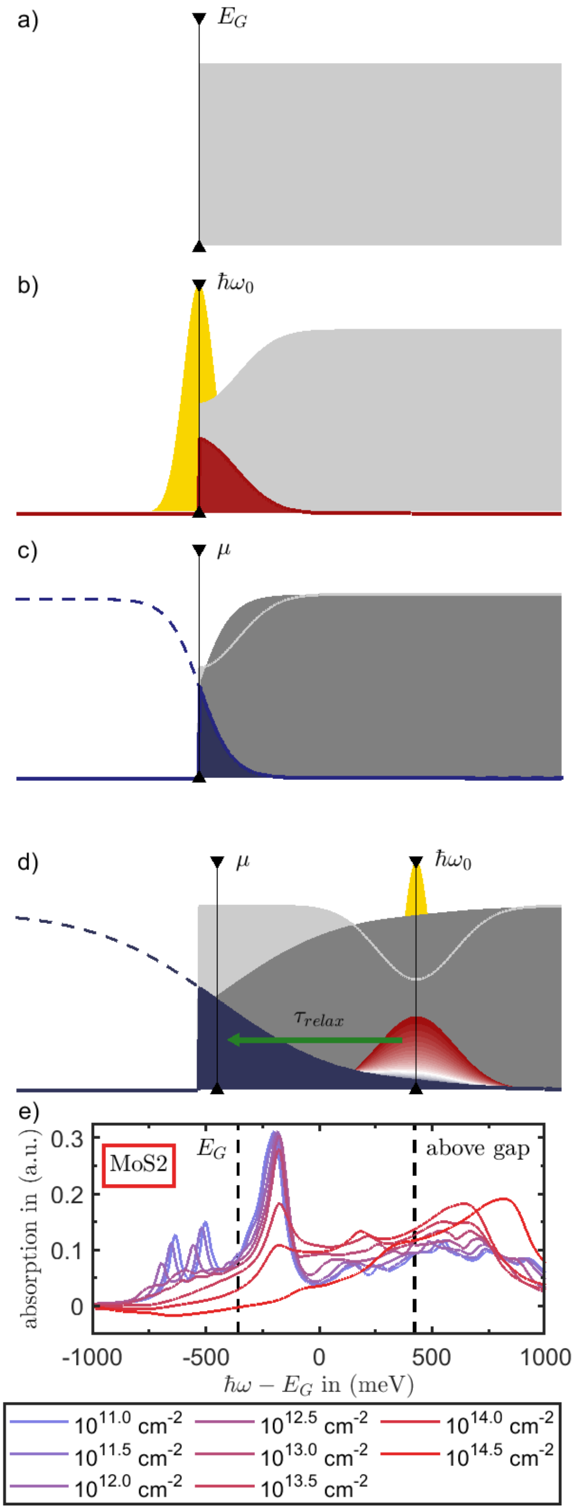

Figure 7.1: **a)** Initial amount of available states (grey) in a simple 2d picture. The band edge is marked by a vertical line. **b)** The laser pulse (yellow) induces a hot carrier distribution (red) at the band edge ($\hbar\omega_0 = E_G$). The present carriers instantly limit the available states (grey). **c)** The carriers relax into a Fermi distribution (blue), the amount of filled states does not change much. The system is instantly in the Pauli blocking regime, when pumping at the band edge.n **d)** If the laser is tuned above the band gap scattering processes (green arrow) empty the states and make them available for refilling. Hence in total a higher density compared to **c)** can be reached when pumping above the band gap. **e)** Calculated optical absorption spectra for monolayer MoS_2 with excitation densities of $1 \times 10^{11}\mathrm{cm}^{-2}$, $1 \times 10^{11.5}\mathrm{cm}^{-2}$, $\ldots$ $1 \times 10^{14.5}\mathrm{cm}^{-2}$ as labeled. The spectra are not shifted in height in order to be able to identify the change in absorption with increasing density. The absorption provides insight into the two-particle density-of-states combined with optical selection rules due to the dipole matrix elements. In contrast to the simplified picture of **a)** to **d)** the peak structure indicates the different and complex behaviour at different pump positions. The peaks are phenomenologically broadenend by the dephasing mechanisms explained in Sec. (7.4).

being in a quasi-equilibrium state right before the recombination sets in is therefore valid. Vice versa all sublinear behaviour of the density has to originate from many-body effects.

In order to elucidate the sequence of microscopic processes occuring during the sample illumination a schematic description is given in Fig. (7.1). For this purpose a simple 2d picture is used, see Fig. (7.1a). The pump laser excites a hot carrier distribution corresponding to its spectral position relative to the quasi-particle band gap Fig. (7.1b). By virtue of carrier-carrier and carrier-phonon interaction, the excited carriers scatter into unoccupied lower lying states and cool down to the lattice temperature forming a Fermi distribution. If the pulse duration is shorter than typical relaxation times the carriers will stay in their initial state, so that further photoexcitation is forbidden by the Pauli exclusion principle Fig. (7.1c). If the pulse duration is longer than typical relaxation times, the initially filled states will be emptied and new carriers can be added by optical excitation, which enables higher excitation densities. The amount of available states is further limited by the spectral position of the laser relative to the Fermi level of the thermalized carriers, compare Fig. (7.1c) and (7.1d). Efficient Pauli blocking sets in as soon as pumping takes place close to or even below the Fermi energy Fig. (7.1c). This is the case if the laser is tuned close to the band gap or if conduction and valence bands are filled at elevated carrier density. If the laser excites carriers in higher bands, scattering processes clear the states thereby enabling a refilling.

While the simplified picture presented above suggests that Pauli blocking is the dominant mechanism controlling the nonlinear optical response, there are other many-body effects present. Band-gap renormalization and the reduction of the exciton binding energy provide cause significant redistribution of states upon pump laser excitation. To bring up a more realistic picture the density-dependent absorption of monolayer MoS_2 is shown in Fig. 7.1e). It is shaped by a material-realistic density-of-states and strong Coulomb interaction between electrons and holes, which gives rise to the excitonic resonances A, B and C [57] that are a characteristic feature of TMD spectra. Due to the combined effect of band-gap renormalization, screening and Pauli blocking, the A and B excitons undergo a redshift under strong photoexcitation before they bleach out, as presented in detail in Chap (6). The resonances completely disappear as soon as the excitation density is increased above the Mott density. The C-peak remains mainly unaffected from photoexcitation.

As is evident from Fig. (7.1e) the asorption spectra change drastically with increasing carrier density. Therefore the wavelength of the pump laser is expected to be decisive for the density of excited carriers. Two different spectral positions are chosen in order to capture the different behaviour of the optical absorption upon increasing density. First, each monolayers is pumped at it's corresponding band edge, which is located between A (B) and B (C) peaks for the tungsten (molybdenum) compounds. Secondly, the monolayers are pumped several hundreds of meV above the band gap and the C exciton.For this second case typical excitation wavelengths of 3.06eV (2.33eV) for the sulfides (selenides) corresponding to a wavelength of 405nm (533nm) are chosen to compensate for the smaller selenide band gaps.

7.2. Description of Excited-Carrier Dynamics

In order to calculate the power-dependence of the total charge carrier density the SBE have been expanded in comparison to Chap. (6). Within the linear regime, the electric field $\mathbf{E}(t)$ provided a broadband probe that could not cause significant occupation. Hence, $\mathbf{E}(t)$ is used here as a pump laser with increased duration and higher field strength. Thus the dynamic of the occupation probability becomes relevant. The occupation defines the total density of electrons and holes at time t as

$$n^{e/h}(t) = \frac{1}{\mathcal{A}} \sum_{\mathbf{k}} f_{\mathbf{k}}^{e/h}(t) \,. \tag{7.1}$$

As main difference to the linear regime presented in Chap (6), $f_{\mathbf{k}}^{e/h}(t)$ is depending on the time. As carrier scattering processes determine the equilibration of highly excited carriers the relaxation time approximation is used (see Sec. (4.5.1)) to describe these processes. The time-dependence and the influence of many-body effects is described by the population equation of the SBE:

$$\frac{\mathrm{d}}{\mathrm{d}t} f_{\mathbf{k}}^{e/h}(t) = \frac{2}{\hbar} \mathrm{Im}\big[(\Omega_{\mathbf{k}}^{he})^{*} \psi_{\mathbf{k}}^{he}\big] - \frac{f_{\mathbf{k}}^{e/h}(t) - F_{\mathbf{k}}^{e/h}}{\tau_R} \,. \tag{7.2}$$

The Rabi energy renormalized by the screened Coulomb interaction is written as $\Omega_{\mathbf{k}}^{he}$ as before. The inter-band Coulomb renormalization gives rise to excitonic resonances below the quasi-particle band gap as well as a redistribution of oscillator strength between band-to-band transitions. This directly influences the absorption. The Coulomb matrix elements are screened by the excited electrons and holes. The dielectric function in quasi static approximation $\varepsilon^{-1}(|\mathbf{q}|)$ is used within the long-wavelength limit (cf. Sec. (4.4.1)). The pump fluence of the pulse is defined as the energy per pulse area and duration applied to the monolayer. It proportional to the squared absolute value of the electric field (see Sec. (4.6.1)):

$$S = \varepsilon_0 c_0 \int \mathrm{d}t \, |\mathbf{E}(t)|^2 \,. \tag{7.3}$$

For the exciting electric field $\mathbf{E}(t)$ a Gaussian-shaped pulse is considered. To model the scattering-induced relaxation and cooling of excited carriers the relaxation time approximation introduced in Sec. (4.5.1) is used. The non-equilibrium carrier population develops into a Fermi distribution $F^{e/h}_{\mathbf{k}}$ for the respective species of charge carriers on a characteristic timescale τ_R. The charge carrier densities that can be photoexcited at a specific fluence is quantified by calculating the steady-state value $\lim\limits_{t\to\infty} n^{e/h}(t)$.
Eq. (7.2) is coupled to the corresponding equation for the microscopic polarizations $\psi^{he}_{\mathbf{k}}(t)$:

$$i\hbar\frac{\mathrm{d}}{\mathrm{d}t}\psi^{he}_{\mathbf{k}}(t) \;=\; \left(\tilde{\varepsilon}^{h}_{\mathbf{k}}+\tilde{\varepsilon}^{e}_{\mathbf{k}}-i\Gamma(n)-\hbar\omega_{det}\right)\psi^{he}_{\mathbf{k}}(t)-\left(1-f^{e}_{\mathbf{k}}(t)-f^{h}_{\mathbf{k}}(t)\right)\Omega^{he}_{\mathbf{k}}\,, \tag{7.4}$$

In order to describe density-depending dephasing for the microscopic polarization, a function $\Gamma(n)$ has been introduced, that will be explained in detail in Sec. (7.4). The renormalized single-particle energies $\tilde{\varepsilon}^{\lambda}_{\mathbf{k}}$ are obtained as can be found in Sec. (4.3) and Refs. [47, 156, 158]. A detailed descritption follows in the next Sec. (7.3). The detuning between the pump laser and the band gap of the unexcited TMD monolayer is given by $\hbar\omega_{det}$. The Pauli exclusion principle enters the theory via the blocking term $\left(1-f^{e}_{\mathbf{k}}(t)-f^{h}_{\mathbf{k}}(t)\right)$. Pauli blocking blue-shifts the Coulomb-bound states described in $\Omega^{he}_{\mathbf{k}}$ due to the filling of states.

7.3. Band Structure Renormalizations

The band structure experiences momentum-dependent renormalizations due to Coulomb interaction between photoexcited carriers as described in Sec. (6.2). This results in a power-dependent detuning between the states and the exciting laser pulse, which is an important mechanism for clearing states. With increasing excitation density, a shrinkage of the band gap as well as a transition from direct to indirect band gaps are expected. [33, 49, 85, 86, 86, 156, 175, 193–195] The different contributions recalled read

$$\varepsilon^{\lambda}_{\mathbf{k}} \;=\; \varepsilon^{0,\lambda}_{\mathbf{k}}+\Sigma^{\mathrm{H},\lambda}_{\mathbf{k}}+\Sigma^{\mathrm{U},\lambda}_{\mathbf{k}}+\Sigma^{\mathrm{SX},\lambda}_{\mathbf{k}}+\Sigma^{\mathrm{CH},\lambda}_{\mathbf{k}}+\Sigma^{\mathrm{GdW},\lambda}_{\mathbf{k}}\,. \tag{7.5}$$

In order to describe the optical response of the excitation properly, two conduction bands are taken into account in addition to the valence band for each spin. These additional bands provide states in the high energy region to be excited by the pump pulse. The Coulomb interaction between electrons in different conduction bands is included and contributes to the renormalizations. However, the uppermost conduction band never assembles enough carriers to contribute to band shifts.

TMD monolayers are often encapsulated in hexagonal boron nitride (hBN), which has become a standard technique to reduce inhomogeneous contributions to the linewidth, stemming for example from surface wrinkling [12]. For this ground state the Coulomb interaction is screened due the dielectric environment and carriers in the filled valence-band [158]. Therefore a dielectric environment for all four investigated TMDs (MoS_2, $MoSe_2$, WS_2, WSe_2) with a dielectric constant of $\varepsilon_r = 4.5$ corresponding to an index of refraction of $n = 2.15$ is taken into account. In addition a gap of 0.3 nm between the monolayer and the surrounding hBN layers is taken into account, reducing the screening [161]. Independent of the current carrier density the ground state band structure undergoes renormalizations $\Sigma^{\mathrm{GdW},\lambda}_{\mathbf{k}}$ induced by the dielectric environment (see Sec. (4.4.4)). These shrink the band gap and thereby shift the spectral position of the exciting laser indirectly. The band-gap shrinkage from GdW renormalization for different substrates can be found in Tab. (4.1).

7.4. Influence of Excitation-Induced Dephasing

The peak structure of the spectra plotted in Fig. (7.1e) and (7.4) depends on the linewidth of excitonic peaks and the band-to-band transitions. Here, the width is determined by the dephasing function $\Gamma(n)$ that enters the SBE (7.4) and dampens the inter-band polarizations. Due to carrier scattering processes [196] there is an excitation-induced contribution to the dephasing [197], rendering $\Gamma(n)$ in general density dependent. A nonlinear dependence of excited carrier density on the pump fluence is therefore expected. For the low-excitation regime (small pump fluence), the dominant contribution to dephasing stems from the coupling of charge carriers to phonons. This effect strongly depends on the lattice temperature and on the TMD material. It has been quantified for the A exciton in Ref. [12] and can be used to fix the value of $\Gamma(n = 0)$. To model the power-dependent contribution, Ref. [34] provides data on the density dependent line broadening. There the increase of the A-exciton linewidth in WS_2 has been extracted from a pump-probe experiment for carrier densities up to several 10^{12} cm^{-2}. The full dissociation of the excitons into unbound carriers marks a turning point in the density dependence of excitation-induced dephasing. It can also be expected that the dephasing rate saturates for large densities due to phase space filling in the carrier-carrier scattering rates. Therefore a $\arctan(x)$ function offers itself to capture

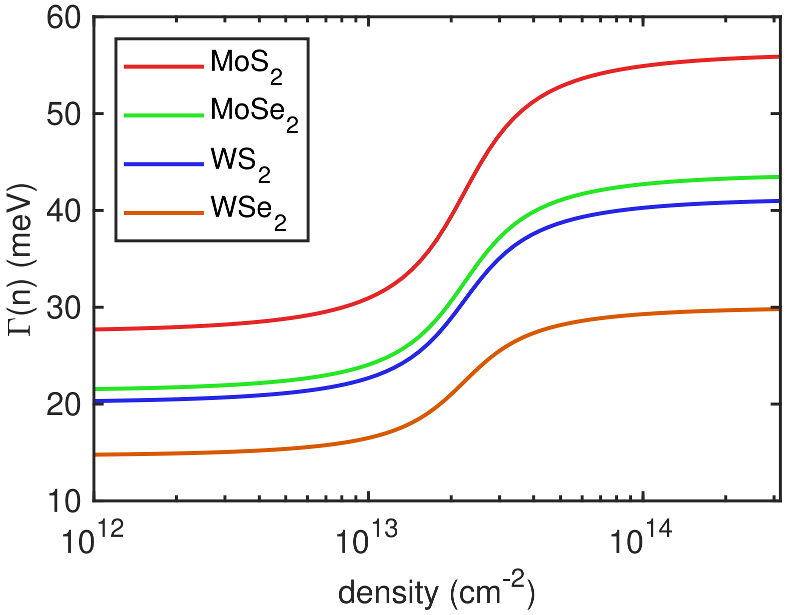

Figure 7.2.: Plot of the model function used to describe the density dependence of the excitation induced dephasing for MoS_2, $MoSe_2$, WS_2 and WSe_2. A detailed description of the model is given in the text.

the dephasing phenomenologically

$$\begin{aligned}\Gamma(n) &= \left[\arctan\left(\frac{n-n_{Mott}}{\eta}-1\right)+\frac{\pi}{2}\right] \\ &\quad \times\frac{\gamma_0(f-1)}{\pi}+\gamma_0\,, \end{aligned} \tag{7.6}$$

where γ_0 is taken from [12] to be 22.5 meV for MoS_2, 17.5 meV for $MoSe_2$, 12 meV for WS_2 and 16.5 meV for WSe_2. The Mott density is approximated as $n_{Mott} = 1\times 10^{13}\text{cm}^{-2}$ [36]. The coefficients $\eta = 1\times 10^{13}\text{cm}^{-2}$ and $f = 2.5$ can be estimated using the data from [34]. It is assumed that n_{Mott}, η and f have the same value for all investigated TMD materials. For MoS_2, this yields a maximum dephasing of 56 meV. The results for the density-dependent dephasing of all materials are presented in Fig. (7.2).

7.5. Charge Carrier Densities in TMDs

The following section contains the numerical results obtained from the theory presented beforehand. The dependence of the excited-carrier density on the pump fluence as obtained from the SBE are given in Fig. (7.3). The pump laser provides fluences of up to 1000μJ cm^{-2}

with a pulse duration of 150 fs. The relaxation time due to carrier-carrier [127] and carrier-phonon [190, 198] scattering is taken to be $\tau_{relax} = 100$ fs.

For pump at the band edge, a nonlinear relation between density and fluence is found, which can be directly understood from the Pauli blocking effect at the band edge. Nevertheless for small fluences the density increases linearly with the pump fluence. This linear behaviour is the result of the compensation between the Pauli blocking and band-gap renormalizations that spectrally shift the band gap away from the pump pulse, thereby opening up free phase space.

For pumping above the band gap, the linear behaviour extends to $20\ \mu$J^{-1} for the selenides and $50\ \mu$J^{-1} for the sulfides, but it is off different origin. Here, the fast scattering enables a refilling of the states close to the pump pulse. In all four investigated materials, the density reaches values of several 10^{14} cm^{-2} for fluences of 1000μJ cm^{-2}. Pumping above the band gap in general yields excited-carrier densities that are larger than for pumping at the band gap. This is in agreement with the simplified picture of available phase space discussed in Fig. (7.1). The largest density that is achievable under the investigated pump conditions is $n \sim 8 \cdot 10^{14}$ cm^{-2} for above-gap pump in MoS$_2$. For MoS$_2$ and WS$_2$, the fluence dependence can be reasonably fit with a linear function up to $50\ \mu$J cm^{-2}, yielding a slope of $2.31\,(1.67) \cdot 10^{12}\mu$J^{-1} for MoS$_2$ (WS$_2$). For MoSe$_2$ (WSe$_2$) the fitting region extends to 20μJ cm^{-2}, yielding a value of $4.20\,(1.70) \cdot 10^{12}\mu$J^{-1}. The Mott density for all materials is reached for fluences below 10μJ cm^{-2}. The two figures (7.4) and (7.5) will provide more insight into the build-up of the excited-carrier densities. The increase of the density and the renormalizations of the different valleys for band-edge pumping is provided in Fig. (7.5). In panels a) and c) the rise of carrier density in the most important band-structure valleys ($\mathbf{K}$, $\mathbf{K}'$, Σ, Σ') is shown. The large densities at Σ/Σ' reflect the drain of electrons from the $\mathbf{K}$-valley, that has been discussed in Sec. (6.2) and (4.3). Though the direct transition at $\mathbf{K}$ accumulates carriers faster, the Σ-valley gathers most carriers after about 0.5 ps. From Fig. (7.5) b) and d) it can be found that a transition to an indirect band gap takes place within less than 1 ps. Since the band-structure renormalizations are induced instantaneously, their characteristic time scale is given by the pump pulse duration and the relaxation time of carriers. Thus renormalizations take place faster than typical radiative recombination times, which are on the order of picoseconds [192] depending on substrate and temperature [191]. Therefore a sublinear increase of photoluminescence experiments is to be expected [39].

The absorption spectra in Fig. (7.4) give insight into the two-particle properties of TMD monolayers including optical selection rules determined by the dipole matrix elements and phenomenological broadening according to Sec. (7.4). When analyzing Fig. (7.4) a) to d) it is evident, that the absorption is not only different for increasing density but also provides a

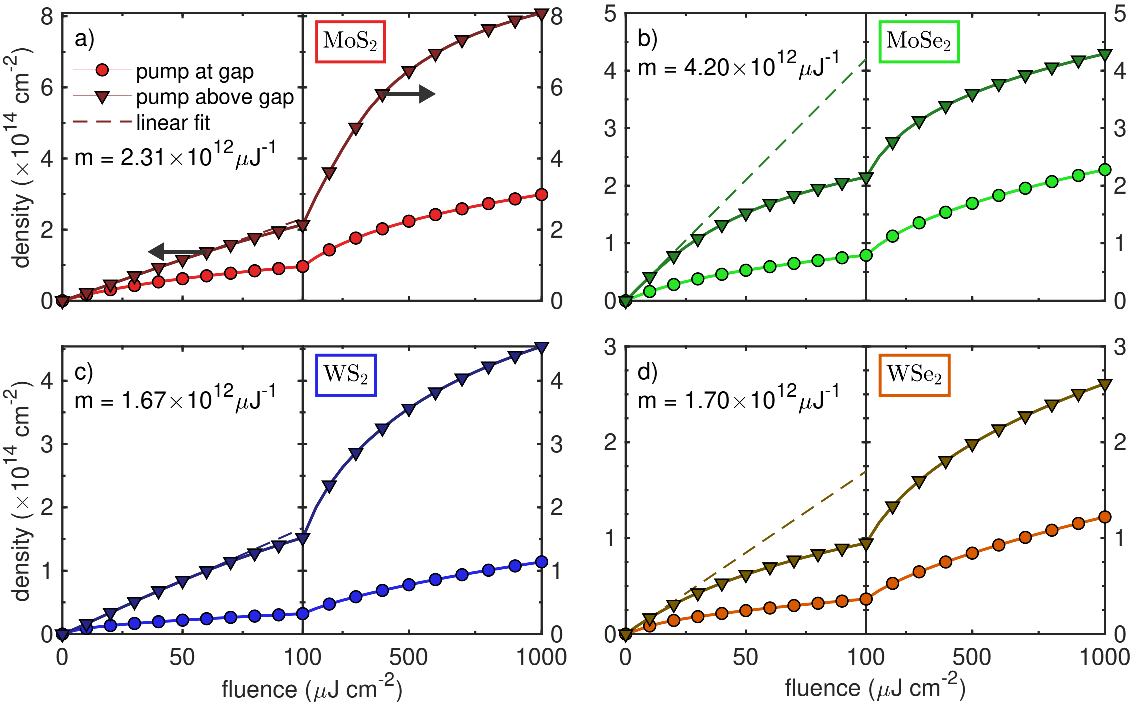

Figure 7.3.: Charge carrier densities for pump fluences of $(0-100)\mu$J cm^{-2} (left plot of each panel) and $(100-1000)\mu$J cm^{-2} (right plot) for **a)** MoS$_2$, **b)** MoSe$_2$, **c)** WS$_2$ and **d)** WSe$_2$ encapsulated in hBN. The calculations have been performed for a pump spectrally located at the band gap of the TMD layer (circles) and for pumping above the band gap (triangles). Pump energies of 3.06eV (2.33eV) for the sulfides (selenides) have been used. The linear fit functions for pumping at the band edge mentioned in the main text are plotted as dashed lines in the left plots. The slope m of the fit functions are given in the respective panels.

complex peak structure in energy. For example for MoS$_2$ the absorption decreases around the A and B peak with increasing density, while it rises for energies above the C peak. A similar behaviour is found for the other materials. Optical gain is identified which enables a decrease of the total density during the pump process. This redistribution of optical weight is a direct result of the interplay between Pauli blocking, renormalizations and scattering. Each density value presented in Fig. (7.3) thus depends strongly on the history of different absorption values, before a steady-state value has been reached. Normalized to the laser spot-size A and the photon energy $h\nu$ together with the pump power P, which converts the absorption α to the density n, according to [62] this accumulation can be viewed as

$$n(t) \quad = \quad \frac{1}{A \cdot h\nu} \int_0^t \mathrm{d}t' \, P(t') \cdot \alpha\big(n(t')\big) \tag{7.7}$$

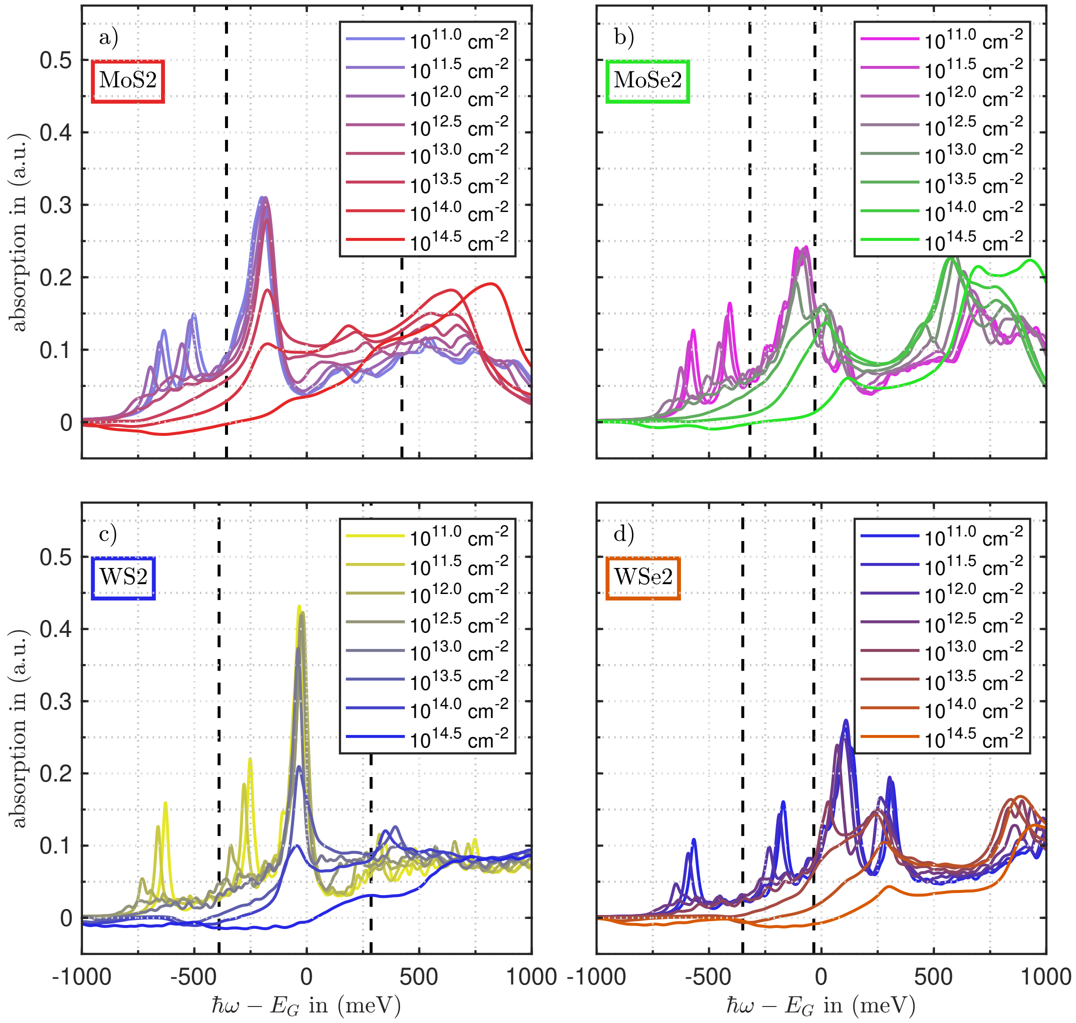

Figure 7.4.: The density-dependent absorption spectra of **a)** MoS_2, **b)** $MoSe_2$, **c)** WS_2 and **d)** WSe_2 encapsulated in hBN and calculated according to the equations of Chap. (6) are given in this plot. For densities ranging from $1 \times 10^{11}\text{cm}^{-2}$ to $3.61 \times 10^{14}\text{cm}^{-2}$ the redshift and bleaching of the A and B peaks can be found within the spectra. The C peak bleaches only far above the Mott density. Spectral weight is shifted to higher energies for increasing density.

Despite the absorption spectra having been calculated in the linear regime with fixed carrier populations as presented in Chap. (6), they help clarifying the density accumulation process. It is possible to estimate $\alpha(n)$ from Fig. (7.4) for a chosen energy in order to calculate Eq. (7.7) taking into account the evolution of the absorption coefficient over time. One should keep in mind, that the theory presented and evaluated above goes beyond this simple rate equation picture by providing a momentum-resolved description of the occupation dynamics in the BZ. Thereby, the optical response in a true non-equilibrium situation is taken into account via $\alpha(\omega, t)$, which yields a microscopic understanding of the accumu-

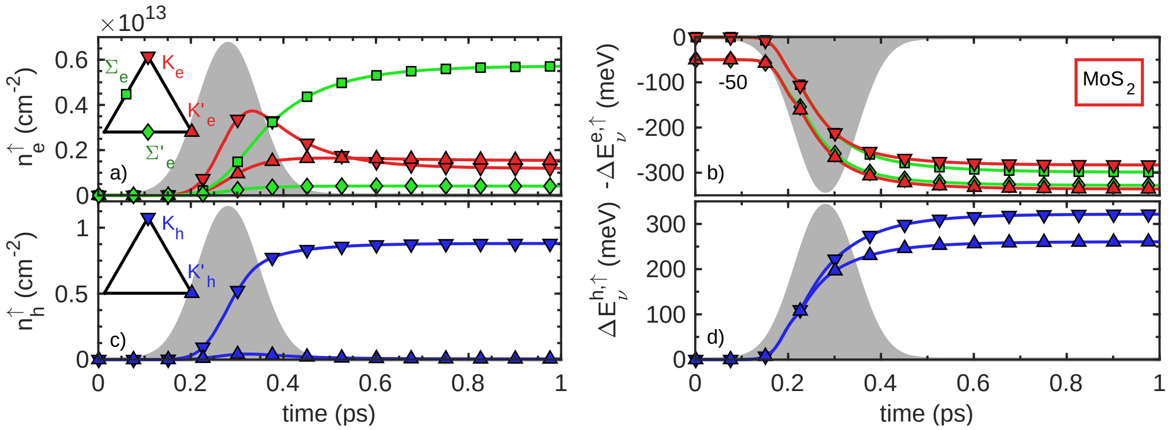

Figure 7.5.: **a),c)**: Spin-up electron and hole density for MoS_2 resolved for the different valleys in the Brillouin zone when pumping at the band gap. **b),d)**: Band-structure renormalizations for the same valleys as in a) and c). Here the curves for $\mathbf{K}'_e$ and $\mathbf{\Sigma}'_e$ have been omitted for better visibility. They show the same overall behaviour as K_e and Σ_e except for the fact that Σ'_e is less renormalized than K'_e. For the spin-down density and renormalizations the non-primed and primed valleys interchange their role.

lation of carrier density.

While the resulting density dependence shows partially linear behaviour for low fluences, this nevertheless originates from a compensation of Pauli blocking an band structure renormalizations. The band structure renormalization shifts the two-particle density-of-states, thereby clearing phase space especially for a pump at the band gap. For a pump above the gap this is still present but small compared to the influence of scattering processes.

7.6. Conclusion

The interplay of processes that occur during photoexcitation of MoS_2, $MoSe_2$, WS_2 and WSe_2 monolayers has been analyzed, resulting in the excited-carrier density depending on the pump fluence. A pump fluence of $1000 \mu\mathrm{J}\ \mathrm{cm}^{-2}$ is necessary to obtain excited-carrier densities of several $10^{14}\ \mathrm{cm}^{-2}$ beyond the Mott density.

When pumping at the band edge, the excited carrier instantaneously block the available phase space (Pauli blocking), thus leading to a nonlinear increase of the carrier density with the pump fluence. However, band structure renormalizations shift the density-of-states away from the pump pulse thereby effectively clearing states. Both effects partially compensate each other leading to a linear increase of the density for low fluences up to $5\ \mu\mathrm{J}\ \mathrm{cm}^{-2}$, while the Mott density for all materials is reached before $10\ \mu\mathrm{J}\ \mathrm{cm}^{-2}$. A pump wavelength above the band gap provides more available phase space for excited carriers, thereby yielding larger maximum carrier densities and a linear regime of power dependence of up to 50μJ cm^{-2}. There, scattering processes provide the main mechanism of clearing states. While Pauli blocking is a main source of the non-linear dependence between fluence and carrier density, its effects are balanced by band structure renormalizations, especially for a pump at the band edge. For pumping above the band gap, scattering processes dominate and enable a refilling of the states, which results in a linear behaviour of the density with the fluence. The many-body effects essentially modify and shift the two-particle density-of-states at the spectral position of the pump laser. However, this effect is weakened by efficient excitation-induced dephasing that smears out the density-of-states.

During the photoexcitation process, band structure renormalizations are found to cause a transition from a direct to an indirect band gap (see Sec. (6.1)) on a time scale below typical exciton recombination times, thereby effectively draining carriers from the direct optical transition at the $\mathbf{K}$- and $\mathbf{K}'$-valleys to dark states.

8. Interlayer Excitons in Twisted TMD Bilayers

The possibility to arbitrarily stack 2d materials offers an alternative way to tailor the properties of a semiconducting device [2]. One prominent example for a twisted systems is bilayer graphene, where there are strong indications for superconductivity when both layers have a (magic) twist angle of about 1.1 ° [18]. Thus the twist angle is crucial to the materials properties [199, 200]. It is experimentally accessible during the stacking process of the exfoliated monolayers [54].

Recently, research focus has shifted towards TMD bilayer systems, as they open up new fields of tailoring excitonic properties. For heterobilayers of type-II band alignment, the formation of interlayer excitons (ILX) has been observed [19, 51, 201–204]. Electron and hole that form these ILX are located in different layers. The ILX exhibit long lifetimes [205, 206], that originates from the spatial seprartion of electron and hole. The geometry of the bilayer system, especially the rotation angle between both layers, is a promising tuning knob for the lifetime of ILX. A periodic change of the band gap originates from the different stacking orders of the rotated top and bottom TMD layer. ILX can get trapped [207, 208] within the minima of this periodic potential. Thus this section is dedicated to studies on twisted TMD bilayers in general and specifically on ILX in twisted TMD heterobilayers.

For the description of the bilayer properties in dependence of the twist angle of the two layers two approaches will be explored, the first to be a straight-forward ground state calculation utilizing the TB-method as described in Ref. [209]. In contrast to this the second approach focusses on describing the properties of ILX. Hence, the relative and center-of-mass motion of ILX will be separated in the limit of small angles [50]. This enables the description of the ILX as composite quasi-particle moving through a periodic potential landscape. Due to the necessity to perform a plane wave expansion, either approach will be numerically demanding for small angles as a large number of expansion coefficients is needed for convergence. The SBE as presented in Chap. (6) and (7), if applied accordingly in future research, can provide a new angle to obtain optical properties.

The first part of this section will be subject to the general properties of the Moiré pattern and it's symmetries in twisted periodic lattices. Together with the TB description of twisted bilayers the results presented there have been explored in cooperation of Ruven Hübner together with Christian Carmesin and the author of this thesis, who both shared the co-supervision of the Bachelor thesis of R. Hübner. The second part aims for calculating the twist angle-dependent lifetime of ILX. All numerical calculations presented in these sections have been obtain jointly by Matthias Florian, Alexander Steinhoff and the author of this thesis. The results are in preparation for publication, which will be done in experimental collaboration with the group of Xiaoqin Li from the University of Texas-Austin.

8.1. Moire Pattern

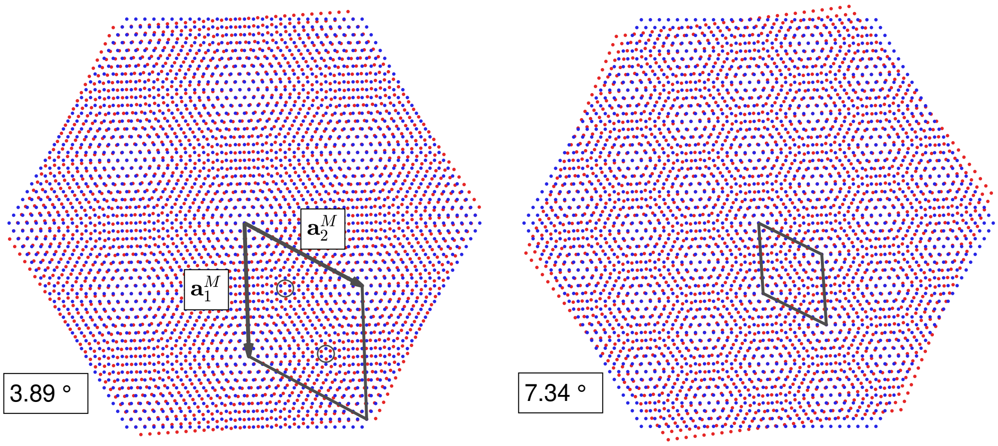

Figure 8.1.: Moiré periodicity in twisted bilayers (top layer in red, bottom layer in blue) and Moiré unit cell (black) for two different commensurate twist angles of $3.89\,°$ (left) and $7.34\,°$ (right). The size of the Moire cell depends inversly on the twist angle. The points of different stacking orders have been marked with circles in the left panel.

Stacking two TMD monolayers on top of each other changes the crystal structure and the symmetries of the system quite drastically. A rotation by the angle θ of the top (t) to the bottom (b) layer with $\mathbf{R}_{t,i} = R(\theta)\mathbf{R}_{b,i}$ and $R(\theta)$ being the 2d rotation matrix induces a new periodicity in the structure. This superlattice is described by the basis vectors that connect two neighbouring points at which the stacking order of the two layers' rotation center is restored. Following a lattice vector of this supercell, the AA-type (M-M) inital stacking changes to AB (M-X) and back again to AA. Thus it appears only when both lattices are commensurate, meaning that the lengths of the lattice vectors have a rational ratio. The real-space basis of the Moiré superlattice labeled as s is thus defined by m unit cells along

$\mathbf{a}_{t/b,1}$-direction and n unit cells along $\mathbf{a}_{t/b,1}$-direction [210]:

$$\mathbf{a}_{s,1} \;=\; m\mathbf{a}_{b,1} + n\mathbf{a}_{b,2} = m\mathbf{a}_{t,1} + n\mathbf{a}_{t,2}\,. \tag{8.1}$$

The second basis vector $\mathbf{a}_{s,1}$ is given by a rotation of 60 °. The angles, where the twisted lattices are commensurate, are defined by using n and m:

$$\cos\theta \;=\; \frac{1}{2}\frac{m^2+n^2+4nm}{m^2+n^2+nm}\,. \tag{8.2}$$

For commensurate and incommensurate lattices the so called Moiré lattice can be constructed, which is plotted for two different angles in Fig (8.1). It defines areas of (approximate) periodicity and is expressed as [210]:

$$\mathbf{a}_1^M = \frac{-\mathbf{a}_2 \times \mathbf{e}_z}{2\sin\theta/2}, \qquad \mathbf{a}_2^M = \frac{-\mathbf{a}_1 \times \mathbf{e}_z}{2\sin\theta/2}\,. \tag{8.3}$$

Along the vector $\mathbf{a}_1^M + \mathbf{a}_2^M$ (in the middle of the two basis vectors) the stacking order of the top and bottom layer varies from M-M (aligned molybdenum atoms) to M-X (molybdenum chalgocen aligned) and finally to the top M being above the chalcogen vacancies back to M-M stacking. Thereby three special points are defined $\mathbf{r}_{n,0} = n(\mathbf{a}_1^M + \mathbf{a}_2^M)/3$ that couple differently to the polarization of the light (see Fig. (8.1)).

For the commensurate case the Moiré basis vectors are identical to those of the superlattice. In $\mathbf{k}$-space the Moiré basis vectors can be constructed by simply taking the difference between two reciprocal basis vectors of the top and bottom layer [209]

$$\mathbf{b}_1^M = \mathbf{b}_{t,1} - \mathbf{b}_{b,1}, \qquad \mathbf{b}_2^M = \mathbf{b}_{t,2} - \mathbf{b}_{b,2}\,. \tag{8.4}$$

The vectors $\mathbf{b}_1^M/\mathbf{b}_2^M$ define the Moiré Brillouin zone (MBZ), that changes its size with the rotation angle θ and is the pendant to the first Brillouin zone of the monolayer case as it is periodically repeated in reciprocal-space, if the lattices are commensurate. The MBZ is plotted in Fig. (8.2). Every lattice site of the reciprocal Moiré lattice vector can be reached by $\mathbf{G}^M = \mathbf{G}_t - \mathbf{G}_b$. While this is true for all reciprocal Moiré vectors, the inverted relation $\mathbf{G}_t - \mathbf{G}_b = \mathbf{G}^M$ is only valid for the commensurate lattices. Otherwise there exist more possibilities to construct $\mathbf{G}_t/\mathbf{G}_b$ from $\mathbf{b}_{t/b,1}/\mathbf{b}_{t/b,2}$. Especially for $|m-n| = 1$, the superlattice and the Moiré lattice are identical. From the considerations of this section it follows directly, that the momenta of the top and bottom layers are related via $\mathbf{k}_t = R(\theta)\mathbf{k}_b$.

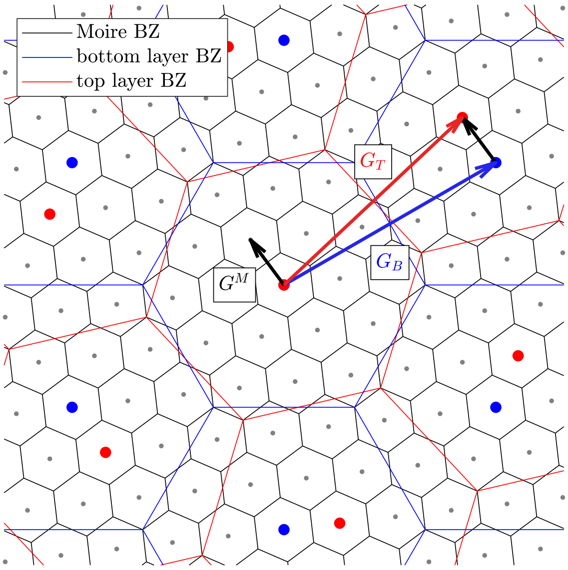

Figure 8.2: Construction and visualization of the Moiré Brillouin zone (MBZ, black) from the top layer (red) and bottom layer (blue) reciprocal lattice vectors according to $\mathbf{G}_t - \mathbf{G}_b = \mathbf{G}^M$. The dots mark the lattice points of the respectively colored lattice. The points of high symmetry within the MBZ (γ, κ, κ') will be marked by the small greek letters corresponding to the labels of the points of high symmetry in the hexagonal BZ of the honeycomb lattice.

8.2. Ground State Description of Twisted Bilayers

In order to describe the electronic properties of twisted bilayers a possible ansatz is the Tight-Binding method. The work of Amorim et al. provides a straight forward yet general model to obtain band structures and coefficients for twisted homo-bilayers, exemplary shown for a graphene bilayer, thereby reproducing the flattening of bands around the magic angle, and for a MoS_2 bilayer. The main goal was to gain basic understanding of the model and to explore possible extensions for future application of the theory, for example to model heterobilayers and incommensurate structures, that may arise from different lattice constants of the top and bottom layer, ultimately leading to a possible description of interlayer excitons. The model for twisted bilayers presented in Ref. [209] will be introduced in the following.

The presented TB-based model does not account for surface wrinkling or strain from bending the layers, that occurs naturally in graphene or TMD layers. Nevertheless, effects such as strain within the layer could be implemented via the Harrison rule (cf. Sec. (3.1.2)). In order to describe strained nanostructures, where the material extends into the third dimension, a procedure similar to Ref. [96] has to be performed.

The full Hamiltonian of the twisted bilayer is given by

$$H = H_T + H_B + H_{TB} + H_{BT} \,. \tag{8.5}$$

The Hamiltonians $H_{T/B}$ contain the isolated monolayer of the top (bottom) layers. Any model using an orbital basis, such as [91], can be applied to this scheme. Using the Wannier representation of creation and annihilation operators, one obtains for the Hamiltonian of the top T or bottom B layer, respectively:

$$H_{T/B} \;=\; \sum_{\mathbf{k}_{T/B},\alpha,\beta} H^{TT/BB}_{\alpha\beta}(\mathbf{k}_{T/B}) c^{\dagger,\alpha}_{T/B,\mathbf{k}_{T/B}} c^{\beta}_{T/B,\mathbf{k}_{T/B}}\,, \tag{8.6}$$

with $H_{\alpha\beta}(\mathbf{k})$ being the Hamiltonian matrix element in $\mathbf{k}$-space. For the interlayer coupling of a twisted bilayer, both the momenta from the top $\mathbf{k}_t$ and the bottom $\mathbf{k}_b$ layer occur, which contribute as

$$H_{TB} \;=\; \sum_{\mathbf{k}_T,\mathbf{k}_B,\alpha,\beta} H^{TB}_{\alpha\beta}(\mathbf{k}) c^{\dagger,\alpha}_{T,\mathbf{k}_T} c^{\beta}_{B,\mathbf{k}_B}\,. \tag{8.7}$$

The relation $(H^{bt})^{\dagger} = H^{TB}$ holds, as the full Hamiltonian is hermitean. The interlayer coupling only occurs, if the generalized umklapp condition is satisfied [209, 211], therefore both momenta are coupled as

$$\mathbf{k}_T + \mathbf{G}_T \;=\; \mathbf{k}_B + \mathbf{G}_B\,. \tag{8.8}$$

The matrix element $H^{TB}_{\alpha\beta}(\mathbf{k})$ becomes

$$H^{TB}_{\alpha\beta}(\mathbf{k},\mathbf{G}_T,\mathbf{G}_B) \;=\; H^{TB}_{\alpha\beta}(\mathbf{k}+\mathbf{G}_T+\mathbf{G}_B) e^{i\mathbf{G}_T\tau_{T,\alpha}} e^{i\mathbf{G}_B\tau_{B,\beta}}\,. \tag{8.9}$$

Here the $\tau_{l,\nu}$ indicates the position of the basis atoms within the primitive unit cell and therefore α, β denotes the sublattice. A new $\mathbf{k}$-vector has been introduced, that is chosen as $\mathbf{k} = \mathbf{k}_b - \mathbf{G}_t$, which directly follows from the umklapp condition (8.8). The umklapp condition expands the full Hamiltonian H into plane-waves, which obey the Moiré periodicity

$\mathbf{G}_M = \mathbf{G}_T - \mathbf{G}_B$. The full Hamiltonian has the properties of a block matrix, with

$$\begin{aligned}
H(\mathbf{k}) &= \begin{pmatrix} H_T(\mathbf{k}) & H_{T/B}(\mathbf{k}) \\ H_{BT}(\mathbf{k}) & H_B(\mathbf{k}) \end{pmatrix} \\
H_{T/B}(\mathbf{k}) &= \begin{pmatrix} H_{T/B}(\mathbf{k}+\mathbf{G}_{T/B,1}) & 0 & \\ 0 & H_{t/b}(\mathbf{k}+\mathbf{G}_{T/B,2}) & \\ & & \ddots \end{pmatrix} \\
H_{TB}(\mathbf{k}) &= \begin{pmatrix} H_{TB}(\mathbf{k}+\mathbf{G}_{B,1}+\mathbf{G}_{T,1}) & H_{TB}(\mathbf{k}+\mathbf{G}_{B,1}+\mathbf{G}_{T,2}) & \dots \\ H_{TB}(\mathbf{k}+\mathbf{G}_{B,2}+\mathbf{G}_{T,1}) & H_{TB}(\mathbf{k}+\mathbf{G}_{B,2}+\mathbf{G}_{T,2}) & \dots \\ \vdots & \vdots & \ddots \end{pmatrix}
\end{aligned} \tag{8.10}$$

The band structure calculated from diagonalizing $H(\mathbf{k})$ is converged, if the bands of interest within the first MBZ are symmetric on a representative path. The number of $\mathbf{G}^M$ from the PW-expansion controls the convergence as it enables the symmetrization of the bands by backfolding. At the same time it is a limitation to the calculation as the matrix size is quadratically increased with $N_{\mathbf{G}^M}$. For a commensurate structure, the number of $\mathbf{G}^M$'s is finite, while for an incommensurate the number is infinite. Therefore the matrix has to be truncated at a certain order of $\mathbf{G}^M$'s. Especially for small angles large matrices arise, that are numerically demanding. Nevertheless, this model provides band structure results for arbitrary angles.

The matrix elements of the interlayer interaction V in real-space are given by

$$H^{tb}_{\alpha\beta}(\mathbf{R}_{T,i}, \mathbf{R}_{B,j}) = \left\langle \mathbf{R}_{T,i}, \alpha, t \middle| V^{\beta,b}(\mathbf{r} - \mathbf{R}_{B,j} - \tau_{B,j}) \middle| \mathbf{R}_{B,j}, \beta, b \right\rangle . \tag{8.11}$$

Transforming into $\mathbf{k}$-space, one has to pay attention to the interaction not being discrete on the lattice sites, but continous.

$$H^{TB}_{\alpha\beta}(\mathbf{q}) = \frac{1}{\mathcal{A}} \int \mathrm{d}^2\mathbf{r} H^{tb}_{\alpha\beta}(\mathbf{r}) e^{-i\mathbf{q}\mathbf{r}} \tag{8.12}$$

In the expression above $H^{tb}_{\alpha\beta}(\mathbf{r})$ will be used as a model function. In the sense of a Slater-Koster model the interaction between neighbouring orbitals can be expressed as σ- or π-binding. The projection on the vector connecting the neighbouring orbitals yields the σ-binding part, while the projection on the perpendicular plane yields the π-binding. Exemplary for p-orbitals on obtains from this projection

$$H^{TB}_{\alpha\beta}(\mathbf{r}) = V_{pp\sigma}(R)\frac{d^2}{R^2} + V_{pp\pi}(R)\frac{r^2}{R^2} , \tag{8.13}$$

where d is the distance between the two orbitals in z-direction and $r = \sqrt{x^2+y^2}$ their lateral distance. It has to be taken care that due to the dependence on a top layer and a bottom layer orbital a basis transformation has to be performed. This procedure transforms the pure orbitals into linear combinations of rotated top and bottom orbitals, for example $|p_x^{t/b}\rangle \rightarrow 1/\sqrt{2}(|p_x^t\rangle + |p_x^b\rangle)$. The transformation is unitary and defined by a rotation matrix $\mathcal{R}(\theta)$ that acts separately on orbitals with different quantum number n.
For the spatial dependence of the Slater-Koster parameter $V_{pp\sigma}$ and $V_{pp\pi}$ the generalized Harrison rule is applied, resulting in

$$V_{pp\sigma}(R) = V^0_{pp\sigma} e^{-\frac{R-d}{r_0}} \quad \text{and} \quad V_{pp\pi}(R) = V^0_{pp\pi} e^{-\frac{R-a/\sqrt{3}}{r_0}} \,. \tag{8.14}$$

The equation above is valid for hexagonal lattices. The values of $V_{pp\sigma}$ and $V_{pp\pi}$ can be found in [209] for the presented example material systems of bilayer graphene and bilayer MoS_2. Having defined all necessary quantities above, the full matrix can be solved by diagonalizing the eigenvalue problem to obtain the single-particle energies of the twisted bilayer system.

8.3. Electronic Properties of Interlayer Excitons

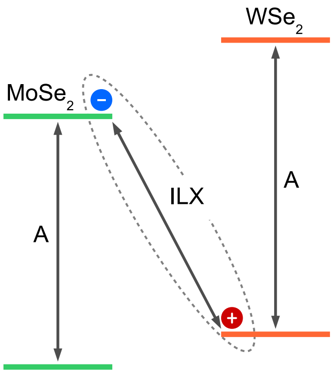

Figure 8.3.: Type-II band alignment at the $\mathbf{K}$-point of a WSe_2/$MoSe_2$ heterobilayer. For the lowest transition electrons are excited into the conduction band of $MoSe_2$, while the holes reside in the valence band of WSe_2.

The electronic properties and excitations in twisted bilayer systems shall be described for small twist angles, in order to obtain an expression for the angle and temperature dependence of the radiative lifetime of ILX. The bilayer system, that serves as an exemplary geometry, is a WSe_2/$MoSe_2$ bilayer. Interlayer excitons form in this bilayer due to the type-II band alignment of the $\mathbf{K}$-point transitions (see Fig. (8.3)). The excited electron and the

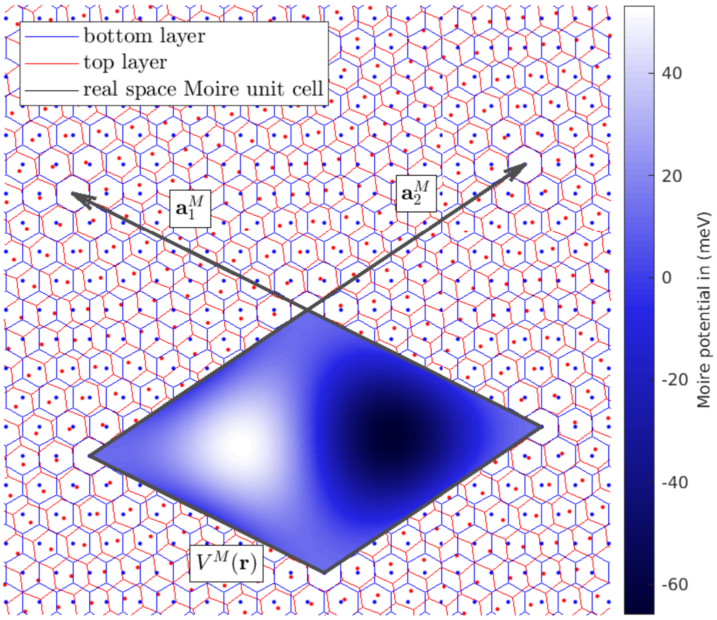

Figure 8.4.: The periodic Moiré potential V^M is plotted within a Moiré unit cell. It represents the band gap change that is induced due to the Moiré periodicity defined by the vectors $\mathbf{a}_1^M$ and $\mathbf{a}_2^M$. The variation of the stacking of the top and the bottom layer changes throughout the Moiré unit cell can be seen from the lattices in the background. In the center-of-mass description the ILX act as composite particles that move through the potential landscape. Thus they will assemble within the minima of V^M.

hole therefore reside in different layers. This causes the lowest optical transition to be $\varepsilon^{\text{ILX}} = \varepsilon_{\mathbf{K}}^{\text{MoSe}_2,e} + \varepsilon_{\mathbf{K}}^{\text{WSe}_2,h}$. By choosing a specific twist angle the band gap is periodically modulated across the Moiré unit cell, due to the change in stacking order that originates from the rotation. This Moiré pattern introduces a periodic potential landscape, in which ILX get trapped [19, 207, 208].

For small twist angles the Moiré unit cell becomes large compared to the Bohr radius of an ILX (~ 1 nm). Thus the ILX is described as a composite quasi-particle that moves through a potential landscape [19]. Thereby it is justified to neglect the relative motion of the ILX. The electronic properties of the ILX are calculated from the center-of-mass Schrödinger equation. The center -of-mass coordinate is defined as $\mathbf{R} = (m_e\mathbf{r}_e + m_h\mathbf{r}_h)/M$, where $M = m_e + m_h$ is the mass of the center-of-gravity.

Following the work of Refs. [50] and [19] the Hamiltonian for the center-of-mass motion of the ILX has the following form in real-space and momentum space respectively:

$$
\begin{aligned}
H &= -\frac{\hbar^2}{2M}\Delta_{\mathbf{R}} + V^{\mathrm{M}}(\mathbf{R})\,, && (8.15)\\
H &= \frac{\hbar^2\mathbf{Q}^2}{2M} + \sum_{\mathbf{G}^M} V^{\mathrm{M}}_{\mathbf{G}^M} e^{i\mathbf{G}^M\mathbf{R}}\,. && (8.16)
\end{aligned}
$$

$V^{\mathrm{M}}(\mathbf{R})$ is the interlayer Moiré potential that arises for commensurate angles in real-space Moiré superlattices. It originates from the band gap change $V^{\mathrm{M}}(\mathbf{R}) = E_G(\mathbf{R}) - \langle E_G\rangle$ when translating the layers and thereby changing the stacking order. Assuming small rotations, each rotated atomic position in the top layer can be identified with a translation in the MBZ and is thus mapped onto DFT calculations of shifted layers as presented in [50]. This parameterization will be used in the following.

In order to calculate the electronic properties of the ILX, a plane wave (PW)-expansion on the MBZ with $\mathbf{Q}$, $\mathbf{G}^M \in$ MBZ is performed, leading to the following expression for the wave function:

$$
\begin{aligned}
\big|\chi\big\rangle &= \sum_{\mathbf{Q},\mathbf{G}^M} \big|\mathbf{Q}+\mathbf{G}^M,\nu\big\rangle\big\langle\mathbf{Q}+\mathbf{G}^M,\nu\big|\chi\big\rangle = \sum_{\mathbf{Q},\mathbf{G}^M} c^{\nu}_{\mathbf{Q}+\mathbf{G}^M}\big|\mathbf{Q}+\mathbf{G}^M,\nu\big\rangle\,, && (8.17)\\
\big\langle\mathbf{r}\big|\chi\big\rangle &= \chi(\mathbf{r}) = \sum_{\mathbf{Q},\mathbf{G}^M} c^{\nu}_{\mathbf{Q}+\mathbf{G}^M} e^{i(\mathbf{Q}+\mathbf{G}^M)\mathbf{r}}\,, && (8.18)\\
\text{with} &\quad \sum_{\mathbf{Q},\mathbf{G}^M,\mathbf{G}^{M\prime}} \big|\mathbf{Q}+\mathbf{G}^M,\nu\big\rangle\big\langle\mathbf{Q}+\mathbf{G}^{M\prime},\nu\big| = \mathbf{1}\,, && (8.19)\\
\text{and} &\quad \big\langle\mathbf{Q}+\mathbf{G}^M,\nu\big|\mathbf{Q}'+\mathbf{G}^{M\prime},\nu\big\rangle = \delta_{\mathbf{Q}+\mathbf{G}^M,\mathbf{Q}'+\mathbf{G}^{M\prime}}\,. && (8.20)
\end{aligned}
$$

These basis states for the excitation of an electron hole pair can be represented by creation/annihilation operators. Within the center-of-mass description all momenta are measured from the $\mathbf{K}_{T/B}$-valley, as the exciton wave function is centered there. For the ILX states $\big|\mathbf{Q}\big\rangle$ one obtains:

$$
\begin{aligned}
\big|\mathbf{Q}\big\rangle &= \frac{1}{\sqrt{\mathcal{A}}}\sum_{\mathbf{k}} \phi_X(\mathbf{k})\hat{a}^{\dagger,c}_{\mathbf{K}_T+\mathbf{k}+m_e/M\mathbf{Q}}\hat{a}^{v}_{\mathbf{K}_B+\mathbf{k}-m_h/M\mathbf{Q}}\big|G\big\rangle && (8.21)\\
\big\langle\mathbf{Q}\big|\mathbf{Q}\big\rangle &\overset{!}{=} 1 \qquad \Rightarrow \qquad \frac{1}{\mathcal{A}}\sum_{\mathbf{k}} |\phi_X(\mathbf{k})|^2 \overset{!}{=} 1\,, && (8.22)
\end{aligned}
$$

with the exciton wave function $\phi_X(\mathbf{k})$. A Wannier equation is used to evaluate $\phi_X(\mathbf{k})$, which respresents the overlap of the electron (hole) wave function in the bottom (top) layer. The exciton Wannier equation is given by

$$\sum_{\mathbf{k}'}\left[\frac{\hbar^2\mathbf{k}^2}{2\mu}\delta_{\mathbf{k}\mathbf{k}'}-V_{|\mathbf{k}-\mathbf{k}'|}\right]\phi_{\mathbf{k}}=-E_B\phi_{\mathbf{k}}\,. \tag{8.23}$$

For the dielectrically screened Coulomb potential $V_{|\mathbf{k}-\mathbf{k}'|}$ the method described in Sec. (4.4.4) is used, reformulated as presented in Ref. [62]. Throughout the calculations it is assumed, that the bilayer is encapsulated within hBN substrate. The full exciton state wave function within the Moiré potential at a certain momentum $\mathbf{q}$ is subsequently evaluated as:

$$\langle\mathbf{q}|\chi\rangle \;=\; \chi(\mathbf{q})=\sum_{\mathbf{Q},\mathbf{G}^M}c^{\nu}_{\mathbf{Q}+\mathbf{G}^M}\langle\mathbf{q}|\mathbf{Q}+\mathbf{G}^M,\nu\rangle=c^{\nu}_{\mathbf{q}}\delta_{\mathbf{q},\mathbf{Q}+\mathbf{G}^M}\,, \tag{8.24}$$

Exploiting the benefits of the PW-expansion the real-space Moiré potential is expressed as Fourier series:

$$V^{\mathrm{M}}(\mathbf{r})=\sum_{\mathbf{G}^M}V^{\mathrm{M}}_{\mathbf{G}^M}e^{i\mathbf{G}^M\mathbf{R}}\,,\qquad V^{\mathrm{M}}_{\mathbf{G}^M}=\frac{1}{\mathcal{A}}\int \mathrm{d}^2\mathbf{r}V^{\mathrm{M}}(\mathbf{r})e^{-i\mathbf{G}^M\mathbf{R}} \tag{8.25}$$

The latter equation enables the calulation of the Fourier coefficients of the potential matrix $V^{\mathrm{M}}_{\mathbf{G}^M}$, where the potential itself is given by a mapping on DFT calculations according to $V^{\mathrm{M}}(\mathbf{r})\approx\sum_{j=1}^{6}V_je^{i\mathbf{G}^M_j\mathbf{r}}$ [50]. $\mathbf{G}^M_j$ represents the first shell of reciprocal Moiré lattice vectors and $V_j=Ve^{i\phi}$ with the parameters V,ϕ given in Tab. (C.4). Due to the $\hat{C}_3$ symmetry $V_{1,3,5}$ are equivalent as well as $V_{2,4,6}$. Additionally $V_1=V_4^*$ holds. The PW-expansion is applied to the total equation, therefore (8.17) is inserted into (8.16):

$$\sum_{\mathbf{Q},\mathbf{G}^M}\left[\frac{\hbar^2\mathbf{Q}'^2}{2M}-E^{\lambda}_{\mathbf{Q}'}+\sum_{\mathbf{G}^{M'}}V^{\mathrm{M}}_{\mathbf{G}^{M'}}e^{i\mathbf{G}^{M'}\mathbf{R}}\right]c^{\nu}_{\mathbf{Q}+\mathbf{G}^M}|\mathbf{Q}+\mathbf{G}^M,\nu\rangle \;=\; 0 \tag{8.26}$$

By multiplying from the right with $\langle\mathbf{Q}+\mathbf{G}^M,\nu|$ one obtains an eigenvalue problem for $c^{\nu}_{\mathbf{Q}+\mathbf{G}^M}$:

$$\sum_{\mathbf{Q},\mathbf{G}^M}\left[\frac{\hbar^2\mathbf{Q}'^2}{2M}\right]\delta_{\mathbf{Q}',\mathbf{Q}+\mathbf{G}^M}c^{\nu}_{\mathbf{Q}+\mathbf{G}^M}+\sum_{\mathbf{Q},\mathbf{G}^M,\mathbf{G}^{M'}}V^{\mathrm{M}}_{\mathbf{G}^M-\mathbf{G}^{M'}}c^{\nu}_{\mathbf{Q}+\mathbf{G}^M-\mathbf{G}^{M'}} \;=\; 0\,, \tag{8.27}$$

which results in the main equation for center-of-mass ILX in a real-space Moiré-potential.

Eigenvalues and -states can be found from diagonalizing the ILX Wannier equation:

$$\frac{\hbar^2}{2M}\left(\mathbf{Q}-\mathbf{G}^M\right)^2 c^{\nu}_{\mathbf{Q}-\mathbf{G}^M}\delta_{\mathbf{G}^M,\mathbf{G}^M} + \sum_{\mathbf{G}^{M\prime}} V^{\mathrm{M}}_{\mathbf{G}^M,\mathbf{G}^{M\prime}} c^{\nu}_{\mathbf{Q}-\mathbf{G}^{M\prime}} \; = \; 0\,, \tag{8.28}$$

where $V^{\mathrm{M}}_{\mathbf{G}^M,\mathbf{G}^{M\prime}} = V^{\mathrm{M}}_{\mathbf{G}^M-\mathbf{G}^{M\prime}}$ are calculated from Eq. (8.25) and the corresponding parametrization of the Moiré potential.
The energies $\varepsilon^{\nu}_{\mathbf{Q}+\mathbf{G}^M}$ and coefficients $c^{\nu}_{\mathbf{Q}+\mathbf{G}^M}$ for center-of-mass ILX state $\left|\mathbf{Q}+\mathbf{G}^M,\nu\right\rangle$ inside the Moiré potential are obtained from this procedure. The calculated ILX wave functions of the lowest (bound) states are localized at the minima of the Moiré potential. The dispersion of the ILX exhibits a flattening of the lowest bands with decreasing twist angle, which occurs due to the simultaneously decreasing size of the MBZ and thereby enhancing the localization of the ILX in the potential minima.

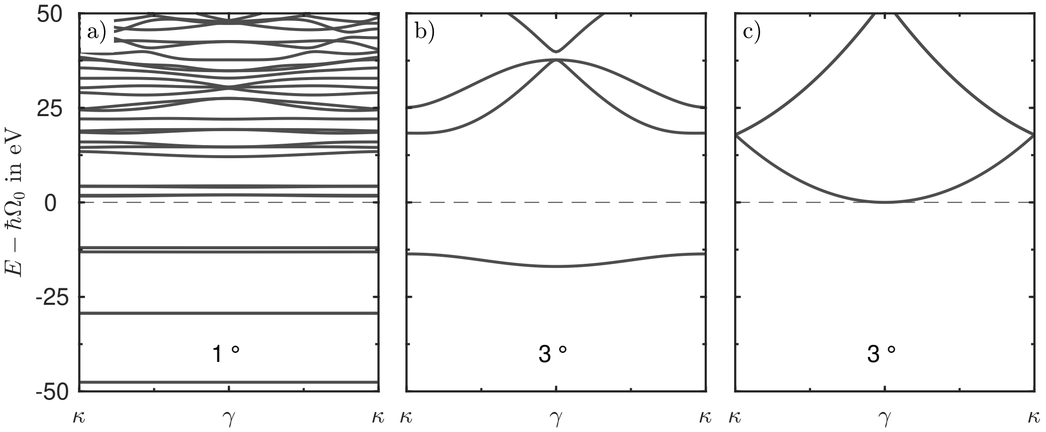

Figure 8.5.: **a)**: Dispersion of a center-of-mass exciton for a twist angle of 1 °. The bound ILX state are nearly flat, while their minimum is always at γ. **b)**: Dispersion of center-of-mass interlayer excitons for 3 °. The number of bound states decreases and the lowest state has a significant curvature. **c)**: Dispersion of center-of-mass interlayer excitons again for 3 ° without the Moiré potential V^M. The parabolic dispersion of the ILX obey only the Moiré periodicity.

8.4. Interlayer Exciton Lifetime

The radiative lifetime of an ILX is calculated by utilizing Fermis Golden Rule for a thermal ensemble [212, 213]. The probability for a transition from an initial ILX state $\left|\chi_\alpha\right\rangle$ to a final photon state $\left|\mathbf{q},\lambda\right\rangle$ is inversly proportional to the lifetime of the ILX. It is given by

$$\begin{aligned} \tau_{ILX}^{-1} &= \frac{2\pi}{\hbar}\sum_{if}|\langle f|H_{LM}|i\rangle|^2\delta(\varepsilon_i-\varepsilon_f)N_i \\ &= \frac{2\pi}{\hbar}\sum_{\mathbf{q},\lambda}\sum_{\alpha}|\langle \mathbf{q},\lambda|H_{LM}|\chi_\alpha\rangle|^2\delta(\varepsilon_{\mathbf{q},\lambda}-\varepsilon_\alpha)N_\alpha \end{aligned} \tag{8.29}$$

with H_{LM} being the light-matter interaction Hamiltonian in minimal coupling derived in Sec. (4.6.1) and $\alpha \in \{\mathbf{Q}+\mathbf{G}^M,\nu\}$. The energy conserving δ-function defines the transition energy while N_α is the thermal occupation of the ILX states, obey a Boltzmann distribution [212]. For the occupation the constraint $\sum_\alpha N_\alpha = 1$ holds, therefore the occupation is normalized to one. The photon state $\left|\mathbf{q},\lambda\right\rangle$ of momentum $\mathbf{q}$ and polarization λ couples to the ILX state $\left|\chi_\alpha\right\rangle$, see (8.24). This ILX state is obtained as described before. The resolution of unity (8.19) is exploited to expand the ILX state in the plane wave basis:

$$\tau_{ILX}^{-1}=\frac{2\pi}{\hbar}\sum_{\mathbf{q},\lambda}\sum_{\mathbf{Q},\nu}\left|\sum_{\mathbf{G}^M,\mathbf{G}^{M\prime}}\langle \mathbf{q},\lambda|H_{LM}|\mathbf{Q}+\mathbf{G}^M,\nu\rangle c^{\nu}_{\mathbf{Q}+\mathbf{G}^M+\mathbf{G}^{M\prime}}\right|^2\delta(\varepsilon_{\mathbf{q},\lambda}-\varepsilon_{\mathbf{Q},\nu})N_{\mathbf{Q},\nu} \tag{8.30}$$

The task is to derive an expression for $\langle \mathbf{q},\lambda|H_{LM}|\mathbf{Q}+\mathbf{G}^M,\nu\rangle$. Recalling the light-matter Hamiltonian from Eq. (4.175) for electrons and holes is the starting point for calculating the transition matrix element in Eq. (8.30):

$$H_{LM} = \frac{e}{m_0}\sum_s\int \mathrm{d}^3\mathbf{r}\hat{\psi}_s^\dagger(\mathbf{r})\mathbf{p}\mathbf{A}(\mathbf{R})\hat{\psi}_s(\mathbf{r}) \tag{8.31}$$

$$= \frac{e}{m_0}\sum_{\mathbf{R},\mathbf{R}',\nu,\nu'}\mathbf{A}(\mathbf{R})a^\dagger_{\mathbf{R},\nu}a_{\mathbf{R}',\nu'}\mathbf{p}^{\nu\nu'}(\mathbf{R}-\mathbf{R}')\,, \tag{8.32}$$

with $\mathbf{p}^{\nu\nu'}(\mathbf{R}-\mathbf{R}')=N^{-1}\sum_\rho e^{i\rho(\mathbf{R}'-\mathbf{R})}\mathbf{p}^{\nu\nu'}(\rho)$ being the momentum operator matrix elements. Furthermore the normal mode expansion of $\mathbf{A}$ (in SI units) is given by [131]

$$\mathbf{A}(\mathbf{R}) = \sum_{\mathbf{q},\lambda}\sqrt{\frac{\hbar}{2\varepsilon_0 c n^2 q\Omega}}\mathbf{e}_{\mathbf{q},\lambda}\left(b_{\mathbf{q},\lambda}e^{i\mathbf{q}_\parallel\mathbf{R}}+b^\dagger_{-\mathbf{q},\lambda}e^{-i\mathbf{q}_\parallel\mathbf{R}}\right)\,. \tag{8.33}$$

By combining (8.32) and (8.33) the following representation of H_{LM} is obtained:

$$\begin{aligned} H_{LM} &= \frac{1}{N}\frac{e}{m_0}\sqrt{\frac{\hbar}{2\varepsilon_0 c n^2 q \Omega}} \sum_{\mathbf{R},\mathbf{R}',\nu,\nu'} \sum_{\mathbf{q},\lambda} a^{\dagger}_{\mathbf{R},\nu} a_{\mathbf{R}',\nu'} \frac{1}{\sqrt{\mathbf{q}}} \\ &\times \sum_{\rho} e^{i\rho(\mathbf{R}'-\mathbf{R})} \mathbf{e}_{\mathbf{q},\lambda} \mathbf{p}^{\nu\nu'}(\rho) \left(b_{\mathbf{q},\lambda} e^{i\mathbf{q}_{\|}\mathbf{R}} + b^{\dagger}_{\mathbf{q},\lambda} e^{-i\mathbf{q}_{\|}\mathbf{R}} \right) . \end{aligned} \tag{8.34}$$

In order to obtain the matrix elements $\langle \mathbf{q}, \lambda | H_{LM} | \mathbf{Q} + \mathbf{G}^M, \nu \rangle$ the excited exciton wave function $|\mathbf{Q}, \nu\rangle$ (cf. Eq. (8.21)) is expressed by using the Wannier representation of the creation (annihilation) operators

$$\begin{aligned} a^{v}_{\mathbf{q}} &= \frac{1}{\sqrt{N}} \sum_{\mathbf{R}} e^{-i\mathbf{q}\mathbf{R}} a^{v}_{\mathbf{R}} , \\ a^{\dagger,c}_{\mathbf{q}} &= \frac{1}{\sqrt{N}} \sum_{\mathbf{R}'} e^{-i\mathbf{q}\mathbf{R}'} a^{\dagger,c}_{\mathbf{R}'} . \end{aligned} \tag{8.35}$$

Throughout the remaining parts of this section it is assumed that the electron and hole forming the ILX have been excited at the $\mathbf{K}$-point. As the electron hole exchange between $\mathbf{K}, \mathbf{K}'$ is weak, excitations from both valleys can be described seperately as they are still connected by time-reversal symmetry. Inducing a finite twist angle $\theta > 0\,°$ leads to a momentum displacement of the valence and the conduction band $\mathbf{Q} = (\mathbf{K}_T + \mathbf{G}_T) - (\mathbf{K}_B + \mathbf{G}_B)$. Thereby the transition from the ILX to the ground state becomes indirect. Using this together with Eqs. (8.35) the ILX state (8.21) is expressed as

$$\begin{aligned} |\mathbf{Q} + \mathbf{G}^M, \nu\rangle &= \frac{1}{\sqrt{\mathcal{A}}}\frac{1}{N^2} \sum_{\mathbf{R},\mathbf{R}'} \phi_X(\mathbf{R}'-\mathbf{R}) e^{i(\mathbf{K}_T\mathbf{R}' - \mathbf{K}_B\mathbf{R})} \\ &\times e^{i(\mathbf{Q}-\mathbf{G}^M)\left(\frac{m_e}{M}\mathbf{R}' + \frac{m_h}{M}\mathbf{R}\right)} \hat{a}^{\dagger,c}_{\mathbf{R}'} \hat{a}^{v}_{\mathbf{R}} |G\rangle \end{aligned} \tag{8.36}$$

In the next step both Eq. (8.34) and (8.36) are combined. The abbreviations $\mathbf{k}_c = \mathbf{K}_T + \mathbf{k} + \frac{m_e}{M}(\mathbf{Q} - \mathbf{G}^M)$ and $\mathbf{k}_v = \mathbf{K}_B + \mathbf{k} - \frac{m_h}{M}(\mathbf{Q} - \mathbf{G}^M)$ are used. Considering $N^{-1}\sum_{\mathbf{R}} e^{i\mathbf{k}\mathbf{R}} = \delta_{\mathbf{k},\mathbf{G}}$ one obtains

$$\begin{aligned} \langle \mathbf{q}, \lambda | H_{LM} | \mathbf{Q} + \mathbf{G}^M, \nu \rangle &= \frac{e}{m_0}\frac{1}{\sqrt{\mathcal{A}}}\sqrt{\frac{\hbar}{2\varepsilon_0 c n^2 q \Omega}} \sum_{\rho,\mathbf{k}} \phi_X(\mathbf{k}) \underbrace{\frac{m_0}{e}\dot{\mathbf{j}}^{vc}_{-\mathbf{q}\lambda}(\rho)}_{\mathbf{p}^{vc}_{-\mathbf{q}\lambda}(\rho)} \\ &\times \sum_{\mathbf{G}_T,\mathbf{G}_B} \delta_{-\rho+\mathbf{q}_{\|}/2-\mathbf{k}_v,\mathbf{G}_B} \delta_{\rho+\mathbf{q}_{\|}/2+\mathbf{k}_v,\mathbf{G}_T} \end{aligned} \tag{8.37}$$

The correspondence between the momentum operator $\mathbf{p}$ and the current operator $\mathbf{j}$ in minimal coupling (see Sec. (4.6.1)) has been used in order to introduce the current operator matrix elements. Though these are depending on the polarization $\mathbf{e}_\pm$ as has been pointed out before, the mixing of $\mathbf{e}_-$-polarized components of $\mathbf{j}$ at $\mathbf{K}$ is small, see Ref. [50]. The matrix elements are thus approximated by their leading Fourier component, which makes them a constant in real-space. It remains $\mathbf{j}^{vc}_{-\mathbf{q}\lambda}(\rho) = \mathbf{D}_+$. The exciton wave function $\phi_X(\mathbf{k})$ represents the relative electron hole wave function. Due to the separation between relative $\mathbf{k}$ and center-of-mass momenta $\mathbf{Q}$ the relative momentum is neglected and therefore not relevant for the momentum conservation. One is left with

$$\begin{aligned}\left\langle \mathbf{q},\lambda\middle| H_{LM} \middle|\mathbf{Q}+\mathbf{G}^M,\nu\right\rangle &= \sqrt{\frac{\hbar}{2\varepsilon_0 c n^2 q\Omega}}\mathbf{D}_+\frac{1}{\sqrt{\mathcal{A}}}\sum_{\mathbf{k}}\phi_X(\mathbf{k}) \\ &\times\sum_{\mathbf{G}^M,\mathbf{G}_T,\mathbf{G}_B}\delta_{\mathbf{Q}-\mathbf{G}^M,(\mathbf{K}_T+\mathbf{G}_T)-(\mathbf{K}_B+\mathbf{G}_B)+\mathbf{q}_\parallel}\,. \qquad (8.38)\end{aligned}$$

The terms within the momentum conserving δ-functions demand $\mathbf{Q}-\mathbf{G}^M = (\mathbf{K}_T+\mathbf{G}_T)-(\mathbf{K}_B+\mathbf{G}_B)+\mathbf{q}_\parallel$. Considering the sums over the reciprocal lattice vector $\mathbf{G}^M$, $\mathbf{G}_T$, $\mathbf{G}_B$ these are to be read as a general umklapp condition. Due to the choice of small angles, which causes the MBZ to be much smaller the the BZs of the top and bottom layer, this condition is ensured for $\mathbf{G}_{T/B}$. The finite momentum induced by the displacement of the top and bottom bands therefore has to be left for the photon $(\mathbf{Q}-\mathbf{G}^M) = (\mathbf{K}_T-\mathbf{K}_B)+\mathbf{q}_\parallel$. Due to the steep disperion of photons the first MBZ provides all necessary contributions. The finite momentum of $\mathbf{K}_T-\mathbf{K}_B$ corresponds the κ-point of the MBZ. In conclusion only ILX at the κ-point of the first MBZ couple to photon states. It is evident that the twist angle effectively enlarges the momentum displacement $\mathbf{K}_T-\mathbf{K}_B$ of the ILX and the photon state. The probability for radiative decay decreases as the transition becomes indirect.

In Eq. (8.30) the sum over λ sums up all polarization contributions of the light giving rise to the light-cone function [212]. According to the findings of discussing the momenta before, six light-cones at the κ/κ'-points appear. Inserting (8.38) into (8.30) one obtains:

$$\begin{aligned}\tau_{ILX}^{-1} &= \frac{2\pi g^{rad}}{\hbar}\frac{\hbar|\phi_X(\mathbf{r}=0)|^2|\mathbf{D}_+|^2}{2\varepsilon_0 c n^2\Omega}\sum_{\nu}\sum_{\mathbf{q}_\parallel,q_z}\frac{N_{\kappa+\mathbf{q}_\parallel,\nu}}{2\sqrt{\mathbf{q}_\parallel^2+q_z^2}}\,\delta\left(\frac{\hbar c}{n}\sqrt{\mathbf{q}_\parallel^2+q_z^2}-\varepsilon_{\mathbf{Q},\nu}\right) \\ &\quad\times\left|c_\kappa^\nu\right|^2\left\{1+\left(1-\left(\frac{\mathbf{q}_\parallel}{\sqrt{\mathbf{q}_\parallel^2+q_z^2}}\right)^2\right)\right\}\,. \qquad (8.39)\end{aligned}$$

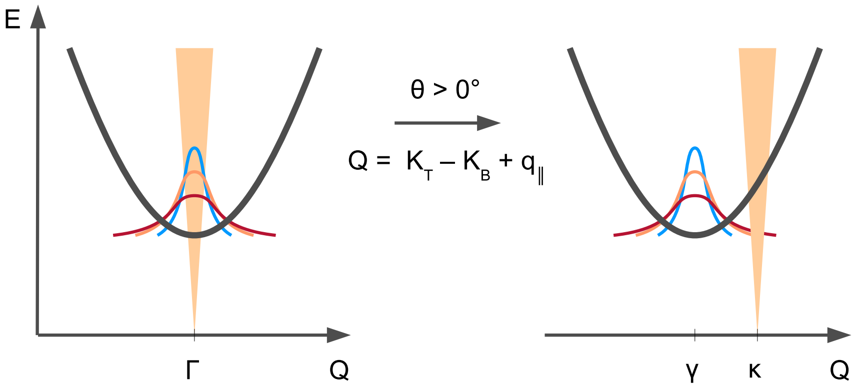

Figure 8.6.: Schematic representation of the influence of the temperature (left) and the indirectness of the ILX transition (right). The broadening of the thermal distribution at Γ/γ causes a redistribution of occupation towards the edges of the BZ. Increasing the twist angle shifts the light-cone away from the γ-point to the κ-point. The finite momentum between the $\mathbf{K}_T$- and $\mathbf{K}_B$-valley causes the ILX to become an indrect exciton.

The sum over the photon momentum $\mathbf{q}_\parallel$ and q_z are written as integral and evaluated. The factor $g^{rad} = 2$ to account for the contribution from the $\mathbf{K}'$-point due to time-reversal symmetry. The energy conversion implied in the δ-function is transformed to a θ-function by evaluating the q_z-integral. This limits the $\mathbf{q}_\parallel$-integral to the maximum momentum provided by the light-cone $q_0^\nu = n\varepsilon/\hbar c$, where $\varepsilon = \varepsilon_{\mathbf{Q},\nu} + E_X$ is determined by the spectral position of the ILX and $n = 2.15$ is the index of refraction for hBN. The integral is evaluated in polar coordinates. After further summarization one is left with

$$\begin{aligned} \tau_{ILX}^{-1} &= \frac{4\pi^2}{\hbar}\frac{\hbar|\phi_X(\mathbf{r}=0)|^2}{2\varepsilon_0 c n^2}\sum_\nu N_{\kappa+\mathbf{q}_\parallel,\nu} \\ &\times \int_0^{q_0^\nu} \mathrm{d}q_\parallel \frac{q_\parallel}{\sqrt{(q_0^\nu)^2 - q_\parallel^2}} \left|\mathbf{D}_+ c_\kappa^\nu\right|^2 \left(1 - \left(\frac{q_\parallel}{q_0^\nu}\right)^2\right) . \end{aligned} \tag{8.40}$$

The angle-dependence of the lifetime is hidden in the plane wave expansion. For small angles it becomes numerically demanding as more and more $\mathbf{G}^M$ have to be taken into account for convergence. The results of evaluating Eq. (8.40) for increasing twist angles and rising temperatures are plotted in Fig. (8.7). The parametrization for the investigated WSe$_2$/MoSe$_2$ bilayer have been taken from Ref. [50] and can be found in Tab. (C.4) in the appendix.

The lifetime in Fig. (8.7a) is in the order of several nanoseconds, whereas typical radiative lifetimes of excitons in TMDs are in the picosecond range [192]. With increasing angle the

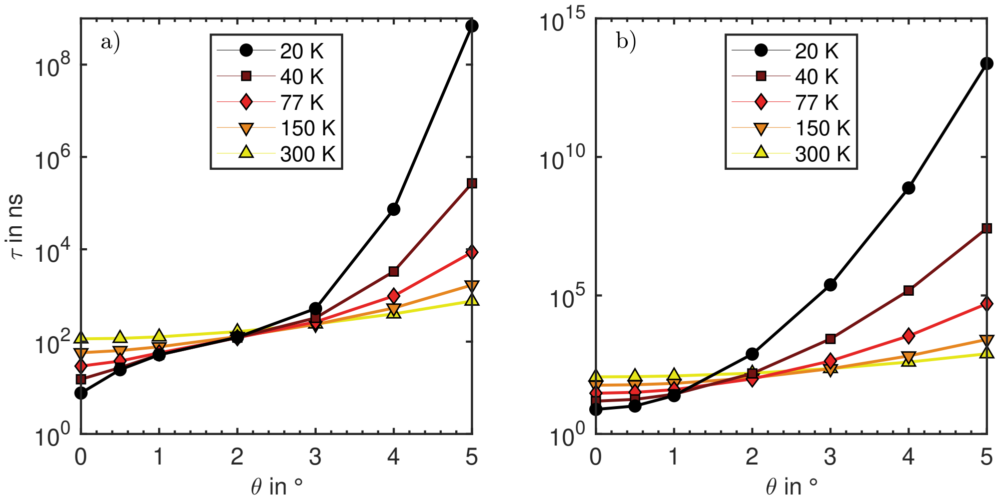

Figure 8.7.: **a)**: Lifetime τ of the ILX in a $WSe_2/MoSe_2$ bilayer for twist angles of $0\,°$, $0.5\,°$, $1\,°$, $2\,°$, $3\,°$, $4\,°$, and $5\,°$ respectively. The temperature has been increased from 20 K to 300 K as labeled. **b)**: Same plot as a) but without the Moiré potential. The values of τ for $0\,°$ are equal for both plots.

lifetime increases drastically for low temperatures, e.g. from $2\,°$ to $3\,°$ for 20 K it rises from $\sim$ 100 ns to nearly $\sim$ 1000 ns. This strong increase is reduced when rising the temperature. For a twist angle of $0\,°$ up to $\sim\ 2\,°$ the lifetime is increased with increasing temperature, above $\sim\ 2\,°$ this behaviour inverts. An increase in temperature broadens the occupation, while for low temperatures a sharp occupation centered at the dipersion minimum γ is found. Nevertheless, the photon and the ILX couple at κ and thus the inverse temperature dependence for lifetimes above and below $2\,°$ reflects the sharpness of the thermal distribution. For zero twist angle the radiative lifetime of the thermalized ILX depends linearly on the temperature [212].

The thermal occupation has its maximum at the MBZ center γ. The light-cone function intersects the ILX dispersion at **Q**-states in the vicinity of κ to contribute to the radiative decay as it intersects the ILX dispersion. From Fig. (8.6) it can be understood that for increasing angles the size of the MBZ increases thereby shifting the light-cone, that is centered at κ, away from the ILX dispersion minimum at γ. For small angles the MBZ decreases in size, which has the sideffect of redistributing the occupation $N_{\mathbf{Q},\nu}$ also to the vincinity of κ. If the MBZ becomes large enough, the dispersion of the ILX states is not negligible, which effectively drains occupation from κ to γ.

The presence of the Moiré potential decreases the maximum value of the lifetime, as can be found by comparing Fig. (8.7a) and (8.7b). The curvature of the lifetime changes sign from low to medium angles, if the Moiré potential is present. The Moiré potential couples different ILX momenta and thereby effectively softens the momentum conservation. Thus more momenta contribute to the transition from an excited ILX to a photon, which overall decreases the lifetime.

8.5. Conclusion

In conclusion the twisted bilayers materials provide interesting physics considering the interlayer excitons. A finite twist angle is the origin of a Moiré pattern, that can be described in terms of the lattice basis vectors as has been shown in the beginning of this chapter. The periodic Moiré lattice can also be described in terms of reciprocal space, where the MBZ is found. This MBZ can be constructed from the difference of the top and bottom layer reciprocal lattice vectors. In order to describe the ground state band structure of twisted bilayers the TB-method within the Slater-Koster ansatz has been utilized to employ a general model. This model introduces an interlayer interaction, that enables hopping between the layers, while it allows for using existing TB-models of monolayers. Though it has been tested for bilayers of the same material, it provides a promising perspective for describing various TMD bilayers. In order to investigate on interlayer excitons that form in bilayers, the Moiré pattern plays a central role. By inducing a band gap change a periodic potential traps the excitons. These interlayer excitons exhibit lifetimes of several nanoseconds. The dependence of the lifetime on the twist angle as well as on the temperature has been calculated. The lifetime changes up to several orders of magnitude when increasing the angle. The dependence on lifetime and angle is a combined effect of the broadening of the ILX occupation for increasing temperatures as well as a change of size of the MBZ when changing the angle. The latter shifts the light-cone, that selects the bright states, towards or away from the dispersion minima at the γ-point in the center of the MBZ, thereby effectively diminishing the occupation. For a finite rotation the ILX transition becomes indirect, which reduces the probability of radiative decay as the light-cone is shifted away from the maxima of the occupation.

9. Conclusion and Outlook

Within this work the optical response of TMD monolayers and bilayers to the photoexcitation of charge carriers has been investigated. As central equation describing the excitations, the semiconductor Bloch equations have been employed.As a starting point exciton eigenvalue problem has been analyzed in form of a Wannier equation, that is contained in the semiconductor Bloch equations. Excitons in TMD monolayers exhibit a non-hydrogenic Rydberg series, due to their two-dimensional polarizable shape, which causes a linear dependence of the dielectric function on the transferred momentum for Coulomb processes. In response to magnetic fields, the large binding energies of excitons necessitate high field strength in order to obtain significant shifts.

The description of the many-body interactions of excited carriers is based on the ground state band structure, which is obtained from DFT+GW calculations that are interpolated on a discretized $\mathbf{k}$-grid. From these *ab-initio*-calculation material-realistic Coulomb matrix elements are obtained, which are necessary to describe the dominant Coulomb interaction of excited charge carriers in TMD monolayers on a material-realistic level. In order to describe different substrate structures, the Wannier function continuum electrostatics-scheme employs macroscopic dielectric screening for the Coulomb matrix elements.

For the description of many-body interactions, the formalism of non-equilibrium Green's functions has been employed. Correlations have been treated in the GW-approximation, that results in the well-established screened exchange Coulomb hole-approximation in the limit of static interaction. Successively, the obtained theoretical description of many-body correlations has been adapted to the characteristic valley structure in the band structure of TMD monolayers. It has been found that the interband exchange interaction is best described by a bare interaction, while the screened exchange and Coulomb hole terms only appear for intraband excitations.

In the context of pump-probe experiments the SBE have been utilized in two different ways. On the one hand, the electric field accounted for a weak ultrashort laser pulse, in order to probe the absorption spectrum. On the other hand, the electric field has been used as a strong pump laser to elucidate the power-dependence of the total charge carrier density. Considering the absorption spectra the optical response of MoS_2, $MoSe_2$, WS_2, and WSe_2

monolayers in the presence of excited carriers has been investigated. Before the recombination of electron and hole pairs, the excited carriers occupy the band structure valleys according to a Fermi distribution of a given density and temperature. Different many-body effects have been identified among which are Pauli blocking, that causes a blueshift of the bound states as well as spectral bleaching of the exciton peaks with increasing density. Due to plasma screening of the excited carriers, the binding energy of the excitons is reduced until they dissociate at the Mott-density. As most important result band structure renormalizations cause a direct-to-indirect transition of the band gap for all considered monolayer TMDs. The combination of the orbital character of Bloch states and electron and hole populations defines the characteristic momentum dependence of the Coulomb interaction for TMDs. Especially the bare electron hole exchange interaction causes a relative shift between the $\mathbf{K}$- and the Σ-valley that leads to indirect band gaps. For elevated densities, the advantage of a direct gap semiconductor thus slowly vanishes, as carriers are drained from the optical bright transition at $\mathbf{K}$ to the Σ-valley. This has a direct impact on TMD monolayers being used as active material of a laser, as the peak gain curves show a characteristic roll-over behaviour due to the hampering of population inversion. The transition to indirect band gaps is also expected to cause a quenching of the photoluminescence intensity for high excitations.

Considering the power dependence of the total charge carrier density the monolayer is illuminated by laser pulses of different fluences. The assumption of a linear absorption coefficient does not reflect the presence of strong many-body interactions that prevail in monolayer TMDs. It is expected, that the total density increases in a non-linear way with the fluence. Nevertheless, it has been demonstrated that the density increases linearly for low fluences up to $5\ \mu\mathrm{J\ cm}^{-2}$ for pumping at the band gap, while a pump above the gap provides linear increase for fluences up to $50\ \mu\mathrm{J\ cm}^{-2}$ ($20\ \mu\mathrm{J\ cm}^{-2}$) for the sulfides (selenides). For a pump at the band gap the effects of Pauli blocking and band structure renormalizations partially compensate each other. Pauli blocking obstructs phase space, while the renormalizations shift the density-of-states away from the pump pulse providing an effective clearing of the states, overall leading to a linear dependence of the density to the fluence. Pumping above the gap, the scattering time of carriers determines whether the density increases linearly with the fluence or not. Excitation induced dephasing dampens the inter-band polarizations by changing the linewidth of the excitonic peaks and band-to-band transitions in dependence of the density. This has been modeled and parameterized to account for nonlinearities from density-dependent dephasing effects. For fluences up to $1000\ \mu\mathrm{J\ cm}^{-2}$ the increase in the density slows down for all four monolayer TMDs.

In the last part TMD heterobilayers of type-II band-alignment, exemplified by a $\mathrm{WSe}_2/\mathrm{MoSe}_2$

bilayer, have been studied. Interlayer excitons, where electron and hole are located in different layers, are of high interest in research due to their long lifetime. A Moiré pattern arises in the bilayer systems, if a finite twist angle between the layers is present. This Moiré periodicity changes the single-particle properties, by inducing a periodic modulation of the band gap. For small angles the relative and center-of-mass motion of interlayer excitons in this Moiré potential have been separated, leaving the interlayer excitons as composite quasi-particle. The lifetime of interlayer excitons has been successively calculated by utilizing Fermis golden rule to describe the radiative decay of a thermalized ensemble of interlayer excitons. The hereby obtained probability for radiative decay of interlayer excitons in a $WSe_2/MoSe_2$ bilayer yields lifetimes on the nanosecond scale. This is several orders of magnitude longer than the lifetime of intralayer excitons, which is on the order of picoseconds. The lifetime strongly depends on the twist angle and the temperature. The twist angle induces a momentum displacement between the conduction and the valence band, that causes the interlayer exciton transition to become indirect. Thereby the light-cone is shifted away from the maximum of the occupation, centered in the first Moiré Brillouin zone. At large twist angles this reduces the probability of radiative decay. Lowering the temperature narrows the distribution of interlayer excitons, which decreases the occupation of states within the light-cone and thus increases the lifetime. A temperature increase causes the opposite. The presence of the Moiré potential opens up possible scattering channels by coupling interlayer excitons of different momenta, thereby overall decreasing the lifetime. In the limit of $\theta = 0\,^\circ$ the lifetime depends linearly on the temperature. An increase of the twist angle increases the lifetime up to several orders of magnitude.

Concluding this last chapter, future perspectives of this work will be shown. A general improvement of the semiconductor Bloch equations used here would be the inclusion of electron-phonon interaction. The calculation of carrier dynamics would directly benefit from material-realistic scattering processes. From a theoretical point of view it is also of interest to treat the Coulomb interaction in the frequency-dependent GW-approximation, thereby obtaining access to the excitation induced dephasing. Other materials such as perovskites exhibit fascinating physical phenomena and could be part of future research. In order to do so an *ab-initio*-ground state calculation is a necessary step towards the theoretical description of many-body effects within novel materials. Concerning the interlayer excitons in bilayer systems, it is of interest to derive a comprehensive theory including the calculation of band structures and absorption spectra. A full microscopical understanding of the dipole coupling strength of interlayer exciton transitions is desired.

Appendix

A. Numerical Treatment of the Coulomb Singularity

When numerically calculating the Coulomb matrix elements, care has to be taken for the discretized matrix elements where $\mathbf{k} = \mathbf{k}'$, as they diverge. This problem can be overcome by analytically calculating the integral over the respective $\mathbf{k}$-point cell or evaluating this integral numerically, which is necessary in the presence of screening. Commonly the integral over the Coulomb matrix and any $\mathbf{k}$-dependent function can be split by adding a zero, which results in discretized form in:

$$\sum_{\mathbf{k}'} V_{\mathbf{k}_i\mathbf{k}'} f_{\mathbf{k}'} \quad = \quad \sum_{\mathbf{k}\neq\mathbf{k}'} V_{\mathbf{k}\mathbf{k}'} f_{\mathbf{k}'} - f_{\mathbf{k}} \sum_{\mathbf{k}\neq\mathbf{k}'} V_{\mathbf{k}\mathbf{k}'} F_{\mathbf{k}\mathbf{k}'} + f_{\mathbf{k}} \int \mathrm{d}\tilde{\mathbf{k}} V_{\mathbf{k}\tilde{\mathbf{k}}} F_{\mathbf{k}\tilde{\mathbf{k}}}\,. \tag{A.1}$$

The remaining integral can be evaluated numerically or in special cases analytically. A factor $F_{\mathbf{k}\mathbf{k}'} = 4\mathbf{k}^2/(\mathbf{k}^2 + \mathbf{k}'^2)^2$ to improve the convergence of the integral expression has been added. For an equidistant grid, like the Monkhorst-Pack grid that has been used here, the integration over the diverging point at $\mathbf{k} = \mathbf{k}'$ can be performed directly. If the bare interaction is calculated the integral can be solved analytically. Therefore the integral is transformed to polar coordinates and the symmetries of the hexagonal-shape area of one $\mathbf{k}$-cell are exploited. This hexagon can be divided into twelve pieces, each being a right-angled triangle. In all of these triangles the relation between the radial component is determined by the current angle of the double integral. The longest radius is determined by half the distance between neighbouring $\mathbf{k}$-points, $\Delta_{\mathbf{k}}/2$. The whole integral has to be normalized by the total area of the $\mathbf{k}$-point in order to avoid conflicts with the numerical weights $w_{\mathbf{k}'}$ of the discretized $\mathbf{k}$-mesh integration. One obtains

$$\begin{aligned} V_\delta^{\mathrm{MP}} \quad &= \quad \frac{e^2}{2\varepsilon_0 w_{\mathbf{k}}} \int \mathrm{d}^2\mathbf{k} \frac{1}{\mathbf{k}} = \frac{12e^2}{2\varepsilon_0} \int\limits_0^{\frac{\pi}{6}} \mathrm{d}\phi \int\limits_0^{\frac{\Delta_{\mathbf{k}}}{2\cos(\phi)}} \mathrm{d}k \frac{k}{k} \\ &= \quad \frac{e^2}{2\varepsilon_0 w_{\mathbf{k}'}} 6 \ln(3) \Delta_{\mathbf{k}'}\,. \end{aligned} \tag{A.2}$$

This integration can be easily adapted for a linear mesh in a Riemann integration for example:

$$V_\delta^{\text{lin}} = \frac{e^2}{2\varepsilon_0 w_{\mathbf{k}}} 12 \cdot 2 \tanh^{-1}\left(\tan\left(\frac{\pi}{8}\right)\right) \cdot \Delta_{\mathbf{k}} \approx \frac{e^2}{2\varepsilon_0 w_{\mathbf{k}}} 12 \cdot 0.8814 \cdot \Delta_{\mathbf{k}'} \,. \tag{A.3}$$

Note that this works only for the bare interaction. Plasma screening, expressed via an inverse dielectric function $\varepsilon^{-1}(\mathbf{q}, \omega)$ will change the integrand function. The transformation to polar coordinates is still useful as long as $\varepsilon^{-1}(\mathbf{q}) = \varepsilon^{-1}(|\mathbf{q}|)$, but the whole integral has to be performed numerically.

B. Derivation of the GW terms

Taking into account only Coulomb matrix elements with the index combinations $\lambda\lambda'\lambda''\lambda'''$, $\lambda\bar{\lambda}\bar{\lambda}'\lambda'$ or $\lambda\bar{\lambda}\lambda'\bar{\lambda}'$ results in a condition for λ, λ_3, λ_4 occuring in Eq. (4.100). This leads to:

$$
\begin{aligned}
(-i\hbar)^3 \sum_{\mathbf{k}',e',e'',e''',h',h'',h'''} \int_{-\infty}^{t} \mathrm{d}t' \Big[\; & G^{>,e'''h'}_{\mathbf{k}'}(t')G^{<,h''h}_{\mathbf{k}}(t')W^{<,eh'h''e'''}_{\mathbf{k}\mathbf{k}'\mathbf{k}\mathbf{k}'}(t',t)G^{\mathrm{R},e'''}_{\mathbf{k}'}(t,t')G^{\mathrm{A},h}_{\mathbf{k}}(t',t) \\
& +G^{>,e'''e'}_{\mathbf{k}'}(t')G^{<,e''h}_{\mathbf{k}}(t')W^{<,ee'e''e'''}_{\mathbf{k}\mathbf{k}'\mathbf{k}\mathbf{k}'}(t',t)G^{\mathrm{R},e'''}_{\mathbf{k}'}(t,t')G^{\mathrm{A},h}_{\mathbf{k}}(t',t) \\
& -G^{<,e'''h'}_{\mathbf{k}'}(t')G^{>,h''h}_{\mathbf{k}}(t')W^{>,eh'h''e'''}_{\mathbf{k}\mathbf{k}'\mathbf{k}\mathbf{k}'}(t',t)G^{\mathrm{R},e'''}_{\mathbf{k}'}(t,t')G^{\mathrm{A},h}_{\mathbf{k}}(t',t) \\
& -G^{<,e'''e'}_{\mathbf{k}'}(t')G^{>,e''h}_{\mathbf{k}}(t')W^{>,ee'e''e'''}_{\mathbf{k}\mathbf{k}'\mathbf{k}\mathbf{k}'}(t',t)G^{\mathrm{R},e'''}_{\mathbf{k}'}(t,t')G^{\mathrm{A},h}_{\mathbf{k}}(t',t) \\
& +G^{<,eh''}_{\mathbf{k}}(t')G^{>,h'''h'}_{\mathbf{k}'}(t')W^{<,h''h'hh'''}_{\mathbf{k}\mathbf{k}'\mathbf{k}\mathbf{k}'}(t,t')G^{\mathrm{R},e}_{\mathbf{k}}(t,t')G^{\mathrm{A},h'}_{\mathbf{k}'}(t',t) \\
& +G^{<,ee'}_{\mathbf{k}}(t')G^{>,e''h'}_{\mathbf{k}'}(t')W^{<,e'h'he''}_{\mathbf{k}\mathbf{k}'\mathbf{k}\mathbf{k}'}(t,t')G^{\mathrm{R},e}_{\mathbf{k}}(t,t')G^{\mathrm{A},h'}_{\mathbf{k}'}(t',t) \\
& -G^{>,eh''}_{\mathbf{k}}(t')G^{<,h'''h'}_{\mathbf{k}'}(t')W^{>,h''h'hh'''}_{\mathbf{k}\mathbf{k}'\mathbf{k}\mathbf{k}'}(t,t')G^{\mathrm{R},e}_{\mathbf{k}}(t,t')G^{\mathrm{A},h'}_{\mathbf{k}'}(t',t) \\
& -G^{>,ee'}_{\mathbf{k}}(t')G^{<,e''h'}_{\mathbf{k}'}(t')W^{>,e'h'he''}_{\mathbf{k}\mathbf{k}'\mathbf{k}\mathbf{k}'}(t,t')G^{\mathrm{R},e}_{\mathbf{k}}(t,t')G^{\mathrm{A},h'}_{\mathbf{k}'}(t',t) \\
& +G^{>,h''h'}_{\mathbf{k}'}(t')G^{<,e'h}_{\mathbf{k}}(t')W^{<,eh'e'h''}_{\mathbf{k}\mathbf{k}'\mathbf{k}\mathbf{k}'}(t',t)G^{\mathrm{R},h''}_{\mathbf{k}'}(t,t')G^{\mathrm{A},h}_{\mathbf{k}}(t',t) \\
& +G^{<,eh'}_{\mathbf{k}}(t')G^{>,e''e'}_{\mathbf{k}'}(t')W^{<,h'e'he''}_{\mathbf{k}\mathbf{k}'\mathbf{k}\mathbf{k}'}(t,t')G^{\mathrm{R},e}_{\mathbf{k}}(t,t')G^{\mathrm{A},e'}_{\mathbf{k}'}(t',t) \\
& -G^{<,h''h'}_{\mathbf{k}'}(t')G^{>,e'h}_{\mathbf{k}}(t')W^{>,eh'e'h''}_{\mathbf{k}\mathbf{k}'\mathbf{k}\mathbf{k}'}(t',t)G^{\mathrm{R},h''}_{\mathbf{k}'}(t,t')G^{\mathrm{A},h}_{\mathbf{k}}(t',t) \\
& -G^{>,eh'}_{\mathbf{k}}(t')G^{<,e''e'}_{\mathbf{k}'}(t')W^{>,h'e'he''}_{\mathbf{k}\mathbf{k}'\mathbf{k}\mathbf{k}'}(t,t')G^{\mathrm{R},e}_{\mathbf{k}}(t,t')G^{\mathrm{A},e'}_{\mathbf{k}'}(t',t) \quad \Big]
\end{aligned}
\tag{B.1}
$$

As praticed before when deriving the SBE, intraband polarizations will be neglected. By identify the remaining $G^{\gtrless,\lambda\lambda'}_{\mathbf{k}}(t')$ with microscopic polarizations $\psi^{\lambda'\lambda}_{\mathbf{k}}(t')$, the remaining functions inside the brackets are summarized:

$$\begin{aligned}\Big[\; & -\psi^{h'e'}_{\mathbf{k}'}(t')[G^{>,h}_{\mathbf{k}}(t')W^{>,eh'he'}_{\mathbf{kk}'\mathbf{kk}'}(t',t) - G^{<,h}_{\mathbf{k}}(t')W^{<,eh'he'}_{\mathbf{kk}'\mathbf{kk}'}(t',t)]G^{\mathrm{R},e'}_{\mathbf{k}'}(t,t')G^{\mathrm{A},h}_{\mathbf{k}}(t',t)\\ & -\psi^{he''}_{\mathbf{k}}(t')[G^{>,e'}_{\mathbf{k}'}(t')W^{>,ee'e''e'}_{\mathbf{kk}'\mathbf{kk}'}(t',t) - G^{<,e'}_{\mathbf{k}'}(t')W^{<,ee'e''e'}_{\mathbf{kk}'\mathbf{kk}'}(t',t)]G^{\mathrm{R},e'}_{\mathbf{k}'}(t,t')G^{\mathrm{A},h}_{\mathbf{k}}(t',t)\\ & -\psi^{h''e}_{\mathbf{k}}(t')[G^{>,h'}_{\mathbf{k}'}(t')W^{>,h''h'hh'}_{\mathbf{kk}'\mathbf{kk}'}(t,t') - G^{<,h'}_{\mathbf{k}'}(t')W^{<,h''h'hh'}_{\mathbf{kk}'\mathbf{kk}'}(t,t')]G^{\mathrm{R},e}_{\mathbf{k}}(t,t')G^{\mathrm{A},h'}_{\mathbf{k}'}(t',t)\\ & -\psi^{h'e'}_{\mathbf{k}'}(t')[G^{>,e}_{\mathbf{k}}(t')W^{>,eh'he'}_{\mathbf{kk}'\mathbf{kk}'}(t,t') - G^{<,e}_{\mathbf{k}}(t')W^{<,eh'he'}_{\mathbf{kk}'\mathbf{kk}'}(t,t')]G^{\mathrm{R},e}_{\mathbf{k}}(t,t')G^{\mathrm{A},h'}_{\mathbf{k}'}(t',t)\\ & -\psi^{he'}_{\mathbf{k}}(t')[G^{>,h'}_{\mathbf{k}'}(t')W^{>,eh'e'h'}_{\mathbf{kk}'\mathbf{kk}'}(t,t') - G^{<,h'}_{\mathbf{k}'}(t')W^{<,eh'e'h'}_{\mathbf{kk}'\mathbf{kk}'}(t,t')]G^{\mathrm{R},h'}_{\mathbf{k}}(t,t')G^{\mathrm{A},h}_{\mathbf{k}'}(t',t)\\ & -\psi^{h'e}_{\mathbf{k}'}(t')[G^{>,e'}_{\mathbf{k}}(t')W^{>,h'e'he'}_{\mathbf{kk}'\mathbf{kk}'}(t,t') - G^{<,e'}_{\mathbf{k}}(t')W^{<,h'e'he'}_{\mathbf{kk}'\mathbf{kk}'}(t,t')]G^{\mathrm{R},e}_{\mathbf{k}}(t,t')G^{\mathrm{A},e'}_{\mathbf{k}'}(t',t)\;\Big]\end{aligned} \tag{B.2}$$

At this point the quasi-equilibrium properties are exploited, thus a Fourer transformation with $t \rightarrow \omega$ is performed and all functions, that still carry two times, will depend only on the relative time $\tau = t - t'$. These are successively replaced by their Fourier representations (see Eq. (4.81)). The KMS relations (4.90) and (4.91) are employed. The populations do not carry a frequency dependence. The retarded and advanced Green's functions, depending only on one time argument, are replaced by their corresponding spectral functions.

$$
\begin{aligned}
& i\hbar \sum_{\mathbf{k}',e',e'',h',h''} \int_{-\infty}^{+\infty} \mathrm{d}t e^{i\omega t} \int_{-\infty}^{t} \mathrm{d}t' \int_{-\infty}^{+\infty} \frac{\mathrm{d}\bar{\omega}}{2\pi} \int_{-\infty}^{+\infty} \frac{\mathrm{d}\omega'}{2\pi} \int_{-\infty}^{+\infty} \frac{\mathrm{d}\omega''}{2\pi} \int_{-\infty}^{+\infty} \frac{\mathrm{d}\omega'''}{2\pi} \\
& \times e^{-i\bar{\omega}t'} e^{-i\omega'(t-t')} e^{-i\omega''(t-t')} e^{-i\omega'''(t-t')} \\
& \times \Big[\quad \psi_{\mathbf{k}'}^{h'e'}(\bar{\omega})[(1-F_{\mathbf{k}}^{h})W_{\mathbf{kk}'\mathbf{kk}'}^{>,eh'he'}(\omega') + F_{\mathbf{k}}^{h}W_{\mathbf{kk}'\mathbf{kk}'}^{<,eh'he'}(\omega')]\hat{A}_{\mathbf{k}'}^{e'}(\omega'')\hat{A}_{\mathbf{k}}^{,h}(\omega''') \\
& \quad + \psi_{\mathbf{k}}^{he''}(\bar{\omega})[(1-F_{\mathbf{k}'}^{e'})W_{\mathbf{kk}'\mathbf{kk}'}^{>,ee'e''e'}(\omega') + F_{\mathbf{k}'}^{e'}W_{\mathbf{kk}'\mathbf{kk}'}^{<,ee'e''e'}(\omega')]\hat{A}_{\mathbf{k}'}^{e'}(\omega'')\hat{A}_{\mathbf{k}}^{h}(\omega''') \\
& \quad + \psi_{\mathbf{k}}^{h''e}(\bar{\omega})[(1-F_{\mathbf{k}'}^{h'})W_{\mathbf{kk}'\mathbf{kk}'}^{<,h''h'hh'}(\omega') + F_{\mathbf{k}'}^{h'}W_{\mathbf{kk}'\mathbf{kk}'}^{>,h''h'hh'}(\omega')]\hat{A}_{\mathbf{k}}^{e}(\omega'')\hat{A}_{\mathbf{k}'}^{h'}(\omega''') \\
& \quad + \psi_{\mathbf{k}'}^{h'e'}(\bar{\omega})[(1-F_{\mathbf{k}}^{e})W_{\mathbf{kk}'\mathbf{kk}'}^{<,eh'he'}(\omega') + F_{\mathbf{k}}^{e}W_{\mathbf{kk}'\mathbf{kk}'}^{>,eh'he'}(\omega')]\hat{A}_{\mathbf{k}}^{e}(\omega'')\hat{A}_{\mathbf{k}'}^{h'}(\omega''') \\
& \quad + \psi_{\mathbf{k}}^{he'}(\bar{\omega})[(1-F_{\mathbf{k}'}^{h'})W_{\mathbf{kk}'\mathbf{kk}'}^{<,eh'e'h'}(\omega') + F_{\mathbf{k}'}^{h'}W_{\mathbf{kk}'\mathbf{kk}'}^{>,eh'e'h'}(\omega')]\hat{A}_{\mathbf{k}}^{h'}(\omega'')\hat{A}_{\mathbf{k}'}^{h}(\omega''') \\
& \quad + \psi_{\mathbf{k}}^{h'e}(\bar{\omega})[(1-F_{\mathbf{k}'}^{e'})W_{\mathbf{kk}'\mathbf{kk}'}^{<,h'e'he'}(\omega') + F_{\mathbf{k}'}^{e'}W_{\mathbf{kk}'\mathbf{kk}'}^{>,h'e'he'}(\omega')]\hat{A}_{\mathbf{k}}^{e}(\omega'')\hat{A}_{\mathbf{k}'}^{e'}(\omega''') \quad \Big]
\end{aligned}
\tag{B.3}
$$

The Green's functions of the greater and lesser screened Coulomb interaction $W^{\gtrless}$ are propagators of plasmons. The spectral function of these plasmons is identified as the retarded inverse dielectric function. Therefore the (bosonic) KMS relations hold and the following can be found [137, 155, 196]:

$$W_{\nu_1\nu_2\nu_3\nu_4}^{>}(\omega) - W_{\nu_1\nu_2\nu_3\nu_4}^{<}(\omega) = 2iV_{\nu_1\nu_2\nu_3\nu_4}\mathrm{Im}\varepsilon_{\mathbf{k}_1-\mathbf{k}_4}^{\mathrm{R},-1}(\omega) \tag{B.4}$$

$$W_{\nu_1\nu_2\nu_3\nu_4}^{>}(\omega) = (1+n_B(\omega))V_{\nu_1\nu_2\nu_3\nu_4}2i\mathrm{Im}\varepsilon_{\mathbf{k}_1-\mathbf{k}_4}^{\mathrm{R},-1}(\omega) \tag{B.5}$$

$$W_{\nu_1\nu_2\nu_3\nu_4}^{<}(\omega) = n_B(\omega)V_{\nu_1\nu_2\nu_3\nu_4}2i\mathrm{Im}\varepsilon_{\mathbf{k}_1-\mathbf{k}_4}^{\mathrm{R},-1}(\omega) \tag{B.6}$$

$$W_{\nu_1\nu_2\nu_3\nu_4}^{\gtrless}(-\omega) = W_{\nu_1\nu_2\nu_3\nu_4}^{\lessgtr}(\omega) \tag{B.7}$$

The properties (B.4) - (B.7) are employed into (B.3). Additionally a substitution of the collision integral from d$t' \to$ dτ is performed. After regrouping the frequencies in the exponential function according to their dependencies inside the integrals, one obtains:

$$
\begin{aligned}
i\hbar \sum_{\mathbf{k}',e',e'',h',h''} \int_{-\infty}^{+\infty} \frac{\mathrm{d}\bar{\omega}}{2\pi} \int_{-\infty}^{+\infty} \mathrm{d}t e^{i(\omega-\bar{\omega})t} \int_{-\infty}^{+\infty} \frac{\mathrm{d}\omega'}{2\pi} \int_{-\infty}^{+\infty} \frac{\mathrm{d}\omega''}{2\pi} \int_{-\infty}^{+\infty} \frac{\mathrm{d}\omega'''}{2\pi} \int_{0}^{+\infty} \mathrm{d}\tau e^{-i(\omega'+\omega''+\omega'''-\bar{\omega})\tau} \\
\times \Big[\quad & \psi_{\mathbf{k}'}^{h'e'}(\bar{\omega})(1 - F_{\mathbf{k}}^{h} + n_B(\omega'))V_{\mathbf{kk}'\mathbf{kk}'}^{eh'he'} 2i\mathrm{Im}\varepsilon_{\mathbf{k}-\mathbf{k}'}^{\mathrm{R},-1}(\omega')\hat{A}_{\mathbf{k}'}^{e'}(\omega'')\hat{A}_{\mathbf{k}}^{h}(\omega''') \\
& + \psi_{\mathbf{k}}^{he''}(\bar{\omega})(1 - F_{\mathbf{k}'}^{e'} + n_B(\omega'))V_{\mathbf{kk}'\mathbf{kk}'}^{ee'e''e'} 2i\mathrm{Im}\varepsilon_{\mathbf{k}-\mathbf{k}'}^{\mathrm{R},-1}(\omega')\hat{A}_{\mathbf{k}'}^{e'}(\omega'')\hat{A}_{\mathbf{k}}^{h}(\omega''') \\
& + \psi_{\mathbf{k}}^{h''e}(\bar{\omega})(1 - F_{\mathbf{k}'}^{h'} + n_B(\omega'))V_{\mathbf{kk}'\mathbf{kk}'}^{h''h'hh'} 2i\mathrm{Im}\varepsilon_{\mathbf{k}-\mathbf{k}'}^{\mathrm{R},-1}(\omega')\hat{A}_{\mathbf{k}}^{e}(\omega'')\hat{A}_{\mathbf{k}'}^{h'}(\omega''') \\
& + \psi_{\mathbf{k}'}^{h'e'}(\bar{\omega})(1 - F_{\mathbf{k}}^{e} + n_B(\omega'))V_{\mathbf{kk}'\mathbf{kk}'}^{eh'he'} 2i\mathrm{Im}\varepsilon_{\mathbf{k}-\mathbf{k}'}^{\mathrm{R},-1}(\omega')\hat{A}_{\mathbf{k}}^{e}(\omega'')\hat{A}_{\mathbf{k}'}^{h'}(\omega''') \\
& + \psi_{\mathbf{k}}^{he'}(\bar{\omega})(1 - F_{\mathbf{k}'}^{h'} + n_B(\omega'))V_{\mathbf{kk}'\mathbf{kk}'}^{eh'e'h'} 2i\mathrm{Im}\varepsilon_{\mathbf{k}-\mathbf{k}'}^{\mathrm{R},-1}(\omega')\hat{A}_{\mathbf{k}}^{h'}(\omega'')\hat{A}_{\mathbf{k}'}^{h}(\omega''') \\
& + \psi_{\mathbf{k}'}^{h'e}(\bar{\omega})(1 - F_{\mathbf{k}}^{e'} + n_B(\omega'))V_{\mathbf{kk}'\mathbf{kk}'}^{h'e'he'} 2i\mathrm{Im}\varepsilon_{\mathbf{k}-\mathbf{k}'}^{\mathrm{R},-1}(\omega')\hat{A}_{\mathbf{k}}^{e}(\omega'')\hat{A}_{\mathbf{k}'}^{e'}(\omega''') \quad \Big]
\end{aligned}
\tag{B.8}
$$

Using $\int_{-\infty}^{+\infty} \frac{\mathrm{d}\bar{\omega}}{2\pi} \int_{-\infty}^{+\infty} \mathrm{d}t e^{i(\omega-\bar{\omega})t} = \int_{-\infty}^{+\infty} \mathrm{d}\bar{\omega}\delta(\omega-\bar{\omega})$ each $\bar{\omega}$ is replaced by ω, therefore the correlation terms are coupled to the frequency ω. The incomplete integral over τ can be re-expressed using the Dirac identity, thereby introducing a Cauchy principal value and a δ-function. Furthermore for the sake of shortness $\Delta\omega = \omega' + \omega'' + \omega''' - \bar{\omega}$ has been introduced.

$$
\begin{aligned}
i\hbar \sum_{\mathbf{k}',e',e'',h',h''} \int_{-\infty}^{+\infty} \frac{\mathrm{d}\omega'}{2\pi} \int_{-\infty}^{+\infty} \frac{\mathrm{d}\omega''}{2\pi} \int_{-\infty}^{+\infty} \frac{\mathrm{d}\omega'''}{2\pi} \left\{ i\mathcal{P}\left(\frac{1}{\Delta\omega}\right) + \pi\delta(\Delta\omega) \right\} \\
\times \Big[\quad & \psi_{\mathbf{k}'}^{h'e'}(\omega)(1 - F_{\mathbf{k}}^{h} + n_B(\omega'))V_{\mathbf{kk}'\mathbf{kk}'}^{eh'he'} 2i\mathrm{Im}\varepsilon_{\mathbf{k}-\mathbf{k}'}^{\mathrm{R},-1}(\omega')\hat{A}_{\mathbf{k}'}^{e'}(\omega'')\hat{A}_{\mathbf{k}}^{h}(\omega''') \\
& + \psi_{\mathbf{k}}^{he''}(\omega)(1 - F_{\mathbf{k}'}^{e'} + n_B(\omega'))V_{\mathbf{kk}'\mathbf{kk}'}^{ee'e''e'} 2i\mathrm{Im}\varepsilon_{\mathbf{k}-\mathbf{k}'}^{\mathrm{R},-1}(\omega')\hat{A}_{\mathbf{k}'}^{e'}(\omega'')\hat{A}_{\mathbf{k}}^{h}(\omega''') \\
& + \psi_{\mathbf{k}}^{h''e}(\omega)(1 - F_{\mathbf{k}'}^{h'} + n_B(\omega'))V_{\mathbf{kk}'\mathbf{kk}'}^{h''h'hh'} 2i\mathrm{Im}\varepsilon_{\mathbf{k}-\mathbf{k}'}^{\mathrm{R},-1}(\omega')\hat{A}_{\mathbf{k}}^{e}(\omega'')\hat{A}_{\mathbf{k}'}^{h'}(\omega''') \\
& + \psi_{\mathbf{k}'}^{h'e'}(\omega)(1 - F_{\mathbf{k}}^{e} + n_B(\omega'))V_{\mathbf{kk}'\mathbf{kk}'}^{eh'he'} 2i\mathrm{Im}\varepsilon_{\mathbf{k}-\mathbf{k}'}^{\mathrm{R},-1}(\omega')\hat{A}_{\mathbf{k}}^{e}(\omega'')\hat{A}_{\mathbf{k}'}^{h'}(\omega''') \\
& + \psi_{\mathbf{k}}^{h'e}(\omega)(1 - F_{\mathbf{k}'}^{h'} + n_B(\omega'))V_{\mathbf{kk}'\mathbf{kk}'}^{eh'e'h'} 2i\mathrm{Im}\varepsilon_{\mathbf{k}-\mathbf{k}'}^{\mathrm{R},-1}(\omega')\hat{A}_{\mathbf{k}}^{h'}(\omega'')\hat{A}_{\mathbf{k}'}^{h}(\omega''') \\
& + \psi_{\mathbf{k}'}^{he'}(\omega)(1 - F_{\mathbf{k}}^{e'} + n_B(\omega'))V_{\mathbf{kk}'\mathbf{kk}'}^{h'e'he'} 2i\mathrm{Im}\varepsilon_{\mathbf{k}-\mathbf{k}'}^{\mathrm{R},-1}(\omega')\hat{A}_{\mathbf{k}}^{e}(\omega'')\hat{A}_{\mathbf{k}'}^{e'}(\omega''') \quad \Big]
\end{aligned}
\tag{B.9}
$$

In the following the quasi-particle approximation is applied, therefore the interaction is considered weak. The imaginary part of the retarded Green's functions is defined as spectral function, which enables another possible solution by first determining the retarded self-energy and successively calculate the spectral function. Here $\Sigma_{\mathbf{k}}^{\mathrm{R},\lambda\lambda'} = \Delta_{\mathbf{k}}^{\lambda\lambda'} + i\Gamma_{\mathbf{k}}^{\lambda\lambda'}$ is chosen to be independent of the frequency. In the time and frequency domain one therefore obtains:

$$
G_{\mathbf{k}}^{\mathrm{R},\lambda}(t-t') = \theta(t-t')e^{-\frac{i}{\hbar}(\varepsilon_{\mathbf{k}}^{0,\lambda} - \Sigma_{\mathbf{k}}^{\mathrm{R},\lambda})(t-t')} \tag{B.10}
$$

$$
G_{\mathbf{k}}^{\mathrm{R},\lambda}(\omega) = \frac{1}{\hbar\omega - \varepsilon_{\mathbf{k}}^{0,\lambda} - \Sigma_{\mathbf{k}}^{\mathrm{R},\lambda}} \tag{B.11}
$$

$$
\hat{A}_{\mathbf{k}}^{\lambda}(\omega) = \frac{1}{\pi}\mathrm{Im}G_{\mathbf{k}}^{\mathrm{R},\lambda}(\omega) = \frac{1}{\pi}\frac{\gamma}{(\hbar\omega - \tilde{\varepsilon}_{\mathbf{k}}^{\lambda})^2 + \gamma^2} \tag{B.12}
$$

Hence, the imaginary part of the self-energy $\Gamma_{\mathbf{k}}^{\lambda\lambda'} = \gamma$ determines the quasi-particle broadening, which is here taken to be constant in $\mathbf{k}$ and independent of the frequency, while the real part renormalizes the single-particle energies $\tilde{\varepsilon}_{\mathbf{k}}^{\lambda} = \varepsilon_{\mathbf{k}}^{0,\lambda} + \Delta_{\mathbf{k}}^{\lambda\lambda'}$.

The remaining frequency integrals are successively solved starting from the inner-most integral over ω'''. The Cauchy principle value can be solved using the Kramers-Kronig relations, that translates the imaginary part of a complex function to the real part and vice versa. For the remaining integral on ω'' the convolution theorem can be exploited. Here the retarded/advanced Green's functions in the time domain can be inserted, resulting in the multiplication of exponential functions. Therefore, the single-particle energies add, as well as the dephasing γ. Overall the integrals yield:

$$\begin{aligned}&\int\limits_{-\infty}^{+\infty} \frac{\mathrm{d}\omega''}{2\pi} \hat{A}^{\lambda}_{\mathbf{k}}(\omega'') \int\limits_{-\infty}^{+\infty} \frac{\mathrm{d}\omega'''}{2\pi} \left\{ i\mathcal{P}\left(\frac{1}{\Delta\omega}\right) + \pi\delta(\Delta\omega) \right\} \hat{A}^{\lambda'}_{\mathbf{k}'}(\omega''') \\ &= \frac{1}{(2\pi)^2} \frac{i}{\hbar} \frac{1}{\hbar\omega - \hbar\omega' - \varepsilon^{\lambda}_{\mathbf{k}} - \varepsilon^{\lambda'}_{\mathbf{k}'} + 2i\gamma}\end{aligned} \tag{B.13}$$

Therefore, a new spectral function arises, that combines both energy poles. This result is inserted into Eq. (B.9) to obtain Eq. (4.105) and (4.106) in the main text.

C. Numerical Parameters

C.1. Ab-initio Fitted Parameters for the Coulomb Interaction

	MoS_2	$MoSe_2$	WS_2	WSe_2
γ in (nm)	0.1932	0.2232	0.2130	0.2297
δ in (nm^2)	0.00395	- 0.00356	0.00720	0.00174
A in (nm^2)	0.08758	0.09546	0.08818	0.09574
U_2 in (meV)	810	837	712	715
U_3 in (meV)	367	376	354	360

Table C.1.: Fitted parameters for the Coulomb interaction, taken from Ref. [36].

C.2. Ab-initio Fitted Parameters for the Microscopic Dielectric Function

	MoS_2	$MoSe_2$	WS_2	WSe_2
a in ($1/nm^2$)	238.3	285.6	394.7	243.0
b	17.836	11.635	29.931	20.764
c in (nm)	0.5107	0.1979	0.5440	0.5761
h in (nm)	0.2740	0.4298	0.1578	0.2489
e	5.739	6.303	4.497	5.305
ε_2	3.077	3.148	2.979	3.028
ε_3	2.509	2.510	2.494	2.481

Table C.2.: Fitted parameters for the microscopic dielectric function, taken from Ref. [36].

C.3. TMD Model Parameters

material	a in (nm)	m_e in (m_0)	m_h in (m_0)	E_G in (meV)	E_X in (meV)
MoS_2	0.3180	0.46	0.41	2638	1900
$MoSe_2$	0.3320	0.31	0.48	2355	1550
WS_2	0.3191	0.31	0.37	2775	2000
WSe_2	0.3325	0.29	0.36	2360	1650

Table C.3.: Model parameters for the four different TMD monolayers. Given are the effective masses of electrons and holes, the band gap from the Wannier interpolation and the spectral position of the A-exciton.

C.4. Interlayer Exciton Model Parameters

material	m_e in (m_0)	m_h in (m_0)	a_{lat} in (nm)	d in (nm)
MoS_2/WS_2	0.42	0.34	0.319	0.615
$MoSe_2/WSe_2$	0.49	0.35	0.332	0.647
material, stacking	$\lvert D_\pm \rvert$ in (pA nm)	V in (meV)	ϕ in (°)	
MoS_2/WS_2, AA	0.17/0.04 $\times 522\frac{e}{\hbar}$	12.4	81.5	
MoS_2/WS_2, AB	0.04/0.10 $\times 522\frac{e}{\hbar}$	1.8	154.5	
$MoSe_2/WSe_2$, AA	0.22/0.06 $\times 443\frac{e}{\hbar}$	11.8	79.5	
$MoSe_2/WSe_2$, AB	0.04/0.12 $\times 443\frac{e}{\hbar}$	1.8	155.2	

Table C.4.: Parameters of the two bilayers systems for different stacking order, obtained from Ref. [50]. Effective masses, lattice constants, the strength of the current operator matrix elements and the parametrization of the Moiré potential are presented above.

C.5. Nanobubble TB Parameters

ε_0	-2.17187 eV
ε_2	-2.07972 eV
t_0	-0.326583 eV
$t_{0\pm2}$	0.561734 eV
t_2	-0.411327 eV
$t_{\mp2\pm2}$	-0.355268 eV
t'_0	-0.0537226 eV
$t'_{0\pm2}$	0.052774 eV
t'_2	0.052774 eV
$t'_{\mp2\pm2}$	-0.123627 eV

Table C.5.: TB parameters for the nanobubble model. ε denote orbital energies while t and t' denote the hopping parameters of the nearest and next-nearest neighbour Mo-atoms, as presented in [96].

List of Publications

1. D. Erben, A. Steinhoff, C. Gies, G. Schönhoff, T.O. Wehling and F. Jahnke,
   Excitation-Induced Transition to Indirect Band Gaps in Atomically Thin Transition-Metal Dichalcigenide Semiconductors
   Phys. Rev. B **98**, 035434 (2018)

2. D. Erben, A. Steinhoff, M. Lorke and F. Jahnke,
   Quantitative and Qualitative Analysis of Charge Carrier Densities in Optically Excited TMD Monolayers,
   in preparation for submission

3. C. Carmesin, M. Lorke, M. Florian, D. Erben, A. Schulz, T. O. Wehling and F. Jahnke,
   Quantum-Dot-Like States in Molybdenum Disulfide Nanostructure Due to the Interplay of Local Surface Wrinkling, Strains, and Dielectric Confinement
   Nano Lett. **19**, 3182 (2018)

4. F. Lohof, A. Steinhoff, M. Florian, M. Lorke, D. Erben, F. Jahnke and C. Gies,
   Prospects and Limitations of Transition Metal Dichalcogenide Laser Gain Materials,
   Nano Lett. **19**, 210 (2019)

Bibliography

[1] K. S. Novoselov, A. K. Geim, S. V. Morozov, D. Jiang, Y. Zhang, S. V. Dubonos, I. V. Grigorieva, and A. A. Firsov. Electric field effect in atomically thin carbon films. *Science*, 306(5696):666–669, October 2004. PMID: 15499015.

[2] A. K. Geim and I. V. Grigorieva. Van der waals heterostructures. *Nature*, 499(7459):419–425, July 2013.

[3] A. K. Geim and K. S. Novoselov. The rise of graphene. *Nature Materials*, 6(3):183–191, March 2007.

[4] A. H. Castro Neto, F. Guinea, N. M. R. Peres, K. S. Novoselov, and A. K. Geim. The electronic properties of graphene. *Reviews of Modern Physics*, 81(1):109–162, January 2009.

[5] In Hyuk Son, Jong Hwan Park, Seongyong Park, Kwangjin Park, Sangil Han, Jaeho Shin, Seok-Gwang Doo, Yunil Hwang, Hyuk Chang, and Jang Wook Choi. Graphene balls for lithium rechargeable batteries with fast charging and high volumetric energy densities. *Nature Communications*, 8(1):1–11, November 2017.

[6] Gage Hills, Christian Lau, Andrew Wright, Samuel Fuller, Mindy D. Bishop, Tathagata Srimani, Pritpal Kanhaiya, Rebecca Ho, Aya Amer, Yosi Stein, Denis Murphy, Arvind, Anantha Chandrakasan, and Max M. Shulaker. Modern microprocessor built from complementary carbon nanotube transistors. *Nature*, 572(7771):595–602, August 2019.

[7] R. I Christy. Sputtered MoS2 lubricant coating improvements. *Thin Solid Films*, 73(2):299–307, November 1980.

[8] Kin Fai Mak, Changgu Lee, James Hone, Jie Shan, and Tony F. Heinz. Atomically thin MoS_2: a new direct-gap semiconductor. *Physical Review Letters*, 105(13):136805, September 2010.

[9] Yi Zhang, Tay-Rong Chang, Bo Zhou, Yong-Tao Cui, Hao Yan, Zhongkai Liu, Felix Schmitt, James Lee, Rob Moore, Yulin Chen, Hsin Lin, Horng-Tay Jeng, Sung-Kwan Mo, Zahid Hussain, Arun Bansil, and Zhi-Xun Shen. Direct observation of the transition from indirect to direct bandgap in atomically thin epitaxial $MoSe_2$. *Nature Nanotechnology*, 9(2):111–115, February 2014.

[10] Chendong Zhang, Yuxuan Chen, Amber Johnson, Ming-Yang Li, Lain-Jong Li, Patrick C. Mende, Randall M. Feenstra, and Chih-Kang Shih. Probing critical point energies of transition metal dichalcogenides: Surprising indirect gap of single layer WSe_2. *Nano Letters*, 15(10):6494–6500, October 2015.

[11] Wei-Ting Hsu, Li-Syuan Lu, Dean Wang, Jing-Kai Huang, Ming-Yang Li, Tay-Rong Chang, Yi-Chia Chou, Zhen-Yu Juang, Horng-Tay Jeng, Lain-Jong Li, and Wen-Hao Chang. Evidence of indirect gap in monolayer WSe_2. *Nature Communications*, 8(1):1–7, October 2017.

[12] F. Cadiz, E. Courtade, C. Robert, G. Wang, Y. Shen, H. Cai, T. Taniguchi, K. Watanabe, H. Carrere, D. Lagarde, M. Manca, T. Amand, P. Renucci, S. Tongay, X. Marie, and B. Urbaszek. Excitonic linewidth approaching the homogeneous limit in MoS_2-based van der waals heterostructures. *Physical Review X*, 7(2):021026, May 2017.

[13] Hong Wang, Xiangwei Huang, Junhao Lin, Jian Cui, Yu Chen, Chao Zhu, Fucai Liu, Qingsheng Zeng, Jiadong Zhou, Peng Yu, Xuewen Wang, Haiyong He, Siu Hon Tsang, Weibo Gao, Kazu Suenaga, Fengcai Ma, Changli Yang, Li Lu, Ting Yu, Edwin Hang Tong Teo, Guangtong Liu, and Zheng Liu. High-quality monolayer superconductor $NbSe_2$ grown by chemical vapour deposition. *Nature Communications*, 8(1):1–8, August 2017.

[14] T. Dvir, F. Massee, L. Attias, M. Khodas, M. Aprili, C. H. L. Quay, and H. Steinberg. Spectroscopy of bulk and few-layer superconducting $NbSe_2$ with van der waals tunnel junctions. *Nature Communications*, 9(1):1–6, February 2018.

[15] Robert Oliva, Magdalena Laurien, Filip Dybala, Jan Kopaczek, Ying Qin, Sefaattin Tongay, Oleg Rubel, and Robert Kudrawiec. Pressure dependence of direct optical transitions in ReS_2 and $ReSe_2$. *npj 2D Materials and Applications*, 3(1):1–8, May 2019.

[16] Jurong Zhang, Ermiao Sun, Xiaolei Feng, Hanyu Liu, Simon A. T. Redfern, V. Kanchana, Guangtao Liu, and Hongbo Wang. Phase transition and superconductivity

in ReS_2, $ReSe_2$ and $ReTe_2$. *Physical Chemistry Chemical Physics*, 20(46):29472–29479, November 2018.

[17] Jiadong Zhou, Jia Shi, Qingsheng Zeng, Yu Chen, Lin Niu, Fucai Liu, Ting Yu, Kazu Suenaga, Xinfeng Liu, Junhao Lin, and Zheng Liu. InSe monolayer: synthesis, structure and ultra-high second-harmonic generation. *2D Materials*, 5(2):025019, March 2018.

[18] Yuan Cao, Valla Fatemi, Shiang Fang, Kenji Watanabe, Takashi Taniguchi, Efthimios Kaxiras, and Pablo Jarillo-Herrero. Unconventional superconductivity in magic-angle graphene superlattices. *Nature*, 556(7699):43–50, April 2018.

[19] Kha Tran, Galan Moody, Fengcheng Wu, Xiaobo Lu, Junho Choi, Kyounghwan Kim, Amritesh Rai, Daniel A. Sanchez, Jiamin Quan, Akshay Singh, Jacob Embley, André Zepeda, Marshall Campbell, Travis Autry, Takashi Taniguchi, Kenji Watanabe, Nanshu Lu, Sanjay K. Banerjee, Kevin L. Silverman, Suenne Kim, Emanuel Tutuc, Li Yang, Allan H. MacDonald, and Xiaoqin Li. Evidence for moiré excitons in van der waals heterostructures. *Nature*, 567(7746):71–75, March 2019.

[20] Qing Hua Wang, Kourosh Kalantar-Zadeh, Andras Kis, Jonathan N. Coleman, and Michael S. Strano. Electronics and optoelectronics of two-dimensional transition metal dichalcogenides. *Nature Nanotechnology*, 7(11):699–712, November 2012.

[21] Deep Jariwala, Vinod K. Sangwan, Lincoln J. Lauhon, Tobin J. Marks, and Mark C. Hersam. Emerging device applications for semiconducting two-dimensional transition metal dichalcogenides. *ACS Nano*, 8(2):1102–1120, February 2014.

[22] Andreas Pospischil, Marco M. Furchi, and Thomas Mueller. Solar-energy conversion and light emission in an atomic monolayer p-n diode. *Nature Nanotechnology*, 9(4):257–261, April 2014.

[23] Britton W. H. Baugher, Hugh O. H. Churchill, Yafang Yang, and Pablo Jarillo-Herrero. Optoelectronic devices based on electrically tunable p-n diodes in a monolayer dichalcogenide. *Nature Nanotechnology*, 9(4):262–267, April 2014.

[24] Jason S. Ross, Philip Klement, Aaron M. Jones, Nirmal J. Ghimire, Jiaqiang Yan, D. G. Mandrus, Takashi Taniguchi, Kenji Watanabe, Kenji Kitamura, Wang Yao, David H. Cobden, and Xiaodong Xu. Electrically tunable excitonic light-emitting diodes based on monolayer WSe_2 p-n junctions. *Nature Nanotechnology*, 9(4):268–272, April 2014.

[25] F. Withers, O. Del Pozo-Zamudio, A. Mishchenko, A. P. Rooney, A. Gholinia, K. Watanabe, T. Taniguchi, S. J. Haigh, A. K. Geim, A. I. Tartakovskii, and K. S. Novoselov. Light-emitting diodes by band-structure engineering in van der waals heterostructures. *Nature Materials*, 14(3):301–306, March 2015.

[26] Sanfeng Wu, Sonia Buckley, John R. Schaibley, Liefeng Feng, Jiaqiang Yan, David G. Mandrus, Fariba Hatami, Wang Yao, Jelena Vučković, Arka Majumdar, and Xiaodong Xu. Monolayer semiconductor nanocavity lasers with ultralow thresholds. *Nature*, 520(7545):69–72, April 2015.

[27] Yu Ye, Zi Jing Wong, Xiufang Lu, Xingjie Ni, Hanyu Zhu, Xianhui Chen, Yuan Wang, and Xiang Zhang. Monolayer excitonic laser. *Nature Photonics*, 9(11):733–737, November 2015.

[28] Omid Salehzadeh, Mehrdad Djavid, Nhung Hong Tran, Ishiang Shih, and Zetian Mi. Optically pumped two-dimensional MoS2 lasers operating at room-temperature. *Nano Letters*, 15(8):5302–5306, August 2015.

[29] Yongzhuo Li, Jianxing Zhang, Dandan Huang, Hao Sun, Fan Fan, Jiabin Feng, Zhen Wang, and C. Z. Ning. Room-temperature continuous-wave lasing from monolayer molybdenum ditelluride integrated with a silicon nanobeam cavity. *Nature Nanotechnology*, 12(10):987–992, October 2017.

[30] F. Lohof, A. Steinhoff, M. Florian, M. Lorke, D. Erben, F. Jahnke, and C. Gies. Prospects and limitations of transition metal dichalcogenide laser gain materials. *Nano Letters*, 19(1):210–217, January 2019.

[31] Deji Akinwande, Nicholas Petrone, and James Hone. Two-dimensional flexible nanoelectronics. *Nature Communications*, 5(1):1–12, December 2014.

[32] Eva A. A. Pogna, Margherita Marsili, Domenico De Fazio, Stefano Dal Conte, Cristian Manzoni, Davide Sangalli, Duhee Yoon, Antonio Lombardo, Andrea C. Ferrari, Andrea Marini, Giulio Cerullo, and Deborah Prezzi. Photo-induced bandgap renormalization governs the ultrafast response of single-layer MoS_2. *ACS Nano*, 10(1):1182–1188, January 2016.

[33] Paul D. Cunningham, Aubrey T. Hanbicki, Kathleen M. McCreary, and Berend T. Jonker. Photoinduced bandgap renormalization and exciton binding energy reduction in WS_2. *ACS Nano*, 11(12):12601–12608, December 2017.

[34] E. J. Sie, A. Steinhoff, C. Gies, C. H. Lui, Q. Ma, M. Rösner, G. Schönhoff, F. Jahnke, T. O. Wehling, Y.-H. Lee, J. Kong, P. Jarillo-Herrero, and N. Gedik. Observation of exciton Redshift-Blueshift crossover in monolayer WS_2. *Nano Letters*, 17(7):4210–4216, July 2017.

[35] Miguel M. Ugeda, Aaron J. Bradley, Su-Fei Shi, Felipe H. da Jornada, Yi Zhang, Diana Y. Qiu, Wei Ruan, Sung-Kwan Mo, Zahid Hussain, Zhi-Xun Shen, Feng Wang, Steven G. Louie, and Michael F. Crommie. Giant bandgap renormalization and excitonic effects in a monolayer transition metal dichalcogenide semiconductor. *Nature Materials*, 13(12):1091, December 2014.

[36] A. Steinhoff, M. Florian, M. Rösner, G. Schönhoff, T. O. Wehling, and F. Jahnke. Exciton fission in monolayer transition metal dichalcogenide semiconductors. *Nature Communications*, 8(1):1166, October 2017.

[37] M. Rösner, C. Steinke, M. Lorke, C. Gies, F. Jahnke, and T. O. Wehling. Two-dimensional heterojunctions from nonlocal manipulations of the interactions. *Nano Letters*, 16(4):2322–2327, April 2016.

[38] Sven Borghardt, Jhih-Sian Tu, Florian Winkler, Jürgen Schubert, Willi Zander, Kristjan Leosson, and Beata E. Kardyna l. Engineering of optical and electronic band gaps in transition metal dichalcogenide monolayers through external dielectric screening. *Physical Review Materials*, 1(5):054001, October 2017.

[39] A. Steinhoff, J.-H. Kim, F. Jahnke, M. Rösner, D.-S. Kim, C. Lee, G. H. Han, M. S. Jeong, T. O. Wehling, and C. Gies. Efficient excitonic photoluminescence in direct and indirect band gap monolayer MoS2. *Nano Letters*, 15(10):6841–6847, October 2015.

[40] Hiram J. Conley, Bin Wang, Jed I. Ziegler, Richard F. Haglund, Sokrates T. Pantelides, and Kirill I. Bolotin. Bandgap engineering of strained monolayer and bilayer MoS2. *Nano Letters*, 13(8):3626–3630, August 2013.

[41] Maja Feierabend, Alexandre Morlet, Gunnar Berghäuser, and Ermin Malic. Impact of strain on the optical fingerprint of monolayer transition-metal dichalcogenides. *Physical Review B*, 96(4):045425, July 2017.

[42] Xiao-Xiao Zhang, Ting Cao, Zhengguang Lu, Yu-Chuan Lin, Fan Zhang, Ying Wang, Zhiqiang Li, James C. Hone, Joshua A. Robinson, Dmitry Smirnov, Steven G. Louie, and Tony F. Heinz. Magnetic brightening and control of dark excitons in monolayer WSe_2. *Nature Nanotechnology*, advance online publication, June 2017.

[43] G. Wang, C. Robert, M. M. Glazov, F. Cadiz, E. Courtade, T. Amand, D. Lagarde, T. Taniguchi, K. Watanabe, B. Urbaszek, and X. Marie. In-plane propagation of light in transition metal dichalcogenide monolayers: Optical selection rules. *Physical Review Letters*, 119(4):047401, July 2017.

[44] Fanyao Qu, A. C. Dias, Jiyong Fu, L. Villegas-Lelovsky, and David L. Azevedo. Tunable spin and valley dependent magneto-optical absorption in molybdenum disulfide quantum dots. *Scientific Reports*, 7:41044, January 2017.

[45] Di Xiao, Gui-Bin Liu, Wanxiang Feng, Xiaodong Xu, and Wang Yao. Coupled spin and valley physics in monolayers of $\mathrm{MoS_2}$ and other group-VI dichalcogenides. *Physical Review Letters*, 108(19):196802, May 2012.

[46] Xiaodong Xu, Wang Yao, Di Xiao, and Tony F. Heinz. Spin and pseudospins in layered transition metal dichalcogenides. *Nature Physics*, 10(5):343–350, May 2014.

[47] A. Steinhoff, M. Rösner, F. Jahnke, T. O. Wehling, and C. Gies. Influence of excited carriers on the optical and electronic properties of MoS2. *Nano Letters*, 14(7):3743–3748, July 2014.

[48] Keliang He, Nardeep Kumar, Liang Zhao, Zefang Wang, Kin Fai Mak, Hui Zhao, and Jie Shan. Tightly bound excitons in monolayer $\mathrm{WSe_2}$. *Physical Review Letters*, 113(2):026803, July 2014.

[49] Alexey Chernikov, Claudia Ruppert, Heather M. Hill, Albert F. Rigosi, and Tony F. Heinz. Population inversion and giant bandgap renormalization in atomically thin WS_2 layers. *Nature Photonics*, 9(7):466, July 2015.

[50] Fengcheng Wu, Timothy Lovorn, and A. H. MacDonald. Theory of optical absorption by interlayer excitons in transition metal dichalcogenide heterobilayers. *Physical Review B*, 97(3):035306, January 2018.

[51] Chendong Zhang, Chih-Piao Chuu, Xibiao Ren, Ming-Yang Li, Lain-Jong Li, Chuanhong Jin, Mei-Yin Chou, and Chih-Kang Shih. Interlayer couplings, moiré patterns, and 2D electronic superlattices in MoS2/WSe_2 hetero-bilayers. *Science Advances*, 3(1):e1601459, January 2017.

[52] Simone Bertolazzi, Jacopo Brivio, and Andras Kis. Stretching and breaking of ultrathin MoS2. *ACS Nano*, 5(12):9703–9709, December 2011.

[53] K. S. Novoselov, A. K. Geim, S. V. Morozov, D. Jiang, M. I. Katsnelson, I. V. Grigorieva, S. V. Dubonos, and A. A. Firsov. Two-dimensional gas of massless dirac fermions in graphene. *Nature*, 438(7065):197–200, November 2005.

[54] Shengxi Huang, Xi Ling, Liangbo Liang, Jing Kong, Humberto Terrones, Vincent Meunier, and Mildred S. Dresselhaus. Probing the interlayer coupling of twisted bilayer MoS2 using photoluminescence spectroscopy. *Nano Letters*, 14(10):5500–5508, October 2014.

[55] Yi-Hsien Lee, Xin-Quan Zhang, Wenjing Zhang, Mu-Tung Chang, Cheng-Te Lin, Kai-Di Chang, Ya-Chu Yu, Jacob Tse-Wei Wang, Chia-Seng Chang, Lain-Jong Li, and Tsung-Wu Lin. Synthesis of large-area MoS2 atomic layers with chemical vapor deposition. *Advanced Materials*, 24(17):2320–2325, 2012.

[56] G. Kioseoglou, A. T. Hanbicki, M. Currie, A. L. Friedman, and B. T. Jonker. Optical polarization and intervalley scattering in single layers of MoS2 and MoSe_2. *Scientific Reports*, 6:25041, April 2016.

[57] Diana Y. Qiu, Felipe H. da Jornada, and Steven G. Louie. Optical spectrum of MoS_2: many-body effects and diversity of exciton states. *Physical Review Letters*, 111(21):216805, November 2013.

[58] Weijie Zhao, Zohreh Ghorannevis, Leiqiang Chu, Minglin Toh, Christian Kloc, Ping-Heng Tan, and Goki Eda. Evolution of electronic structure in atomically thin sheets of WS_2 and WSe_2. *ACS Nano*, 7(1):791–797, January 2013.

[59] Yinsheng Guo, Dezheng Sun, Bin Ouyang, Archana Raja, Jun Song, Tony F. Heinz, and Louis E. Brus. Probing the dynamics of the metallic-to-semiconducting structural phase transformation in MoS2 crystals. *Nano Letters*, 15(8):5081–5088, August 2015.

[60] Shiang Fang, Rodrick Kuate Defo, Sharmila N. Shirodkar, Simon Lieu, Georgios A. Tritsaris, and Efthimios Kaxiras. Ab initio tight-binding hamiltonian for transition metal dichalcogenides. *Physical Review B*, 92(20):205108, November 2015.

[61] A. R. Klots, A. K. M. Newaz, Bin Wang, D. Prasai, H. Krzyzanowska, Junhao Lin, D. Caudel, N. J. Ghimire, J. Yan, B. L. Ivanov, K. A. Velizhanin, A. Burger, D. G. Mandrus, N. H. Tolk, S. T. Pantelides, and K. I. Bolotin. Probing excitonic states in suspended two-dimensional semiconductors by photocurrent spectroscopy. *Scientific Reports*, 4:6608, October 2014.

[62] Jue Wang, Jenny Ardelean, Yusong Bai, Alexander Steinhoff, Matthias Florian, Frank Jahnke, Xiaodong Xu, Mackillo Kira, James Hone, and X.-Y. Zhu. Optical generation of high carrier densities in 2D semiconductor heterobilayers. *Science Advances*, 5(9):eaax0145, September 2019.

[63] Andrea Splendiani, Liang Sun, Yuanbo Zhang, Tianshu Li, Jonghwan Kim, Chi-Yung Chim, Giulia Galli, and Feng Wang. Emerging photoluminescence in monolayer MoS2. *Nano Letters*, 10(4):1271–1275, April 2010.

[64] Alexey Chernikov, Timothy C. Berkelbach, Heather M. Hill, Albert Rigosi, Yilei Li, Ozgur Burak Aslan, David R. Reichman, Mark S. Hybertsen, and Tony F. Heinz. Exciton binding energy and nonhydrogenic rydberg series in monolayer WS_2. *Physical Review Letters*, 113(7):076802, August 2014.

[65] Gerd Plechinger, Philipp Nagler, Ashish Arora, Robert Schmidt, Alexey Chernikov, Andrés Granados del Águila, Peter C. M. Christianen, Rudolf Bratschitsch, Christian Schüller, and Tobias Korn. Trion fine structure and coupled spin-valley dynamics in monolayer tungsten disulfide. *Nature Communications*, 7(1):1–9, September 2016.

[66] Jingzhi Shang, Xiaonan Shen, Chunxiao Cong, Namphung Peimyoo, Bingchen Cao, Mustafa Eginligil, and Ting Yu. Observation of excitonic fine structure in a 2D transition-metal dichalcogenide semiconductor. *ACS Nano*, 9(1):647–655, January 2015.

[67] Yumeng You, Xiao-Xiao Zhang, Timothy C. Berkelbach, Mark S. Hybertsen, David R. Reichman, and Tony F. Heinz. Observation of biexcitons in monolayer WSe¡sub¿¡b¿2¡/b¿¡/sub¿. *Nature Physics*, 11(6):477–481, June 2015.

[68] Yanhao Tang, Kin Fai Mak, and Jie Shan. Long valley lifetime of dark excitons in single-layer WSe 2. *Nature Communications*, 10(1):1–7, September 2019.

[69] Hyun Seok Lee, Min Su Kim, Hyun Kim, and Young Hee Lee. Identifying multiexcitons in MoS_2 monolayers at room temperature. *Physical Review B*, 93(14):140409, April 2016.

[70] David K. Zhang, Daniel W. Kidd, and Kálmán Varga. Excited biexcitons in transition metal dichalcogenides. *Nano Letters*, 15(10):7002–7005, October 2015.

[71] Guan-Hao Peng, Ping-Yuan Lo, Wei-Hua Li, Yan-Chen Huang, Yan-Hong Chen, Chi-Hsuan Lee, Chih-Kai Yang, and Shun-Jen Cheng. Distinctive signatures of the spin-

and momentum-forbidden dark exciton states in the photoluminescence of strained WSe_2 monolayers under thermalization. *Nano Letters*, 19(4):2299–2312, April 2019.

[72] M. Szyniszewski, E. Mostaani, N. D. Drummond, and V. I. Fal'ko. Binding energies of trions and biexcitons in two-dimensional semiconductors from diffusion quantum monte carlo calculations. *Physical Review B*, 95(8):081301, February 2017.

[73] Ilkka Kylänpää and Hannu-Pekka Komsa. Binding energies of exciton complexes in transition metal dichalcogenides and effect of dielectric environment. *Physical Review B*, 92(20), November 2015. arXiv: 1508.06737.

[74] Alexander Steinhoff, Matthias Florian, Akshay Singh, Kha Tran, Mirco Kolarczik, Sophia Helmrich, Alexander W. Achtstein, Ulrike Woggon, Nina Owschimikow, Frank Jahnke, and Xiaoqin Li. Biexciton fine structure in monolayer transition metal dichalcogenides. *Nature Physics*, 14(12):1199–1204, December 2018.

[75] Maja Feierabend, Zahra Khatibi, Gunnar Berghäuser, and Ermin Malic. Dark exciton based strain sensing in tungsten-based transition metal dichalcogenides. *Physical Review B*, 99(19):195454, May 2019.

[76] Sabrine Ayari and Sihem Jaziri. Dynamics of free and localized excitons in two-dimensional transition metal dichalcogenides. *physica status solidi (b)*, 256(6):1800682, June 2019.

[77] Ziliang Ye, Ting Cao, Kevin O'Brien, Hanyu Zhu, Xiaobo Yin, Yuan Wang, Steven G. Louie, and Xiang Zhang. Probing excitonic dark states in single-layer tungsten disulphide. *Nature*, 513(7517):214–218, September 2014.

[78] Gerd Plechinger, Philipp Nagler, Julia Kraus, Nicola Paradiso, Christoph Strunk, Christian Schüller, and Tobias Korn. Identification of excitons, trions and biexcitons in single-layer WS_2. *physica status solidi (RRL) - Rapid Research Letters*, 9(8):457–461, August 2015.

[79] Kai Hao, Judith F. Specht, Philipp Nagler, Lixiang Xu, Kha Tran, Akshay Singh, Chandriker Kavir Dass, Christian Schüller, Tobias Korn, Marten Richter, Andreas Knorr, Xiaoqin Li, and Galan Moody. Neutral and charged inter-valley biexcitons in monolayer MoSe 2. *Nature Communications*, 8(1):1–7, June 2017.

[80] Fanyao Qu, Helena Bragança, Railson Vasconcelos, Fujun Liu, S.-J. Xie, and Hao Zeng. Controlling valley splitting and polarization of dark- and bi-excitons in monolayer WS_2 by a tilted magnetic field. *2D Materials*, 6(4):045014, July 2019.

[81] Andor Kormányos, Viktor Zólyomi, Neil D. Drummond, Péter Rakyta, Guido Burkard, and Vladimir I. Fal'ko. Monolayer MoS_2: trigonal warping, the Γ valley, and spin-orbit coupling effects. *Physical Review B*, 88(4):045416, July 2013.

[82] Lei Wang, Zhuo Wang, Hai-Yu Wang, Gustavo Grinblat, Yu-Li Huang, Dan Wang, Xiao-Hui Ye, Xian-Bin Li, Qiaoliang Bao, AndrewThye-Shen Wee, Stefan A. Maier, Qi-Dai Chen, Min-Lin Zhong, Cheng-Wei Qiu, and Hong-Bo Sun. Slow cooling and efficient extraction of c-exciton hot carriers in MoS 2 monolayer. *Nature Communications*, 8(1):1–8, January 2017.

[83] C. Steinke, D. Mourad, M. Rösner, M. Lorke, C. Gies, F. Jahnke, G. Czycholl, and T. O. Wehling. Noninvasive control of excitons in two-dimensional materials. *Physical Review B*, 96(4):045431, July 2017.

[84] Hongliang Shi, Hui Pan, Yong-Wei Zhang, and Boris I. Yakobson. Quasiparticle band structures and optical properties of strained monolayer MoS_2 and WS_2. *Physical Review B*, 87(15):155304, April 2013.

[85] Shiyuan Gao and Li Yang. Renormalization of the quasiparticle band gap in doped two-dimensional materials from many-body calculations. *Physical Review B*, 96(15):155410, October 2017.

[86] Fang Liu, Mark E. Ziffer, Kameron R. Hansen, Jue Wang, and Xiaoyang Zhu. Direct determination of band-gap renormalization in the photoexcited monolayer MoS_2. *Physical Review Letters*, 122(24):246803, June 2019.

[87] J. C. Slater and G. F. Koster. Simplified LCAO method for the periodic potential problem. *Physical Review*, 94(6):1498–1524, June 1954.

[88] P. Vogl, Harold P. Hjalmarson, and John D. Dow. A semi-empirical tight-binding theory of the electronic structure of semiconductors. *Journal of Physics and Chemistry of Solids*, 44(5):365–378, January 1983.

[89] Per-Olov Löwdin. On the Non-Orthogonality problem connected with the use of atomic wave functions in the theory of molecules and crystals. *The Journal of Chemical Physics*, 18(3):365–375, March 1950.

[90] Gui-Bin Liu, Wen-Yu Shan, Yugui Yao, Wang Yao, and Di Xiao. Three-band tight-binding model for monolayers of group-VIB transition metal dichalcogenides. *Physical Review B*, 88(8):085433, August 2013.

[91] A. C. Dias, Fanyao Qu, David L. Azevedo, and Jiyong Fu. Band structure of monolayer transition-metal dichalcogenides and topological properties of their nanoribbons: Next-nearest-neighbor hopping. *Physical Review B*, 98(7):075202, August 2018.

[92] Habib Rostami, Rafael Roldán, Emmanuele Cappelluti, Reza Asgari, and Francisco Guinea. Theory of strain in single-layer transition metal dichalcogenides. *Physical Review B*, 92(19):195402, November 2015.

[93] Habib Rostami, Ali G. Moghaddam, and Reza Asgari. Effective lattice hamiltonian for monolayer MoS_2: tailoring electronic structure with perpendicular electric and magnetic fields. *Physical Review B*, 88(8):085440, August 2013.

[94] E. Ridolfi, D. Le, T. S. Rahman, E. R. Mucciolo, and C. H. Lewenkopf. A tight-binding model for MoS2monolayers. *Journal of Physics: Condensed Matter*, 27(36):365501, August 2015.

[95] E. Cappelluti, R. Roldán, J. A. Silva-Guillén, P. Ordejón, and F. Guinea. Tight-binding model and direct-gap/indirect-gap transition in single-layer and multilayer MoS_2. *Physical Review B*, 88(7):075409, August 2013.

[96] Christian Carmesin, Michael Lorke, Matthias Florian, Daniel Erben, Alexander Schulz, Tim O. Wehling, and Frank Jahnke. Quantum-dot-like states in molybdenum disulfide nanostructures due to the interplay of local surface wrinkling, strain, and dielectric confinement. *Nano Letters*, 19(5):3182–3186, May 2019.

[97] E. Khestanova, F. Guinea, L. Fumagalli, A. K. Geim, and I. V. Grigorieva. Universal shape and pressure inside bubbles appearing in van der waals heterostructures. *Nature Communications*, 7:ncomms12587, August 2016.

[98] Gabriella D. Shepard, Obafunso A. Ajayi, Xiangzhi Li, X.-Y. Zhu, James Hone, and Stefan Strauf. Nanobubble induced formation of quantum emitters in monolayer semiconductors. *2D Materials*, 4(2):021019, 2017.

[99] Pascale Senellart, Glenn Solomon, and Andrew White. High-performance semiconductor quantum-dot single-photon sources. *Nature Nanotechnology*, 12(11):1026–1039, November 2017.

[100] Johannes Kern, Iris Niehues, Philipp Tonndorf, Robert Schmidt, Daniel Wigger, Robert Schneider, Torsten Stiehm, Steffen Michaelis de Vasconcellos, Doris E. Reiter, Tilmann Kuhn, and Rudolf Bratschitsch. Nanoscale positioning of single-photon emitters in atomically thin WSe_2. *Advanced Materials*, 28(33):7101–7105, September 2016.

[101] Artur Branny, Gang Wang, Santosh Kumar, Cedric Robert, Benjamin Lassagne, Xavier Marie, Brian D. Gerardot, and Bernhard Urbaszek. Discrete quantum dot like emitters in monolayer $MoSe_2$: spatial mapping, magneto-optics, and charge tuning. *Applied Physics Letters*, 108(14):142101, April 2016.

[102] Artur Branny, Santosh Kumar, Raphaël Proux, and Brian D. Gerardot. Deterministic strain-induced arrays of quantum emitters in a two-dimensional semiconductor. *Nature Communications*, 8:ncomms15053, May 2017.

[103] Carmen Palacios-Berraquero, Dhiren M. Kara, Alejandro R.-P. Montblanch, Matteo Barbone, Pawel Latawiec, Duhee Yoon, Anna K. Ott, Marko Loncar, Andrea C. Ferrari, and Mete Atatüre. Large-scale quantum-emitter arrays in atomically thin semiconductors. *Nature Communications*, 8:ncomms15093, May 2017.

[104] Matthew R. Rosenberger, Chandriker Kavir Dass, Hsun-Jen Chuang, Saujan V. Sivaram, Kathleen M. McCreary, Joshua R. Hendrickson, and Berend T. Jonker. Quantum calligraphy: Writing single-photon emitters in a two-dimensional materials platform. *ACS Nano*, 13(1):904–912, January 2019.

[105] Archana Raja, Andrey Chaves, Jaeeun Yu, Ghidewon Arefe, Heather M. Hill, Albert F. Rigosi, Timothy C. Berkelbach, Philipp Nagler, Christian Schüller, Tobias Korn, Colin Nuckolls, James Hone, Louis E. Brus, Tony F. Heinz, David R. Reichman, and Alexey Chernikov. Coulomb engineering of the bandgap and excitons in two-dimensional materials. *Nature Communications*, 8:15251, May 2017.

[106] Sverre Froyen and Walter A. Harrison. Elementary prediction of linear combination of atomic orbitals matrix elements. *Physical Review B*, 20(6):2420–2422, September 1979.

[107] P. Hohenberg and W. Kohn. Inhomogeneous electron gas. *Physical Review*, 136(3B):B864–B871, November 1964.

[108] Gerd Czycholl. *Theoretische Festkörperphysik Band 1: Grundlagen: Phononen und Elektronen in Kristallen*. Springer Spektrum, 4 edition, 2016. DOI: 10.1007/978-3-662-47141-8.

[109] W. Kohn and L. J. Sham. Self-consistent equations including exchange and correlation effects. *Physical Review*, 140(4A):A1133–A1138, November 1965.

[110] W. Kohn. Nobel lecture: Electronic structure of matter - wave functions and density functionals. *Reviews of Modern Physics*, 71(5):1253–1266, October 1999.

[111] John P. Perdew, Kieron Burke, and Matthias Ernzerhof. Generalized gradient approximation made simple. *Physical Review Letters*, 77(18):3865–3868, October 1996.

[112] John P. Perdew, Matthias Ernzerhof, and Kieron Burke. Rationale for mixing exact exchange with density functional approximations. *The Journal of Chemical Physics*, 105(22):9982–9985, December 1996.

[113] Jochen Heyd, Gustavo E. Scuseria, and Matthias Ernzerhof. Hybrid functionals based on a screened coulomb potential. *The Journal of Chemical Physics*, 118(18):8207–8215, April 2003.

[114] F. Aryasetiawan and O. Gunnarsson. The GW-method. *Reports on Progress in Physics*, 61(3):237–312, March 1998.

[115] John P. Perdew. Density functional theory and the band gap problem. *International Journal of Quantum Chemistry*, 28(S19):497–523, 1985.

[116] M. Shishkin and G. Kresse. Implementation and performance of the frequency-dependent GW method within the PAW framework. *Physical Review B*, 74(3):035101, July 2006.

[117] Patrick Duffy, Delano P. Chong, Mark E. Casida, and Dennis R. Salahub. Assessment of kohn-sham density-functional orbitals as approximate dyson orbitals for the calculation of electron-momentum-spectroscopy scattering cross sections. *Physical Review A*, 50(6):4707–4728, December 1994.

[118] Arash A. Mostofi, Jonathan R. Yates, Young-Su Lee, Ivo Souza, David Vanderbilt, and Nicola Marzari. wannier90: A tool for obtaining maximally-localised wannier functions. *Computer Physics Communications*, 178(9):685–699, May 2008.

[119] Nicola Marzari, Arash A. Mostofi, Jonathan R. Yates, Ivo Souza, and David Vanderbilt. Maximally localized wannier functions: Theory and applications. *Reviews of Modern Physics*, 84(4):1419–1475, October 2012.

[120] Andor Kormányos, Viktor Zólyomi, Neil D. Drummond, and Guido Burkard. Spin-orbit coupling, quantum dots, and qubits in monolayer transition metal dichalcogenides. *Physical Review X*, 4(1), March 2014. arXiv: 1310.7720.

[121] Z. Y. Zhu, Y. C. Cheng, and U. Schwingenschlögl. Giant spin-orbit-induced spin splitting in two-dimensional transition-metal dichalcogenide semiconductors. *Physical Review B*, 84(15):153402, October 2011.

[122] J. P. Echeverry, B. Urbaszek, T. Amand, X. Marie, and I. C. Gerber. Splitting between bright and dark excitons in transition metal dichalcogenide monolayers. *Physical Review B*, 93(12):121107, March 2016.

[123] Søren Ulstrup, Antonija Grubišić Čabo, Deepnarayan Biswas, Jonathon M. Riley, Maciej Dendzik, Charlotte E. Sanders, Marco Bianchi, Cephise Cacho, Dan Matselyukh, Richard T. Chapman, Emma Springate, Phil D. C. King, Jill A. Miwa, and Philip Hofmann. Spin and valley control of free carriers in single-layer WS_2. *Physical Review B*, 95(4):041405, January 2017.

[124] Weijie Zhao, R. M. Ribeiro, Minglin Toh, Alexandra Carvalho, Christian Kloc, A. H. Castro Neto, and Goki Eda. Origin of indirect optical transitions in few-layer MoS2, WS_2, and WSe_2. *Nano Letters*, 13(11):5627–5634, November 2013.

[125] Agnieszka Kuc, Thomas Heine, and Andras Kis. Electronic properties of transition-metal dichalcogenides. *MRS Bulletin*, 40(7):577–584, July 2015.

[126] A. Kuc, N. Zibouche, and T. Heine. Influence of quantum confinement on the electronic structure of the transition metal sulfide TS2. *Physical Review B*, 83(24):245213, June 2011.

[127] A. Steinhoff, M. Florian, M. Rösner, M. Lorke, T. O. Wehling, C. Gies, and F. Jahnke. Nonequilibrium carrier dynamics in transition metal dichalcogenide semiconductors. *2D Materials*, 3(3):031006, August 2016.

[128] Joshua O. Island, Agnieszka Kuc, Erik H. Diependaal, Rudolf Bratschitsch, Herre S. J. van der Zant, Thomas Heine, and Andres Castellanos-Gomez. Precise and reversible band gap tuning in single-layer $MoSe_2$ by uniaxial strain. *Nanoscale*, 8(5):2589–2593, January 2016.

[129] Hartmut Haug and Antti-Pekka Jauho. *Quantum Kinetics in Transport and Optics of Semiconductors*. Springer Series in Solid-State Sciences. Springer-Verlag, Berlin Heidelberg, 2 edition, 2008. DOI: 10.1007/978-3-540-73564-9.

[130] Mackillo Kira and Stephan W. Koch. *Semiconductor Quantum Optics*. Cambridge University Press, Cambridge; New York, 2011.

[131] Gerd Czycholl. *Theoretische Festkörperphysik Band 2: Anwendungen: Nichtgleichgewicht, Verhalten in äußeren Feldern, kollektive Phänomene*. Springer Spektrum, 4 edition, 2017. DOI: 10.1007/978-3-662-53701-5.

[132] R. Binder and S. W. Koch. Nonequilibrium semiconductor dynamics. *Progress in Quant. Electron.*, 19(4/5), 1995.

[133] K. Henneberger and V. May. Nonequilibrium green's functions and kinetic equations for highly excited semiconductors: I. general considerations. *Physica A: Statistical Mechanics and its Applications*, 138(3):537–556, October 1986.

[134] K. Henneberger. Resonant laser excitation and electron-hole kinetics of a semiconductor: I. nonequilibrium green's function treatment and fundamental equations. *Physica A: Statistical Mechanics and its Applications*, 150(2):419–438, June 1988.

[135] P Danielewicz. Quantum theory of nonequilibrium processes, i. *Annals of Physics*, 152(2):239–304, February 1984.

[136] Wilfried Schäfer and Martin Wegener. *Semiconductor optics and transport phenomena*. Springer, Berlin; New York, 2002.

[137] D. Kremp, M. Schlanges, and W.-D. Kraeft. *Quantum Statistics of Nonideal Plasmas*. Springer, Berlin, 2005.

[138] L. P. Kadanoff and G. Baym. *Quantum Statistical Mechanics*. W. A. Benjamin, 1962.

[139] M. Kira, F. Jahnke, W. Hoyer, and S. W. Koch. Quantum theory of spontaneous emission and coherent effects in semiconductor microstructures. *Progress in Quantum Electronics*, 23(6):189–279, 1999.

[140] Alexander L. Fetter and John Dirk Walecka. *Quantum Theory of Many-Particle Systems*. Dover Publications Inc., Mineola, New York, 2003.

[141] M. Gell-Mann and F. Low. Bound states in quantum field theory. *Phys. Rev.*, 84, 1951.

[142] L. V. Keldysh. Diagram technique for non-equilibrium processes. *Soviet Physics - JETP*, 20:1018, 1965.

[143] J. Schwinger. Brownian motion of a quantum oscillator. *J. Math. Phys.*, 2:407, 1961.

[144] Lars Hedin. New method for calculating the one-particle green's function with application to the electron-gas problem. *Physical Review*, 139(3A):A796–A823, August 1965.

[145] Gordon Baym and Leo P. Kadanoff. Conservation laws and correlation functions. *Physical Review*, 124(2):287–299, October 1961.

[146] P. Gartner, L. Bányai, and H. Haug. Coulomb screening in the two-time keldysh-green-function formalism. *Physical Review B*, 62(11):7116–7120, September 2000.

[147] R. Binder and S. W. Koch. Nonequilibrium semiconductor dynamics. *Progress in Quant. Electron.*, 19(4/5), 1995.

[148] Alexander Steinhoff. *Korrelationseffekte angeregter Ladungsträger in Halbleiter-Nanostrukturen am Beispiel von InGaAs-Quantenpunkten und atomaren MoS_2-Monolagen*. Dissertation, Universität Bremen, Bremen, November 2014.

[149] Michael Lorke. *Optical gain and laser properties of semiconductor quantum-dot systems*. Dissertation, Universität Bremen, Bremen, February 2009.

[150] F. Jahnke, M. Kira, and S. W. Koch. Linear and nonlinear optical properties of quantum confined excitons in semiconductor microcavities. *Z. Physik B*, 104:559, 1997.

[151] F. Jahnke, M. Kira, W. Hoyer, and S. W. Koch. Influence of correlation effects on the excitonic semiconductor photoluminescence. *phys. stat. sol (b)*, 221(1):189, 2000.

[152] Eike Verdenhalven, Rolf Binder, Andreas Knorr, and Ermin Malić. Derivation of the screened bloch equations and application to carbon nanostructures. *Chemical Physics*, 413:3–10, February 2013.

[153] Paul C. Martin and Julian Schwinger. Theory of many-particle systems. i. *Physical Review*, 115(6):1342–1373, September 1959.

[154] A. Steinhoff, T. O. Wehling, and M. Rösner. Frequency-dependent substrate screening of excitons in atomically thin transition metal dichalcogenide semiconductors. *Physical Review B*, 98(4):045304, July 2018.

[155] Th. Bornath, D. Kremp, and M. Schlanges. Two-particle problem in a nonequilibrium many-particle system. *Physical Review E*, 60(6):6382–6394, December 1999.

[156] D. Erben, A. Steinhoff, C. Gies, G. Schönhoff, T. O. Wehling, and F. Jahnke. Excitation-induced transition to indirect band gaps in atomically thin transition-metal dichalcogenide semiconductors. *Physical Review B*, 98(3):035434, July 2018.

[157] R. E. Groenewald, M. Rösner, G. Schönhoff, S. Haas, and T. O. Wehling. Valley plasmonics in transition metal dichalcogenides. *Physical Review B*, 93(20):205145, May 2016.

[158] M. Rösner, E. Şaşıoğlu, C. Friedrich, S. Blügel, and T. O. Wehling. Wannier function approach to realistic coulomb interactions in layered materials and heterostructures. *Physical Review B*, 92(8):085102, August 2015.

[159] W. Hanke and L. J. Sham. Local-field and excitonic effects in the optical spectrum of a covalent crystal. *Physical Review B*, 12(10):4501–4511, November 1975.

[160] G. Schönhoff, M. Rösner, R. E. Groenewald, S. Haas, and T. O. Wehling. Interplay of screening and superconductivity in low-dimensional materials. *Physical Review B*, 94(13):134504, October 2016.

[161] Matthias Florian, Malte Hartmann, Alexander Steinhoff, Julian Klein, Alexander W. Holleitner, Jonathan J. Finley, Tim O. Wehling, Michael Kaniber, and Christopher Gies. The dielectric impact of layer distances on exciton and trion binding energies in van der waals heterostructures. *Nano Letters*, 18(4):2725–2732, April 2018.

[162] Pierluigi Cudazzo, Ilya V. Tokatly, and Angel Rubio. Dielectric screening in two-dimensional insulators: Implications for excitonic and impurity states in graphane. *Physical Review B*, 84(8):085406, August 2011.

[163] L. V. Keldysh. Coulomb interaction in thin semiconductor and semimetal films. *JETP Lett.*, 29(11), June 1979.

[164] Timothy C. Berkelbach, Mark S. Hybertsen, and David R. Reichman. Theory of neutral and charged excitons in monolayer transition metal dichalcogenides. *Physical Review B*, 88(4):045318, July 2013.

[165] Aidan. P. Rooney, Aleksey Kozikov, Alexander N. Rudenko, Eric Prestat, Matthew J. Hamer, Freddie Withers, Yang Cao, Kostya S. Novoselov, Mikhail I. Katsnelson, Ro-

man Gorbachev, and Sarah J. Haigh. Observing imperfection in atomic interfaces for van der waals heterostructures. *Nano Letters*, 17(9):5222–5228, September 2017.

[166] Michael Rohlfing. Electronic excitations from a perturbative LDA $+ GdW$ approach. *Physical Review B*, 82(20):205127, November 2010.

[167] Kirsten T. Winther and Kristian S. Thygesen. Band structure engineering in van der waals heterostructures via dielectric screening: the GΔW method. *2D Materials*, 4(2):025059, 2017.

[168] Hendrik J. Monkhorst and James D. Pack. Special points for brillouin-zone integrations. *Physical Review B*, 13(12):5188–5192, June 1976.

[169] Gunnar Berghäuser and Ermin Malic. Analytical approach to excitonic properties of MoS_2. *Physical Review B*, 89(12):125309, March 2014.

[170] Andreas V. Stier, Kathleen M. McCreary, Berend T. Jonker, Junichiro Kono, and Scott A. Crooker. Exciton diamagnetic shifts and valley zeeman effects in monolayer WS 2 and MoS 2 to 65 tesla. *Nature Communications*, 7(1):1–8, February 2016.

[171] Maciej Koperski, Maciej R. Molas, Ashish Arora, Karol Nogajewski, Miroslav Bartos, Jan Wyzula, Diana Vaclavkova, Piotr Kossacki, and Marek Potemski. Orbital, spin and valley contributions to zeeman splitting of excitonic resonances in $MoSe_2$, WSe_2 and WS_2 monolayers. *2D Materials*, 6(1):015001, October 2018.

[172] A. V. Stier, N. P. Wilson, K. A. Velizhanin, J. Kono, X. Xu, and S. A. Crooker. Magnetooptics of exciton rydberg states in a monolayer semiconductor. *Physical Review Letters*, 120(5):057405, feb 2018.

[173] Alexey Chernikov, Arend M. van der Zande, Heather M. Hill, Albert F. Rigosi, Ajanth Velauthapillai, James Hone, and Tony F. Heinz. Electrical tuning of exciton binding energies in monolayer WS_2. *Physical Review Letters*, 115(12):126802–126807, 2015.

[174] S. Latini, T. Olsen, and K. S. Thygesen. Excitons in van der waals heterostructures: The important role of dielectric screening. *Physical Review B*, 92(24):245123, December 2015.

[175] Yafeng Xie, Saifeng Zhang, Yuanxin Li, Ningning Dong, Xiaoyan Zhang, Lei Wang, Weimin Liu, Ivan M. Kislyakov, Jean-Michel Nunzi, Hongji Qi, Long Zhang, and Jun Wang. Layer-modulated two-photon absorption in MoS2: probing the shift of the excitonic dark state and band-edge. *Photonics Research*, 7(7):762–770, July 2019.

[176] G. Aivazian, Zhirui Gong, Aaron M. Jones, Rui-Lin Chu, J. Yan, D. G. Mandrus, Chuanwei Zhang, David Cobden, Wang Yao, and X. Xu. Magnetic control of valley pseudospin in monolayer WSe¡sub¿¡b¿2¡/b¿¡/sub¿. *Nature Physics*, 11(2):148–152, February 2015.

[177] Yilei Li, Jonathan Ludwig, Tony Low, Alexey Chernikov, Xu Cui, Ghidewon Arefe, Young Duck Kim, Arend M. van der Zande, Albert Rigosi, Heather M. Hill, Suk Hyun Kim, James Hone, Zhiqiang Li, Dmitry Smirnov, and Tony F. Heinz. Valley splitting and polarization by the zeeman effect in monolayer $\mathrm{MoSe_2}$. *Physical Review Letters*, 113(26):266804, December 2014.

[178] Antonija Grubišić Čabo, Jill A. Miwa, Signe S. Grønborg, Jonathon M. Riley, Jens C. Johannsen, Cephise Cacho, Oliver Alexander, Richard T. Chapman, Emma Springate, Marco Grioni, Jeppe V. Lauritsen, Phil D. C. King, Philip Hofmann, and Søren Ulstrup. Observation of ultrafast free carrier dynamics in single layer MoS2. *Nano Letters*, 15(9):5883–5887, September 2015.

[179] R. Bertoni, C. W. Nicholson, L. Waldecker, H. Hübener, C. Monney, U. De Giovannini, M. Puppin, M. Hoesch, E. Springate, R. T. Chapman, C. Cacho, M. Wolf, A. Rubio, and R. Ernstorfer. Generation and evolution of spin-, valley-, and layer-polarized excited carriers in inversion-symmetric $\mathrm{WSe_2}$. *Physical Review Letters*, 117(27):277201, December 2016.

[180] Yizhi Ge and Amy Y. Liu. Phonon-mediated superconductivity in electron-doped single-layer MoS_2: a first-principles prediction. *Physical Review B*, 87(24):241408, June 2013.

[181] M. Rösner, S. Haas, and T. O. Wehling. Phase diagram of electron-doped dichalcogenides. *Physical Review B*, 90(24):245105, December 2014.

[182] Matthew Z. Mayers, Timothy C. Berkelbach, Mark S. Hybertsen, and David R. Reichman. Binding energies and spatial structures of small carrier complexes in monolayer transition-metal dichalcogenides via diffusion monte carlo. *Physical Review B*, 92(16):161404, October 2015.

[183] Yuxuan Lin, Xi Ling, Lili Yu, Shengxi Huang, Allen L. Hsu, Yi-Hsien Lee, Jing Kong, Mildred S. Dresselhaus, and Tomás Palacios. Dielectric screening of excitons and trions in single-layer MoS2. *Nano Letters*, 14(10):5569–5576, 2014.

[184] Mads L. Trolle, Thomas G. Pedersen, and Valerie Véniard. Model dielectric function for 2D semiconductors including substrate screening. *Scientific Reports*, 7:39844, January 2017.

[185] Yeongsu Cho and Timothy C. Berkelbach. Environmentally sensitive theory of electronic and optical transitions in atomically thin semiconductors. *Physical Review B*, 97(4):041409, January 2018.

[186] Philipp Steinleitner, Philipp Merkl, Philipp Nagler, Joshua Mornhinweg, Christian Schüller, Tobias Korn, Alexey Chernikov, and Rupert Huber. Direct observation of ultrafast exciton formation in a monolayer of WSe_2. *Nano Letters*, 17(3):1455–1460, March 2017.

[187] L. Meckbach, J. Hader, U. Huttner, J. Neuhaus, J. T. Steiner, T. Stroucken, J. V. Moloney, and S. W. Koch. Ultrafast band-gap renormalization and build-up of optical gain in monolayer MoTe_2. *Physical Review B*, 101(7):075401, February 2020.

[188] Alexander W. Bataller, Robert A. Younts, Avinash Rustagi, Yiling Yu, Hossein Ardekani, Alexander Kemper, Linyou Cao, and Kenan Gundogdu. Dense Electron-Hole plasma formation and ultralong charge lifetime in monolayer MoS2 via material tuning. *Nano Letters*, 19(2):1104–1111, February 2019.

[189] Yuanzheng Li, Jia Shi, Heyu Chen, Yang Mi, Wenna Du, Xinyu Sui, Chuanxiu Jiang, Weizhen Liu, Haiyang Xu, and Xinfeng Liu. Slow cooling of high-energy c excitons is limited by intervalley-transfer in monolayer MoS2. *Laser & Photonics Reviews*, 13(4):1800270, 2019.

[190] Malte Selig, Gunnar Berghäuser, Archana Raja, Philipp Nagler, Christian Schüller, Tony F. Heinz, Tobias Korn, Alexey Chernikov, Ermin Malic, and Andreas Knorr. Excitonic linewidth and coherence lifetime in monolayer transition metal dichalcogenides. *Nature Communications*, 7(1):1–6, November 2016.

[191] Maurizia Palummo, Marco Bernardi, and Jeffrey C. Grossman. Exciton radiative lifetimes in two-dimensional transition metal dichalcogenides. *Nano Letters*, 15(5):2794–2800, May 2015.

[192] H. H. Fang, B. Han, C. Robert, M. A. Semina, D. Lagarde, E. Courtade, T. Taniguchi, K. Watanabe, T. Amand, B. Urbaszek, M. M. Glazov, and X. Marie. Control of the exciton radiative lifetime in van der waals heterostructures. *Physical Review Letters*, 123(6):067401, August 2019.

[193] Søren Ulstrup, Antonija Grubišić Čabo, Jill A. Miwa, Jonathon M. Riley, Signe S. Grønborg, Jens C. Johannsen, Cephise Cacho, Oliver Alexander, Richard T. Chapman, Emma Springate, Marco Bianchi, Maciej Dendzik, Jeppe V. Lauritsen, Phil D. C. King, and Philip Hofmann. Ultrafast band structure control of a two-dimensional heterostructure. *ACS Nano*, 10(6):6315–6322, June 2016.

[194] Xiaopeng Fan, Weihao Zheng, Hongjun Liu, Xiujuan Zhuang, Peng Fan, Yanfang Gong, Honglai Li, Xueping Wu, Ying Jiang, Xiaoli Zhu, Qinglin Zhang, Hong Zhou, Wei Hu, Xiao Wang, Xiangfeng Duan, and Anlian Pan. Nonlinear photoluminescence in monolayer WS 2 : parabolic emission and excitation fluence-dependent recombination dynamics. *Nanoscale*, 9(21):7235–7241, 2017.

[195] Mingu Kang, Beomyoung Kim, Sae Hee Ryu, Sung Won Jung, Jimin Kim, Luca Moreschini, Chris Jozwiak, Eli Rotenberg, Aaron Bostwick, and Keun Su Kim. Universal mechanism of band-gap engineering in transition-metal dichalcogenides. *Nano Letters*, 17(3):1610–1615, March 2017.

[196] G. Manzke, T. Klähn, and K. Henneberger. Quantum kinetics and linear optical response of semiconductors. *physica status solidi (c)*, 0(5):1480–1483, 2003.

[197] M. Lorke, J. Seebeck, T. R. Nielsen, P. Gartner, and F. Jahnke. Excitation dependence of the homogeneous linewidths in quantum dots. *physica status solidi c*, 3(7):2393–2396, 2006.

[198] Alejandro Molina-Sánchez, Maurizia Palummo, Andrea Marini, and Ludger Wirtz. Temperature-dependent excitonic effects in the optical properties of single-layer MoS_2. *Physical Review B*, 93(15):155435, April 2016.

[199] Hiral Patel, Lujie Huang, Cheol-Joo Kim, Jiwoong Park, and Matt W. Graham. Stacking angle-tunable photoluminescence from interlayer exciton states in twisted bilayer graphene. *Nature Communications*, 10(1):1–7, March 2019.

[200] A. Mishchenko, J. S. Tu, Y. Cao, R. V. Gorbachev, J. R. Wallbank, M. T. Greenaway, V. E. Morozov, S. V. Morozov, M. J. Zhu, S. L. Wong, F. Withers, C. R. Woods, Y.-J. Kim, K. Watanabe, T. Taniguchi, E. E. Vdovin, O. Makarovsky, T. M. Fromhold, V. I. Fal'ko, A. K. Geim, L. Eaves, and K. S. Novoselov. Twist-controlled resonant tunnelling in graphene/boron nitride/graphene heterostructures. *Nature Nanotechnology*, 9(10):808–813, October 2014.

[201] Jonas Kiemle, Florian Sigger, Michael Lorke, Bastian Miller, Kenji Watanabe, Takashi Taniguchi, Alexander Holleitner, and Ursula Wurstbauer. Hybridized indirect excitons in MoS2/WS_2 heterobilayers. *arXiv:1812.10697 [cond-mat]*, December 2018. arXiv: 1812.10697.

[202] Philipp Nagler, Gerd Plechinger, Mariana V. Ballottin, Anatolie Mitioglu, Sebastian Meier, Nicola Paradiso, Christoph Strunk, Alexey Chernikov, Peter C. M. Christianen, Christian Schüller, and Tobias Korn. Interlayer exciton dynamics in a dichalcogenide monolayer heterostructure. *2D Materials*, 4(2):025112, June 2017.

[203] Simon Ovesen, Samuel Brem, Christopher Linderälv, Mikael Kuisma, Tobias Korn, Paul Erhart, Malte Selig, and Ermin Malic. Interlayer exciton dynamics in van der waals heterostructures. *Communications Physics*, 2(1):1–8, February 2019.

[204] Chenhao Jin, Emma C. Regan, Danqing Wang, M. Iqbal Bakti Utama, Chan-Shan Yang, Jeffrey Cain, Ying Qin, Yuxia Shen, Zhiren Zheng, Kenji Watanabe, Takashi Taniguchi, Sefaattin Tongay, Alex Zettl, and Feng Wang. Identification of spin, valley and moiré quasi-angular momentum of interlayer excitons. *Nature Physics*, pages 1–5, August 2019.

[205] Pasqual Rivera, John R. Schaibley, Aaron M. Jones, Jason S. Ross, Sanfeng Wu, Grant Aivazian, Philip Klement, Kyle Seyler, Genevieve Clark, Nirmal J. Ghimire, Jiaqiang Yan, D. G. Mandrus, Wang Yao, and Xiaodong Xu. Observation of long-lived interlayer excitons in monolayer MoSe 2 -WSe 2 heterostructures. *Nature Communications*, 6(1):1–6, February 2015.

[206] Bastian Miller, Alexander Steinhoff, Borja Pano, Julian Klein, Frank Jahnke, Alexander Holleitner, and Ursula Wurstbauer. Long-lived direct and indirect interlayer excitons in van der waals heterostructures. *Nano Letters*, 17(9):5229–5237, September 2017.

[207] Hongyi Yu, Gui-Bin Liu, Jianju Tang, Xiaodong Xu, and Wang Yao. Moiré excitons: From programmable quantum emitter arrays to spin-orbit-coupled artificial lattices. *Science Advances*, 3(11):e1701696, November 2017.

[208] Kyle L. Seyler, Pasqual Rivera, Hongyi Yu, Nathan P. Wilson, Essance L. Ray, David G. Mandrus, Jiaqiang Yan, Wang Yao, and Xiaodong Xu. Signatures of moiré-trapped valley excitons in MoSe 2 /WSe 2 heterobilayers. *Nature*, 567(7746):66–70, March 2019.

[209] B. Amorim. General theoretical description of angle-resolved photoemission spectroscopy of van der waals structures. *Physical Review B*, 97(16):165414, April 2018.

[210] Pilkyung Moon and Mikito Koshino. Optical absorption in twisted bilayer graphene. *Physical Review B*, 87(20):205404, May 2013.

[211] Mikito Koshino. Interlayer interaction in general incommensurate atomic layers. *New Journal of Physics*, 17(1):015014, January 2015.

[212] Axel Esser, Erich Runge, Roland Zimmermann, and Wolfgang Langbein. Photoluminescence and radiative lifetime of trions in GaAs quantum wells. *Physical Review B*, 62(12):8232–8239, September 2000.

[213] Lucio Claudio Andreani, Francesco Tassone, and Franco Bassani. Radiative lifetime of free excitons in quantum wells. *Solid State Communications*, 77(9):641–645, March 1991.

Danksagung

Zum Abschluss dieser Arbeit möchte ich mich bei den Menschen bedanken, ohne die diese Arbeit nicht hätte entstehen können.

Mein Dank gilt zuallererst Herrn Prof. Dr. Jahnke, nicht nur für die Betreuung und das Gutachten der Dissertation und die zahlreichen fruchtbaren Diskussionen, sondern auch für die Aufnahme in die Arbeitsgruppe. Für die Übernahme des Zweitgutachtens bedanke ich mich bei Frau Prof. Dr. Caterina Cocchi von der Universität Oldenburg sehr herzlich.
Herrn Prof. Dr. Tim Wehling danke ich für die gute Zusammenarbeit und die vielen Diskussionen über die diversen Themen, die in diese Arbeit eingeflossen sind. Ich bedanke mich ebenfalls für die Bereitschaft als Prüfer zur Verfügung zu stehen. Des Weiteren möchte ich mich bei Frau Prof. Dr. Kathrin Sebald bedanken, welche ebenfalls als Prüferin bereit stand.
Meinen Kollegen und weiteren Betreuern Alexander Steinhoff, Michael Lorke, Matthias Florian und Christopher Gies gilt mein Dank ebenso für die Beantwortung meiner vielen Fragen wie für das Korrekturlesen dieser Dissertation. Für die produktive Zusammenarbeit und die vielen hilfreichen Diskussionen bedanke ich mich außerdem bei Christian Carmesin, Mawussey Segnon, Frederik Lohof und Joel Buchgeister. Euch gilt mein Dank auch für die hervorragende Arbeitsatmosphäre im Büro.
Ich möchte mich auch bei den Master- und Bachelor-Studenten für die produktive Zeit bedanken. Mein Dank gilt hierbei besonders Leon Hetzel, Laura Martens und Ruven Hübner, deren Betreuung ich zum Teil übernehmen durfte.
Bei Andreas Beuthner und Klaus Bowe bedanke ich mich für die technische Unterstützung im Büro.

Mein größter Dank gilt meiner Familie, meiner Frau Sina und meinem Sohn Felix Jonathan insbesondere. Ohne euch wäre diese Arbeit nie möglich gewesen und ich danke euch für eure Geduld und euer Verständnis sowie dafür mir immer den Rücken gestärkt und freigehalten zu haben.